NTNU – Trondheim
Norwegian University of
Science and Technology

Alternative Methods for Curing of TCO Thin Films

Lise Helmine Haugesten

Chemical Engineering and Biotechnology

Submission date:	June 2014
Supervisor:	Ingeborg Kaus, IMTE
Co-supervisor:	Fride Vullum-Bruer, IMT Katherine Inzani, IMT

Norwegian University of Science and Technology
Department of Materials Science and Engineering

Preface

This master thesis has been carried out at the Department of Materials Science and Engineering at the Norwegian University of Science and Technology (NTNU) during spring 2014 as part of a Master of Science degree in Chemical Engineering and Biotechnology. The thesis is a continuation of a specialization project carried out in the fall 2013.

I would like to thank my supervisor Adjunct Associate Professor Ingeborg Kaus and my two co-supervisors Associate Professor Fride Vullum-Bruer and PhD-candidate Katherine Inzani for the time and consideration you have put into my work. A special thanks goes to Fride Vullum-Bruer for giving guidance on the writing process. Additional thanks goes out to Yingda Yu, Julian R Tolchard, Sidsel Meli Hanetho, Sandra Helen Skjærvø, Eli Beate Larsen, John Walmsley and Pei Na Kui for help with the experimental work, training and providing answers to my questions.

I would like to thank Ursula Gibson and Morten Kildemo at the Department of Physics for guiding me with respect to the optical characterization and introducing me to the master students Nelly-Ann Molland and Thomas Brakstad who have been of great help.

A thanks goes to the nanolab staff for training and assistance, with a special thanks to Ken Roger Ervik and Espen Rogstad. In addition I would also like to thank the ceramics group, especially the solar group. Last but not least I want to thank my fellow students for sharing frustrations and long working hours in the study room.

Eli Beate Larsen performed the thermogravimetrical analysis in Figure C.10 in "Appendix C Study of Precipitation and Precursor Quality". The Auger electron spectroscopy measurements in Figure 4.1 were conducted by John Walmsley. Thomas Brakstad performed the measurements and modeling of the ellipsometry data that was used in section "4.7 Optical Properties".

I hereby declare that this master thesis has been executed independently and according to the rules and regulations of the Norwegian University of Science and Technology.

Trondheim, June 2014

Lise Helmine Haugesten

Abstract

Transparent conducting oxides have a unique combination of properties as they are both optical transparent in the visible region of the electromagnetic spectrum, and obtain a near-metallic conductivity. This makes them extensively used in a wide variety of technological applications. The industrial demand for developing better, cheaper, and faster methods for producing these materials is increasing continuously. Thus, the motivation for this master thesis is to find a cheaper and faster way to produce transparent conductive oxides while still retaining the optoelectronic properties. A possible way of doing this is by replacing the conventional furnace heat-treatment step of sol-gel derived transparent conductive oxides with photochemical activation. The aim of this work is hence to compare the quality of sol-gel derived indium tin oxide and indium zinc oxide thin films cured using thermal and ultraviolet radiation methods.

Indium tin oxide and indium zinc oxide thin films were prepared by spin coating a sol synthesized by an environmental friendly Pechini method onto glass and silicon substrates. The thin films were subsequently characterized with respect to crystal structure, morphology, optical properties, and electrical properties.

The thermally cured indium tin oxide and indium zinc oxide thin films obtained a non-directional phase pure cubic bixbyite crystal structure, while the ultraviolet curing at room temperature and 150 °C gave an amorphous structure. By studying the morphology of the thin films it could be observed that the thermal curing gave the highest homogeneity, while the ultraviolet curing at 150 °C gave the lowest homogeneity. The same trend was also found for surface roughness, where the lowest roughness was obtained for the thermally cured films. The thin films obtained a high optical transparency with an average value of 88-97 % in the visible region of the electromagnetic spectrum. No clear trend could be seen with regards to the effect of the different curing methods on the absolute value of the transparency, whereas an evident trend was seen for the curve shape. The transmission curves had an absorption band edge at about 300 nm, and a band gap of 3.8 eV and 3.7 eV was observed for indium tin oxide and indium zinc oxide, respectively. The optical constants refractive index and extinction coefficient indicates a difference in the optical properties for indium tin oxide and indium zinc oxide. For the thermally cured indium tin oxide thin films the lowest resistivity values obtained on glass and silicon substrates were 2.8×10^{-3} Ω cm and 2.2×10^{-3} Ω cm, respectively, while the lowest resistivity values obtained for the indium zinc oxide thin films on glass and silicon substrates were 0.4 Ω cm and 0.1 Ω cm, respectively. It was not possible to obtain resistivity measurements for any of the ultraviolet curing methods, indicating that these films are non-conducting. This is most likely due to incomplete decomposition of organics in the thin films.

Sammendrag

Transparente ledende oksider har den unike egenskapen av å være både optisk transparente i det synlige området av det elektromagnetiske spekteret og ha nær-metallisk ledningsevne. Dette gjør dem svært anvendelige innenfor en lang rekke teknologiske bruksområder. Den industrielle etterspørselen for å utvikle bedre, billigere og raskere metoder for å produsere disse materialene er stadig økende. Motivasjonen for denne masteroppgaven er derfor å finne en billigere og raskere måte å produsere transparente ledende oksider på og samtidig beholde de optoelektroniske egenskapene. En mulig måte å gjøre dette på er ved å erstatte det konvensjonelle varmebehandlingstrinnet i ovn av transparente ledende oksider produsert ved sol-gel metoder, med fotokjemisk aktivering. Hensikten med dette masterarbeidet er således å sammenligne kvaliteten av indiumtinnoksid og indiumsinkoksid tynnfilmer behandlet ved hjelp av termisk og ultrafiolett stråling.

Tynnfilmer av indiumtinnoksid og indiumsinkoksid ble laget gjennom en miljøvennlig Pechini metode og deponert på glass og silisium substrater ved hjelp av ”spin coating”. Tynnfilmene ble deretter karakterisert med hensyn til krystallstruktur, morfologi, optiske og elektriske egenskaper.

De termisk behandlede indiumtinnoksid og indiumsinkoksid tynnfilmene oppnår en kubisk bixbyite krystallstruktur av ren fase, mens ultrafiolett behandling ved rom-temperatur og 150 °C ga en amorf struktur. Ved å studere morfologien til tynnfilmene kan det observeres at den termiske behandlingen ga høyest homogenitet, mens ultrafiolett behandling ved 150 °C ga lavest homogenitet. Den samme rekkefølge ble også funnet for overflateruhet, hvor lavest ruhet ble oppnådd for de termisk behandlede filmene. Det ble observert godt reproduserbare verdier av høy optisk transparens med en gjennomsnittsverdi på 88 til 97 % i det synlige området av det elektromagnetiske spekteret for tynnfilmene. Ingen klar trend kan sees med hensyn til effekten av de forskjellige behandlingsmetodene på den absolutte verdien av transparensen, mens en tydelig trend ble sett for kurvefasongen. Transmisjonsspektrene hadde en båndabsorpsjonskant rundt 300 nm, og et bånd gap på 3,8 eV og 3,7 eV ble observert for henholdsvis indiumtinnoksid og indiumsinkoksid. De optiske konstantene brytningsindeks og ekstinksjonskoeffisient indikerer at det er en forskjell i de optiske egenskapene for indiumtinnoksid og indiumsinkoksid. Den laveste resistiviteten som ble oppnådd for de termisk behandlede indiumtinnoksid tynnfilmene deponert på glass- og silisiumsubstrater var henholdsvis $2{,}8\times10^{-3}$ Ω cm og $2{,}2\times10^{-3}$ Ω cm, mens den laveste resistiviteten som oppnås for indiumsinkoksid tynnfilmene deponert på glass- og silisiumsubstrater var henholdsvis 0,4 Ω cm og 0,1 Ω cm. Det var ikke mulig å foreta målinger av resistiviteten for noen av tynnfilmene behandlet med ultrafiolett stråling, noe som indikerer at disse filmene er ikke-ledende. Dette skyldes mest sannsynlig en ufullstendig nedbrytning av organiske materialer i tynnfilmene.

Table of contents

1. Introduction

Transparent conductive oxides (TCOs) are materials with a unique combination of transparent and conductive properties[1]. The main optoelectronic properties for TCOs are near-metallic conductivity, high optical transparency in the visible region of the electromagnetic spectrum, and high reflectance in the infrared region. There is a growing interest for these materials, which is reflected by the thousands of papers published the last few years concerning TCOs. TCO properties can be found in indium, tin, zinc, cadmium and gallium oxides. Together they make up what is called the TCO composition space. It is also common to use various mixtures of them. Most of the work on TCOs has been empirical, and even though the application history of TCOs is long, the theoretical understanding of the material is not complete [1]. The TCO industry is still dominated by minor variants of indium, tin, and zinc oxides, but there is an increasing realization that these materials are no longer sufficient to meet the needs of all TCO applications. The main TCO application areas are flat panel displays, energy efficient windows, and photovoltaic devices [1, 2]. Emerging application fields are transparent thin film transistors, flexible transparent electronics, organic light emitting diodes, electrochromic windows, and optical arrays [1].

Since the 1960s indium oxide doped with tin oxide, also known as indium tin oxide (ITO), has been the TCO of choice due to its optimal properties [2]. ITO has the best combination of electrical conductivity and optical transparency known to date. Environmental stability, reproducibility and good morphology add to the list of good properties. ITO has a large market share for use as a transparent electrode, which is one of its main applications [1]. A disadvantage with ITO is the price [3]. Indium is a limited resource. This combined with increasing usage makes ITO an expensive material causing a growing demand for less expensive materials. Despite this, it is predicted that ITO will continue to be important for the well established transparent electrode market, like the flat panel display industry, and for applications where performance matters more than price [3]. Another promising TCO candidate is indium oxide doped with zinc oxide, which exhibit rivaling or even exceeding electrical and optical properties compared to other TCOs [4-6]. Indium zinc oxide (IZO) has also attracted considerable interest due to the high possible doping level of zinc, which makes IZO a less expensive choice compared to ITO [7, 8].

The electrical properties of a thin film TCO depends on the preparation method, the deposition parameters used for the deposition technique, and the subsequent heat treatment step [9]. It has been shown that different fabrication methods yield comparable conductivity when adjusting the deposition parameters correctly. TCO thin films can be deposited by a range of techniques including direct current and radio frequency sputtering, chemical vapor deposition, spray pyrolysis, vacuum evaporation, pulsed laser deposition, and sol-gel methods combined with spin coating and dip coating.

When making metal-oxide films by a wet chemical method a subsequent curing step is necessary to get high quality films [10-13]. Conventionally, this is done at relatively high temperatures (400-700 °C) in a furnace for a long period of time to decompose and crystallize the film. Keeping a high temperature for a long time is both energy consuming and time consuming, making the heat treatment step costly. The high temperature also prevents these films from being compatible with flexible polymer substrates, as the substrates will decompose. When producing a solar cell the different layers need to be assembled in a specific sequence to avoid ruining the previous layers. Due to the high annealing temperature of TCOs the sequence of layers is fixed, as the TCO layer often has to be deposited first. The high curing temperature is therefore also negative with regards to the production of solar cells.

Flexible substrates have a major growth opportunity in the fields of thin film electronics and photovoltaics [3]. Using polymer substrates makes it possible to produce lightweight, low cost, transparent, shock resistant, and bendable electronics [14]. A transparent thin film transistor is shown in Figure 1.1 as an example of a high-performance flexible electronic device.

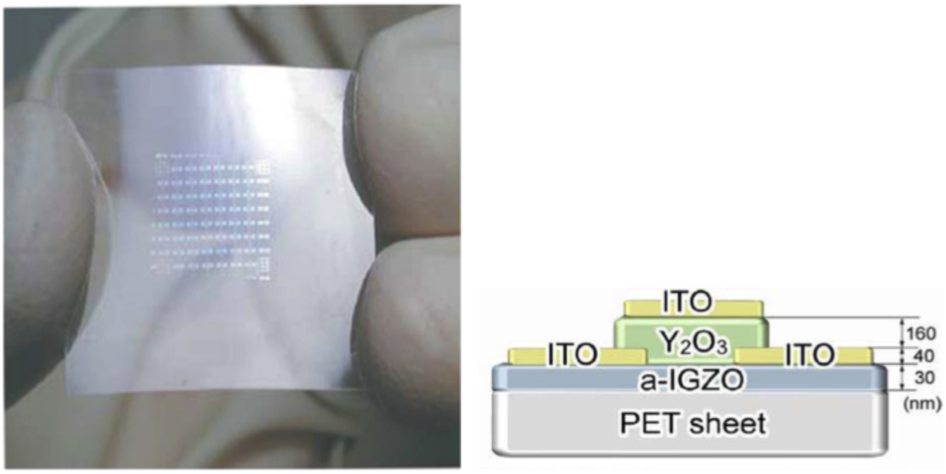

Figure 1.1: Room temperature fabricated flexible transparent thin film transistor. Left: A photograph of the transparent thin film transistor sheet. Right: A schematic model of the transparent thin film transistor. An amorphous metal oxide semiconductor is used for the active channel [14].

The industrial demand for better TCO materials is continuously increasing, and the need to develop better, cheaper, and faster methods to produce these materials needs to be investigated further. An alternative curing method could be photochemical activation of sol-gel derived thin films [12]. A cold conversion or curing technology for sol-gel films would considerably enlarge the applicability of these films, and curing by ultraviolet (UV) irradiation is found to be a promising technology [15]. Using wet chemical methods this curing method has proven to produce high-performance and operationally stable metal-oxide thin films at room temperature [12]. There are several motivational factors for why we would want to use a UV lamp instead of a furnace. A UV lamp gives a lower production cost. The curing step is more efficient as the curing is faster and only moderate heating is necessary. In addition, it is easy and cheap to implement a UV lamp into a production line. The small amounts of extra heat generated by the UV lamp makes it a suitable curing method for thin films on polymer substrates, thus flexible transparent electronics like the one in Figure 1.1 can be produced. The low curing temperature will also give more flexibility with regards to the production steps in a solar cell. Thin films produced by this method have shown comparable transistor mobility and operational stability as thermally cured thin films [12]. A range of metal oxides can be photo-chemically activated. For use in industrial applications chemicals in the synthesis can be switched with UV-decomposable additives/solvents, and the UV energy density can be increased.

Instead of a crystalline product, UV curing will generally give an amorphous film. Such thin films are often called amorphous metal oxide semiconductors (AOSs) instead of TCOs. A TCO and an amorphous metal oxide semiconductor have similar properties, but a lower conductivity is often seen for the amorphous metal oxide semiconductors due to the amorphous state of the films. Amorphous metal oxide semiconductor thin films with a high enough conductivity can replace TCOs in most applications. In addition to the TCO applications, amorphous metal oxide semiconductors with semiconducting electrical properties can be used in other applications. This includes the active channel layer in a thin film transistor as seen in Figure 1.1 and the a-Si:H active region in thin film solar cells as shown in Figure 1.2.

The main goal of this master thesis is to compare the quality of thin films prepared using a conventional heat treatment step and photochemical activation. These will be referred to as thermal and UV curing, respectively. This is done by performing UV curing at both room temperature and 150 °C and compare with thin films thermally cured using a rapid thermal process furnace at 530 °C. An environmental friendly modified Pechini method developed by Sunde et al. [16] is chosen to prepare the ITO and IZO solutions, which is deposited on glass and silicon substrates by spin coating. In addition to the main goal, studying the effect of composition and substrate on the thin films and the reproducibility will be emphasized. Characterization with respect to the optical and electrical properties, crystal structure, elemental composition, morphology, and topography will contribute to a wider understanding of how UV-curing, composition, and substrate influence the thin films and indicate necessary improvements of the process for further work.

1.2 Transparent Conductive Oxides in Solar Cells

The fastest growing segment of the TCO market is photovoltaic cells, where TCOs are widely used as transparent electrodes [1, 17]. Thin film solar cells are often fabricated in the superstrate configuration. This means that the light enters the active region through a glass substrate as can be seen in Figure 1.2, which illustrates a silicon thin film solar cell [18]. For this specific cell the fabrication commences from the front to the back, and the TCO front contact must be robust enough to resist all subsequent deposition layers and post-deposition treatments.

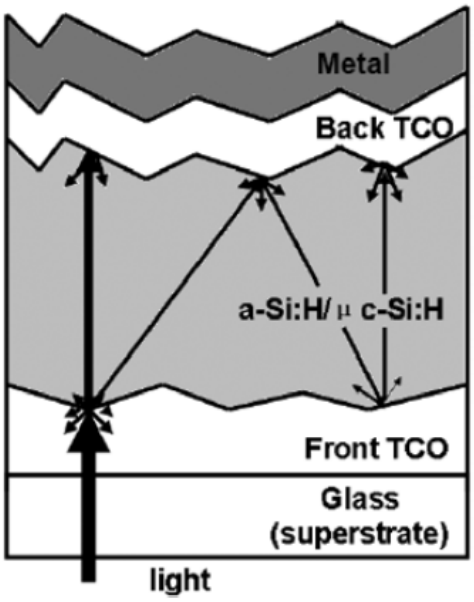

Figure 1.2: A schematic of the cross section of a thin film p–i–n solar cell with a-Si:H/μc-Si:H as absorber material and TCO as front and back contacts [18].

When the visible light hits the silicon semiconductor material in the solar cell in Figure 1.2, which has a much smaller band gap than the TCO, electrons will be excited from the valence band to the conduction band. The silicon layer is the active region, thus the region where the current is generated. This type of electron generation will not happen in the TCO layer, even though it is classified as an n-type semiconductor, because the TCO band gap is too big. The large band gap is necessary for the TCO to be transparent. Even though electrons are not generated inside the TCO by visible light, the TCO layer is able to conduct the electrons generated in the silicon semiconductor through mechanisms involving defects, mainly oxygen vacancies. Thus, a TCO can act as a current collector in a solar cell.

High efficiency for the thin film solar cell is achieved by increasing the path length of the incoming light [18]. The path length is increased through light scattering at the silicon-TCO interface due to the different refractive indexes. This also causes the light to get trapped in the silicon layer. Due to the light trapping, the thickness of the silicon layer can be reduced. This lowers the cost and enhances the performance of the device [19].

The electrical contacts need to be conductive so they can extract the current generated in the solar cell. Transparency is also required for the front electrical contacts to let light into the absorber region. TCOs are therefore a good choice for a top contact. The TCO layer is deposited to increase light scattering and electrical conductivity [17, 18]. The efficiency of the solar cell is highly dependent on the TCO properties. Properties of the TCO should be low electrical resistivity combined with high optical transparency and textured surface to ensure optimal scattering. The low resistivity makes sure that the generated current is transported efficiently. A high optical transmittance increases the amount of light reaching the active absorber layer. In addition to the TCO front contact, a TCO back contact is used as a back reflector and a diffusion barrier [20].

In a typical solar cell produced today, the top contact is widely-spaced thin metal strips, often called fingers, that supply current to two wider metal strips called bus bars perpendicular to the fingers [21]. The top electrical contact is usually formed by screen printing giving metal grid dimensions of 2 mm wide bus bars and 150 μm fingers separated by spaces on the order of 3 mm. This method is inexpensive, simple, and can be automated, but requires a firing at 700 °C for a few minutes. Silver is the material that is most used for the top current collectors in todays solar cells, as it has excellent conductivity. The metal strips must be as thin as possible to allow light to pass through to the active region of the solar cell. Silver is not transparent, and some of the active region is lost as the silver electrodes are deposited on the solar cell. For a standard solar cell, the total shading loss is ~9 %. Therefore, the main motivation for using TCOs instead of silver as the top contact is to eliminate this loss and thus increase the efficiency of the solar cell.

2. Theory

This part is divided up in four sections. First, important characteristics like the crystal structure and the optoelectronic properties will be introduced for the TCOs In_2O_3, ITO and IZO. Second, the synthesis of the thin films will be addressed followed by the alternative curing method studied in this master thesis. The last section presents some important characterization methods that are relevant for this thesis.

2.1 Crystal Structure

The resulting films after spin coating are amorphous. An amorphous solid lacks the long-range order of a crystal, and to crystallize the film a curing temperature above the crystallization temperature is necessary. The crystallization temperature varies between different materials, but also varies internally for one material depending on factors like thin film composition and deposition method.

In this master thesis the thin film synthesis is taken from Sunde et al. [16]. They showed that ITO with 10 mol% Sn crystallizes into a nano-crystalline powder at ~300 °C. Jung et al. [22] prepared IZO thin films with 16 mol% Zn by direct current magnetron sputtering. X-ray diffraction and differential thermal analysis were used to study the crystallization behavior of the IZO thin films. The crystallization temperature was found to be between 500 °C and 600 °C. A similar crystallization temperature for IZO thin films is found by Gonçalves et al. [23] and Yaglioglu et al. [24], where an annealing temperature of 500 °C is found to give crystalline films when using sputtering as the deposition technique.

In_2O_3 crystallizes into two different structures; body centered cubic and hexagonal [25]. The body centered cubic bixbyite structure is the one obtained at ambient conditions, while the hexagonal corundum phase is only obtained at high temperatures or pressures. The bixbyite crystal structure belongs to space group Ia3, number 206 and the lattice structure is equal to fluorite [25]. Figure 2.1 shows the unit cell for this structure.

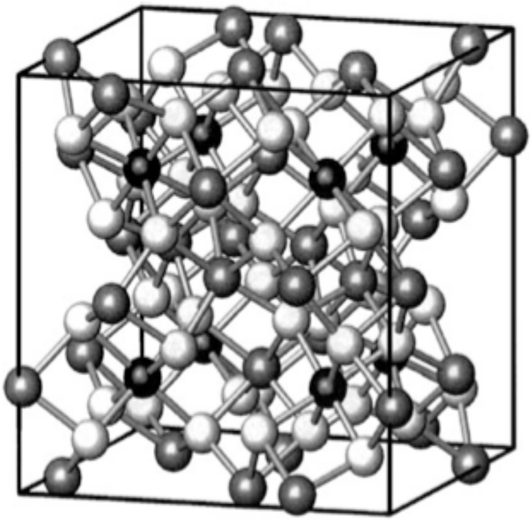

Figure 2.1: A conventional unit cell for the cubic bixbyite crystal structure of In_2O_3. The black and grey spheres correspond to 8b indium and 24d indium ions respectively and white spheres correspond to the 48e oxygen ions [26].

Compared to fluorite a fourth of the anions is missing in the bixbyite crystal structure resulting in empty oxygen lattice sites, which are often referred to as interstitial positions [25, 26]. The unit cell is rather complex and consist of 80 atoms with 32 cations distributed on two different sites, as can be seen in Figure 2.2. Both cation sites are centered in a distorted cube coordinated to six oxygen atoms.

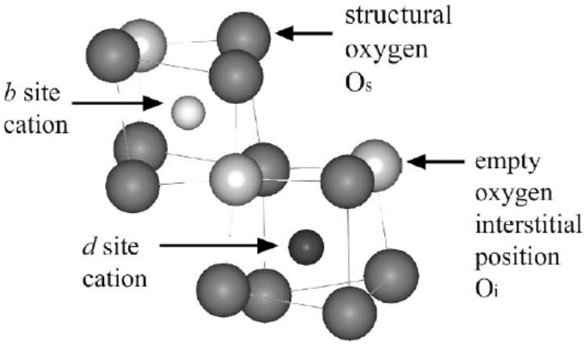

Figure 2.2: A representation of the different sites in the In_2O_3 unit cell [25].

Sunde et al. [16] prepared ITO thin films with a doping level of 10 mol% Sn through the sol-gel process followed by spin coating on glass substrates and annealing at 530 °C. In Figure 2.3 a diffractogram for the thin film is presented together with the reference pattern of the cubic In_2O_3 structure. From the figure it can be seen that the ITO thin film crystallize into the bixbyite structure of In_2O_3 without obtaining a preferred orientation.

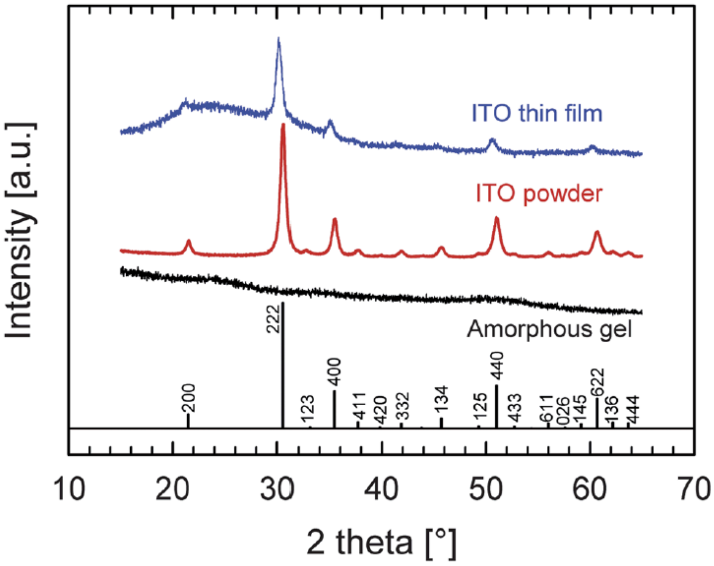

Figure 2.3: A diffractogram showing a 10 layered ITO thin film of 10 mol% Sn, ITO powder annealed at 400 °C, and an amorphous gel of ITO after evaporation of the solvent. Both the powder and gel contains 5 mol% Sn. The reference pattern for the cubic structure of In_2O_3, space group Ia3, is shown below the diffractograms. The figure is reprinted from Sunde et al. [16].

IZO thin films are found to obtain a variety of crystal structures when studying the literature. Which structure that is obtained depends on parameters like the film deposition method, deposition parameters, and film composition. A set of articles will be discussed in the following section to present this.

IZO thin films in the indium rich region are thought to be In_2O_3 doped with ZnO. As already discussed above, pure In_2O_3 obtains the cubic bixbyite structure. Pure ZnO have the hexagonal wurtzite structure [27].

An overweight of the crystalline IZO films in literature crystallizes in a preferred orientation, and only the main diffraction line can be seen. For the zinc rich films, which obtain the hexagonal wurtzite structure, this means the (002) diffraction line. The indium rich films, which obtain the cubic bixbyite structure, crystallize in the (222) direction. For the middle region compositions, layered homologous phases of the type $Zn_kIn_2O_{k+3}$ are found. This structure evolution with doping level of zinc is found for a wide variety of deposition methods including low pressure metal-organic chemical vapor deposition [4], pulsed laser deposition [28, 29], co-sputtering [30] and is even found for sol-gel films deposited on glass substrates using spin coating [8] or dip coating [31].

The variation of the crystal structure with the mole fraction x = Zn/(Zn+In) for IZO thin films synthesized by the sol-gel method, deposited on glass substrates using spin coating, and annealed at 650 °C is presented in the work by Lee and Park [8]. The diffractograms obtained for the thin films are found in Figure 2.4. From the figure it can be seen that the x = 0.20 diffractogram corresponds to the In_2O_3 structure. They claim that this diffractogram has a preferred orientation along the (222) plane. For x = 0.33 it is assumed that In_2O_3 coexist with a homologous phase. For the x = 0.50 and 0.66 diffractograms, a clear diffraction line for the homologous phases $Zn_2In_2O_5$ and $Zn_3In_2O_6$, respectively appear. When x = 0.80 the structure found from the diffractogram is ZnO, showing a preferred direction along the (002) diffraction line.

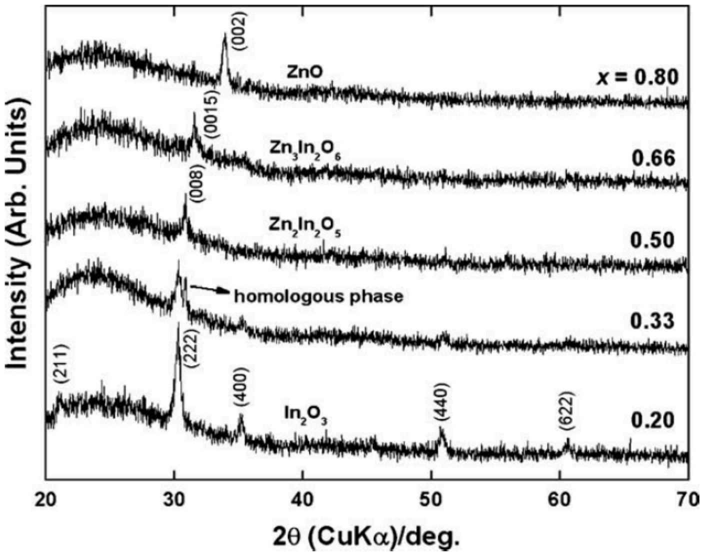

Figure 2.4: Diffractograms of In_2O_3-ZnO spin coated thin films at different atomic ratios annealed at 650 °C. The atomic ratios Zn/(Zn+In) are abbreviated to *x*. The figure is reprinted from Lee and Park [8].

Tsay et al. [32] achieved amorphous sol-gel derived IZO thin films through spin coating on glass substrates, drying at 150 °C, and curing using a KrF excimer laser. Also Koo et al. [33] got amorphous IZO thin films regardless of the composition. Thin films of the compositions 20, 30, 40, 50 and 60 mol% Zn were synthesized through the sol-gel method by spin coating on SiO_2/Si substrates and heat treatment at 300 °C. Li et al. [7] obtained an amorphous structure of IZO thin film prepared through the sol-gel synthesis deposited on glass using spin coating and heat treatment at 500 °C. Diffractograms were obtained for zinc concentrations in the range 25 mol% to 75 mol%. All the diffractograms showed an amorphous structure, but for the 50 mol% and 40 mol% Zn concentrations the diffractograms have a weak peak corresponding to the (222) diffraction line for the In_2O_3 structure. In the work by Gonçalves et al. [23] IZO thin films in the indium rich region were deposited onto glass at room temperature by radio frequency magnetron sputtering. The as-deposited films were amorphous, but annealing the films at 500 °C gave a non-directional crystalline thin film with the In_2O_3 structure.

Heat treatment below the crystallization temperature will of course give amorphous thin films, but amorphous regions are also found to appear as an effect of doping level. Compositionally graded IZO thin films deposited by co-sputtering from In_2O_3 and ZnO targets onto glass substrates at 100 °C was reported by Taylor et al. [30]. The as-deposited IZO thin films are crystalline for both high and low zinc contents, separated by a compositionally wide amorphous region. For a zinc content less than 15 mol% a clear diffraction peak corresponding to the (222) diffraction line of In_2O_3 is obtained. For compositions ranging from 16 mol% to 45 mol% Zn the IZO thin films are amorphous, while the zinc rich IZO thin films show a strong diffraction line along the (002) direction of ZnO.

2.1.1 Solid Solubility

A tin content up to about 20 mol% can be doped into In_2O_3, while still obtaining the bixbyite structure during crystallization [34-36]. The phase diagram for the In_2O_3-SnO_2 system can be seen in Figure 2.5, and it is the indium-rich side that is most interesting with regards to applications in technology. The common amount of tin doping in In_2O_3 is 5 to 10 mol%, but the thermodynamically stable solid solubility is only around 2 mol% Sn below 1200 °C [37]. This means that most ITO materials used in applications in fact is out of equilibrium and obtains what is called a metastable solid solution. It is relatively easy to obtain high doping concentrations of tin in ITO and it is suggested that this is because of the slow kinetics of the exsolution of excess tin compared to the solubility limit.

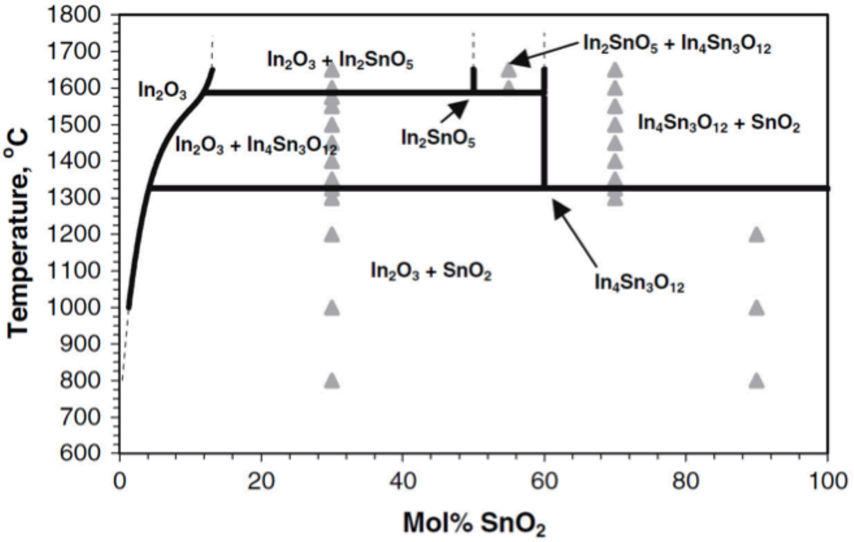

Figure 2.5: Phase diagram for the In_2O_3-SnO_2 system [34]. The grey triangles denote the starting compositions used to obtain the compositional data.

The In_2O_3-ZnO phase diagram is given in Figure 2.6. At temperatures >1000 °C In_2O_3 and ZnO react to form a series of homologous compounds with the chemical composition $Zn_kIn_2O_{k+3}$, which can be seen in the phase diagram and especially in the zinc-rich side of the diagram [38]. The homologous compounds are structurally similar to ZnO, thus narrow regions of solid solution may exist. No solid solubility of zinc into In_2O_3 or indium into ZnO is seen from the phase diagram. In literature IZO thin films with a variety of zinc concentrations are seen. Li et al. [7] prepared sol-gel derived IZO thin films for use in thin film transistors as the active channel layer and found that a doping level of 40 mol% Zn gave the best thin film transistor performance.

The phase diagram presents equilibrium phases of bulk material. During thin film deposition non-equilibrium conditions are often seen, but a phase diagram showing the stable phases can still be helpful for interpreting obtained data.

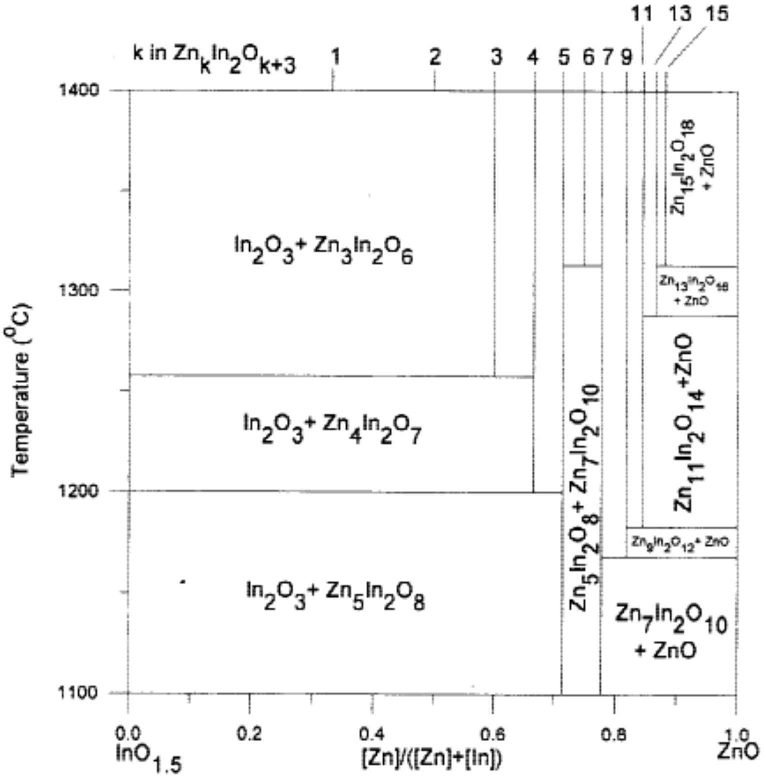

Figure 1.6: The In_2O_3-ZnO phase diagram over the temperature range of 1100-1400 °C [38].

2.1.2 Lattice Parameter

The radius of an In^{3+} cation is 0.80 Å, while the radius of Sn^{4+} and Zn^{2+} cations are 0.69 Å and 0.74 Å respectively [39]. So, by substituting indium with any of these in an In_2O_3 crystal structure, a lattice contraction would be expected if only considering cation radius. Frank and Köstlin [40] performed experiments were they studied the effect of tin doping on the In_2O_3 lattice parameter in reducing and oxidizing atmosphere. Figure 2.7 a) shows that lattice contraction is seen for low doping amounts, while an increase in lattice parameter occur at higher doping levels. The increase in lattice parameter at higher doping levels can be explained by the higher effective charge of the Sn^{4+} ions compared to In^{3+} that causes repulsive forces [41]. These repulsive forces are not fully compensated for by shielding electrons, thus an increase in lattice parameter is seen. In oxidizing conditions the oxygen vacancy concentration is negligible as extra oxygen atoms occupy the interstitial oxygen vacancy sites to compensate the extra charge from the Sn^{4+} cations. A reducing atmosphere is often used when preparing ITO and In_2O_3 to reduce the amount of compensating interstitial oxygen. It is seen from Figure 2.7 a) that the lattice parameter is larger for the reduced state compared to the oxidized state [40]. Figure 2.7 b) shows the difference in lattice parameter between the reduced and oxidized state together with the difference in carrier concentration. They both increase linearly until they reach a limit at about 6 at% Sn where they remain constant.

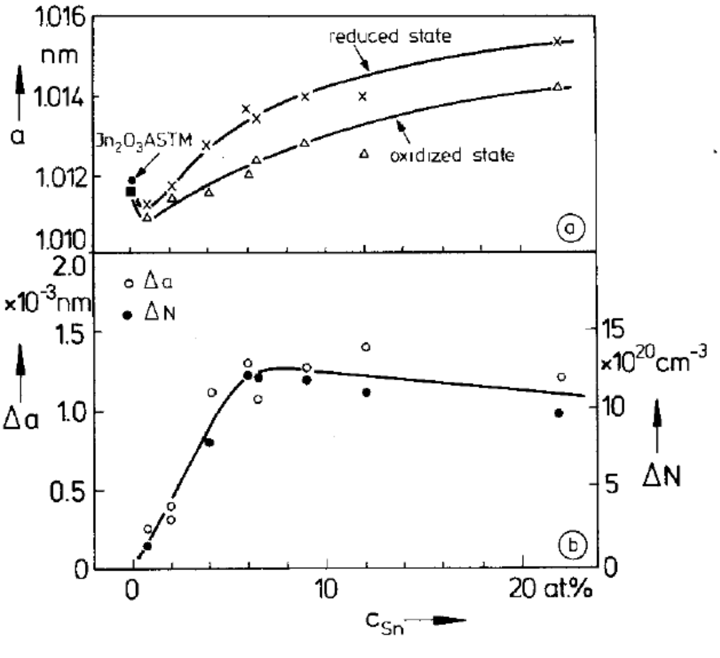

Figure 2.7: a) The dependence of lattice parameter on the level of tin doping in In_2O_3 films for reducing (x) and oxidizing (Δ) conditions. b) Lattice parameter decrease and carrier concentration decrease of oxidation of reduced films against level of tin doping. The figure is reprinted from Frank and Köstlin [40].

The cubic bixbyite crystal structure of In_2O_3 has a lattice parameter of 10.117 Å [25, 42]. The lattice parameter of ITO films have been found to be in the range 10.118-10.31 Å [43]. Sunde et al. [16] obtained a lattice parameter of 10.121 Å for pure In_2O_3 powder and 10.130 Å for ITO powder with a doping level of 10 mol% Sn. Both powders were calcinated at 600 °C. A lattice parameter of 10.153 Å was observed for an ITO thin film with a doping level of 10 mol% Sn heat treated at 530 °C.

No values for the lattice parameter of IZO thin films with the cubic bixbyite crystal structure of In_2O_3 could be found in literature. The lattice parameter values found are for zinc rich IZO thin films, which has the hexagonal wurtzite crystal structure [38, 44].

2.2 Optoelectronic Properties

In_2O_3 based TCOs are extensively used in technology applications, due to their optoelectronic properties. Despite this, the physical mechanisms behind the optoelectronic properties have not been investigated to a large degree. One of the reasons appears to be the difficulty of performing theoretical electronic structure calculations on the complex unit cell of In_2O_3.

In most cases, both the optical and electrical performance is crucial for the applicability of TCO films. In the following section, the trade-off between the conductivity and transparency will be introduced. For each application one should find the optimized relationship between the transparency and conductivity.

For a semiconductor to be transparent in the visible region of the electromagnetic spectrum the band gap must be larger than 3 eV [43]. At room temperature oxides with a band gap of 3 eV or more are insulators. To make them conductive, doping or non-stoichiometry is needed [9]. This will give free carriers that can be donated to the conduction band. Doping can result in the well-known phenomenon Burstein-Moss shift of the Fermi level, causing an increase in the effective band gap [45].
The principles for the Burnstein-Moss shift are as follows. When the conduction band is empty the band gap is intrinsic. However, when the carrier concentration is increased the lowest states in the conduction band become filled and an increased energy is necessary in order to excite electrons from the valence to the conduction band. A rule of thumb is: the higher the Fermi level, the more conductive the TCO. Then again a too high doping level will shift the plasma frequency and thus limit the optical transparency.

Conductivity and transparency are strongly related [43]. As seen in Figure 2.8 both sheet resistance, R_{sh}, and the average visible transmittance, T, decreases with increased thickness of the TCO layer. There is a trade-off between the two, as conductivity improves the layer gets less transparent. The conductivity is dependent on film thickness, because stoichiometry and morphology change with thickness [43]. For ITO the thickness of the film should be less than 150 nm to obtain satisfying transparency, but it should not be too thin, as this will lower the electrical conductivity.

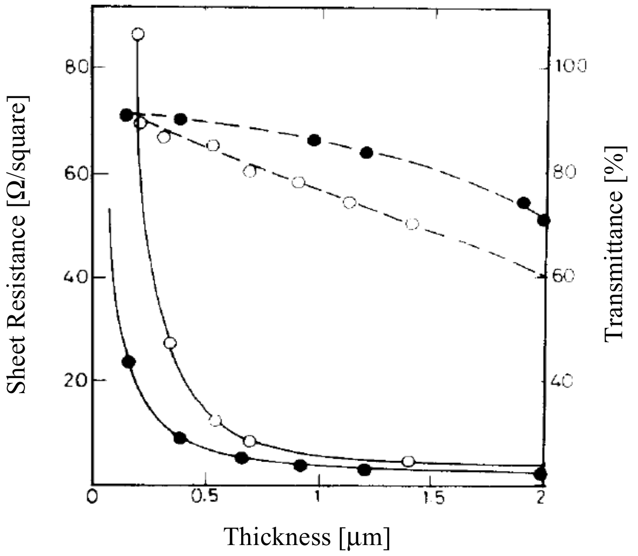

Figure 2.8: Dependence of the sheet resistance (solid line) and the average visible transmittance (dotted line) on the film thickness. Where • denote ITO and o denote fluorine-doped SnO_2. The figure is modified from Chopra et al. [43].

Both optical and electrical properties are strongly dependent on film thickness, charge carrier concentration, morphology, crystal structure, stoichiometry and type of impurities present [9]. This means that the electrical and optical properties are highly dependent on the preparation method [46].

From the following sections it will become clear that the electronic and optical properties of In_2O_3, ITO and IZO are strongly related.

2.2.1 Optical Properties

The high optical transparency of In_2O_3 is due to the large band gap, which is caused by the strong metal-oxygen bond [10]. The value and the nature of the In_2O_3 band gap have been extensively disputed, but the most widely used value for the bulk band gap of In_2O_3 is 3.75 eV [45, 47]. More recently however it was shown that the fundamental band gap is direct and has a value of 2.9 eV [48]. Why the observed band gap is often in the 3.75 eV range, can be explained by symmetry forbidden transitions at the top of the valence band. Strong absorption is only observed when electrons are excited from 0.81 eV below the highest energy valence bands. This energy level is marked by the green line denoted $\Gamma_8(T_u)$ in Figure 2.9 a). From the calculated absorption spectrum in Figure 2.9 b) it can be observed that the onset of optical absorption is 0.81 eV higher in energy than the fundamental band gap.

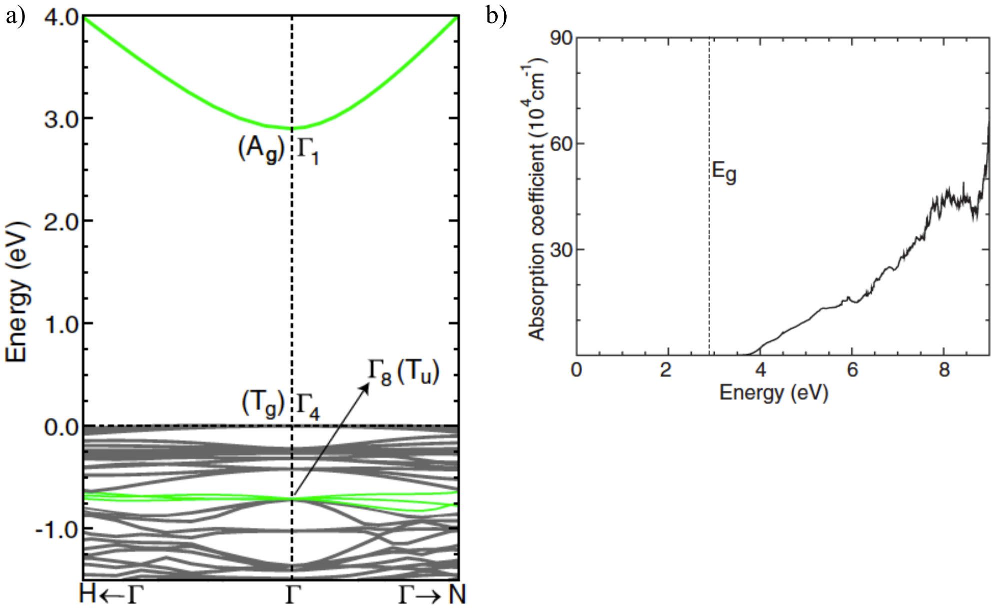

Figure 2.9: a) Band structure of In_2O_3. Strong optical absorption only occurs when electrons are excited from energy bands 0.81 eV below the highest energy valence bands. b) Calculated absorption spectrum of bulk In_2O_3. The fundamental band gap is 0.81 eV lower in energy than the onset of strong optical absorption. The figures are taken from [48].

It was showed by Ambrosini et al. [49] that localized doping levels of tin form a dopant band which overlaps with the conduction band of In_2O_3. Odaka et al. [50] reported that the overall features of the density of states of In_2O_3 were almost conserved when doped with tin, except from the appearance of a new band below the valence band. That the original conduction band is only slightly disturbed might be due to the coinciding symmetry of the donor band and the original conduction band. Further investigations showed that the carrier generation in ITO occurs through an intermediate case between two scenarios. The first scenario is that tin atoms donate their electrons directly to an indium 5s-like conduction band. In the second scenario the tin-like donor band itself becomes the conduction band of ITO. Based on the theory above, the bulk band gap of ITO will be similar to that of In_2O_3 with a fundamental band gap of about 2.9 eV and an observed band gap around 3.75 eV.

Pure ZnO has a band gap of 3.3 eV [28]. This band gap, as for In_2O_3, is intrinsic with a direct main interband transition. Naghavi et al. [28] prepared IZO thin films with compositions ranging from In_2O_3 to ZnO by pulsed laser deposition. Figure 2.10 shows the obtained band gap as a function of mole fraction Zn. A band gap of 3.56 eV is found for IZO containing 40 mol% Zn. For the region below 40 mol% Zn a decrease of the band gap together with an increase in the carrier concentration is seen compared to pure In_2O_3. This behavior does not conform to the Moss-Burstein theory, but is assumed to be caused by Zn^{2+} ionized impurities that act as electron traps in the In_2O_3 lattice. As the content of these defects increase, the corresponding localized levels within the band-gap overlaps the bottom of the conduction band releasing the trapped electrons and also causing a reduction of the band gap.

In the work by Ito et al. [51] a band gap between 3.48-3.84 eV was obtained for direct current magnetron sputtering of indium-rich IZO thin films. Gonçalves et al. [23] reports a band gap of 3.87 eV for as-deposited indium-rich IZO thin films made by radio frequency magnetron sputtering. IZO thin films are in general known to have a smaller band gap than ITO thin films [28].

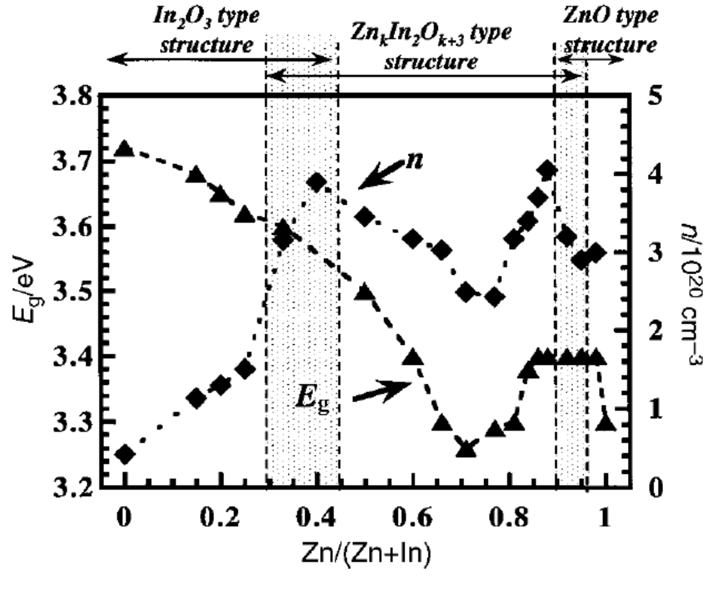

Figure 2.10: Dependence of carrier concentration, *n*, and the optical band gap E_g on the mole fraction of zinc in IZO [28].

Average visible transmittance, *T*, is a good way to specify transparency. For In_2O_3 films, the optical transparency in the visible region is around 75 to 90 % [52, 53].

ITO thin films are used extensively as transparent electrodes for optoelectronic devices, thus a high transparency in the visible region is required for such applications. The optical transparency in the visible region of the electromagnetic spectrum is around 85 to 90 % for ITO films depending on the level of tin doping [35, 49]. Figure 2.11 shows optical transmission spectra for ITO thin films prepared using an aqueous sol-gel method and spin coating for depositing different numbers of layers [16]. A transmittance of 80 % or higher is seen in the visible region of the electromagnetic spectrum for all the films.

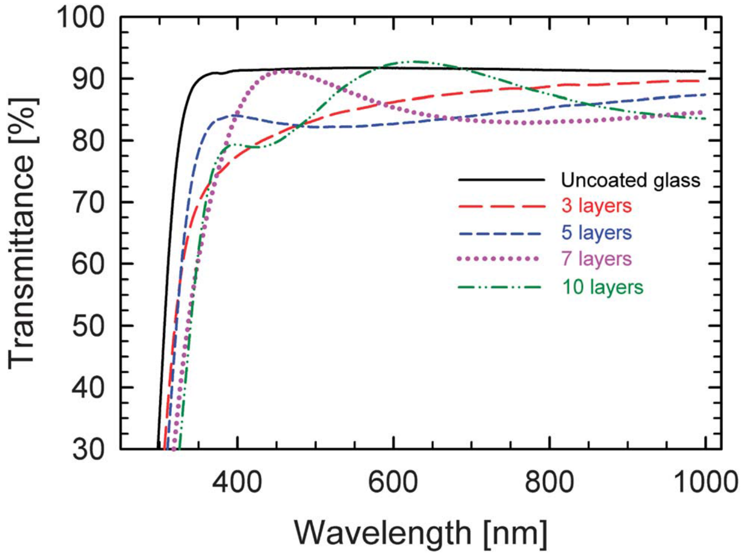

Figure 2.11: Transmittance of sol-gel derived ITO thin films prepared with different numbers of deposition layers using spin coating [16].

Kim et al. [6] prepared IZO thin films by the sol-gel method. The thin films were deposited on glass substrates by spin coating followed by heat treatment at 400-780 °C, giving a resulting film thickness of 60 nm. The thin films had compositions ranging from x=0.33-0.78 mole fraction of Zn. The optical transmission spectra obtained for the thin films are presented in Figure 2.12. An average optical transmittance above 80 % in the visible region was obtained for all the films. The highest optical transmittance is found for 50 mol% Zn where the average transmittance in the visible range of the electromagnetic spectrum was 86.8 %.

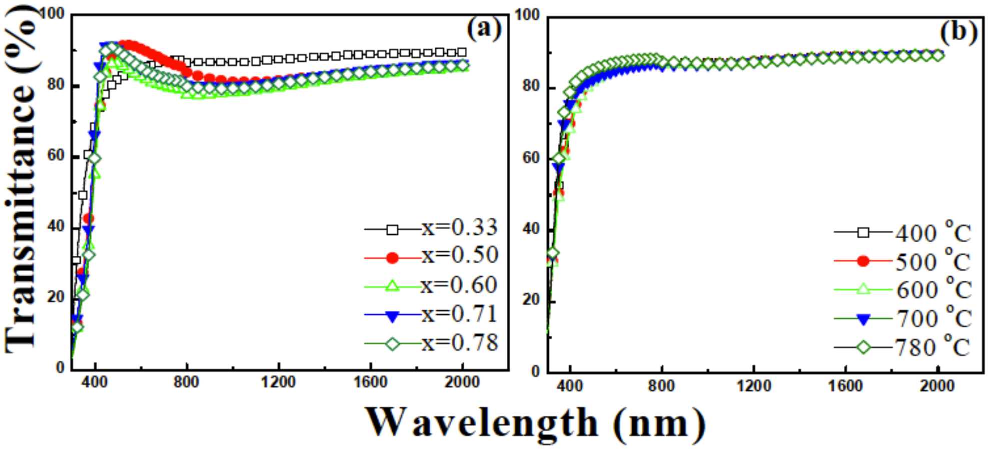

Figure 2.12: Optical transmission spectra for IZO thin films (a) heat treated at 780 °C with compositions ranging from x= 0.33-0.78 mole fraction of zinc and (b) with a doping level of 33 mol% Zn at different heat treatment temperatures [6].

2.2.2 Electrical Properties

Electrical conductivity, σ, is dependent on both the number of charge carriers, N, and the mobility, μ, as can be seen in Equation 2.1 [9]

$$\sigma = N\mu e \tag{2.1}$$

where e is the electronic charge. To get a high electrical conductivity both N and μ should be large. Enhancement of the conductivity is often obtained through doping. For doping of a TCO material to be successful the dopant must be soluble in the host lattice, the donor level must be shallow to retain the large band gap and the dopant must not be compensated by an intrinsic defect [54].

In In_2O_3 films there is a high carrier concentration, $N\approx10^{19}$-10^{20} cm^{-3}, which is the main contribution to the relatively high conductivity [43]. In_2O_3 films have mobilities in the range 10-75 cm^2/ V s, depending on the film preparation. The low mobilities are due to scattering mechanisms like ionized impurity and grain boundary scattering. The resistivity, ρ, of In_2O_3 films are in the order of 10^{-3}-10^{-4} Ω cm [43, 55, 56].

ITO thin films prepared under optimized conditions have a charge carrier concentration of 10^{21} cm^{-3} and a mobility value between 30-50 cm^2/V s. ITO thin films prepared by physical deposition methods generally obtain lower resistivities than thin films prepared through wet chemical methods. Resistivity values 1.28×10^{-4} Ω cm and 1.29×10^{-4} Ω cm, which are obtained through direct current and radio frequency sputtering respectively, are representative values for the physical deposition methods [57]. A resistivity value of $\sim2\times10^{-3}$ Ω cm has been reported in literature for acetate based ITO thin films produced using wet chemical methods, spin coating, and heat treatment at 600 °C [58]. Ethylene glycol sol-gel based ITO thin films spin coated on glass and heat treated at 550 °C for 30 minutes followed by a post annealing at 300 °C for 30 minutes obtained a minimum resistivity of

6×10^{-4} Ω cm [59]. The aqueous sol-gel process used in this master thesis developed by Sunde et al. [16] was found to give a resistivity of 4.59×10^{-3} Ω cm for ITO thin films with a tin content of 10 mol%. The thin films were deposited on glass substrates using spin coating followed by heat treatment at 530 °C.

Resistivity as a function of the doping level of tin is given in Figure 2.13 [40]. At low tin doping levels the resistivity decreases due to increased number of charge carriers. The resistivity reaches a minimum value between 5-10 mol% Sn before it increases due to tin-oxygen associates. The minimum resistivity is dependent on the synthesis and the deposition parameters, but the value is normally between 5-10 mol% Sn [9].

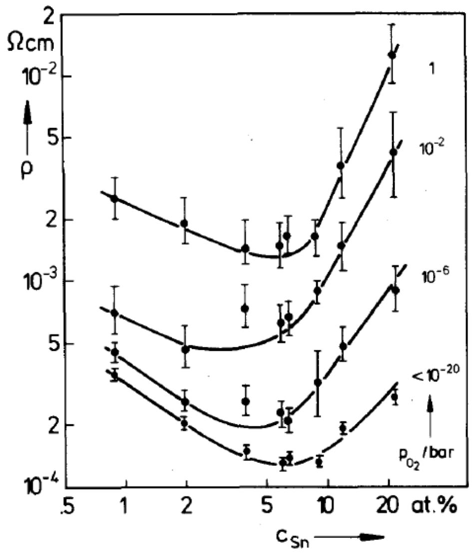

Figure 2.13: Resistivity measurements of spray pyrolysis derived ITO thin films heat treated at 500 °C as a function of doping level at% Sn [40]. The parameter for the different plots is oxygen partial pressure of the annealing atmosphere.

Lee and Park [8] obtained a minimum resistivity of 1.5×10^{-3} Ω cm, a maximum carrier concentration of 3.0×10^{20} cm^{-3} and a mobility of ~13 cm^2/V s for crystalline IZO films with 50 mol% Zn prepared through the sol-gel method and spin coating onto glass substrates. The heat treatment was performed at 650 °C. Tsay et al. [32] prepared sol-gel derived IZO thin films with 60 mol% Zn deposited onto glass substrates by spin coating and dried at 150 °C followed by KrF excimer laser curing. The best electrical properties obtained for the amorphous films was a resistivity of 1.33 Ω cm, carrier concentration of 4.0×10^{17} cm^{-3} and a mobility of ~12.8 cm^2/V s.

Yaglioglu et al. [5] prepared pure In_2O_3, ITO of 17 mol% Sn and IZO of 28 mol% Zn thin films through direct current magnetron sputtering. The thin films were deposited on glass substrates at room temperature and at 350 °C under optimal sputtering conditions. The obtained electrical properties and structure is listed in Table 2.1.

Table 2.1: Electrical properties and structure of direct current magnetron processed In_2O_3, ITO and IZO thin films deposited at optimal sputtering conditions. The films that obtain the amorphous structure are deposited at room temperature, while the crystalline thin films are deposited at 350 °C. Values are taken from [5].

Compostion	Structure	Resistivity [Ω cm]	Carrier density [cm^{-3}]	Mobility [$cm^2/V\ s$]
In_2O_3	Amorphous	7.48×10^{-4}	1.88×10^{20}	44.5
ITO	Amorphous	7.18×10^{-4}	2.18×10^{20}	41.4
IZO	Amorphous	5.96×10^{-4}	2.02×10^{20}	51.9
In_2O_3	Bixbyite	1.73×10^{-3}	7.90×10^{19}	46.0
ITO	Bixbyite	2.23×10^{-4}	6.03×10^{20}	46.4
IZO	Bixbyite	4.20×10^{-4}	4.30×10^{20}	34.8

From the table, it can be seen that the amorphous films obtain nearly identical carrier density, while the mobility of amorphous IZO is higher than for pure In_2O_3 and ITO resulting in a slightly lower resistivity for amorphous IZO. For the crystalline films, the highest carrier density and mobility is seen for ITO giving the lowest resistivity. The crystalline IZO thin film also obtains a lower resistivity than pure In_2O_3 due to a higher carrier density obtained, despite that a lower mobility is seen.

Indium oxide can have metallic, semiconducting or insulating characteristics [10]. By controlling the defects in the material the electronic characteristics of In_2O_3 can be tuned. Defects include oxygen vacancies and indium interstitials. In its stoichiometric form, In_2O_3, indium oxide is insulating and in the oxygen-deficient form, $In_2O_{3-\delta}$, indium oxide is an n-type semiconductor. That conductivity in indium oxide arises from oxygen vacancies has been confirmed through thermogravimetrical analysis and electron probe microanalysis [40, 60]. By increasing the amount of oxygen vacancies metallic characteristics can be obtained. The degree of oxygen deficiency depends on impurity concentration and synthesis conditions. A way of increasing the amount of oxygen vacancies is thus to use a reducing atmosphere during heat treatment of the film. The defect equilibrium can be described by Equation 2.2 [61].

$$O_O^X \rightarrow V_O^{\bullet\bullet} + 2e' + \frac{1}{2}O_2(g) \tag{2.2}$$

Since the free electrons are produced from oxygen vacancies the oxygen deficiency can be predicted from the carrier concentration to be less than 1 % [60]. This limits the maximum conductivity of In_2O_3. It is found that the conventional picture of two electrons per oxygen vacancy as shown in Equation 2.2 cannot be directly applied to these films, but works as an approximation model. To get sufficient conductivity for most applications doping is necessary [1].

When doping In_2O_3 with tin each tin donates one electron to the conduction band causing n-type doping [47]. Also in the IZO films n-type conduction is seen, and should also here originate from the formation of oxygen vacancies that donates free electrons [62].

The nearly identical carrier density of amorphous In_2O_3, ITO and IZO obtained by Yaglioglu et al. [5], seen from Table 2.1, suggests that neither zinc nor tin contributes substantially with carriers to the amorphous In_2O_3 structure. Since no doping is present in the pure amorphous In_2O_3 structure, it can also be assumed that oxygen vacancy-like defects are the primary source of carriers in these films. From Table 2.1 it can be seen that amorphous ITO obtains a higher resistivity than crystalline ITO. This is due to an inefficient activation of tin in the amorphous structure and the presence of tin-oxygen complexes that act as scatter centers increasing the scattering [5]. In addition, these complexes do not contribute to the carrier concentration. As it can be seen from Table 2.1, the decrease in resistivity for crystalline In_2O_3 when doped with zinc is caused by the increase in carrier density. In the amorphous state, the decrease in the resistivity of In_2O_3 when doped with zinc is caused by the increase in mobility.

As already mentioned doping is necessary to get sufficient conductivity for most applications. But, even doping has its limits. Mobility and charge carrier concentration are related to each other creating an upper conductivity limit. They are both dependent on the oxidation state and the dopant concentration in a complicated manner [40]. At constant oxygen pressure the mobility will decrease with increasing tin doping concentration due to increased scattering. The mobility-limiting scattering can arise from different sources such as phonons, grain boundaries and neutral and ionized point defects.

2.3 Thin Film Synthesis

There are a number of different possible techniques for depositing TCO thin films. The techniques can be divided into the two main categories physical and chemical. For deposition of TCO films, sputtering, which is a physical vapor deposition method, is the most extensively used industrial technique [9, 10, 63]. In sputtering, a target material is bombarded with energetic ions ejecting atoms that deposit on the substrate [64]. This means that a significantly amount of the target material ends up as waste on the chamber walls, resulting in low deposition yields [65]. It is expensive to set up and maintain a sputter deposition line. Sputtered films are also inconvenient for flexible devices due to their brittleness.

Another possibility is wet chemical methods [12, 16]. Solution deposition is usually done using spin coating [16, 66, 67], spray coating [68-70] or dip coating [67, 71, 72]. Spin coating is an easy deposition process that gives highly reproducible results. It is therefore a widely used method for depositing uniform films onto flat substrates. The general principle of the method is as follows [73, 74]. An excess amount of precursor solution is applied onto a substrate. The substrate is then rotated and the rotation is accelerated to high speed. The result is a uniform thin film. Thin films composed of multiple layers can be obtained by repeating the spin coating procedure several times. When performing spin coating there is a number of parameters that will influence the thickness and microstructure of the film. The most important parameters are rotating speed, viscosity of solution, precursor concentration, wetting properties, spin time, acceleration, amount of solution deposited, number of layers deposited and age of solution. If the spin coating parameters are not optimal it can lead to a range of different flaws in the film including film cracking, pinholes and unwanted film patterns.

Even though the electrical conductivity of the thin films is generally not as good, wet chemical methods have several advantages compared to physical techniques [9]. One important advantage is that solution based methods are cost effective, as the equipment is simpler and less expensive [46, 65]. Another advantage is better material utilization and high throughput. By adding trace amounts of dopants to the solution complex films are obtained and the composition is easily adjusted and controlled [75]. Good homogeneity is also obtained since the mixing occurs at the molecular level. In addition, vacuum is seldom necessary for wet chemical methods giving fewer restrictions to the chamber size [65]. This makes it possible to coat a variety of shapes and sizes. One downside to wet chemical deposition when considering large-scale production, is that multiple layers need to be deposited in order to obtain satisfying conductivity [9, 16, 59]. This is negative as it is time consuming and equipment demanding.

For the precursor solution in wet chemical methods a solvent is needed. This solvent can either be organic or water. When compared to aqueous systems, organic solvents give better control over particle surface properties, crystallinity, size, and shape [46, 67]. A downside with organic solvents is that they are potentially harmful to humans and the environment. They are in addition often flammable and expensive. Water is much more environmental friendly and is especially preferred for large-scale use as in industry. It is also an advantage that aqueous based preparation routes are less expensive and that water is readily available.

The sol-gel process is a suitable wet-chemical method for TCO thin film deposition. Main application areas for the sol-gel method are production of coatings, fibers and powders [76]. One of the most technologically important aspects of sol-gel processing is that prior to gelation, the fluid sol is ideal for preparing thin films by common methods as dip coating, spin coating spinning and spray coating. Applications for thin films and coatings made through the sol-gel process are optical coatings, electronic films, protective films, and porous films.

The most important advantage of sol-gel is the ability to precisely control the microstructure of the deposited film. For spin coating, the film microstructure depends on the size and extent of branching (or aggregation) of the solution species prior to film deposition, and the relative rates of condensation and evaporation during film deposition.

A sol is a colloidal suspension of solid particles in a liquid, where the colloid has a size ~1-1000 nm [76]. When preparing a colloid in the sol-gel process the precursor used is a metal or metalloid element surrounded by various ligands. The sol-gel process is a kinetically controlled process where the reactions, hydrolysis and condensation, are exothermal and will occur spontaneously. Through these reactions the properties of the material is changed, turning the sol into a gel. An example is the abrupt increase of the viscosity. The gelation occurs through the formation of clusters that grow by condensation of polymers or aggregation of particles until the clusters collide. When the clusters collide, links are formed between the clusters forming one giant cluster. This giant cluster is the gel.

As already mentioned, when making films using a sol-gel method the film is deposited while the solution is still in the sol-stage. The film then gels at the substrate surface, and is converted into an oxide film conventionally through a heat treatment step [15]. The heat decomposes the organics giving a metal-oxygen network. The gel normally needs to be heated to a temperature above 500 °C to be completely converted into an oxide film.

Films are denser than bulk gels, because rapid evaporation causes films to remain compliant so that the capillary pressure collapses the pores during drying [76]. For thin films the deposition and evaporation steps overlap, inducing a competition between evaporation, which compacts the structure, and continuing condensation reactions, which stiffens the structure increasing the resistance against compaction. During film formation the condensation rate can be controlled by varying the pH of the sol, while evaporation rate can be controlled by varying the partial pressure of the solvent. The dependence of the hydrolysis and condensation reaction rates on the pH of the solution for silicates is shown in Figure 2.14 [77]. The hydrolysis reaction is dominant for low pH, while the condensation reaction becomes dominating for $pH > 4$.

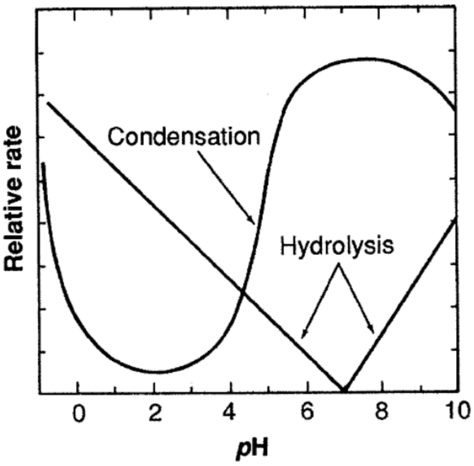

Figure 2.14: The rates of hydrolysis and condensation reactions for silicon alkoxide solutions as a function of pH [77].

Thin films that are stable can become unstable during heat treatment due to large defects such as pinholes. If the hole has a radius smaller than a critical value it will shrink, while a hole with a radius larger than the critical value will grow. The growth of holes can lead to break up of the film into islands giving a non-homogeneous covering of the substrate. When the grain size is larger than the film thickness grain boundary grooves can reach the substrate, which results in island formation. The size of the islands is determined by surface energy [78]. Break up of a continuous film into islands is driven by capillarity [79]. Especially polycrystalline microstructure is sensitive to breakup, as grain boundaries and three-grain junctions give large perturbations in the film [79]. There are three possible film-substrate configurations: the completely covered substrate, the uncovered substrate and the partially connected film (the grain boundary intercepts the substrate). A schematic of these are shown in Figure 2.15. The stable configuration is the one that gives the minimum value for the total energy.

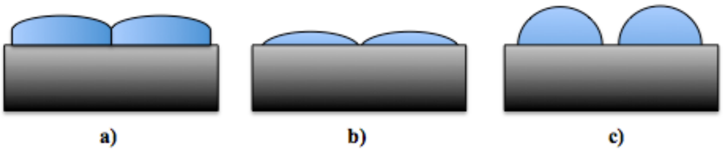

Figure 2.15: The stable configurations of a polycrystalline film on a substrate a) the completely covered substrate b) the partially connected film c) the uncovered substrate.

The precursor solutions used for sol-gel synthesis are generally either non-network forming metal ions in solution (inorganic approach) or network-forming polymers in solution (organic approach) [76]. For the inorganic approach the metal ions often have low solubility in water, and the solubility is usually enhanced by adding a complexing agent. The solubility of the metal ions in water is also influenced by pH and temperature of the sol. How pH influences the solubility is individual for each metal ion, while a higher temperature generally gives higher solubility. If the concentration of metal ions is increased above the solubility limit, the metal ions will precipitate out. The less water soluble the precursor is a combination of lower concentration, higher temperature and higher amount of complexing agents is needed to avoid precipitation of the precursor. pH and concentration of precursors are important parameters that affect the viscosity of the sol extensively. A higher viscosity gives thicker films when spin coating.

Even though the standard sol-gel process can be used for a wide range of applications, it has disadvantages like expensive cation alcoxide precursors [67, 80]. Another very popular wet chemical method is the Pechini method, which is a modified sol-gel method [16, 81]. Here other precursors can be used as the requirement of the metals involved forming suitable hydroxo complexes is eliminated.

2.3.1 The Pechini Method

The Pechini method was developed in 1967 specifically designed for the preparation of thin films [82]. Suitable metal salts are dissolved in the proper solvent and mixed at a molecular level. The problem is to avoid segregation and precipitation, which easily occurs due to the different solubility of the salts. To ensure a uniform film the cations have to be evenly distributed as the solvent evaporates. In the Pechini method this is done through a polyesterification reaction [16, 75, 81]. By adding a bi- or tridendate organic chelating agent as citric acid, cation complexes are formed. This increases the cation solubility in the solvent and precipitation is avoided. The complexes are linked together by adding a polyalcohol like ethylene glycol. By heating the solution the acid and the alcohol react through an esterification process as shown in Equation 2.3:

$$ROOH + R'OH \rightarrow ROOR' + H_2O \qquad (2.3)$$

The polymerization results in gelation of the solution. The rigid polymer network will hinder movement of the cations ensuring uniform distribution. The idea of the Pechini method is to trap precipitated salts in an organic matrix. By heat-treating the gel, either a homogenous metal-oxide powder or a film can be obtained.

An illustration of the condensation process in the Pechini method at an early stage is shown in Figure 2.16 [81].

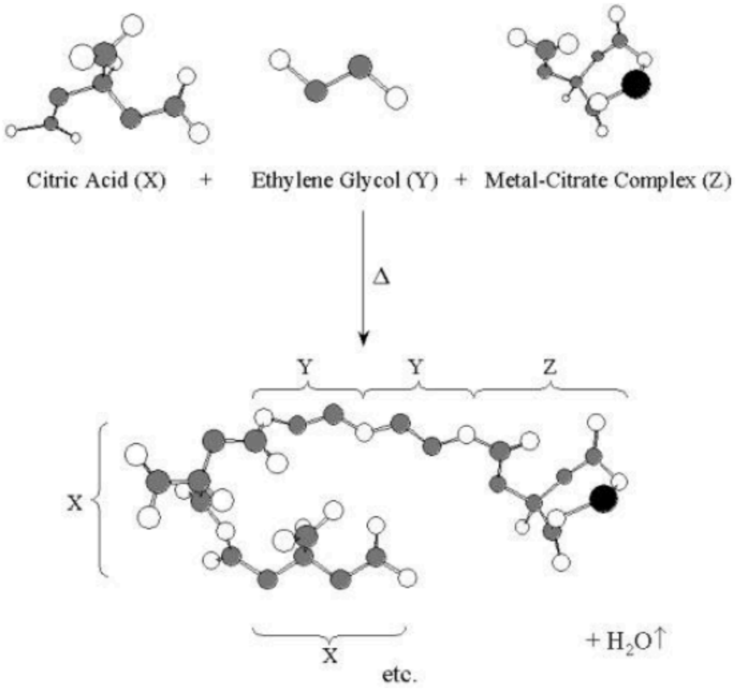

Figure 2.16: Schematic of the early stages of the polymerization in the Pechini method [81].

Figure 2.17 shows the reaction mechanism of metal complexation and esterification during the Pechini process [83]. It can be seen that two hydroxyl groups (-OH) interact with the metal cation (M^+) to form a complex. The metal complexes are then distributed homogenously throughout the solution by a network of organics, in this case citric acid and ethylene glycol, which forms through condensation.

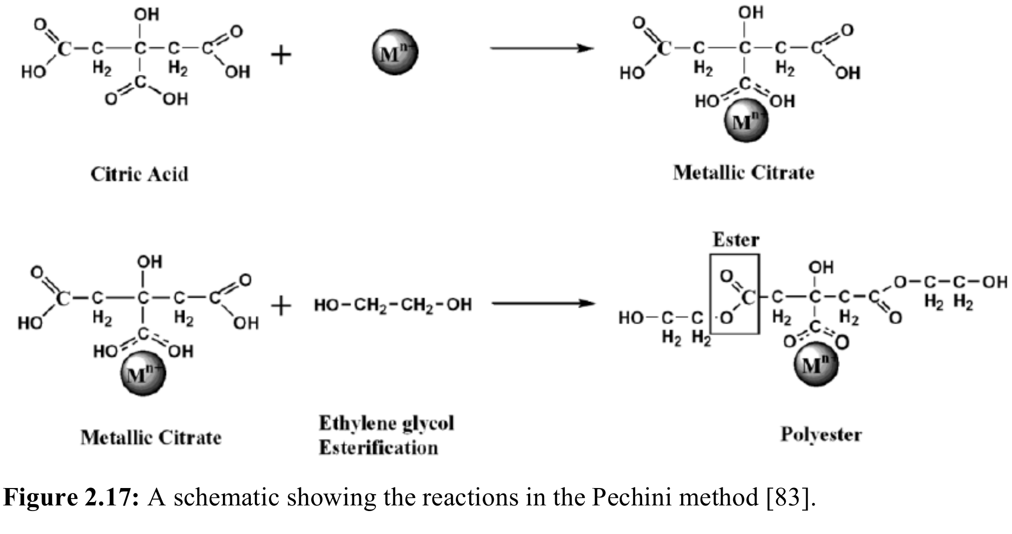

Figure 2.17: A schematic showing the reactions in the Pechini method [83].

A variety of metals form stable complexes with chelating agents [81]. Loads of variations of the Pechini method is thus found in literature. It is most often the chelating agent that is varied. The ability of the chelating agent to solubilize metal ions is of huge importance for the metal ions that form insoluble precipitates in water [75]. In the modified Pechini method for preparing ITO thin films and powders reported by Sunde et al. [16] acetic acid is used as chelating agent. Acetic acid has only one carboxyl group, which assumingly means that proper gel formation is not possible for this synthesis. It is assumed that bonding between the acid group and the metal cations are strong enough to keep the cations apart even though a network is not formed. The reason for this is not fully understood. What role ethylene glycol then plays in the solution is not well understood either. It has been observed that precipitation occur in this synthesis [16, 84, 85] and Otter [84] showed that a higher content of organics could be added to avoid precipitation. The Pechini method is an easy synthesis route that can produce complex oxides with exceptionally good homogeneity. The work done by Sunde et al. [16] showed that this synthesis route could give high quality thin films of high nanocrystallinity, homogeneity, and phase purity.

2.3.2 Wetting

In the modified aqueous Pechini method by Sunde et al. [16] a wetting agent was necessary to ensure satisfying wetting of the substrate. Wettability can be described by Young´s equation [86]:

$$\cos\theta = \frac{\gamma_{SV} - \gamma_{SL}}{\gamma_{LV}} \qquad (2.4)$$

Where θ is the contact angle between the liquid-vapor (LV) and solid-liquid (SL) interfaces as illustrated in Figure 2.19. γ_{SV}, γ_{SL} and γ_{LV} denote the surface tension of the interfaces between solid-vapor (SV), SL and LV as seen in Figure 2.18. To get wetting a contact angle less than 90^{o} is needed. By looking at Equation 2.4 it is clear that $\theta < 90^{o}$ corresponds to $\gamma_{SV} > \gamma_{SL}$.

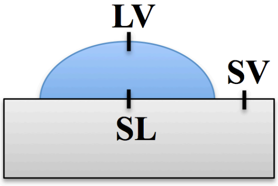

Figure 2.18: An illustration of the different interfaces present for a droplet of solution on a substrate.

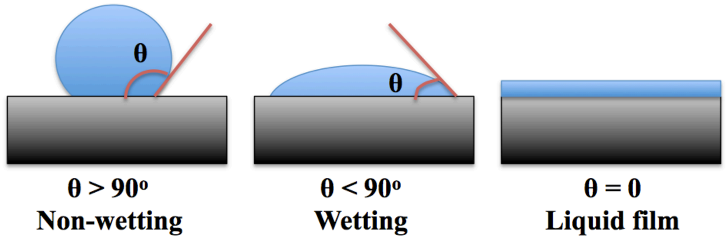

Figure 2.19: The illustration shows possible liquid-surface interactions for a droplet on a substrate.

2.4 Photochemical Activation of Thin Films

High quality metal-oxide films can be produced by wet chemical methods, and the subsequent conventional furnace heat-treatment step can potentially be replaced by photochemical activation.

The densification of the sol-gel films by irradiating with UV is caused by scission of organic compounds [15]. Bonds like C-H, O-H, and C-C can be cleaved, and photo annealing is known to remove hydrogen, hydroxyl groups, and water from low-temperature deposited oxide films. It is observed that many reactions take place simultaneously upon irradiation, and it is shown that the irradiation enhances the condensation reaction in the film. One can expect that the UV-induced annealing reactions will be diffusion or rate limited. UV curing of sol-gel films can be made more effective by irradiating in vacuum or inert atmosphere, and by heating the gel film to such temperatures that the reaction products like water evaporate [15].

Using UV radiation for curing is not new to industry as it is already used extensively in industrial processes. Some of the areas where UV curing is applied in production is for coatings, paints, electronics, optical fibers, dental compositions, and hydrogels [87]. Industrially curing is often performed using a moving belt to transport the material underneath one or more lamps. Curing time is then controlled by the speed of the belt. UV curing is a low-cost option. The equipment is simple, small, and cheap to purchase and operate. If it is possible to replace an existing curing method with UV-curing, it is likely to improve productivity and speed of the production line. It will lower the cost and energy use, and also open up the possibility for production of new and possibly also better products. Changing curing method might also enable elimination of flammable and polluting solvents in the synthesis lowering the health risk and reducing the polluting emissions.

A high-intensity UV lamp like the excimer lamp is best for industrial applications, but because of the limited availability low-pressure mercury lamps are still extensively used [15]. A low-pressure mercury lamp produces a polychromatic spectrum with intensive emission lines ranging in energy levels from 2.8 to 6.0 eV [87]. The main emission peaks from such a lamp are 254 nm and 185 nm. The lamp gives off a combined effect from light in the UV, visible, and infrared region. As already mentioned, when curing thin films by using a UV lamp the atmosphere should be inert. This is to prevent the formation of reactive ozone [12]. Oxygen molecules in air can react into ozone by absorbing the 185 nm emission from the UV lamp, decreasing the photochemical activation efficiency. A reduction in the photochemical activation efficiency can cause insufficient cleavage of the C-O bonds and poor densification of the films. This type of lamp is suitable for applications where slow cure rate is tolerated. Examples are liquid crystal displays and resist technology for the production of microchips.

For photochemical activation to occur in a film, it must have a strong light absorption for the main emission peaks of the UV radiation source. TCOs absorb light with short wavelength and typically have an absorption band edge at ~300 nm making them possible to photochemically activate using a low-pressure mercury lamp [1]. But, to create a TCO film photochemical activation also has to occur in the film when organics and solvents are still present.

Kim et al. [12] proposed that radiation from a low-pressure mercury lamp, especially the high energy radiation with wavelength 185 nm could induce cleavage of the C-O bonds in sol-gel processed IZO, IGZO and In_2O_3 thin films. This cleavage is thought to activate the metal cations into forming a M-O network. In addition to the UV irradiance, the infrared radiance was found to be an important energy contributor for the removal of organics and the reorganization of the M-O network. Infrared radiance is the amount of infrared energy emitted by the UV source and is often given as the temperature it generates on the sample surface. By studying the trends of atomic composition and electrical properties with curing time, the photochemical activation could be divided into two stages: a rapid chemical condensation followed by gradual structural rearrangement and densification. The high degree of densification that is seen after 60 minutes is proposed to be due to UV-assisted photolysis and reorganization of the M-O network leading to decomposition of organics. Kim et al. synthesized the In_2O_3, IZO and IZGO thin films by photochemically activating the as-spun films using a low-pressure mercury lamp. Similar area densities, thicknesses, atomic binding states (such as M-O bonding), optical transmittance, and band gap were found for films cured by UV lamp and furnace at 350 °C. The best electrical properties and uniformity was obtained for films cured between 90-120 minutes. An infrared radiance of 150 °C is induced by the UV lamp, and the temperature is found to flatten out at this value as further irradiation does not give a higher temperature. If the metal-oxide films are cooled on a cooling stage to about 40-70 °C during UV irradiation, or if they are cured using a furnace at 150 °C without UV irradiation, the resulting films show little or no electrical conductivity. Films UV cured in nitrogen show excellent properties, while films UV cured in air show poor properties and are unstable even though a higher temperature of 180 °C is obtained.

Asakuma et al. [88] investigated structural changes in ZnO thin films synthesized using sol-gel and spin coating when irradiated with a low-pressure mercury lamp. The formation of Zn (s) in a porous gel film was found to occur for films pre-heated at 60 °C, while hexagonal ZnO crystals in a dense amorphous structure was obtained for films pre-heated at 100 °C. The thin films were irradiated for 25-400 hours under ambient conditions and the irradiation was found to decompose the residual organics like the COO groups. It was determined that the photo-induced structural changes like the crystallization and reduction of ZnO were not correlated to the decomposition of the residual organics.

Imai et al. [89] reported on the structural changes in In_2O_3 sol-gel derived thin films caused by UV irradiation. The formation of crystalline indium metal was obtained when a low-pressure mercury lamp was used, while UV beams from an ArF excimer laser was found to give crystalline In_2O_3 films.

Ohishi et al. [90] prepared amorphous insulating tantalum oxide thin films at room temperature by combining the sol-gel method with photo-irradiation. The electrical characteristics were nearly the same as those of films prepared by sputtering, chemical vapor deposition, or the sol-gel method combined with conventional heat treatment. Nishizawa et al. [91] produced crystalline ZrO_2 thin films by the sol-gel method through low-temperature UV curing giving good electrical properties.

Hirai et al. [92] prepared ZrO_2 coatings through the sol-gel process and UV curing at ambient conditions, giving an enhanced corrosion resistance of the aluminum substrate compared to heat treated films.

Calzada et al. [93] obtained sol-gel derived $PbTiO_3$ based ferroelectric thin films using a low-temperature UV irradiation assisted process. Non-irradiated films prepared at the same temperature did not show a ferroelectric response and the UV assisted film showed ferroelectric properties similar to those reported for non-irradiated films prepared at higher temperatures.

Imai et al. [94] found that sol-gel derived amorphous silica films could be significantly densified by using UV radiation from a synchrotron in ultrahigh vacuum. Van de Leest [15] found that thin sol-gel films based on hydrolyzed alkoxy compounds could be cured using UV radiation at low temperature and that the precursor could be tailored to give a particular film structure for use in specific applications.

2.4.1 Photophysics

UV radiation is a form of electromagnetic radiation, meaning that it propagates in space as waves of electronic and magnetic fields [95]. According to quantum theory electromagnetic waves carry discrete amounts of energy. The magnitude of energy is dependent on the frequency of radiation, were a higher frequency (or a shorter wavelength) gives higher energy. To break a bond, the energy absorbed by a molecule must exceed the bond energy. Thus, both the energy of the radiation and the amount of energy absorbed by the material are critical factors. Table 2.2 shows the bond strength between different atoms in polyatomic molecules.

Table 2.2: Bond strength in polyatomic molecules [95].

Bond	Strength [kJ/mol]
C – H	420-560
C – C	300-720
C – Cl	320-460
C – N	120-300
C – O	~1000
C = O	500-700
H – O	370-500
O – O	150-210
S – O	>550
Si – Si	330-370

The amount of energy that crosses the surface of a sample is determined by reflection and scattering, thus these are also important factors. UV is a surface technique, meaning most of the events initiated by UV radiation occur near the surface [87]. This is because the absorption of photons is governed by the Beer-Lambert law, which is given in Equation 2.5. It is therefore difficult to cure thick films using UV radiation, especially if they are pigmented.

$$I = I_0 10^{-\varepsilon c d} \qquad (2.5)$$

In the above equation I is the intensity of the transmitted light, I_0 is the intensity of the incident light, ε is the molar extinction coefficient, c is concentration of absorbing species, and d is the optical path length.

The absorption of energy occurs in a single step, thus the difference in final and initial energy levels of a molecule is equal to the energy of the absorbed photon. When a molecule absorbs UV radiation, the molecule becomes excited [95]. This only happens if the energy carried by the photon, hv, is exactly equal to the energy required for absorption and excitation. Since the energy difference between the normal and excited state has to equal *hv*, which wavelengths that can be absorbed is restricted. An excited molecule is able to enter into chemical reactions, meaning both the formation of new chemical bonds and the breaking up of existing bonds.

The energy of radiation can cause different molecular transitions like electronic transitions, but also rotational, translational, and vibrational mode transitions. When a molecule absorb energy there are eight possible outcomes for disposal of the excitation energy:

1. Dissociation ($AB^* \rightarrow A + B$)
2. Reaction with other species ($AB^* + C \rightarrow AC + B$ or ABC)
3. Isomerization ($AB^* \rightarrow BA$)
4. Ionization ($AB^* \rightarrow AB^+ + e^-$)
5. Deactivation ($AB^* \rightarrow AB$ + energy dissipation)
6. Intramolecular energy transfer ($ABC^* \rightarrow AB^*C$)
7. Intermolecular energy transfer ($AB^* + CD \rightarrow AB + CD^*$)
8. Luminescence ($AB^* \rightarrow AB + hv$)

The first four processes are photochemical, while the last four processes are photophysical conversions.

2.5 Characterization

In this part, the main characterization methods used in this master thesis will be addressed.

2.5.1 Gracing Incident X-ray Diffraction

The basic principle of standard X-ray diffraction is as follows; the sample is illuminated with a monochromatic X-ray beam and the angle at which constructive interference occurs is measured. The interaction between the X-ray beam and the crystal can according to Bragg´s law, Equation 2.6, be seen as a reflection of the incident X-ray on the lattice plane of the crystal [96].

$$n\lambda = 2d_{hkl}\sin(\theta) \tag{2.6}$$

In Equation 2.6 n is an integer defining the order of diffraction, λ is the wavelength, d_{hkl} is the distance between the lattice planes and θ is the angle between the X-ray beam and the lattice plane. The relation between the Miller Indices *hkl,* the lattice parameter a and the distance between two lattice planes d_{hkl} shown in Equation 2.7 holds for cubic crystals [96]. As θ is measured through X-ray diffraction and the wavelength of the X-ray beam is known, the dimensions of the cubic unit cell are easily determined.

$$d_{hkl} = \frac{a}{\sqrt{h^2 + k^2 + l^2}} \tag{2.7}$$

X-ray radiation penetrates deep into a sample; so conventional X-ray diffraction is not surface sensitive [97-99]. To be able to study the surface of a sample the gracing incidence X-ray diffraction technique is used. This is a specific set-up on the X-ray diffraction instrument. By performing the measurements at low incident angles the signal from the top layer of the sample is maximized relative to the signal from the substrate and background. This makes it possible to do phase analysis and evaluate the crystallography of thin films in the range of 10 nm to 200 nm into the sample. The incident angle is typically 0.3° to 3°, which increases the path length of the X-ray beam through the film [100]. In this set-up, which is shown in a simplified manner in Figure 2.20, the incident beam is made nearly parallel to the sample surface by Göbel mirrors. It is very difficult to adjust these mirrors perfectly and if it is not done accurately the peaks can shift approximately 0.1° between runs. The Soller slit on the detector side only allows those beams that are nearly parallel to each other to reach the detector, making the diffracted beam parallel. During the collection of the diffraction spectrum the sample and source does not move, thus the incident angle, θ_1, the beam path length, and the irradiated area are held constant. The detector moves around the sample with an angle θ_2 between the sample and the diffracted beam. The counts are recorded as a function of 2θ, as the relation $2\theta = \theta_1+\theta_2$ is valid throughout the scan. Several other set-ups can be used for equivalent thin film measurements. The gracing incidence X-ray diffraction set-up explained above is specific for the instrument used in this master thesis.

An advantage of gracing incidence X-ray diffraction compared to X-ray diffraction is that all peaks of an impurity or contamination are visible in the diffractogram. This is due to the large stationary area on the surface hit by the incidence beam during the scan. Another advantage of X-ray diffraction techniques is that they are non destructive, thus the samples can be used in further analysis. One limitation to the gracing incidence X-ray diffraction set-up is that it is not suitable if the film has a high degree of preferred orientation, for example epitaxial films.

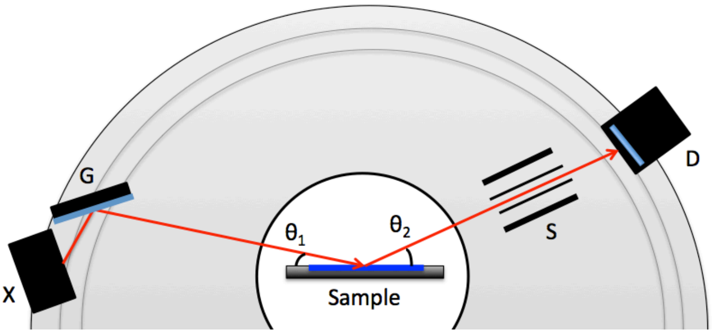

Figure 2.20: Set-up of the diffractometer showing the beam path. Included in the schematic are the X-ray tube (X), the Göbel mirror (G), the Soller slit (S) and the detector (D), the incidence angle θ_1 and the variable angle θ_2.

2.5.2 Scanning Electron Microscopy

Scanning electron microscopy (SEM) is used to characterize materials and surfaces on the micrometer and nanometer scale [101]. An electron source (e.g. a heated filament) generates an electron beam and when the electrons hit the sample the electron-sample interaction generates a range of different signals that are emitted from the sample and collected by suitable detectors. Due to the excellent depth of focus in SEM the images look three-dimensional.

The electrons from the filament may be scattered elastically or inelastically when they hit the sample. Elastic scattering gives electrons that are called backscattered electrons (BSE). This signal can be used to see topography and to differ between areas with varying mean atomic number or different crystallographic directions. Inelastic scattering gives the rest of the different signals except backscattered electrons. Secondary electrons (SE) are useful to observe topographic surfaces, as only the secondary electrons generated in the top layers of the sample will have enough energy to escape the sample. Continuous X-ray radiation is unwanted background radiation that limits the determination of the chemical composition of the sample. Other signals that can be detected by SEM are characteristic X-ray radiation and Auger electrons. The signals are used for compositional and elemental analysis. The chemical composition can be determined qualitatively and also a quantitative determination of the chemical composition can be obtained. The quantitative determination by energy dispersive X-ray spectroscopy (EDS) is not accurate but can be used to give an indication, especially on the ratio between elements. The energy resolution of the EDS used in this thesis is 0.124 keV. This means that elements that sends out signals that lie closer to each other in energy than 0.124 keV cannot be separated by the detector, but are seen as one diffraction line in the spectrum. Thus it is not possible to quantify each of the two elements correctly. Due to the detector protecting beryllium window that absorbs radiation from elements lighter than sodium, it is impossible to detect this and lighter elements using SEM. The doping level of tin in the thin films can be determined using Auger electron spectroscopy due to its high accuracy with respect to quantification. Still, X-ray photoelectron spectroscopy is the first choice for quantifying the tin content because it is a bit more sensitive, and more information about the chemistry is obtained. The quantification using X-ray photoelectron spectroscopy is also obtained for a larger region of the sample, which is good if the sample is homogenous.

The signals mentioned in the above section have different emission depths, meaning that they give information from different depths of the sample. In Figure 2.21 the relative differences in emission depth are shown for the main signals found in SEM. The emission depth of electrons is typically 10 Å, while secondary electrons has an emission depth approximately between 50 Å to 500 Å. The emission depth of backscattered electrons and characteristic X-ray are from around 0.1 μm to a few μm depending on the acceleration voltage and the weight of the elements analyzed, where a high acceleration voltage combined with light elements give a high emission depth.

Auger electron spectroscopy is a surface technique as the Auger electrons only escape from the top part of the surface (even though they are generated as deep as the characteristic X-ray signal). Additionally, Auger electron spectroscopy is a high resolution technique. It is often referred to in literature that the resolution is only restricted by the diameter of the electron beam, giving a resolution of 1-2 nm. This is not entirely true as Auger electrons are also generated from the backscattered electron signal, which lowers the maximum possible resolution. The maximum theoretical resolution possible for the instrument used in this thesis is around 10 nm, while in practice the resolution is between 20-50 nm.

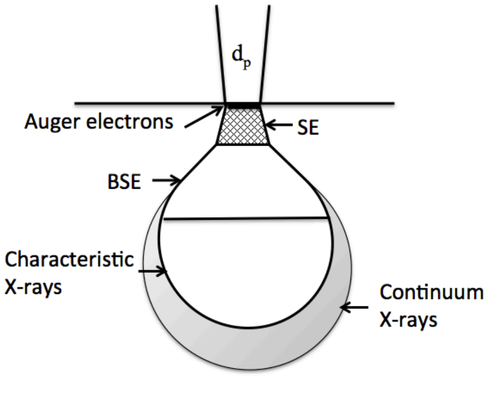

Figure 2.21: Schematic of the emission depth for the different signals generated in SEM. d_p is the diameter of the electron beam.

A variety of different samples can be studied using SEM without extensive sample preparation. The sample should be free from fat and oil and it should not contain easily evaporated substances as the chamber is under vacuum. In addition, the samples need to be conductive or else charging will occur as the electrons accumulate on the surface of the sample. This will lead to poor image quality. Avoiding charging might be possible by using low acceleration voltage, but the most used technique is to coat the sample with a conductive layer of for example carbon or gold. The thickness of the layer is on the order of 100 to 1000 Å.

2.5.3 Surface Roughness and Topography

Stylus based techniques are well suited for studying the roughness and topography of thin films. Both atomic force microscopy (AFM) and profilometry are stylus techniques, which means that the roughness and topography of a film is measured by monitoring the deflections of a fine-tipped stylus as it is dragged along the surface of the film.

A profilometer is used to reproduce the profile of a sample surface. The raw data from the profilometer can be used to calculate a wide range of different sets of parameters like roughness, waviness, height and geometry parameters. The most common representation of surface roughness is the arithmetic average of absolute value, R_a, which is given in Equation 2.8 [102]. Another roughness parameter is the root mean squared given in Equation 2.9

$$R_a = \frac{1}{n}\sum_{i=1}^{n}|y_i| \tag{2.8}$$

$$R_{RMS} = \sqrt{\frac{1}{n}\sum_{i=1}^{n}(y_i)^2} \tag{2.9}$$

where y_i is the distance from the average height of a profile (the mean line) for measurement i, and n is the number of measurements. R_a is the average of a set of surface peaks and valleys, while R_{RMS} is the root mean square average of the profile height deviations from the mean line. From the equations above, it can be seen that a single large peak will raise R_{RMS} more than the R_a value. Therefore, R_{RMS} is always large than R_a.

AFM offers three-dimensional shape measurements of a surface with accuracy in the nanometer scale [103]. An AFM can be operated in both liquid and air, and can also be operated in the different modes contact, non-contact, and tapping mode. For contact mode where the stylus tip is brought in contact with the sample surface, the dominating forces between the tip and sample surface is strong elastic repulsion forces. The strong force between the sample and the tip during measurements gives a high image resolution. One downside with contact mode, is that the dragging motion of the tip as it moves over the surface combined with the adhesive forces between the tip and surface can cause substantial damage to both sample and probe and create artifacts in the image.

2.5.4 Ellipsometry

There are two main classes of thin film measurements, optical and stylus based techniques [104]. Stylus instruments are limited in speed and accuracy, and a step in the film is required to measure film thickness. Optical techniques are usually preferred when measuring thin films because they are accurate, nondestructive and require little or no sample preparation.

Optical techniques determine thin-film characteristics by measuring how the films interact with light and are mainly used to measure the thickness, roughness, and optical constants of a film [104]. Reflection occurs whenever light crosses the interface between materials with different refractive indexes. Refractive index, n, and extinction coefficient, k, describe how light propagates through a film. The refractive index is defined as the ratio of the speed of light in vacuum to the speed of light in the material. The extinction coefficient is a measure of how much light that is absorbed in the material. When $k = 0$ a transmittance of 100 % is obtained.

The two most common optical techniques are spectral reflectance and ellipsometry [104]. Spectral reflectance measures the amount of light reflected from a thin film when the incidence light is perpendicular to the surface, while ellipsometry measures reflectance at non-normal incidence angles and at two different polarizations. Ellipsometry is considered to be a more powerful technique than reflectance as the two different polarization measurements provide twice as much information for the analysis. The non-normal incidence angles also make ellipsometry more sensitive to very thin layers. In addition, variable-angle ellipsometry can be used to take reflectance measurements at many different incidence angles, increasing the amount of information even further.

This technique is very sensitive as it is based on the relative phase change in a beam of polarized light reflected from the surface of a sample [104]. The values that are actually measured by the ellipsometer is the polarization states, Ψ and Δ, which is related to the Fresnel reflection coefficients R_p and R_s for p- ansd s- polarized light, respectively as shown in Equation 2.10.

$$\frac{R_p}{R_s} = \tan(\Psi)e^{i\Delta} \tag{2.10}$$

This ratio is a complex number and also includes the relative phase change, Δ, which makes the measurement very sensitive.

There are several factors that determine the validity of the obtained ellipsometry measurements [104]. When measuring film thickness, the wavelengths used for the measurements should not be too much smaller or larger than the film thickness. The visible and UV wavelengths are best for thin films in the range 1 Å to 1 µm. Also, the thickness of the film should be as uniform as possible in the measured spot. Ellipsometry is best for smooth surfaces, and the roughness features should be less than ~10 % of the probe beam wavelength for the measurements to be valid.

A schematic of the ellipsometer used in this master thesis showing the components of the instrument is presented in Figure 2.22 [104].

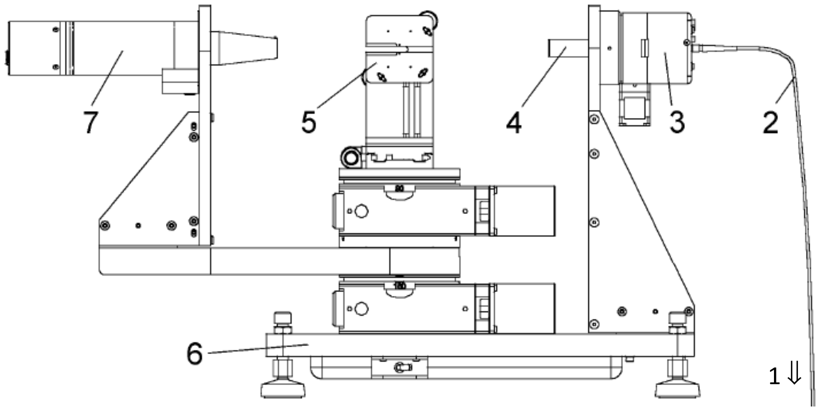

Figure 2.22: A modified schematic of the Wollam Co. variable angle ellipsometer showing the components of the instrument: 1) monochromator, 2) fiber optic cable, 3) input unit with polarizer, 4) alignment detector, 5) sample stage, 6) goniometer base for automated angle control, 7) detector unit with rotating analyzer and solid state detectors [104].

When determining material properties from experimental data obtained by the ellipsometer there is a basic procedure that is followed, as the sample parameters of interest are not measured directly [104]. The procedure can be divided into four steps; measurement, model, fit, and results. A model is developed based on some known parameters (wavelength of incident light, the incident beam polarization state, and the angle incidence) and unknown parameters (film thickness and optical constants). A best possible fit of the model to the measured data is obtained by varying the unknown physical parameters. The quality of the match between the data calculated from the model and the experimental data is quantified by the mean-squared error. The mean-squared error obtains a positive value when the calculated data deviates from the experimental data, and is zero when they match exactly. The minimum value for the mean-squared error is obtained for the best fit, and only one set of parameters should give the minimum mean-squared error.

It is also possible to measure the transmittance of transparent samples by using the ellipsometer. The principle of the method is to detect how much light that travels through a material by measuring how much of the incoming light that gets out [105]. A light source with a known spectrum is used as the incoming light, I_0, and a detector measures the amount of light out, I. The relation between transmittance, T, I_0 and I is shown in Equation 2.11.

$$T = \frac{I}{I_0} \tag{2.11}$$

From the transmittance measurements the absorption coefficient, α, can be calculated as shown in equations 2.12 and 2.13 if the thickness of the film, *d*, is known.

$$I = I_0 e^{-\alpha d} \tag{2.12}$$

Equation 2.13 is obtained by rearranging Equation 2.12.

$$\alpha = \frac{1}{d}\ln\left(\frac{I}{I_0}\right) = \frac{1}{d}\ln(T) \tag{2.13}$$

The absorption coefficient can further be used to calculate the band gap. Equation 2.14 describes the photon energy dependence of the absorption coefficient near the absorption edge [62]. The band gap, E_g, can then be found by plotting α^2 versus the photon energy, *hv,* and extrapolate the linear portion near the absorption edge of the plot to $\alpha^2 = 0$.

$$\alpha \propto (hv - E_g)^{1/2} \tag{2.14}$$

2.5.5 Conductivity Measurements by the van der Pauw Method

A practical way to specify conducting characteristics for TCO films are through resistivity, ρ, and sheet resistance, R_{sh}. Conductance [S] and resistance [Ω] are both dependent on the geometry of the sample, while conductivity [S/cm], resistivity [Ω cm] and sheet resistance [Ω/square] are material properties. This makes them easy to compare to values found in literature. The sheet resistance is related to resistivity and conductivity through Equation 2.15 for films [43].

$$R_{sh} = \frac{\rho}{d} = \frac{1}{\sigma d} \tag{2.15}$$

Where *d* is thickness of the film and σ is the conductivity.

The resistivity for a flat arbitrary shape can be calculated by using the van der Pauw method for conductivity measurements without knowing the current pattern [106]. An arbitrary shaped sample is shown in Figure 2.23. The current is only able to go around holes, hence the sample must not contain any cracks. In addition the contacts need to be small and they should be placed at the periphery of the sample. The thickness of the samples needs to be uniform.

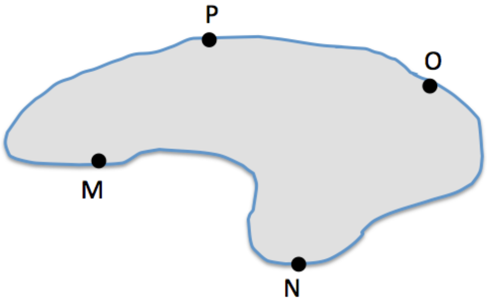

Figure 2.23: A flat sample of arbitrary shape.
M, N, O and P denote the four contact points.

The relations needed to calculate the resistivity, found in Equation 2.16 and Equation 2.17, was introduced by van der Pauw and holds for all samples of arbitrary shape.

$$\rho = \frac{\pi d}{\ln 2} \frac{R_{MN,OP} + R_{NO,PM}}{2} f \tag{2.16}$$

The value of the correction factor, *f*, is calculated from Equation 2.17 by using numerical iteration.

$$\frac{R_{MN,OP} - R_{NO,PM}}{R_{MN,OP} + R_{NO,PM}} = \frac{f}{\ln 2} \cosh^{-1} \frac{e^{\frac{\ln 2}{f}}}{2} \tag{2.17}$$

$R_{MN,OP}$ is defined as the voltage drop from O to P divided by the current measured from M to N, where M, N, O and P are the four contact points depicted in Figure 2.23. $R_{NO,PM}$ is defined analogously. $R_{MN,OP}$, $R_{NO,PM}$, and d can be measured. Resistivity is then the only unknown in Equation 2.16.

3. Experimental

The first part of this section presents the thin film preparation. This includes information on the solution synthesis, the substrates, the solution deposition, and the curing step. The second part gives details on the different characterization methods used.

3.1 Preparation of Thin Films

The thin films were prepared using a wet chemical method, more specifically a modified aqueous Pechini method developed by Sunde et al. [16]. In Figure 3.1 the steps of the process is shown, including the deposition and the curing step.

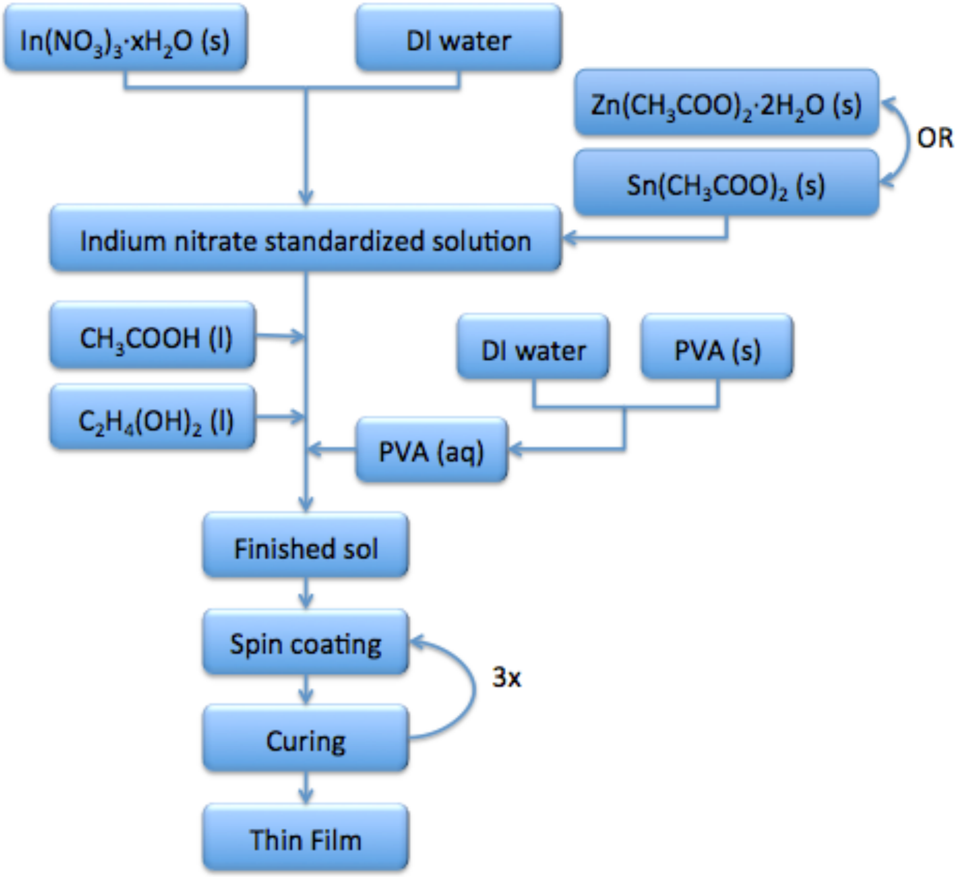

Figure 3.1: A flow chart illustrating the thin film synthesis. DI water is short for deionized water and PVA is short for polyvinyl alcohol.

3.1.1 Chemicals

The metal precursors used to prepare the thin films were indium (III) nitrate hydrate (>99.9 % trace metal basis), tin (II) acetate (>99.9 % trace metal basis) and zinc acetate dihydrate (>99.0 %) all from Sigma Aldrich. Acetic acid (reagentplus ≥ 99 %, Sigma Aldrich) was used as a complexing agent and ethylene glycol (EMSURE®, Merck) was added to obtain esterification. 3 weight% polyvinyl alcohol (Sigma Aldrich) was added to improve the wetting properties of the solution. Deionized water was used as solvent. Table 3.1 presents the chemicals used to prepare the thin films, their function, chemical formula and molar mass.

Table 3.1: The chemicals used for the preparation of thin films together with their function, chemical formula and molar mass [39].

Chemical	**Function**	**Chemical formula**	**Molar mass [g/mol]**
Indium (III) nitrate hydrate	Precursor	$In(NO_3)_3 \cdot xH_2O$	300.83 (anhydrous)
Tin (II) acetate	Doping precursor	$Sn(CH_3COO)_2$	236.79
Zinc acetate dihydrate	Doping precursor	$Zn(CH_3COO)_2 \cdot 2H_2O$	219.51
Acetic acid	Complexing agent	CH_3COOH	60.05
Ethylene glycol	Gelation agent	$C_2H_4(OH)_2$	62.07
Polyvinyl alcohol	Wetting agent	$(C_2H_4O)_x$	~85 000 – 124 000

3.1.2 Parameters

In this work In_2O_3 thin films doped with 5, 10 and 15 mol% Sn and 40 mol% Zn were prepared. An overview of the solutions prepared together with their composition and mol% is presented in Table 3.2.

Table 3.2: The different compositions of the thin films prepared in this work.

Name	Composition	mol% In	mol% Sn	mol% Zn
ITO5%	$In_{1.9}Sn_{0.1}O_{3.05}$	95	5	-
ITO10%	$In_{1.8}Sn_{0.2}O_{3.10}$	90	10	-
ITO15%	$In_{1.7}Sn_{0.3}O_{3.15}$	85	15	-
IZO40%	$In_{1.2}Zn_{0.8}O_{2.6}$	60	-	40

A total number of 28 different thin films were made by varying solution composition, solution nr, substrate and curing method, as can be seen in the thin film overview in Table 3.3. Solution nr denotes separate solutions made for the different compositions in the exact same manner, thus in theory there should be no difference between these solutions. RTP denotes the rapid thermal process heat-treatment. UV denotes the UV curing at room temperature and UVHT denotes the high temperature UV curing at 150 °C Abbreviations for the thin film names are built up as follows: Composition-Solution nr-Substrate-Curing method. In “Appendix B Thin Film Library” an additional overview of the thin films is given. This can be used to complement the thin film overview in Table 3.3.

Table 3.3: Thin film overview. RTP denotes the rapid thermal process heat-treatment. UV denotes the UV curing at room temperature and UVHT denotes the high temperature UV curing at 150 °C.

Composition	**Solution nr**	**Substrate**					
		Glass			*Si wafer*		
		Curing method			**Curing method**		
		RTP	*UV*	*UVHT*	*RTP*	*UV*	*UVHT*
ITO5%	1	x			x		
	2	x			x		
ITO10%	1	x			x		
	2	x			x		
	3	x	x	x	x	x	x
ITO15%	1	x			x		
	2	x			x		
IZO40%	1	x			x		
	2	x			x		
	3	x	x	x	x	x	x

3.1.3 Standardization of Indium Nitrate Solution

Since the indium (III) nitrate hydrate precursor contains variable amounts of crystal water, it was necessary to standardize the indium nitrate solution to determine the cation concentration in the solution. The indium (III) nitrate hydrate precursor was dissolved in deionized water and stirred overnight. Four crucibles were preheated to the actual standardization temperature to evaporate the water they had absorbed and then weighed. Approximately 2 ml of the solution was added to one of the crucibles and its weight was measured. This was repeated for all the crucibles as quickly as possible to avoid the crucible absorbing water from the air and evaporation of the solution. Subsequently, the crucibles were placed in an oven. Atmosphere during the heating was air. The heating rate was 50 °C/h up to 100 °C. Such a low heating rate was used to avoid heavy boiling. Holding time at 100 °C was 3 hours. From 100 °C to 1100 °C the heating rate was raised to 200 °C/h. Holding time at 1100 °C was 6 hours. The crucibles were cooled down to 400 °C at a rate of 200 °C/h, picked out of the oven and placed in a desiccator. The heating program is illustrated in Figure 3.2.

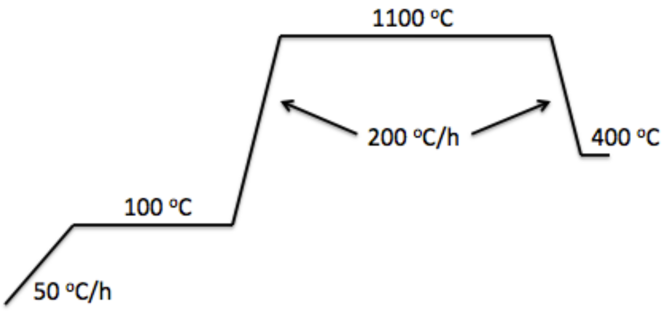

Figure 3.2: Heating program for the standardization of the indium nitrate solution.

During the heat treatment, the chemical reaction shown in Equation 3.1 occurred giving In_2O_3 powder as the product in the crucibles.

$$2In(NO_3)_3 \cdot xH_2O(aq) \rightarrow In_2O_3(s) + 3NO_2(g) + xH_2O(g) \tag{3.1}$$

When the crucibles had reached room temperature they were weighed. By determining the resulting amount of In_2O_3 powder, number of mol In^{3+} cations per gram of solution was calculated using Equation 3.2.

$$c_{In^{3+}} = \frac{2m_{In_2O_3}}{M_{In_2O_3} \cdot m_{sol}} \tag{3.2}$$

Where m_{In2O3} is the mass of In_2O_3 powder and m_{sol} is the mass of solution. For the standardization to be successful, the standard deviation between the four parallels should not be larger than the order of 10^{-7} mol In^{3+}/g solution.

3.1.4 Procedure

To make the solutions in Table 3.2, stoichiometric amounts of the indium nitrate standardized solution and doping precursor was mixed. The solution was heated to about 80 °C on a hot plate and stirred with a magnetic stirrer. The organics, acetic acid and ethylene glycol, were added according to a molar ratio of 1:1.5 between cation concentration in solution and the organic. The heating procedure on the hot plate was repeated. Deionized water was added to dilute the solution, obtaining the wanted cation concentration of 0.4 M. A solution of deionized water with 3 weight% polyvinyl alcohol was added in a 1:1 volume ratio giving a resulting cation concentration of 0.2 M. The actual weight of chemicals used in each solution is listed in “Appendix A Preparation of Solutions”.

3.1.5 Preparation of Substrates and Spin Coating

A spin coater (Laurell Technologies, WS-400B-6NPP-LITE/ AS) was used to make the thin films by spinning the finished sol onto substrates. The substrates used were either glass (microscope slides, VWR) or n-type silicon wafers. An exception is the three thin films on silicon substrate made from the IZO40% solution nr 3, see Table 3.3, here p-type silicon wafers were used. Details on the n- and p-type silicon substrates can be found in tables 3.4 and 3.5.

Table 3.4: Properties of the n-type silicon substrate.

N-type Si wafer	
Doping	Phosphorus
Orientation	<100>
Thickness	256 - 306 μm
Resistance	5 - 10 Ω
Finish	Single-side polished
Supplier	Si-Mat

Table 3.5: Properties of the p-type silicon substrate.

P-type Si wafer	
Doping	Boron
Orientation	<100>
Thickness	256 - 306 μm
Resistance	0.01 - 0.02 Ω
Finish	Single-side polished
Supplier	Si-Mat

For thin films made using solution nr 1, see Table 3.3, the glass substrates were cut into a square shape with the dimensions 25 mm × 25 mm, while the silicon substrates were cut into a square shape with the dimensions 20 mm × 20 mm. For thin films made using solution nr 2 and solution nr 3 both types of substrates were cut into a square shape with the dimensions 12 mm × 12 mm. The glass substrates were cut using a diamond scribe, while the silicon substrates were cut using a scalpel. The glass substrates were rubbed with soap and water, rinsed in deionized water and sonicated in ethanol for 10 minutes before they were dried with an airbrush. Nitrogen was used to blow of dust on the silicon substrates after cutting.

A syringe with a 0.2 μm filter was used to deposit excess amount (about 20 droplets for the large substrates and 15 droplets for the small substrates) of the finished sol onto the substrates. A filter was used to avoid precipitates in the thin films. The substrates were then spun using a spin coater at 3000 rpm for 45 seconds. Figure 3.3 depicts the spin coater utilized and Figure 3.4 illustrates the four steps of the spin coating process. When the substrates are spun the acceleration cause spin-up, which means that most of the solution is spun off as centripetal forces make the solution flow slowly outwards from the center of the substrate. Spin-off is when the rotation speed becomes constant, and more fluid is ejected at the perimeter as droplets. The film thickness is decreased uniformly. The last step of the spin coating process is evaporation. At this step evaporation of solvent further decrease the film thickness resulting in a thin film. A hot plate at 80 °C was used to pre-cure the substrates for 10 minutes followed directly by the curing step. Three layers of solution were deposited on each substrate using the procedure explained above for all layers. The curing step was repeated after every deposited layer. Solution age when spin coating and curing were performed was 1 day for all the thin films except for the UVHT cured thin films, which had a solution age of 2 days.

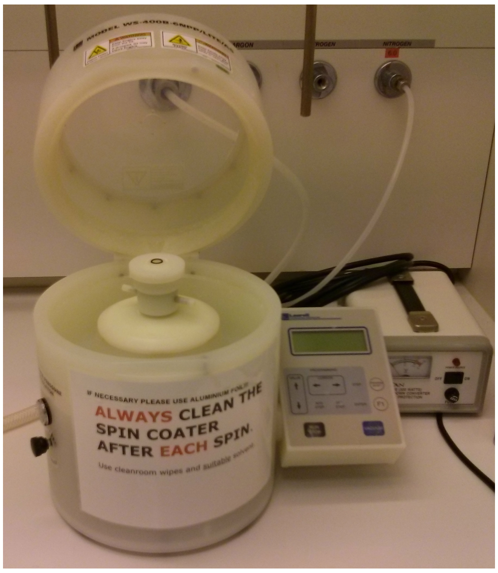

Figure 3.3: Picture of the Laurell Technologies, WS-400B-6NPP-LITE/ AS spin coater utilized.

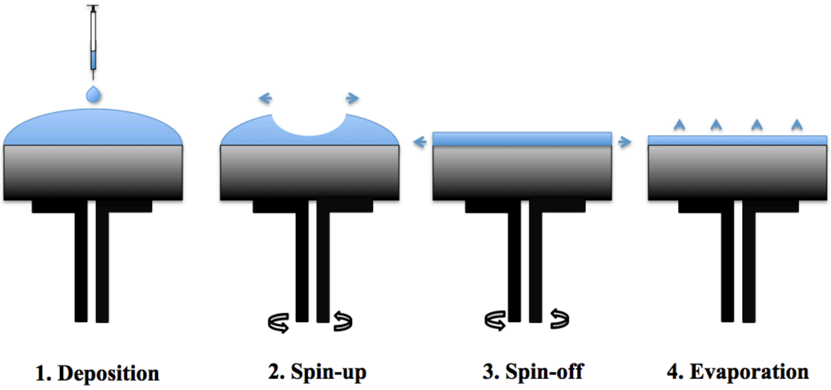

Figure 3.4: The steps of the spin coating process.

3.1.6 Curing

For the curing step two methods were used: 1) A rapid thermal process furnace (Jipelec, Jetfirst 200 mm) and 2) A UV-curing system (an in-house modified Novascan, PSDP-UV4) with an airtight chamber, heating stage, and nitrogen atmosphere. For the master thesis, several changes were done to the UV set-up used in the specialization project [107] to get a more efficient UV curing. Pictures of the original and modified UV set-ups are shown in Figure 3.5.

Figure 3.5: The picture to the left shows the original Novascan, PSDP-UV4 UV set-up, while the picture to the right shows the modified UV set-up. The UV lamp is secured in the lid of the chamber for both set-ups.

The UV lamp and control stage was kept from the original set-up. The original set-up had an airtight chamber with a quartz glass on top, inside a larger chamber where the lamp was secured in the lid. The main contribution to a higher UV lamp efficiency was to remove the quartz glass. For the modified set-up the sample to UV lamp distance is approximately 1 cm, which is a shorter distance than was possible for the original set-up. This will also increase the UV lamp efficiency. The modified set-up does not have an adjustable stage, and it is not possible to vary the sample to lamp distance. The modified set-up also has a heating element making it possible to obtain a higher curing temperature. A temperature at the thermocouple of 150 °C was determined to be a reasonable maximum temperature. Going to temperatures above this could damage the apparatus and be harmful to the surroundings.

Using the rapid thermal process furnace for heat-treatment of In_2O_3 and ITO thin films prepared by the synthesis used in this thesis has already been proven successful [16]. In this thesis the thermally cured thin films are used mainly to compare with the

UV cured thin films, but also to study the reproducibility of the thin films and the effect of tin doping. Solution nr 1, 2, and 3 in Table 3.3 were made using the same procedure. The reason for making theoretically equal solutions and thus thin films was as mentioned above to study the reproducibility of the thin films. The rapid thermal process furnace curing was performed at 530 °C for 1 hour under vacuum (10^{-2} mbar). Before onset of the heating, the furnace chamber was purged with nitrogen gas to assure an inert atmosphere. Both the spin coater and the rapid thermal process furnace are situated in a cleanroom ISO7 (NTNU NanoLab).

The possibility of curing the thin films using a UV lamp instead of the furnace was studied making 8 thin films as seen in Table 3.3. The different UV cured thin films were made by combining two different thin film compositions, two different substrates, and two different curing temperatures. UV curing was performed at room temperature and at 150 °C, both with a duration of 2 hours and a sample to lamp distance of about 1 cm.

The temperature of the thin films during UV exposure was monitored using a thermocouple. The thermocouple was placed in contact with the top surface of an uncoated substrate as shown in the picture to the right in Figure 3.5. Before the UV lamp was turned on, the samples were placed in the chamber and the lid was secured with screws. The chamber was emptied by a vacuum pump, followed by purging with nitrogen. After a while, a stable flow between 10 to 20 mL/min was obtained in the chamber. In addition to a flow meter at the inlet, a bubble flask was placed at the outlet of the chamber to control the nitrogen flow. A diagram showing the UV set-up is presented in Figure 3.6.

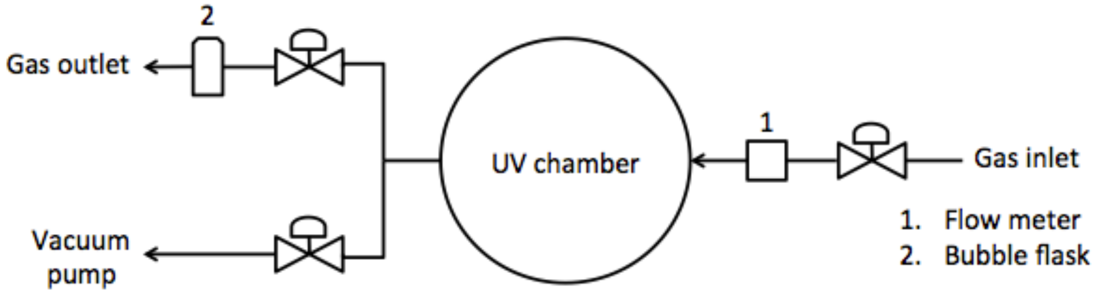

Figure 3.6: A diagram of the UV set-up. The gas used is nitrogen.

For the UV curing method the next step after obtaining a stable nitrogen flow is to turn on the UV lamp for 2 hours. After 2 hours, the nitrogen was turned off and the samples were taken out. For the UVHT curing method the next step after obtaining a stable nitrogen flow was to turn on the heating element. The heating element cannot be pre-set to a specific heating program and the temperature is not the same at the heating element and the sample, so the temperature is controlled manually by observing the temperature measured by the thermocouple. The heating element control was set to 300 °C and the thin films were heated for 20-25 minutes to between 125-130 °C. The UV lamp was turned on and after about 10 minutes a temperature of 150 °C was reached at the thermocouple. Then the heating element control was ramped down to 250 °C in steps of 10 °C over a time period of 15 minutes. A stable temperature of 150 °C was reached at the thermocouple. By summing up the steps from the heating element was turned on, it is seen that a stable temperature of 150 °C was reached after 45 minutes. The heating program is designed to get as little overshooting of the temperature at the thermocouple as possible and then to keep the temperature stable at 150 °C. When the 2-hour UV curing was done the heating element was turned off. The lid and nitrogen flow was kept on until the temperature had sunken to around 100 °C after about 10 minutes. Then the nitrogen was turned off, the lid was removed and the thin films were cooled until the thermocouple read 70 °C before they were picked out of the chamber.

Graphs showing the temperature versus time during the UV curing at room temperature and high temperature are presented in figures 3.7 and 3.8 respectively. The graphs are representative for curing of all the three layers.

In Figure 3.7 no external heat is applied, and the increase in temperature reflects the heating caused by the UV lamp. The difference in heat capacity between the silicon and glass substrate causes the silicon to heat up faster, but as seen from Table 3.6 the same maximum temperature is reached after 2 hours. The maximum temperature for the original UV set-up can also be seen in Table 3.6. The higher temperature seen for the modified UV set-up is due to removal of the quartz glass, the shorter lamp-sample distance, and a lower nitrogen flow.

Figure 3.8 reflects the temperature control during the UVHT curing step and shows the amount of temperature overshoot. From the graph, the heating, holding, and cooling stages can also be seen as described in the section above. The start and maximum temperature for this curve is given in Table 3.6. For the original UV set-up, the maximum temperature given in Table 3.6 is after 5 hours of UV curing.

Table 3.6: Start and maximum temperatures during the UV curing of the thin films. Where RT is room temperature and HT is high temperature (150 °C).

UV set-up	Start T [°C]	Maximum T [°C]
RT, Si	29.8	47.6
RT, Glass	23.2	47.8
Original	23.0	42.6
HT	24.6	152.6

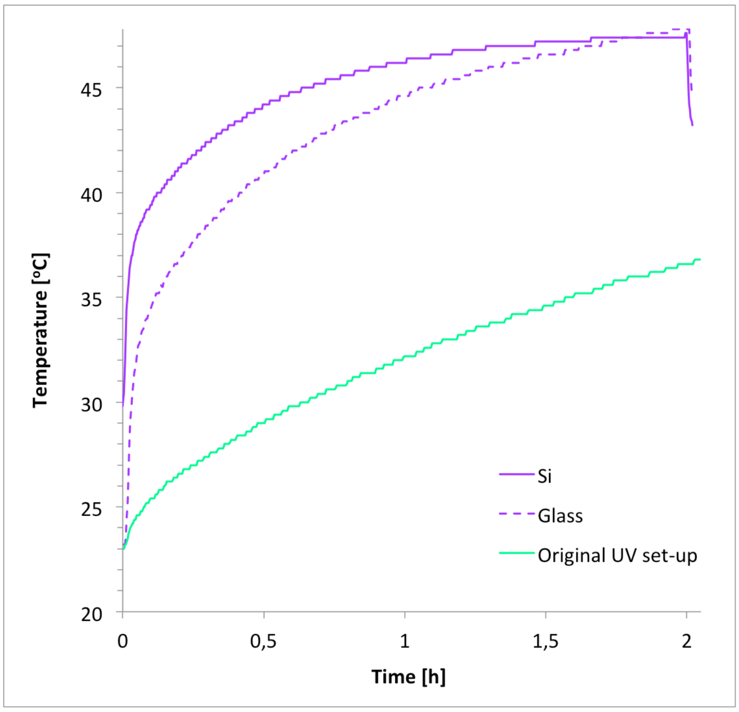

Figure 3.7: A graph showing the dependence of the temperature on the time irradiated by UV light at room temperature. The purple curves are for the modified UV set-up, while the green curve is for the original UV set-up (glass substrate) from the specialization project [107].

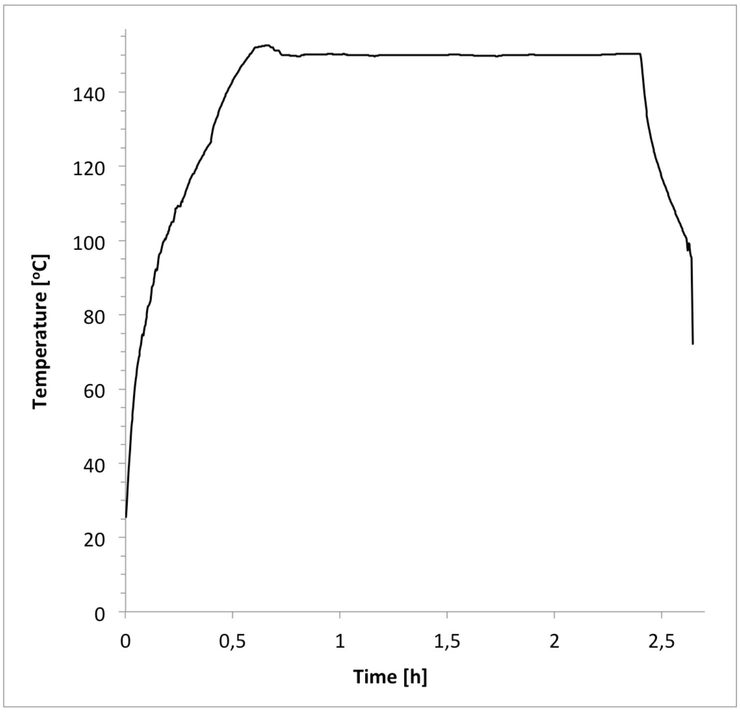

Figure 3.8: The heating program for the high temperature UV curing step.

3.2 Characterization

The following techniques were utilized to investigate the electrical and optical properties of the thin films as well as the morphology, crystal structure, elemental composition, and topography.

3.2.1 Auger Electron Spectroscopy

Auger electron spectroscopy (JEOL JAMP-9500 Auger Microprobe) was performed using an acceleration voltage of 10 kV and an energy resolution of 0.3% of the pass energy. The samples were tilted the standard 30° towards the detector and an area of the size $121 \times 121\ \mu m^2$ was scanned. Argon ions were utilized for sputtering using an acceleration voltage of 500 kV for 15 seconds.

3.2.2 Gracing Incident X-ray Diffraction

Gracing incident X-ray diffraction (Bruker D8 Advance DaVinci X-ray Diffractometer) with $CuK\alpha_1$ radiation was used to study the structure of the thin films. Scanning parameters were 60 minutes, 15 to 65 $°2\theta$ and the incident angle was $\theta_1 = 2°$. The software by Bruker, Diffrac.Suite EVA V3.1, was used for the structure analysis and the lattice parameter was found through Pawley refinement using the software Diffrac.Suite Topas 4.2. Pawley refinement was performed using a hkl-phase, and the space group used was Ia3 number 206. The lattice parameter calculations are based mainly on the peak positions in the diffractogram and not on the shape of the peaks. More details on the Pawley refinement is found in “Appendix D Pawley Refinement”.

The sample preparation was done as follows. For the thin films on glass substrates, the sample was centered in a deep sample holder on top of plasticine and then pushed down till it reached the level of the sample holder edge. The silicon substrates were quite fragile, and needed a gentler treatment. The first step was to place a dummy glass substrate into the deep sample holders in the same manner as explained above. Then the silicon substrate was centered on top of the glass. An oily substance was used to get surface tension between the silicon and the glass substrates to avoid sliding. To get the silicon substrate lined with the sample holder edge the sample was pushed down a second time. By having a dummy glass substrate underneath the silicon substrate the force applied when pushing was distributed to the glass, and fracture of the silicon substrate was avoided.

3.2.3 Optical Light Microscopy

Optical light microscopy (Carl Zeiss Zeiss AxoScope A1 for Reflected light BF – DIC/POL) was used to quickly map the differences in morphology for the different thin films. The pictures were taken in bright field with fully open apertures and at 5x magnification. The focus was adjusted frequently to get the thin film surface in focus. Optical light microscopy is a good method for getting an overview of the thin films as switching samples are quick (no vacuum chamber as in SEM) and it is easy to control where you are on the thin film. Based on the optical light microscopy pictures a selection of thin films was chosen for a closer study using SEM.

3.2.4 Scanning Electron Microscopy

Figure 3.9: Thin film preparation in SEM.

A selection of the thin films was imaged using SEM (Low Vacuum Field emission gun, Zeiss Supra 55 VP) and the secondary electron signal. The set-up parameters are an acceleration voltage of 10 kV, an aperture of 30 μm, and a working distance ~8 mm. The main magnifications were 500, 10 000 and 40 000 giving pictures in the μm to nm scale.

Sample preparation was necessary to avoid charging. A conductive “bridge” was made from the thin film to the sample holder by using aluminum foil and aluminum tape as shown in Figure 3.9. The non-conductive thin films on glass substrates had to be coated with a carbon sputterer.

The SEM is equipped with an EDS (EDAX-AMETEK) used for elemental analysis. The set-up parameters used for the EDS measurements are an aperture of 60 μm, a working distance of 10 mm, a voltage of 15 kV, and high current.

3.2.5 Profilometer

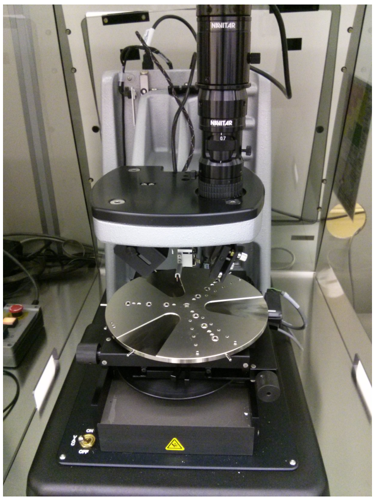

Figure 3.10: The Veeco Dektak 150 utilized for the profilometer scans.

The surface profile of the thin films was obtained by a profilometer (Veeco Dektak 150) to determine the roughness of the thin films. The Veeco Dektak 150, which can be seen in Figure 3.10, is a contact stylus profilometer with a diamond stylus tip of radius 12.5 μm. The maximum scan length is 55 mm and the maximum range in the vertical direction is 524 μm. The scan parameters were as follows. The scan type was set to standard scan and the profile was set to hills and valleys. The measurement range was 6.5 μm (gives a maximum resolution of 1 Å in the vertical direction) and the force from the stylus on the thin film was set to 3 mg. The two standard settings for the scan length and scan time were 1 mm and 30 seconds respectively.

3.2.6 Atomic Force Microscopy

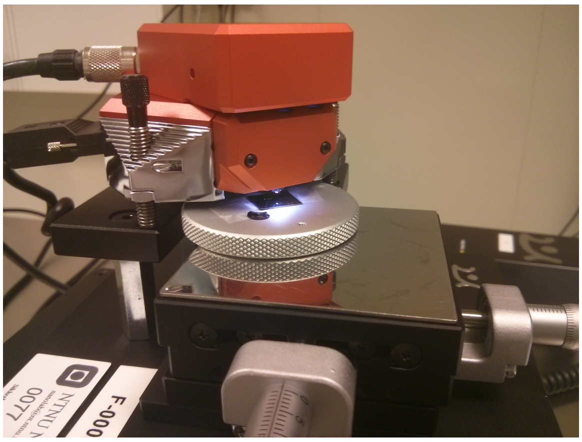

Figure 3.11: The atomic force microscopy apparatus easyScan 2.

The surface topography and roughness of the thin films were studied by AFM (NanoSurf easyScan 2). The NanoSurf easyScan 2 can be operated in two modes, tapping or contact mode. The instrument was used in contact mode with a SICONA tip (AppNano) of tip radius < 10 nm using air as the measuring medium. The tip has a built in alignment system making it unnecessary to align or adjust the laser. Areas of $31 \times 31\ \mu m^2$ and $1 \times 1\ \mu m^2$ on the thin film were scanned using a time per line of 1 second. Maximum scan range of the instrument is 70 μm and maximum range in the vertical direction is 14 μm. The collected data was obtained through the software NanoSurf easyScan 2. The AFM apparatus used is shown in Figure 3.11. The output from the AFM is 3D-pictures of the surface structure, revealing the topography and roughness of the thin film surface.

3.2.7 Spectrophotometry

The optical transmission of the thin films was measured using a light source perpendicular to the thin film surface with wavelengths from 170 nm to 1100 nm and a spectrometer (Avantes AvaSpec-2048). The transmission spectra were obtained through the software AvaSoft 8.0.

In transmittance mode, the transmittance, *T*, at a pixel *n* is calculated using the Equation 3.3 [105].

$$T_n = 100 \cdot \frac{sample_n - dark_n}{ref_n - dark_n} \tag{3.3}$$

Where air was used as the reference. Due to the necessity of a transparent sample only the thin films on glass substrates could be studied.

3.2.8 Ellipsometry

A selection of the thin films was analyzed using an ellipsometer (J. A. Woollam Co. RC2). The light source was a xenon lamp with wavelengths from 210 to 1700 nm and the measurements were performed at three different incidence angles of 55°, 65°, and 75°. Two different detectors, a Si and an InGaAs detector were used to collect the data. The Si detector collected the light from 210 to 1000 nm while the InGaAs detector collected the light from 1000 to 1700 nm. The measurements were analyzed using the CompleteEASE software. A model that describes the thin film is constructed in the software to calculate the predicted response. The collected data are then compared to the calculated prediction, and regression is used to improve the model to best match the collected data. The ITO and IZO thin films were modeled using one Drude model, one Gaussian model and one Tauc-Lorentz model. From this model, parameters like thin film thickness, surface roughness, refractive index and extinction coefficient could be obtained.

Ellipsometry can also be used to obtain transmission spectra for the thin films on glass substrates. For this type of measurement the light source is placed perpendicular to the thin film surface and transmission spectra for the wavelengths 210 to 1700 nm are obtained.

3.2.9 Conductivity Measurements by the van der Pauw Method

To calculate the electrical resistivity of the thin films an in-house built van der Pauw apparatus was used. The apparatus measures the conductance, *G*, by utilizing four platinum electrodes. The conductance is related to resistance, *R*, as shown in Equation 3.4 making it possible to calculate the resistivity as discussed earlier in the theory section “2.5.5 Conductivity measurements by the van der Pauw method”.

$$R = \frac{1}{G} \tag{3.4}$$

The set-up of the apparatus is shown in Figure 3.12. Alumina pipes together with a metal holder make up the sample holder. Alumina is used as isolation to avoid short-circuiting.

The thin films were placed with the film facing down. A metal clamp, fastened by springs, was used to hold the sample in place and to get an even pressure distribution over the four platinum electrodes. The horizontal top part of the metal clamp is inside an alumina pipe. The electrodes were placed near the corners of the sample. The top of the metal clamp, the four electrodes, and the sample can be seen in Figure 3.12.

The schematic to the left below the photograph in Figure 3.12 shows the position of the electrodes on the sample and the actual numbering of the electrodes for this specific apparatus. 1, 2, 3 and 4 corresponds to N, O, P, and M respectively in section 2.5.5.

The schematic in the middle and to the right show how the current and voltage were applied. The schematic to the right is the horizontal set-up corresponding to $R_{MN,OP}$ in Equation 2.16. Here current was forced from electrode 4 to electrode 1 and the voltage drop between electrode 2 and 3 was measured. The middle schematic shows the vertical measuring set-up corresponding to $R_{NO,PM}$ in Equation 2.16. Here current was forced from electrode 3 to 4 and the voltage drop between electrode 1 and 2 was measured. All the thin films were measured at ambient conditions at a constant voltage of 1 V.

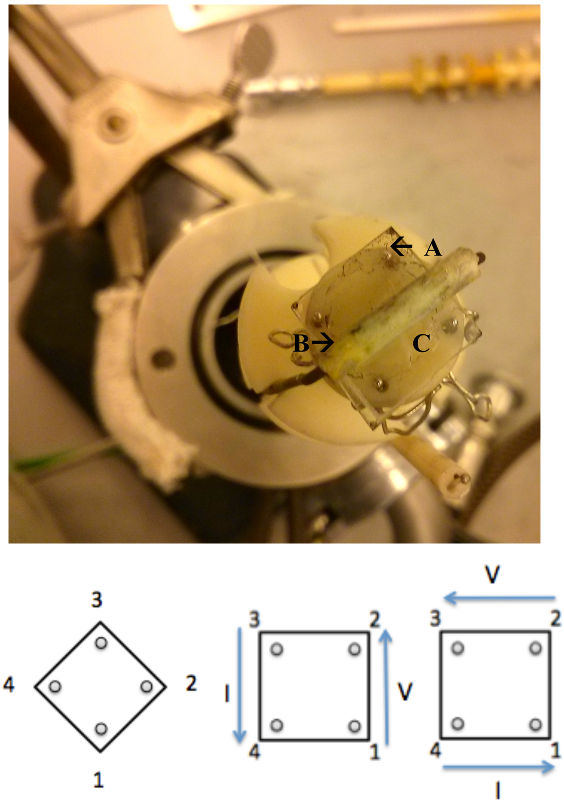

Figure 3.12: A photograph showing the set-up of the van der Pauw apparatus. A is a platinum electrode, B is the metal clamp and C is the sample. Below to the left is a schematic of the sample showing the positioning of the four electrodes. The middle and right schematic show how current, *I*, and voltage, *V*, were applied to obtain conductance measurements.

4. Results

In the following sections the results from the characterization of the thin films are presented. Several characterization methods including gracing incidence X-ray diffraction, scanning electron microscopy, atomic force microscopy and ellipsometry were used to study the quality and properties of the TCO thin films. The process steps for making the different thin films were executed according to an identical protocol.

Even though the main goal of the thesis was to study the UV curing process and compare the UV cured thin films to the thermally cured thin films, more thermally cured than UV cured thin films were made. Both a reproducibility study and different doping levels of tin were only studied for the thermal curing. This is mainly due to the time consumed by the rebuilding and installation of the UV set-up. Therefore, only a selected number of samples were UV-cured. This also affects the result and discussion part that concerns the thermally cured thin films more than expected with regards to the main goal of the thesis.

All the characterization of the In_2O_3 thin film from the specialization project [107] was redone in the master thesis. Only the van der Pauw conductivity measurements were kept and recalculated.

4.1 Precipitation During Synthesis and Quality of Precursor

For the IZO solutions the zinc precursor dissolved easily and the solutions became transparent during the steps of the synthesis. This was not the case for the ITO solutions that remained turbid. After less than 1 hour a slightly yellow precipitate had fallen to the bottom of the solutions, and more precipitate was seen in the solutions of higher nominal doping levels. The amount of precipitate seemed to be constant over time, and when removed new precipitation did not occur. It was also attempted to calculate the tin concentration in the solutions after removal of the precipitate, but this was not successful as explained in "Appendix C Study of Precipitation and Precursor Quality". By using X-ray diffraction the structure of the precipitate was found to be SnO_2. The pH of the indium nitrate standardized solution was measured, and a resulting pH = 1.17 was found. The quality of the tin (II) acetate precursor was studied using thermogravimetrical analysis, energy dispersive X-ray spectroscopy, and X-ray diffraction. It could not be determined if the precursor had oxidized in the box or if the precursor was contaminated. Despite this a new box of the same precursor was used for the remaining solution synthesis. However, similar amounts of precipitation were still observed in the solutions. By comparing the diffraction spectra for the new and old oxidized precursor two diffraction lines that do not conform to the SnO_2 structure was observed in the diffractogram for the old precursor. These were not present in the diffractogram for the new precursor. A more thoroughly study is found in "Appendix C Study of Precipitation and Precursor Quality".

It was planned to prepare the same number of thin films for all compositions, but based on the problems with precipitation it was determined to exclude tin doping as a parameter. This can be seen from Table 3.3 in the experimental section "3.1.2 Parameters", hence no thin films with 5 mol% and 15 mol% tin were prepared using the new precursor.

4.2 Auger Electron Spectroscopy

Based on the results in the previous section it was determined to identify the level of tin doping in the thin films. This was done using Auger electron spectroscopy.

The best method for determining the tin concentration in the films was thought to be X-ray photoelectron spectroscopy, as explained in theory section "2.5.2 Scanning Electron Microscopy". Due to downtime of the instrument it was determined to do Auger electron spectroscopy instead, which is also a suitable technique. In Figure 4.1 the spectra for the three different doping levels of tin are presented, and it is seen that the tin content increases with increasing nominal doping level. Low intensity diffraction lines are seen for carbon, indicating that the thin film surfaces were clean. Despite this, a mild ion sputtering was performed to remove the surface carbon to see if even better results could be obtained.

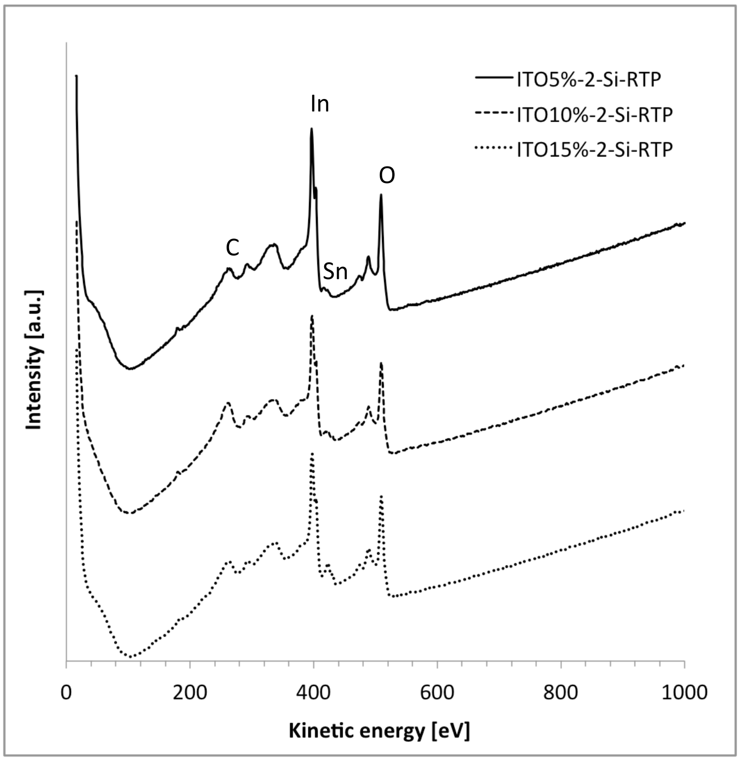

Figure 4.1: Spectra obtained from Auger electron spectroscopy for thin films of three different nominal doping levels of tin.

Tables 4.1 and 4.2 present the results from the elemental analysis for the non-sputtered and sputtered films. The non-sputtered ITO5% film has a doping level 42 % lower than the nominal, while the ITO10% and ITO15% films have a doping level 33 % and 39 %, respectively lower than the nominal. This gives an average of 38 % lower measured doping level compared to the nominal.

When comparing Table 4.2 to Table 4.1 the content of oxygen and tin is found to decrease with sputtering, while the content of indium increase. The decrease in oxygen is approximately the same for all the films, while the ITO5% thin film has a decrease in tin of ~15 % with sputtering, while the two other thin films have a much higher decrease of ~50 %.

Table 4.1: Elemental composition of the thin films for the three different nominal doping levels before sputtering.

Thin film	mol% O	mol% In	mol% Sn
ITO5%-2-Si-RTP	61.6	36.4	2.1
ITO10%-2-Si-RTP	62.0	34.8	3.3
ITO15%-2-Si-RTP	61.8	32.3	5.9

Table 4.2: Elemental composition of the thin films for the three different nominal doping levels after sputtering.

Thin film	Mol% O	Mol% In	Mol% Sn
ITO5%-2-Si-RTP	58.5	39.7	1.8
ITO10%-2-Si-RTP	58.8	39.5	1.7
ITO15%-2-Si-RTP	58.6	38.7	2.7

4.3 Crystal Structure

Diffractograms that are representative for the ITO and IZO thin films are presented in Figure 4.2, where intensity is plotted as a function of 2θ. The diffractograms for all the crystalline thin films are given in "Appendix D Pawley Refinement". A diffractogram for the In_2O_3 thin film made in the specialization project [107] is also included in Figure 4.2 as a reference pattern for the bixbyite structure of In_2O_3. The diffractograms show that all the thermally cured thin films obtain the cubic bixbyite structure with no preferred direction of growth. The IZO40%-1-Si-RTP diffractogram in Figure 4.3 is equivalent to the diffractogram for ITO5%-1-Si-RTP in Figure 4.2. The IZO40%-1-Si-RTP diffractogram is included to show that the IZO thin films actually do obtain the cubic bixbyite structure of In_2O_3, and not the hexagonal wurtzite or the cubic structure of ZnO. No crystalline secondary phases are detected in any of the diffractograms.

The diffractograms for the UV and UVHT cured thin films are equivalent and show an amorphous structure.

For both the crystalline and amorphous thin films there is a difference between the diffractograms depending on the different substrates. The amorphous glass substrate emerges as a broad peak from approximately 20° to 35° 2θ. For the thin films on silicon substrate, which is single crystalline, the baseline is flat and no trace of the substrate can be seen in the diffractogram. For the crystalline thin films a higher crystallinity is obtained for the thin films deposited on silicon substrates than the ones deposited on glass substrates.

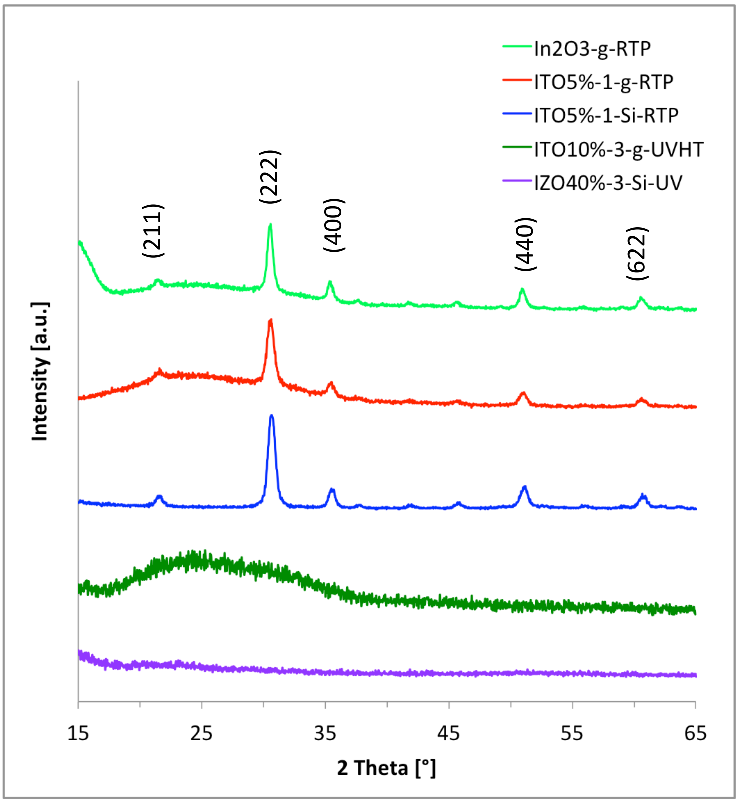

Figure 4.2: Diffractograms representative for the ITO and IZO thin films. Included is also a reference diffractogram showing the cubic bixbyite crystal structure of the In_2O_3 thin film prepared in the specialization project [107]. The legends refer to thin film names and represents different curing methods and substrates.

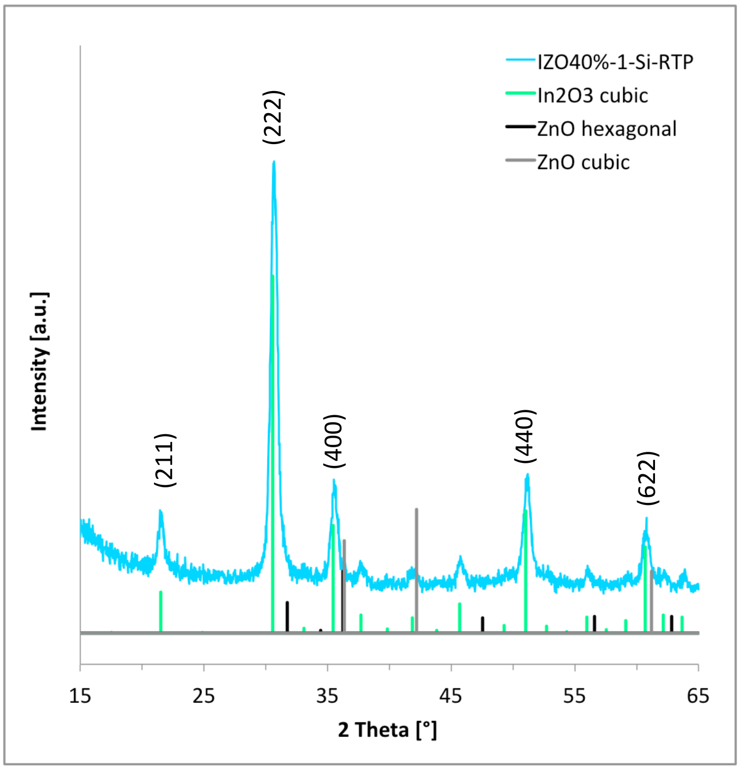

Figure 4.3: A diffractogram representative for the thermally cured IZO thin films together with a reference pattern showing the cubic bixbyite crystal structure of In_2O_3, the hexagonal wurtzite crystal structure of ZnO, and the cubic crystal structure of ZnO.

4.4 Lattice Parameter

The lattice parameters for the thermally cured thin films are obtained through Pawley refinement, and are presented in Figure 4.4 and Figure 4.5. More details on the refinement parameters, fits and results are found in “Appendix D Pawley Refinement”.

The lattice parameters for the thermally cured ITO thin films deposited using three different solutions and on two different substrates are plotted against the nominal doping level of mol% Sn in Figure 4.4. The lattice parameter for the thermally cured In_2O_3 thin film on glass substrate prepared in the specialization project [107] is also included in addition to lattice parameter literature values re-plotted from the work of Frank and Köstlin [40]. Exact values were not found in the reference, and the values were obtained by reading off the plot for the oxidized curing conditions. The literature values show the normal trend found for In_2O_3 doped with tin, which is a decrease in lattice parameter for low concentrations of tin followed by an increase in lattice parameter for higher concentrations of tin. The original plot is found in Figure 2.7 section “2.1.2 Lattice Parameter”.

The In_2O_3-g-RTP thin film shows a higher lattice parameter than the reference value, but fits well with the trend of the “solution nr 1, glass” data series. In this master thesis no information is obtained for the region below the nominal doping of 5 mol% Sn. For higher doping levels a trend where the lattice parameter increase with doping is seen for all the data series. An exception is the 10 mol% point for solution nr 2 on glass that does not conform with the trend. No trend can be seen with regards to the slope as a function of doping level. Due to the uncertainty in the actual doping level of the films, it is unknown how the lattice parameter values should be shifted relative to the x-axis. The lattice parameters obtained are found to lie in the same range as the literature values, but there is little purpose in discussing how the absolute values fit with the literature values due to the uncertainty in shift along the x-axis.

A study of the reproducibility was performed by making the same solution up to three times. In general a good reproducibility is found for the lattice parameter, but some variation is seen between the different solutions. The variation is larger for the thin films on glass substrates than for the thin films on silicon substrates. To quantify this, the standard deviation between the lattice parameters of the different solutions for each solution composition is calculated and the largest value for each substrate is presented. For glass the largest standard deviation between the different solutions is 0.006 Å. For silicon the largest standard deviation is 0.002 Å.

A distinct difference in lattice parameter can be seen between the films deposited on glass and silicon substrates, as the thin films deposited on silicon substrates lie in a lower range.

In Figure 4.5 the lattice parameters for the IZO thin films deposited on two different substrates are plotted against solution nr. The lattice parameter for the thermally cured In_2O_3 thin film on glass substrate from the specialization project [107] is also included in this plot. There seem to be a trend for both substrate types that the highest lattice parameter value is observed for the thin films made from solution nr 2 and the lowest lattice parameter values are found for thin films made from solution nr 3. It is clear from the figure that doping In_2O_3 with zinc decreases the lattice parameter.

Also for the IZO thin films a good reproducibility is found for the lattice parameter, and some variation is seen between the lattice parameters for the different solutions. This is quantified by calculating the standard deviation in lattice parameters for the different solutions for each substrate. For glass the standard deviation is 0.003 Å. For silicon the standard deviation is 0.011 Å, which is caused by the highly deviating value for the IZO40%-3-Si-RTP thin film. This value is not thought to be reliable and by excluding it, a standard deviation of 0.002 Å is obtained.

A distinct difference in the lattice parameter with the substrate is also seen for the IZO thin film, but here it is the thin films on silicon that obtain the highest lattice parameter values (if the solution nr 3 value for IZO on silicon substrate is excluded). This causes the lattice parameters of the ITO and the IZO thin films on silicon substrates to lie in the same range.

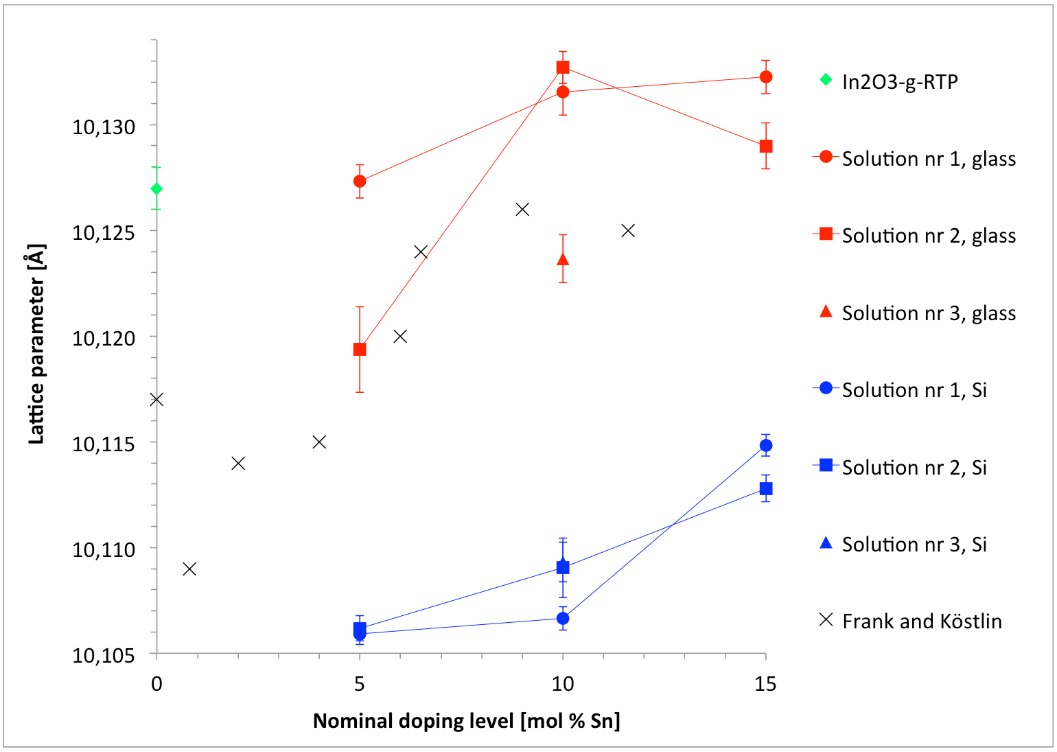

Figure 4.4: Lattice parameters for the thermally cured ITO thin films plotted as a function of nominal doping level mol% Sn. The legends refer to the solution nr and substrate used for the thin film deposition. The top most legend refers to the thermally cured In_2O_3 thin film on glass prepared in the specialization project [107]. The bottom most legend refers to literature values re-plotted from the work by Frank and Köstlin [40].

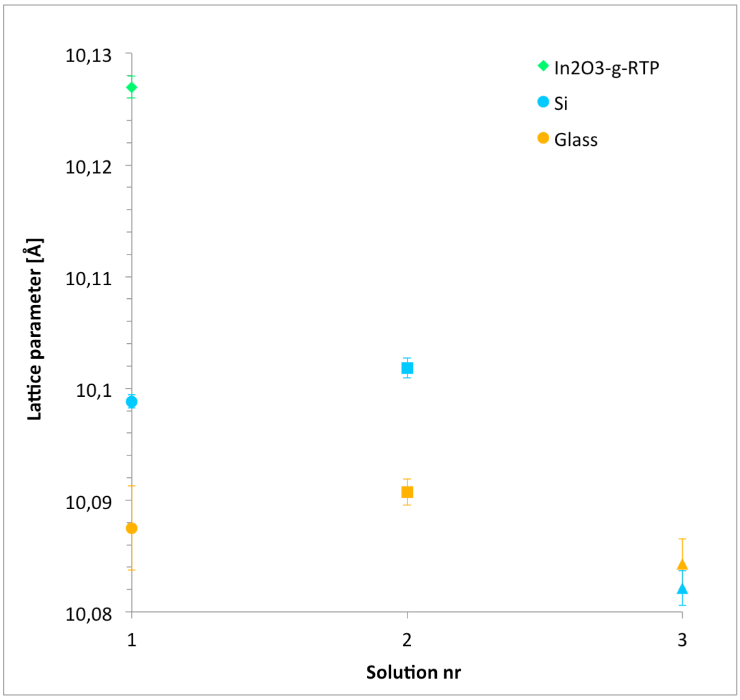

Figure 4.5: Lattice parameters for the thermally cured IZO thin films plotted as a function of solution nr. The legends refer to the substrate utilized for the thin film deposition. The top most legend refers to the thermally cured In_2O_3 thin film on glass from in the specialization project [107].

4.5 Morphology

The first part of this section covers what is detected by the naked eye, followed by overview images taken in the optical light microscope, and SEM images revealing the microstructure and nanostructure of the thin films. In the two last parts, roughness and topography of the thin films are studied using a profilometer and AFM.

4.5.1 Appearance

The thin films shown in figures 4.6 and 4.7 represent the ITO and IZO thin films on glass substrates. In Figure 4.6 thin film a) is thermally cured, thin film b) is UV cured and thin film c) is UVHT cured. It is possible to see a distinct difference in the appearance between the thin films cured by the different methods. The thermally cured thin films are transparent, but a black contour is seen around the edges. Thin film a) shown in Figure 4.6 is representative for the ITO thin films on glass substrates, while the thermally cured IZO thin films are shown in Figure 4.7. The UV cured thin films looks transparent, and no difference can be seen when comparing to an uncoated glass substrate. The UVHT cured thin films are transparent, but have a yellow color.

The thin films deposited on silicon substrates are presented in Figure 4.8 through Figure 4.13. It was not possible to take the images from the same angle. This gives a cluttered appearance, but it was thought useful to include these images to get an idea of how successful the spin coating was for each thin film.

Most of the thin films obtain a typical spin coating pattern, having a blue region as a contour around a homogenous orange central region. Exceptions are the IZO40%-3-Si-RTP, ITO10%-3-Si-UV, IZO40%-3-Si-UV, and IZO40%-3-Si-UVHT thin films in figures 4.11 to 4.13 respectively, which look non-homogenous. The central regions are mostly homogenous, but defects that appear as light spots can be seen in the ITO5%-1-Si-RTP and IZO40%-1-Si-RTP thin films in Figure 4.8 and 4.11, respectively.

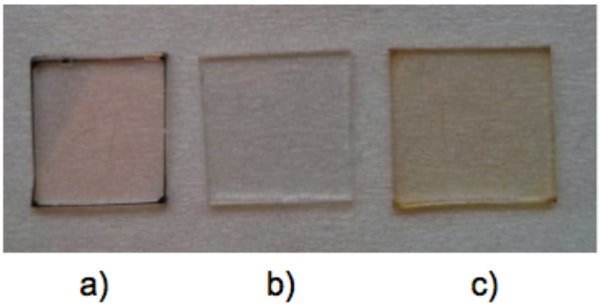

Figure 4.6: Photograph showing representative thin films for the a) thermal, b) UV, and c) UVHT curing methods. The thermally cured thin film is only representative for the ITO thin films.

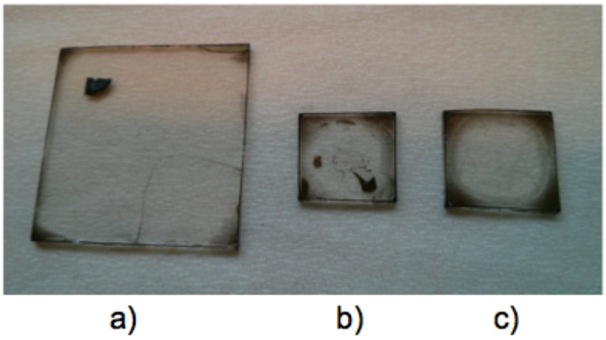

Figure 4.7: Photograph of the thermally cured IZO thin films a) IZO40%-1-g-RTP, b) IZO40%-2-g-RTP, and c) IZO40%-3-g-RTP. The black area in the upper left corner of thin film a) is part of a carbon tape that could not be removed after SEM analysis.

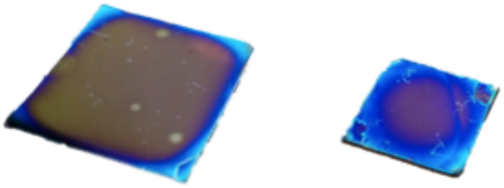

ITO5%-1-Si-RTP ITO5%-2-Si-RTP

Figure 4.8: The thermally cured thin films synthesized by deposition of ITO5% solutions nr 1, and nr 2 on silicon substrates.

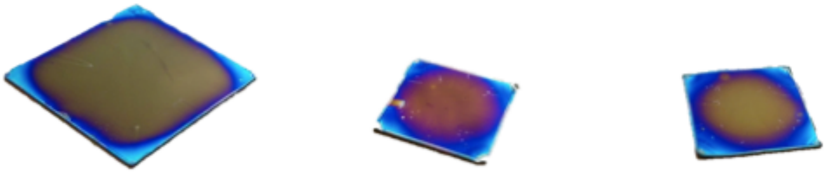

ITO10%-1-Si-RTP ITO10%-2-Si-RTP ITO10%-3-Si-RTP

Figure 4.9: The thermally cured thin films synthesized by deposition of ITO10% solutions nr 1, nr 2, and nr 3 on silicon substrates.

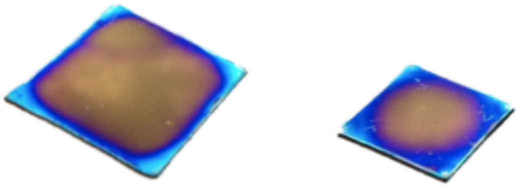

ITO15%-1-Si-RTP ITO15%-2-Si-RTP

Figure 4.10: The thermally cured thin films synthesized by deposition of ITO15% solutions nr 1, and nr 2 on silicon substrates.

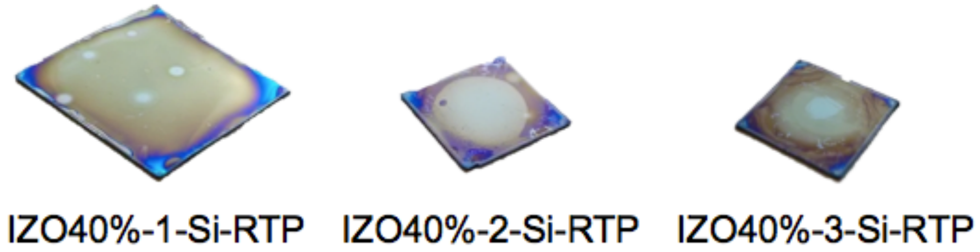

Figure 4.11: The thermally cured thin films synthesized by deposition of IZO40% solutions nr 1, nr 2, and nr 3 on silicon substrates.

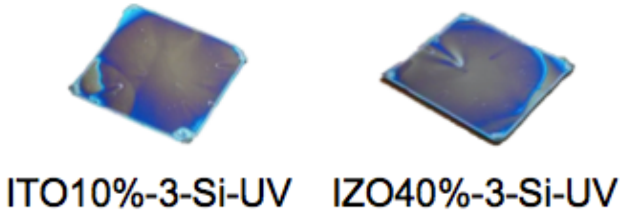

Figure 4.12: The UV cured thin films synthesized by deposition of ITO10%, and IZO40% solutions nr 3 on silicon substrates.

Figure 4.13: The UVHT cured thin films synthesized by deposition of ITO10%, and IZO40% solutions nr 3 on silicon substrates.

4.5.2 Optical Light Microscopy

Optical light microscopy was used to get an overview of the thin films. Based on these images, it was also determined which thin films to study in the SEM.

All the thin films were studied in the optical light microscope, but it was only taken images of the thin films that differed from each other. Images along the diagonal are presented for the thin films where large deviations with respect to microstructure, defects and homogeneity are seen. The thin films that are most representative are also presented with images of the diagonal. A typical image of the middle region is shown for the thin films that did not show large variations across the film.

The schematic to the left in Figure 4.14 shows how the images taken along the diagonal are presented, giving them a number from 1 to 6. The exceptions are Figure 4.26 and 4.27, which are presented like shown in Figure 4.15. The right schematic shows where on the thin film the image was taken. Image 1 and 6 shows the corners of the thin film, and the images 2 to 5 are taken between these corners along the line shown in the schematic. The respective small version of the figures 4.14 and 4.15 are found above each assembly of images.

The optical light microscopy images in Figure 4.16 are of thin film ITO15%-1-g-RTP, but represent all the ITO thin films thermally and UV cured and is also representative for the IZO40%-1-g-RTP and IZO40%-3-g-UV thin films. Based on the images in Figure 4.16 the thermally cured thin films seem homogeneous and have few flaws.

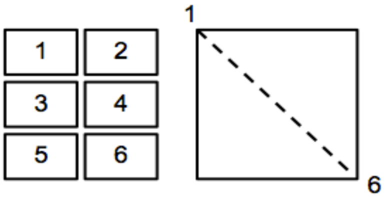

Figure 4.14: Schematic relating how the optical light microscopy images are presented (left) versus where on the thin film the images were taken (right).

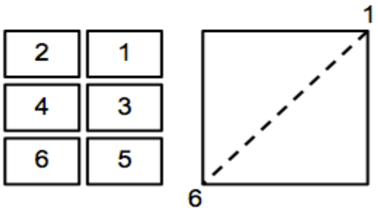

Figure 4.15: Schematic relating how the optical light microscopy images in figures 4.26 and 4.27 are presented (left) versus where on the thin film the images were taken (right).

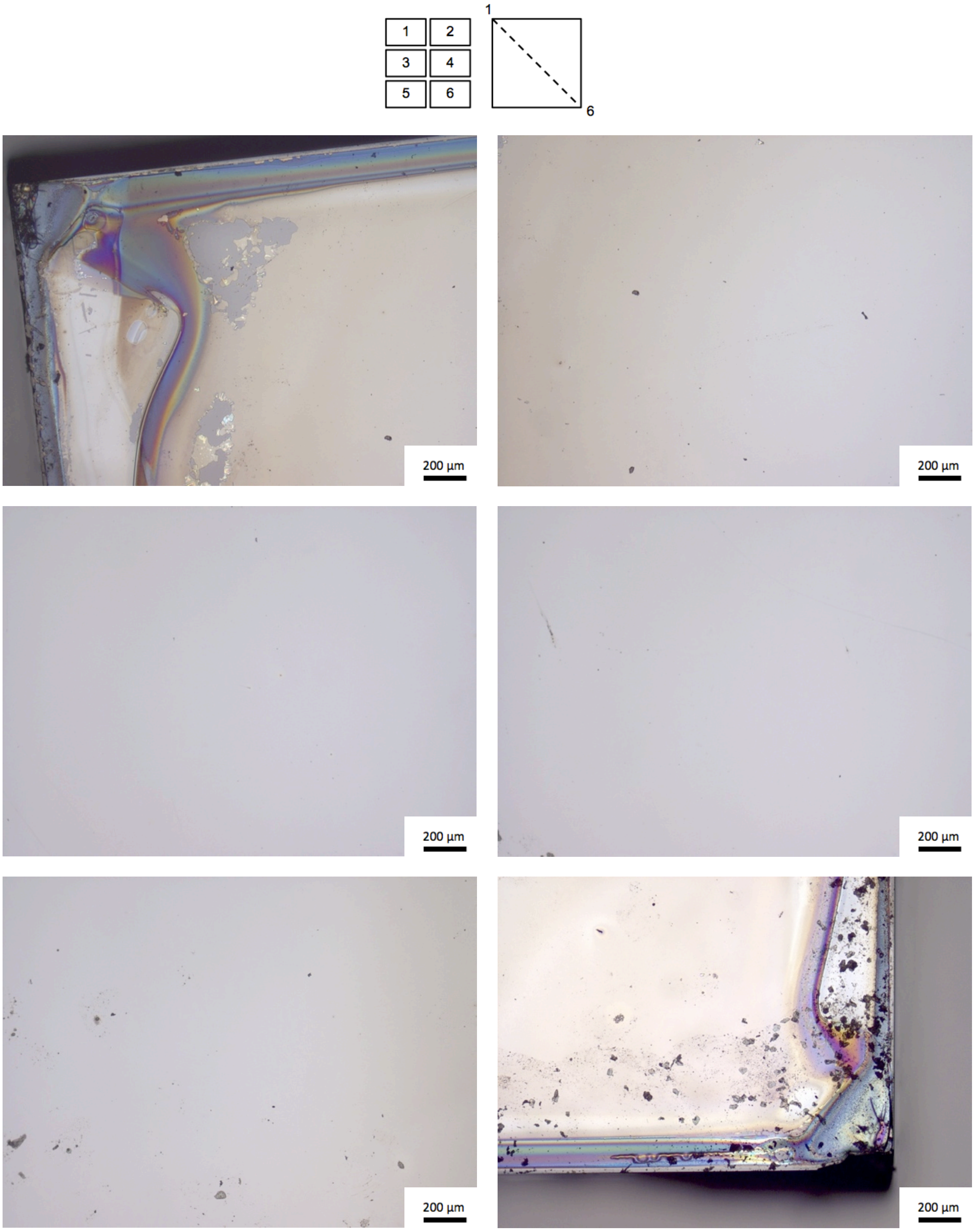

Figure 4.16: Optical light microscopy images showing the diagonal of the ITO15%-1-g-RTP thin film. These images are representative for all the thermally and UV cured ITO thin films on glass. They are also representative for the IZO40%-1-g-RTP and IZO40%-3-g-UV thin films.

The following part will present the thin films on glass substrates that look different from the thin film shown in Figure 4.16.

Figure 4.17 shows a representative region of thin film IZO40%-2-g-RTP. This thin film looks non-homogenous with a dark and light phase. There are also some diagonal white stripes in the thin film, which are distributed randomly across the film. The horizontally lighter and darker areas are not a part of the film, but caused by the engraving in the glass on the back of the substrate.

In Figure 4.18 the diagonal of thin film IZO40%-3-g-RTP is depicted. The darker region seen in image 1, 2, 5, and 6 is the same region as the black region seen in Figure 4.7. The middle images 3 and 4 shows less homogeneity than showed in Figure 4.16.

The ITO and IZO UVHT cured thin film on glass, shown in Figure 4.19 and Figure 4.20, have a different microstructure than the other films and do not look homogenous. The ITO and IZO thin films also differs a bit from each other. For the ITO film, the spotted pattern is of a smaller size than for the IZO film and lines are seen. The lines do not form a specific pattern, but are randomly distributed across the thin film.

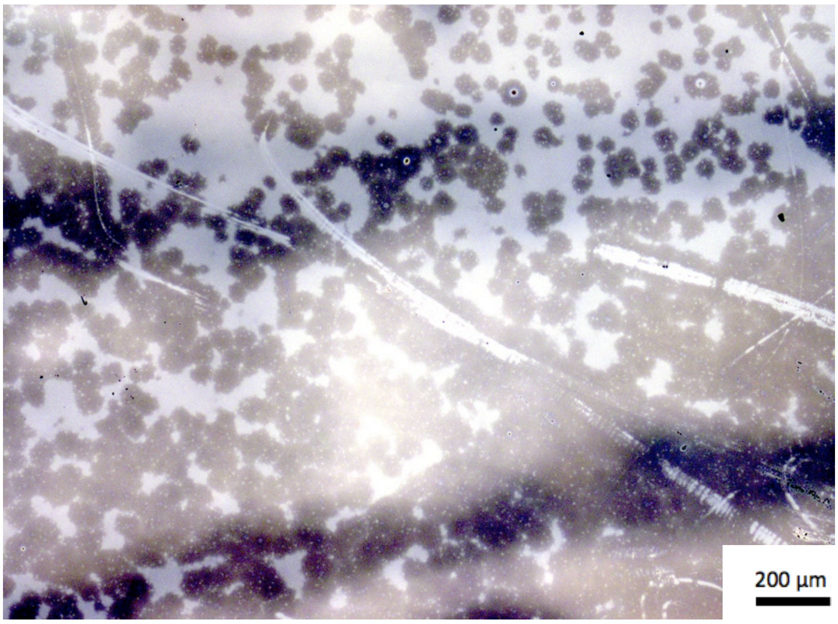

Figure 4.17: Optical light microscopy image of a typical region of thin film IZO40%-2-g-RTP.

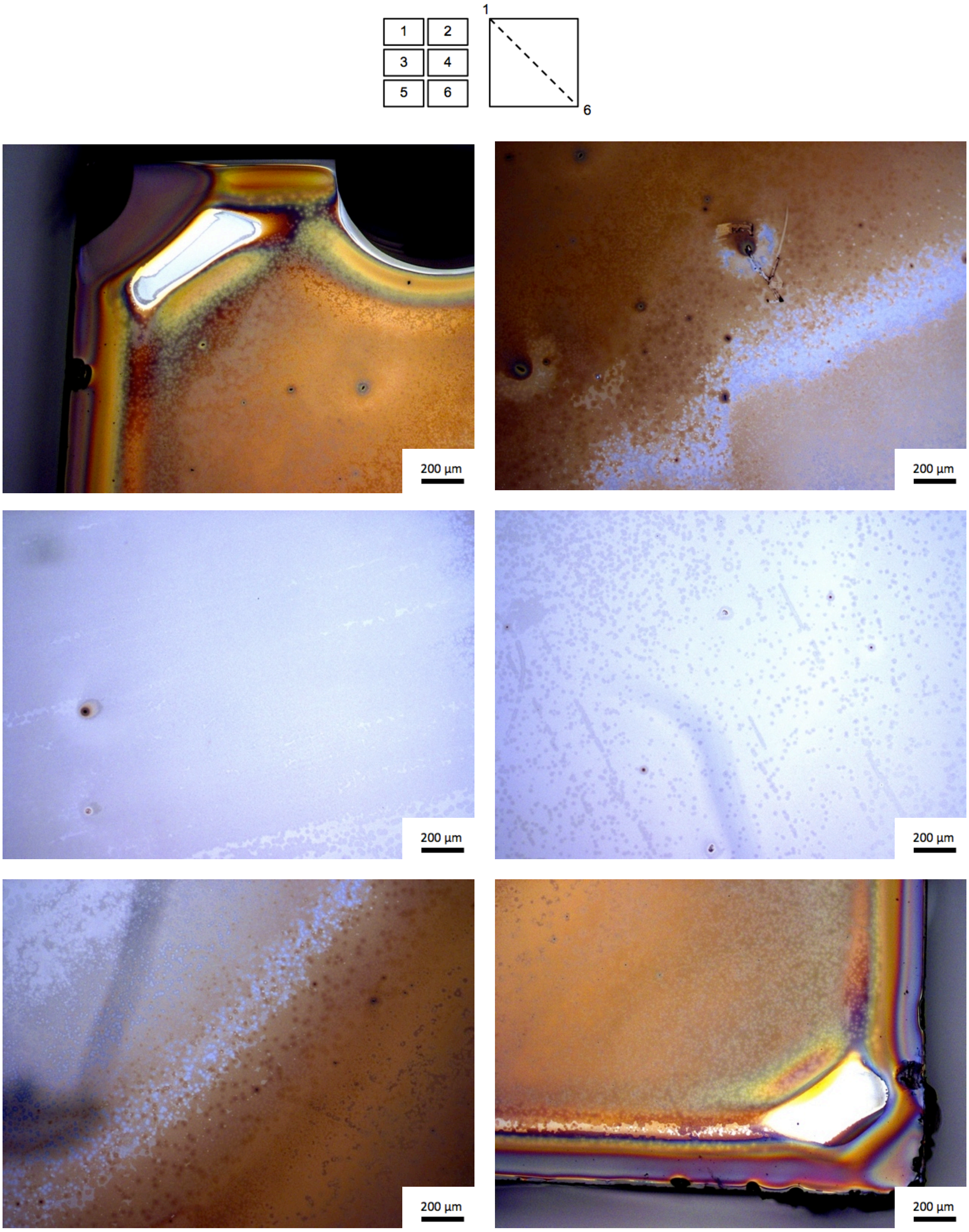

Figure 4.18: Optical light microscopy images showing the diagonal of the IZO40%-3-g-RTP thin film.

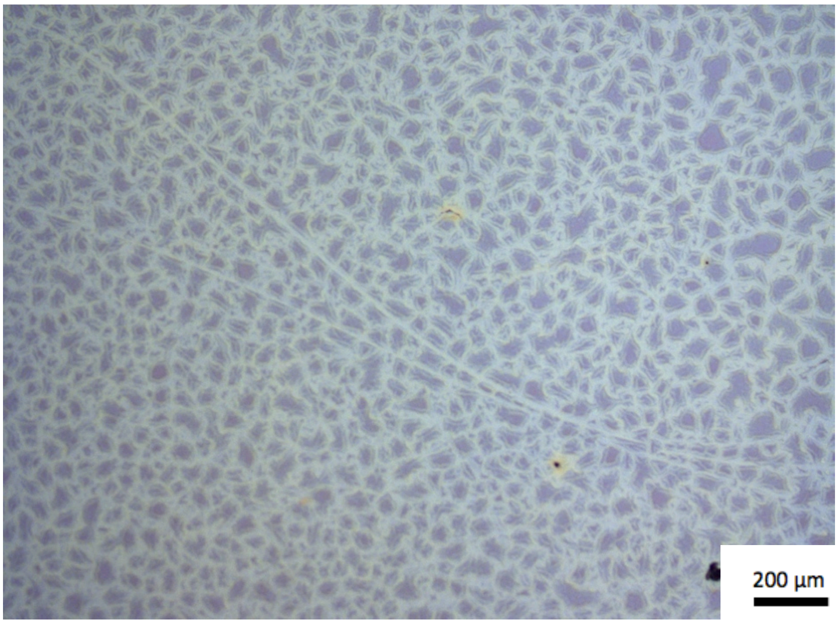

Figure 4.19: Optical light microscopy image showing a representative region of thin film ITO10%-3-g-UVHT.

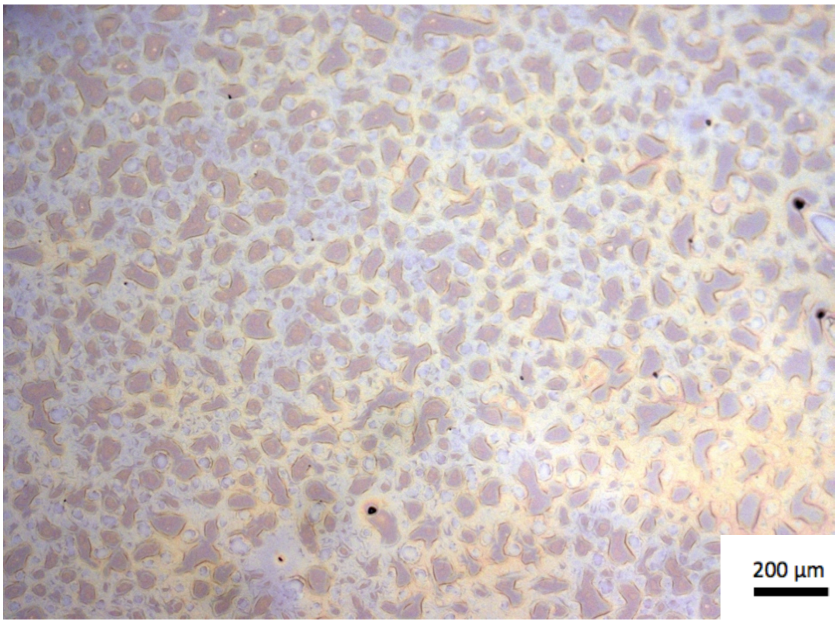

Figure 4.20: Optical light microscopy image showing a representative region of thin film IZO40%-3-g-UVHT.

The next section will cover the optical light microscopy images of the thin films deposited on silicon substrates.

Figure 4.21 depicts the diagonal of thin film ITO15%-1-Si-RTP, but represents all the thermally cured ITO thin films on silicon substrates. The images show a homogeneous film with respect to microstructure and few defects are seen.

Typical areas of thin films IZO40%-1-Si-RTP and IZO40%-2-Si-RTP are shown in Figure 4.22 and Figure 4.23, respectively, while the diagonal of thin film IZO40%-3-Si-RTP is presented in Figure 4.24. They look less homogenous than the film shown in Figure 4.21. Both the IZO40%-1-Si-RTP and IZO40%-2-Si-RTP thin films seems to have more defects, while IZO40%-3-Si-RTP shows variations in the microstructure.

The images presented in Figure 4.25 are of the thin film ITO10%-3-Si-UV, but are also representative for the ITO40%-3-Si-UV thin film. The thin films do not seem to have many defects, but they seem to be inhomogeneous with regards to thickness, and do not show the typical spin coating pattern.

In Figure 4.26 the diagonal of the thin film ITO10%-3-Si-UVHT is presented, showing a different microstructure than the other thin films. In addition to some round features, randomly oriented stripes are seen across the thin film. Figure 4.27 presents the diagonal of thin film IZO40%-3-Si-UVHT, which also show a different microstructure than the other thin films. The microstructure also varies across the diagonal of the thin film.

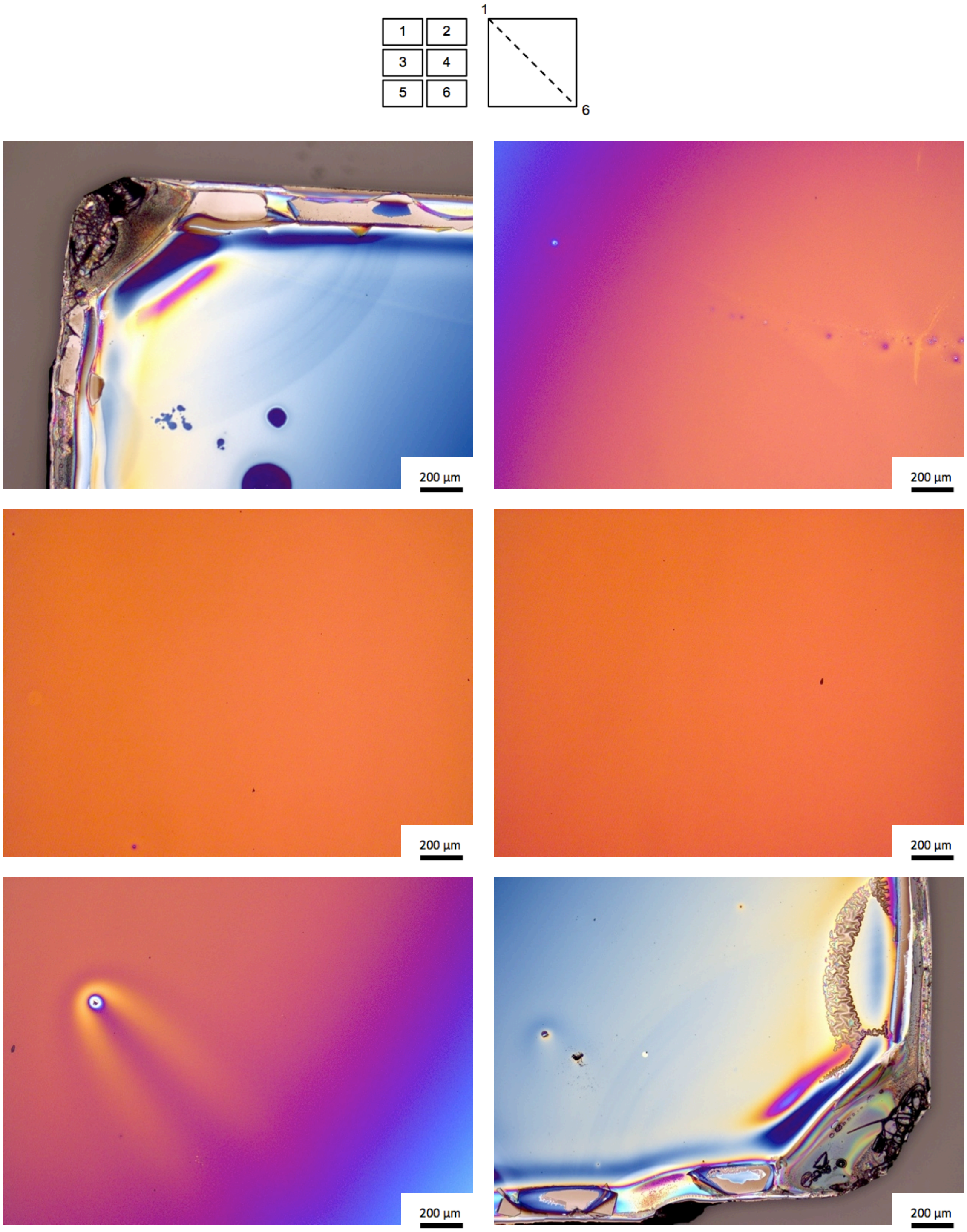

Figure 4.21: Optical light microscopy images showing the diagonal of the ITO15%-1-Si-RTP thin film. These images are representative for all the thermally cured ITO thin films on silicon substrates.

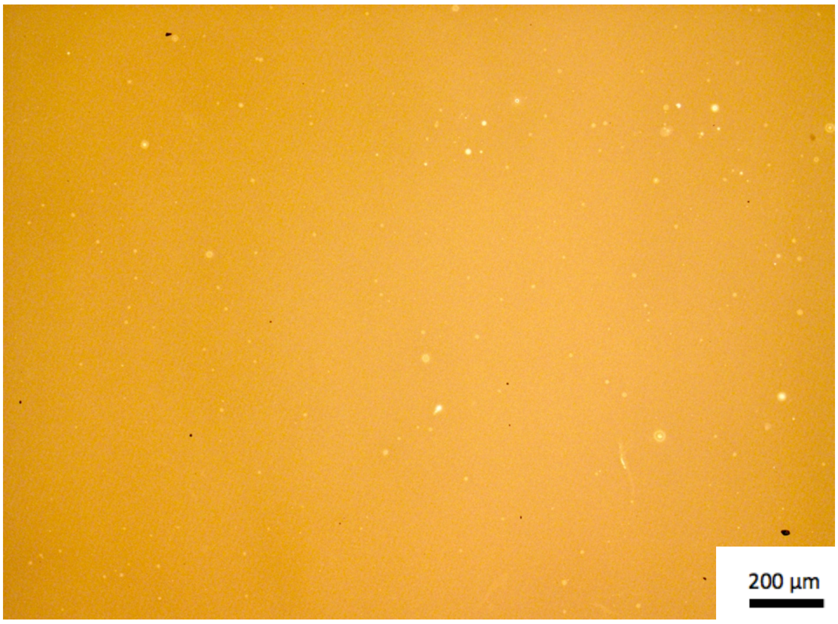

Figure 4.22: Optical light microscopy image showing a typical region of the IZO40%-1-Si-RTP thin film.

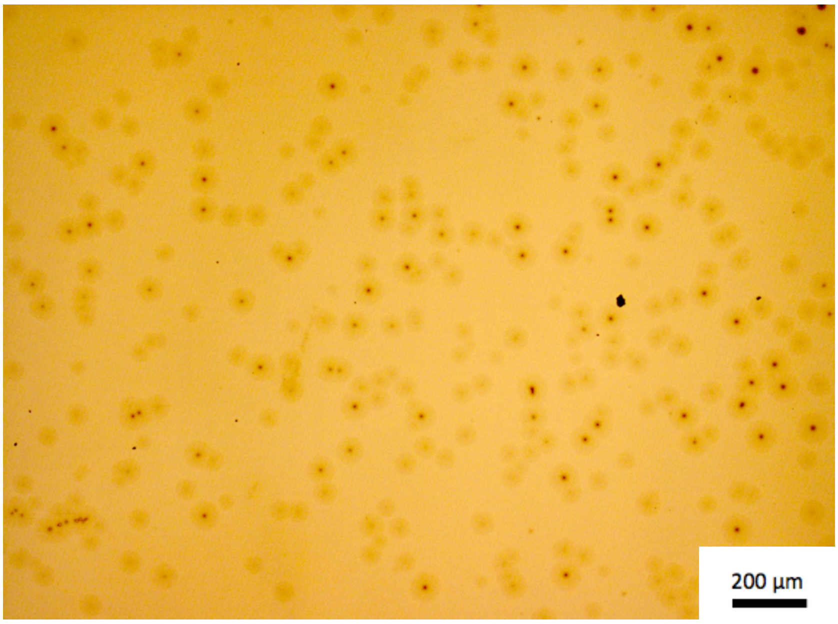

Figure 4.23: Optical light microscopy image showing a typical region of the IZO40%-2-Si-RTP thin film.

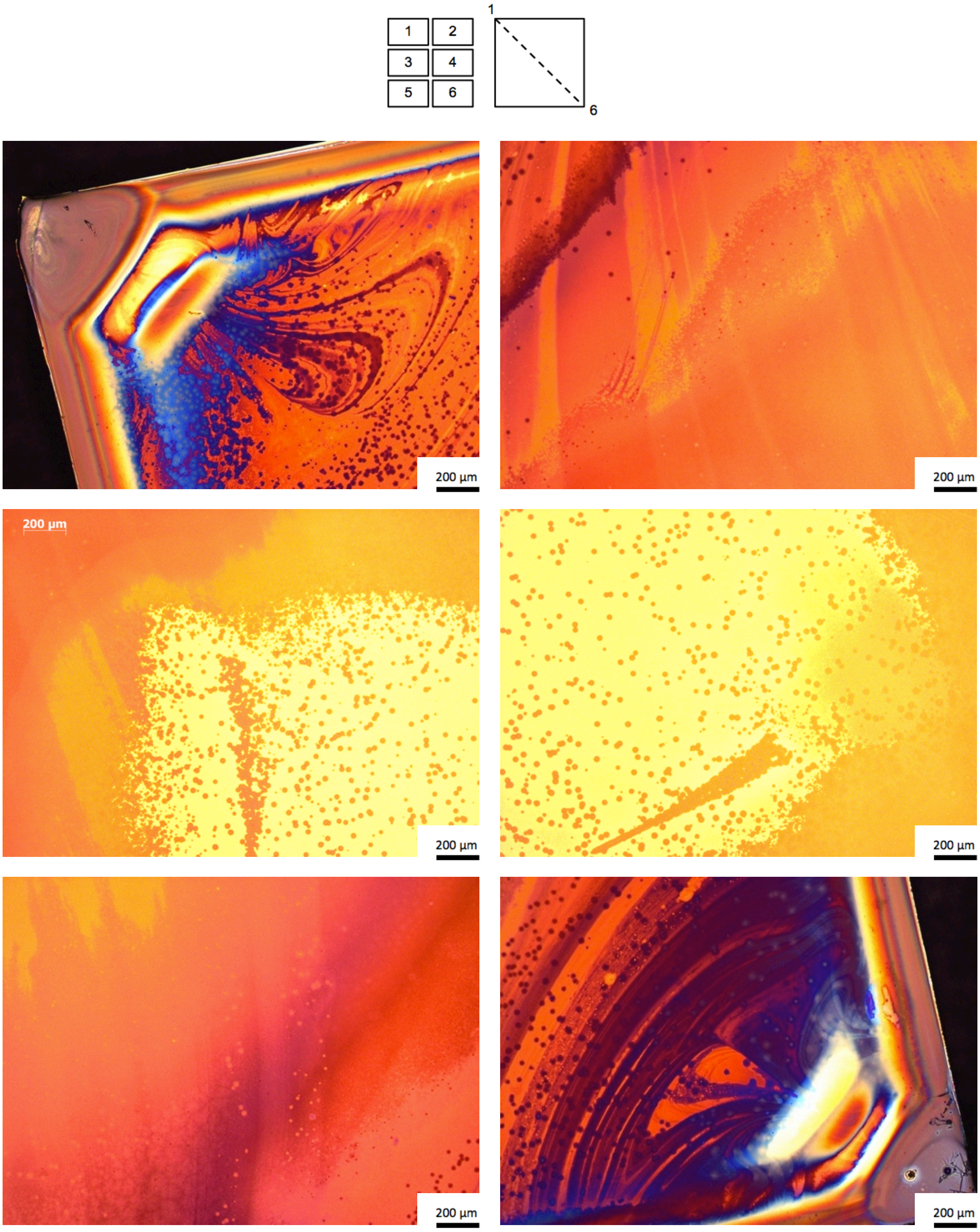

Figure 4.24: Optical light microscopy images showing the diagonal of the IZO40%-3-Si-RTP thin film.

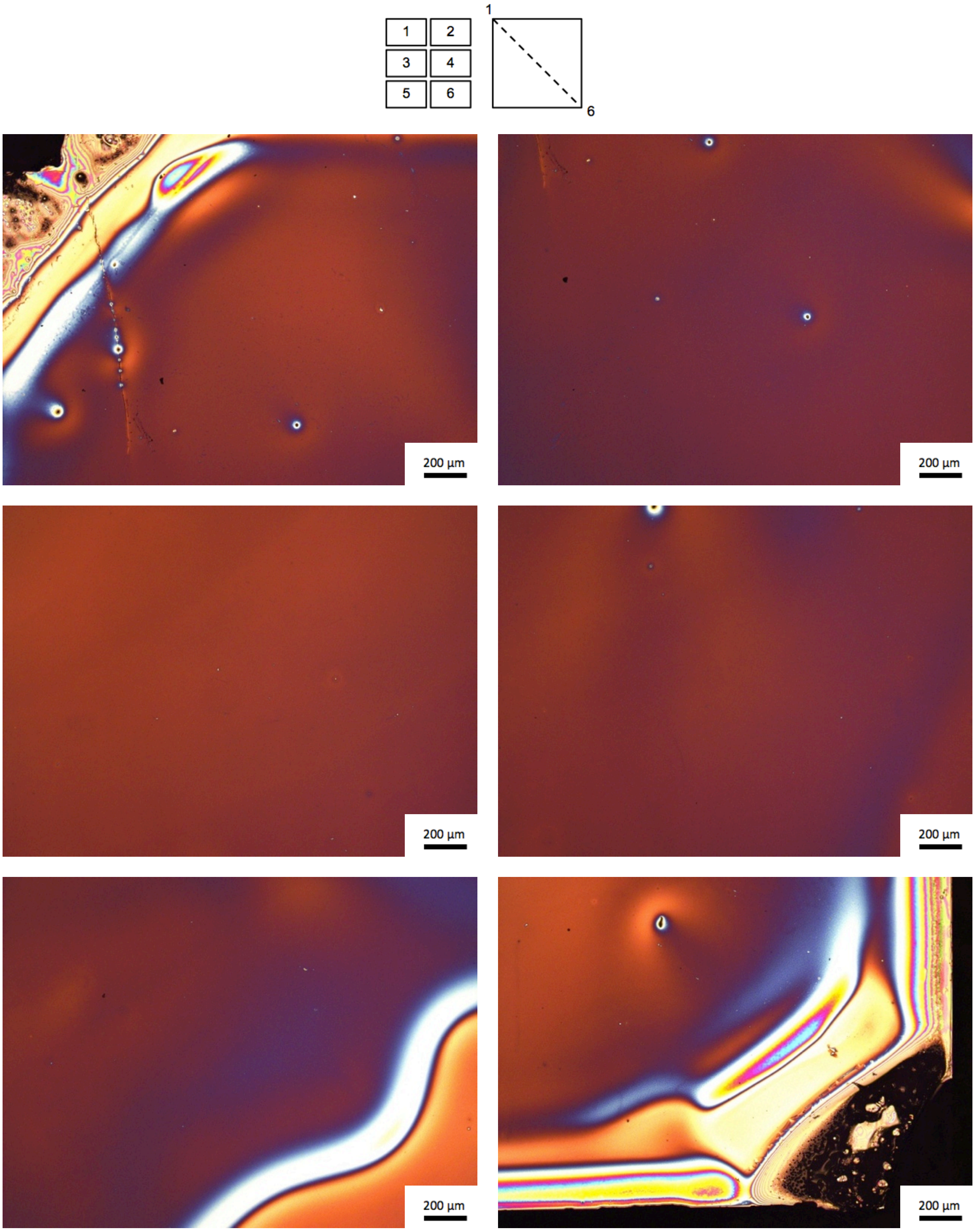

Figure 4.25: Optical light microscopy images showing the diagonal of the ITO10%-3-Si-UV thin film. These images are also representative for the IZO40%-3-Si-UV thin film.

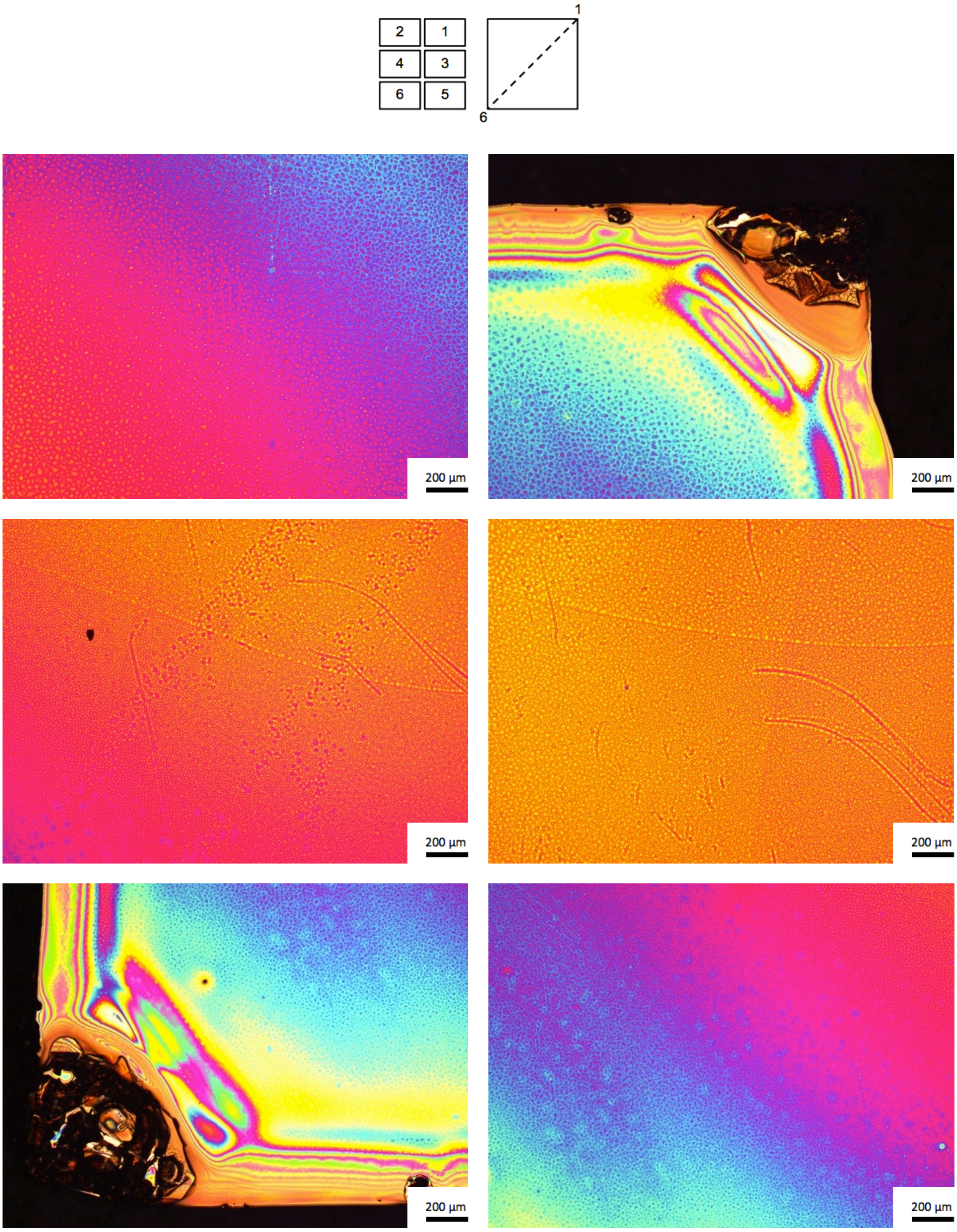

Figure 4.26: Optical light microscopy images showing the diagonal of the ITO10%-3-Si-UVHT thin film.

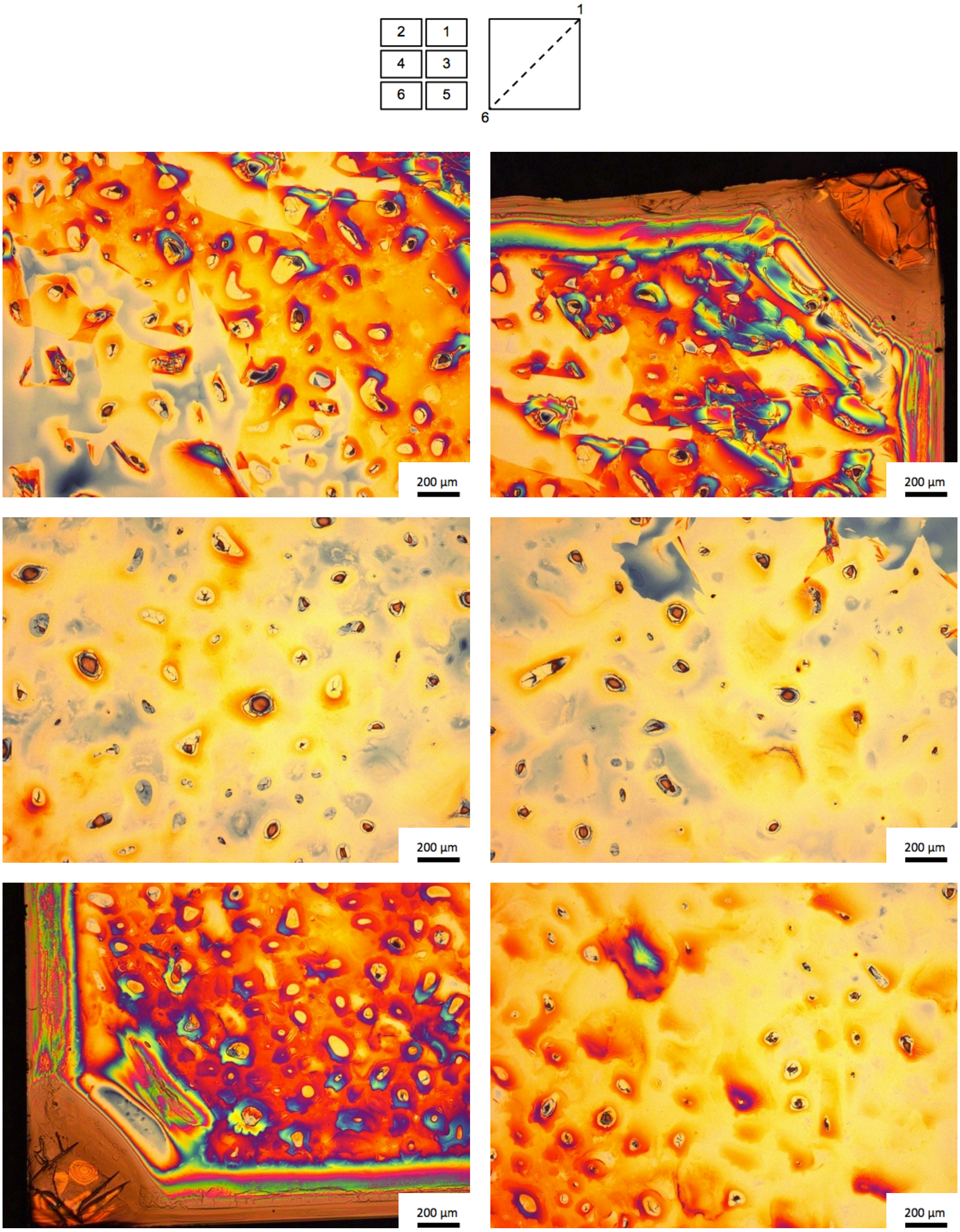

Figure 4.27: Optical light microscopy images showing the diagonal of the IZO40%-3-Si-UVHT thin film.

Based on the optical light microscopy images in the section above it was determined to study thin films ITO15%-1-g-RTP, IZO40%-2-g-RTP, IZO40%-3-g-RTP, ITO10%-3-g-UVHT, IZO40%-3-g-UVHT, ITO15%-1-Si-RTP, IZO40%-1-Si-RTP, IZO40%-2-Si-RTP, IZO40%-3-Si-RTP, ITO10%-3-Si-UV, ITO10%-3-Si-UVHT and IZO40%-3-Si-UVHT, which all look different in the optical light microscopy, using the SEM. The thin films IZO40%-1-g-RTP, ITO10%-3-g-UV and IZO40%-3-g-UV are also studied in the SEM to see if they look the same as thin film ITO15%-1-g-RTP at a higher magnifications. Also thin film IZO40%-3-Si-UV is studied in the SEM to see if it looks similar to the ITO10%-3-Si-UV thin film at high magnification.

4.5.3 Scanning Electron Microscopy

SEM is used to study the microstructure up close and even the nanostructure of the thin films. The SEM images for the thin films listed in the above section are found in figures 4.29 to 4.40 and “Appendix E Morphology”. In figures 4.29 to 4.31 typical images of thermally cured thin films are shown. For the UV and UVHT cured thin films, only eight samples were made and all of these are included in figures 4.32 to 4.40.

The thin films are sensitive to beam damage, as can be seen in some of the images. This effect emerges when the beam is focused at one spot for a longer period of time. Beam damage effects are mostly avoided in the images by moving to a place nearby the point where focus was obtained, before taking the image. Which images that include a beam damage is specified in each figure.

The images are taken at different magnifications. High magnification is used to take images at two different points on the thin film, which are shown in Figure 4.28. Point 1 is situated in the center, while point 2 is situated 1 × 1 mm^2 along the diagonal from point 1. Low magnification is used to take overview images of the diagonal of the thin films in the same way as for the optical light microscopy images, see Figure 4.14. The low magnification image presented is typical for the entire surface of the thin film.

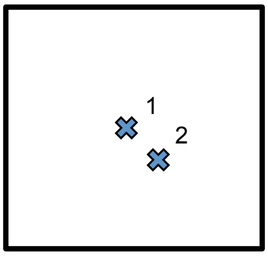

Figure 4.28: A schematic illustrating where on the thin films the high magnification images are taken.

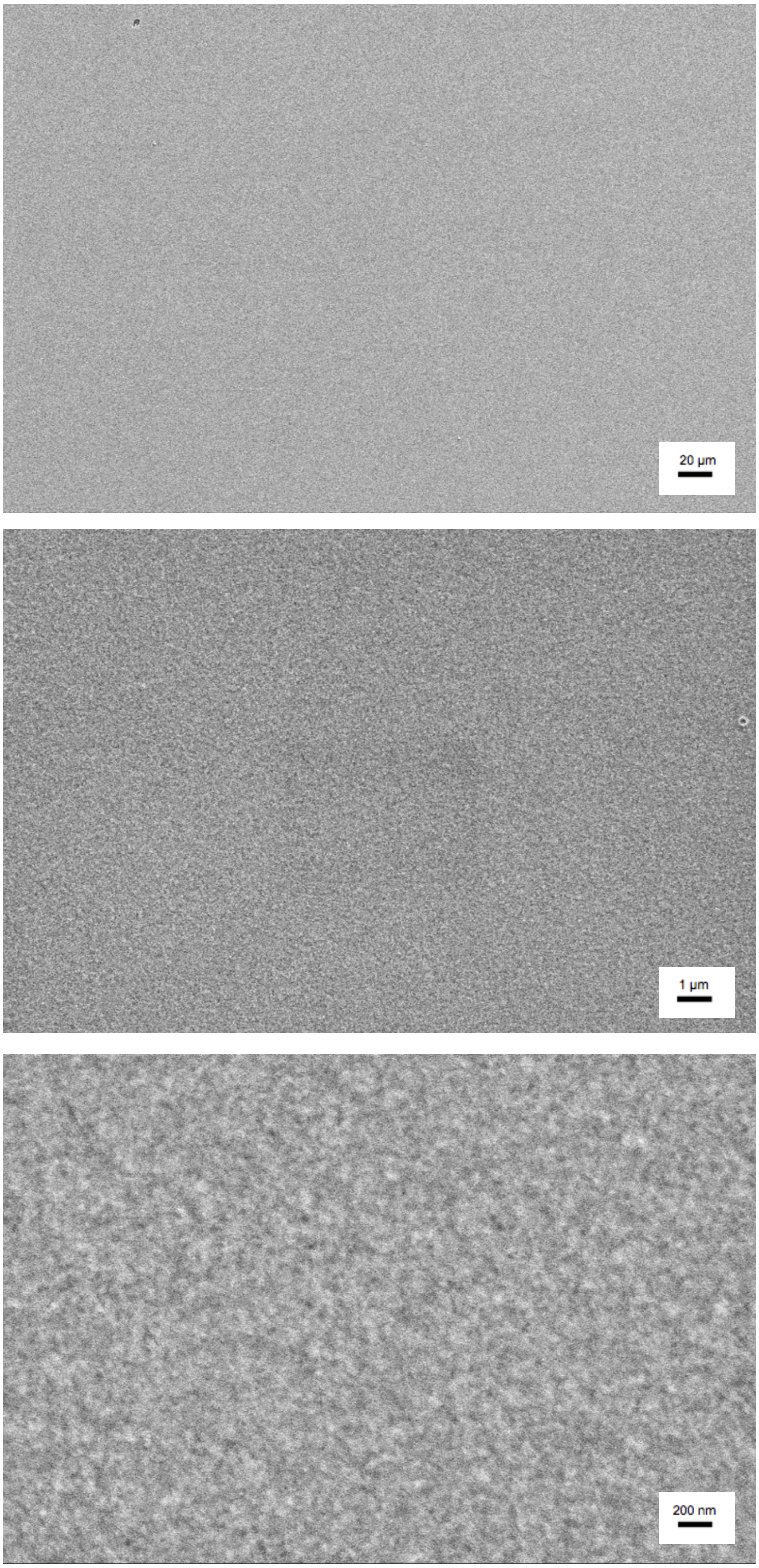

Figure 4.29: SEM images of the ITO15%-1-g-RTP thin film. A quadratic beam damage effect is seen in the center of the middle image.

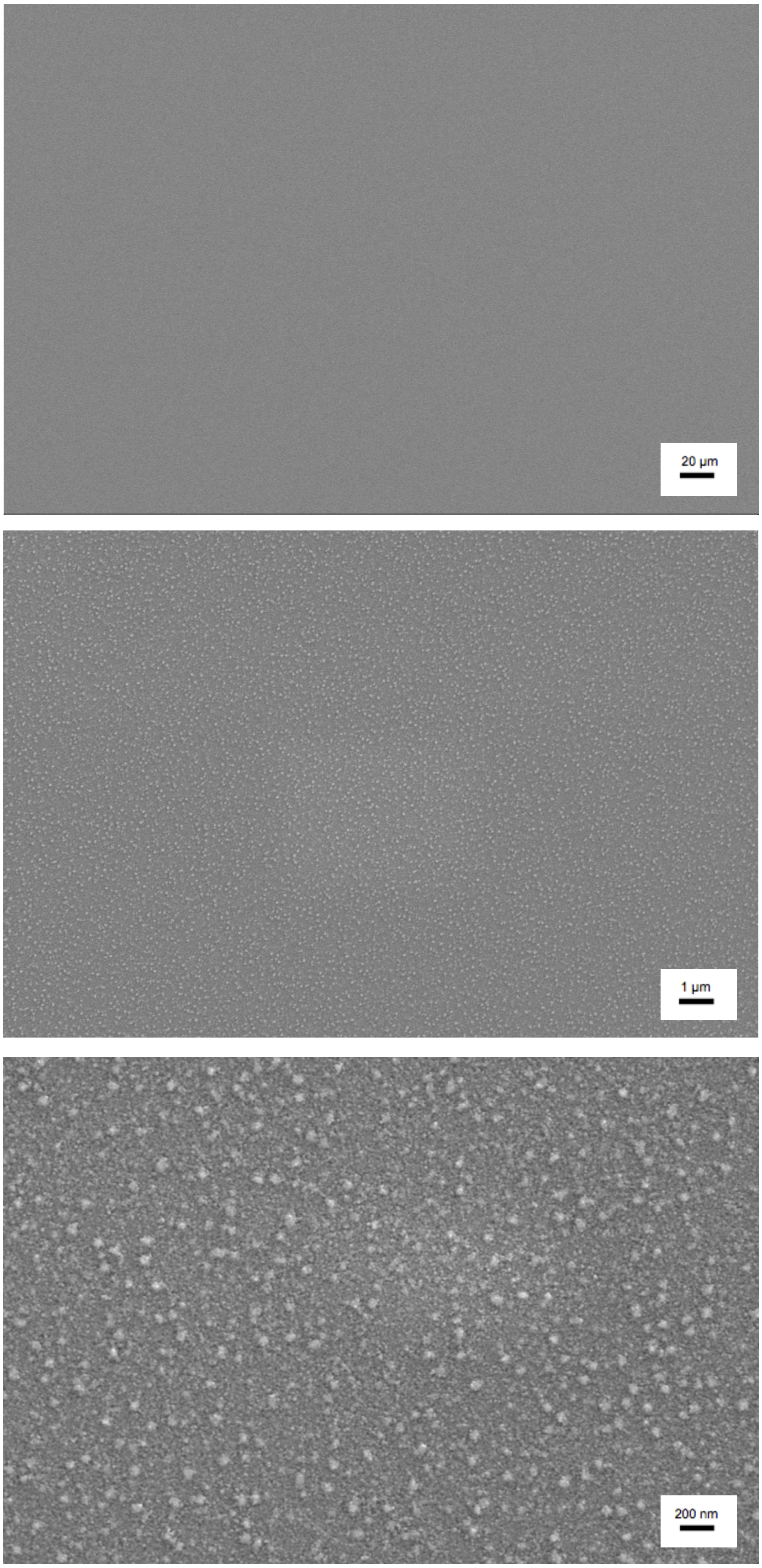

Figure 4.30: SEM images of the IZO40%-1-g-RTP thin film. A quadratic and circular beam damage effect is seen in the center of the middle and lower image respectively.

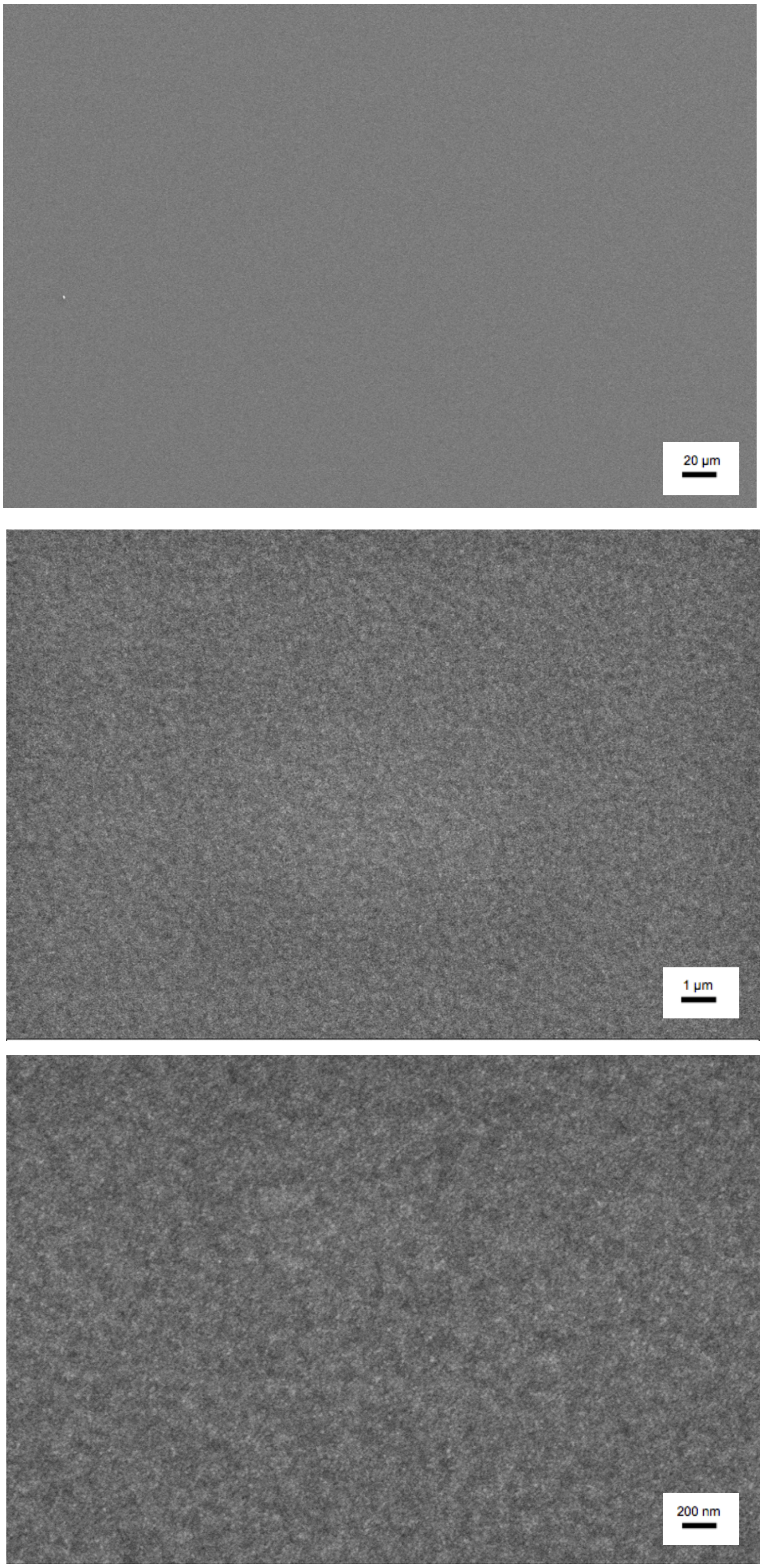

Figure 4.31: SEM images of the ITO15%-1-Si-RTP thin film. These images are representative for all the thermally cured thin films on silicon substrate. A quadratic beam damage effect is seen in the center of the middle image.

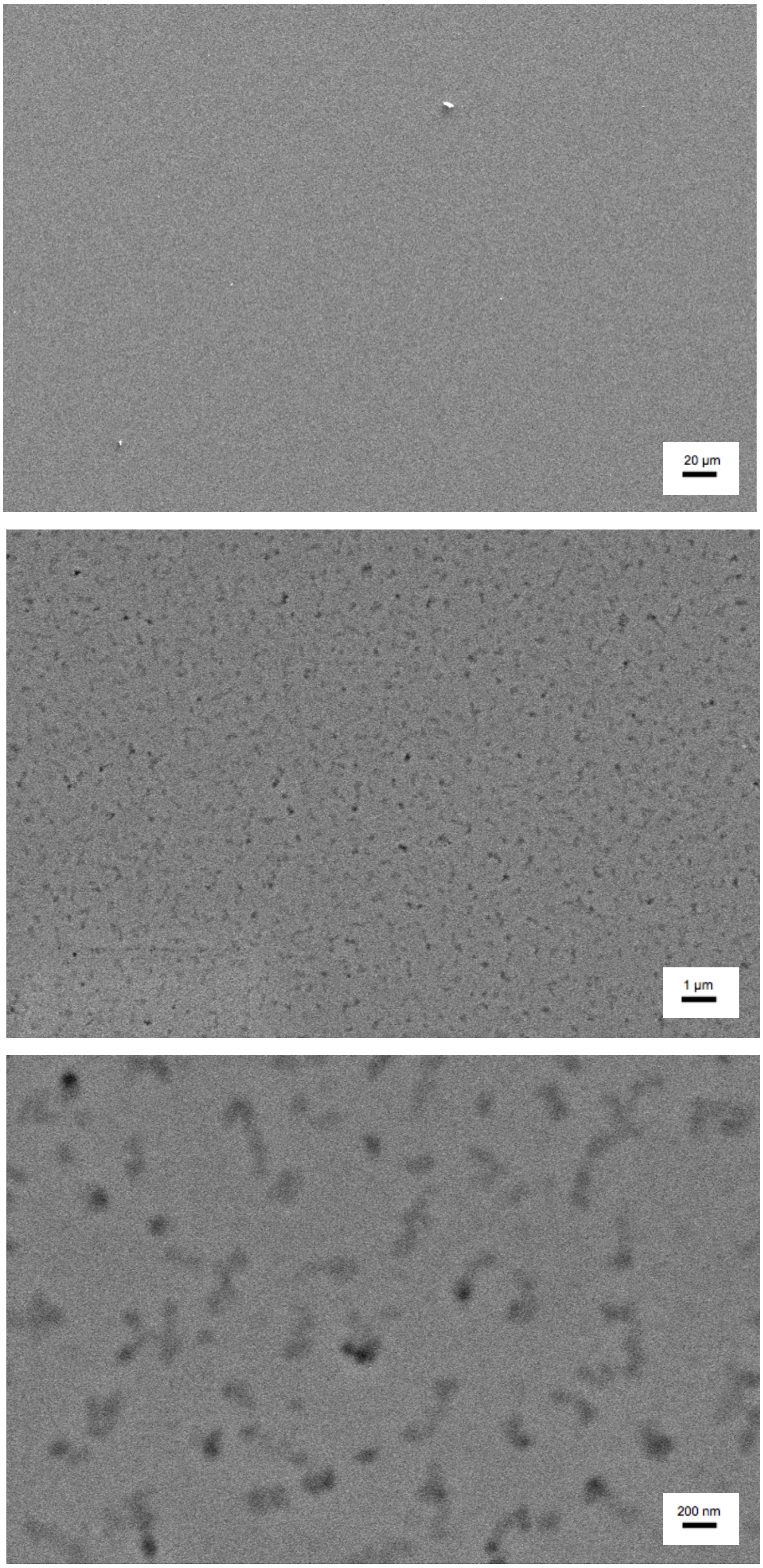

Figure 4.32: SEM images of the ITO10%-3-g-UV thin film.

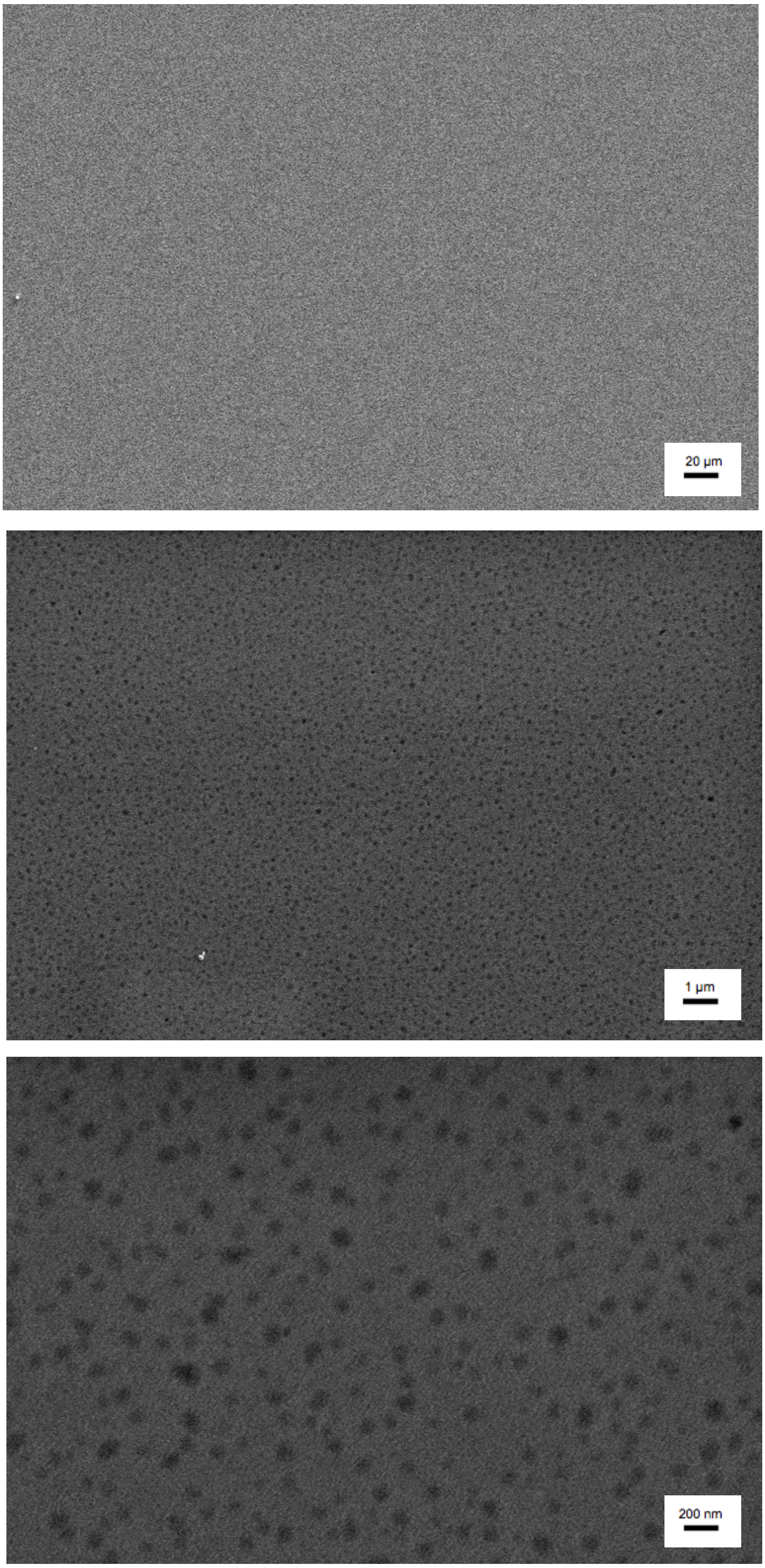

Figure 4.33: SEM images of the ITO10%-3-Si-UV thin film.

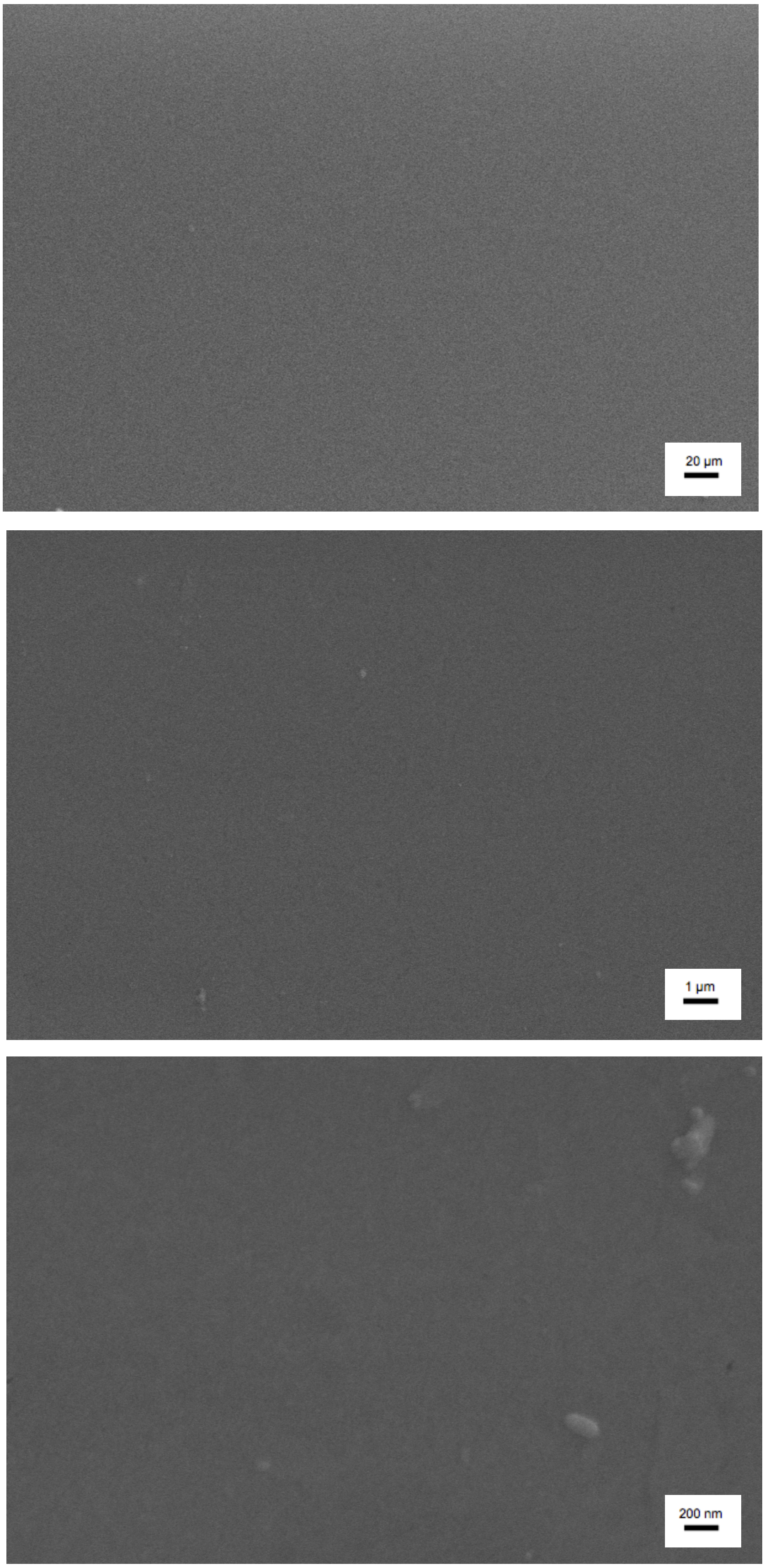

Figure 4.34: SEM images of the IZO40%-3-g-UV thin film.

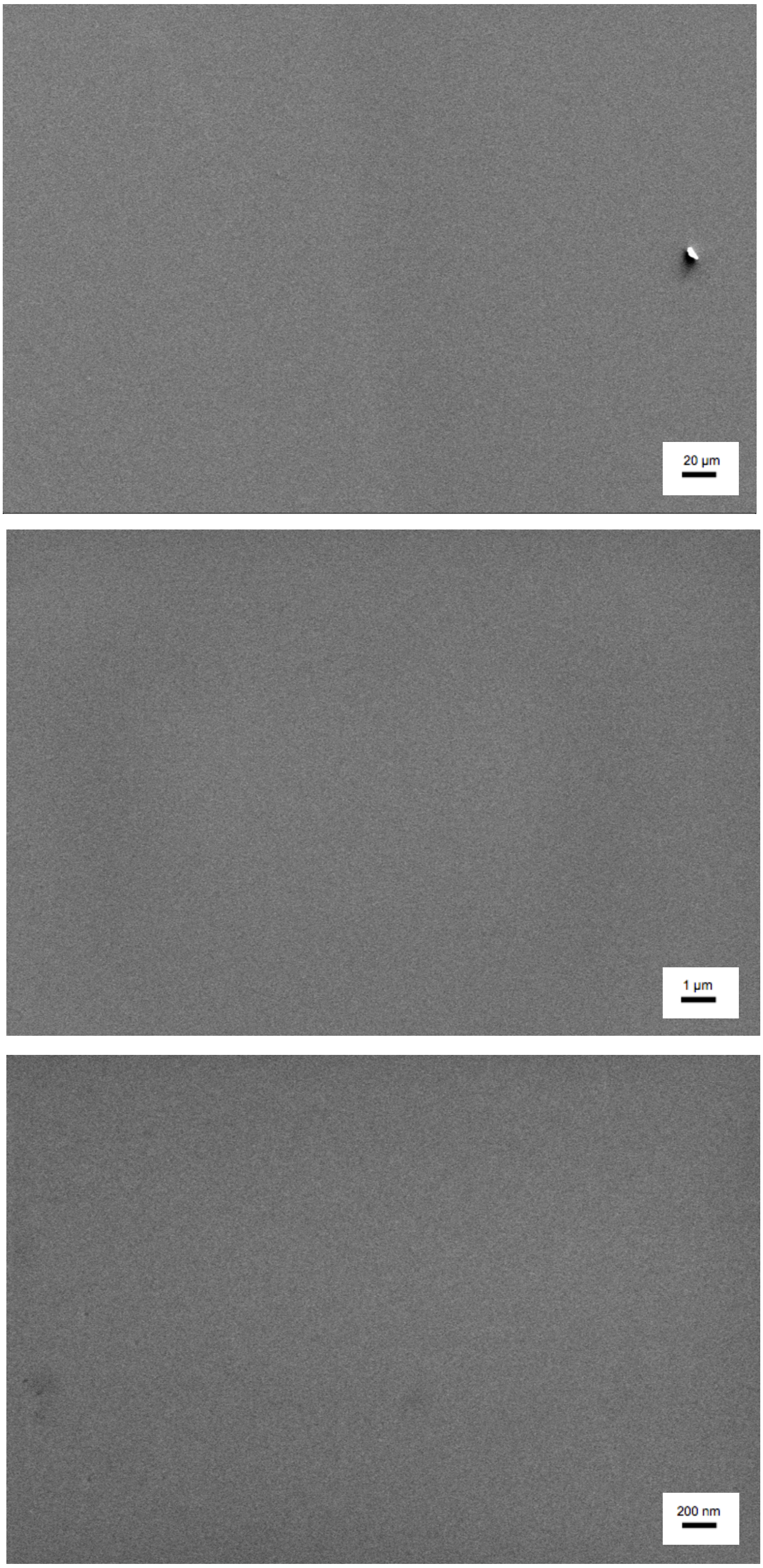

Figure 4.35: SEM images of the IZO40%-3-Si-UV thin film.

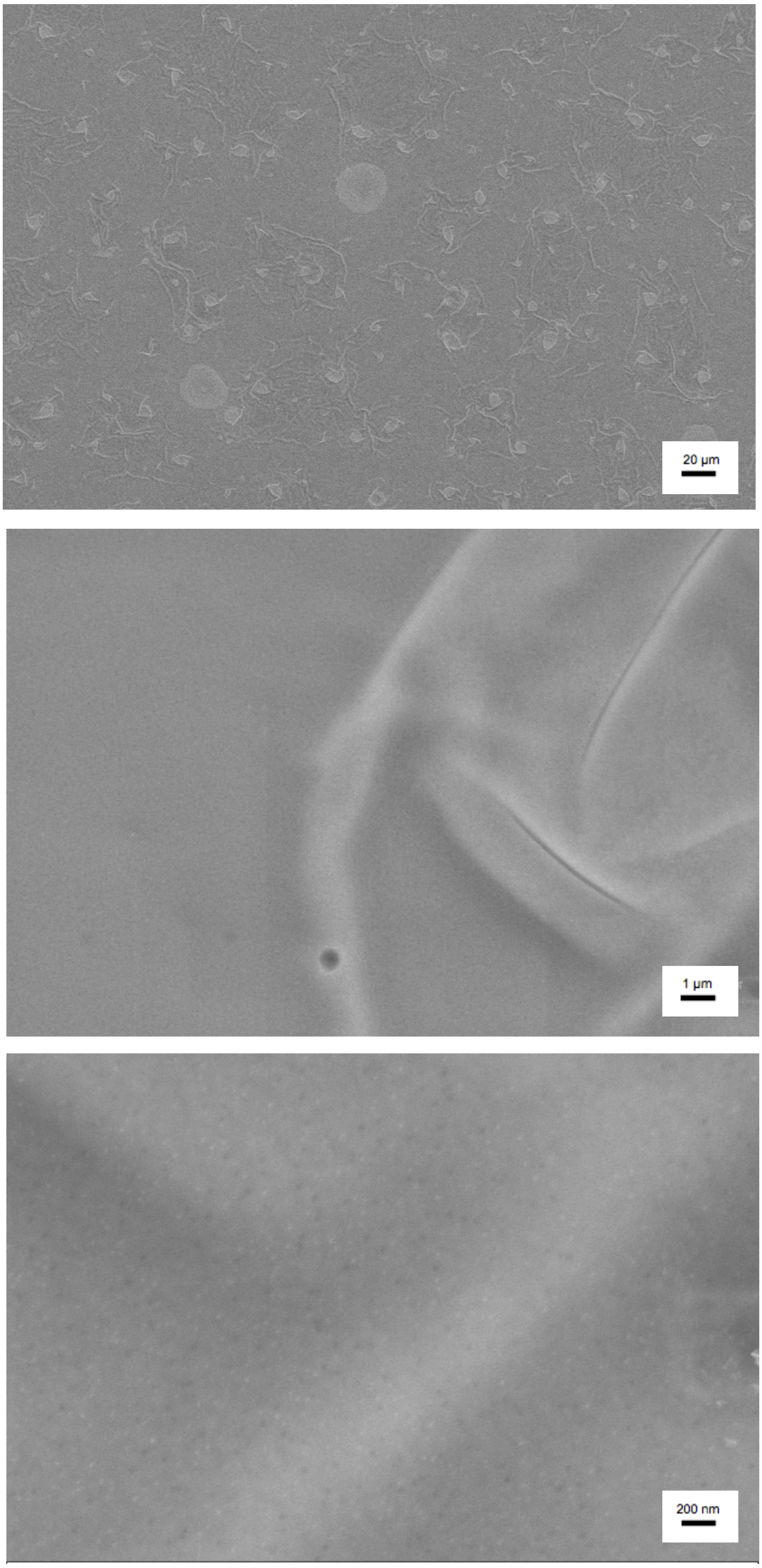

Figure 4.36: SEM images of the ITO10%-3-g-UVHT thin film.

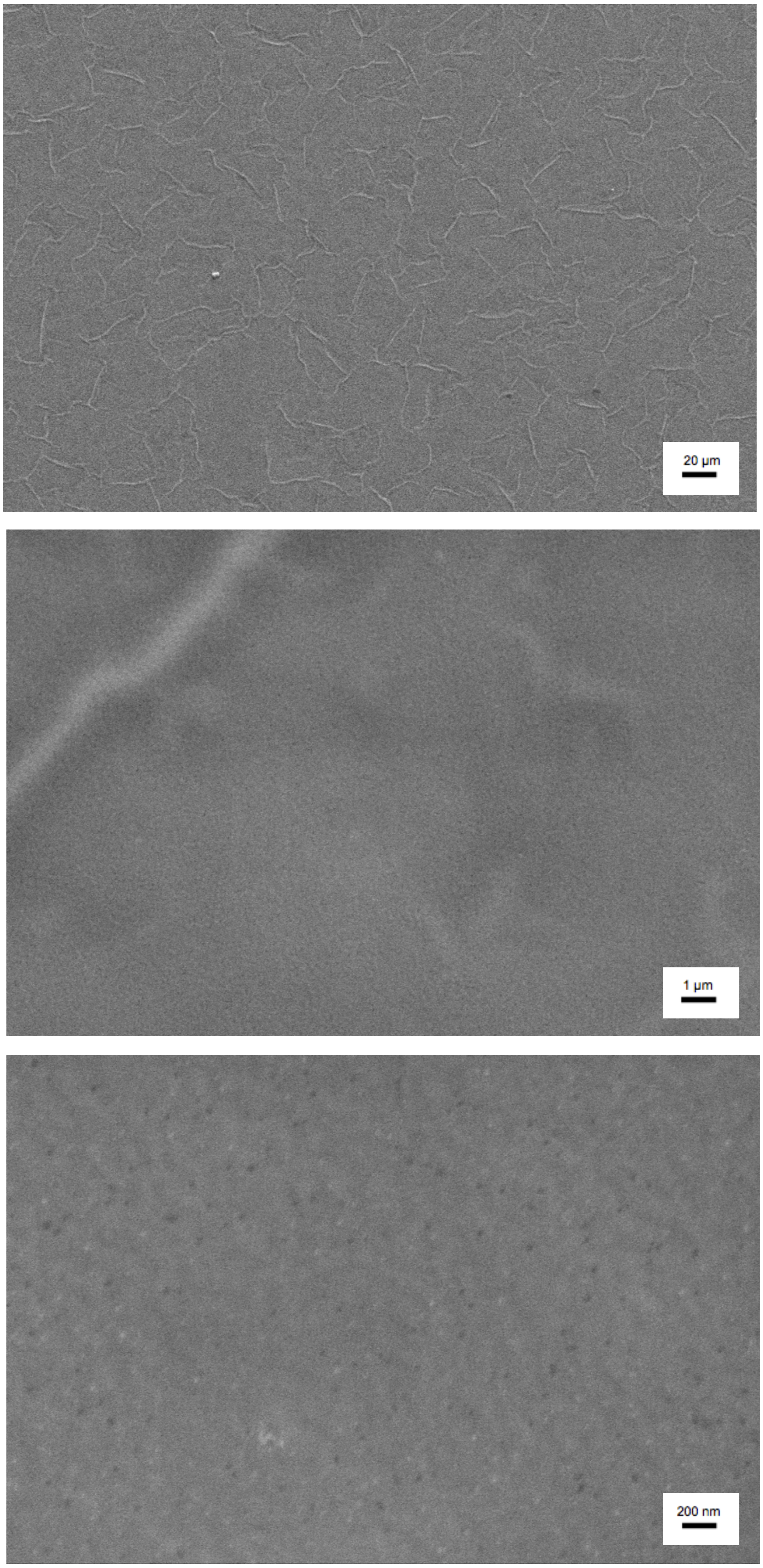

Figure 4.37: SEM images of the ITO10%-3-Si-UVHT thin film.

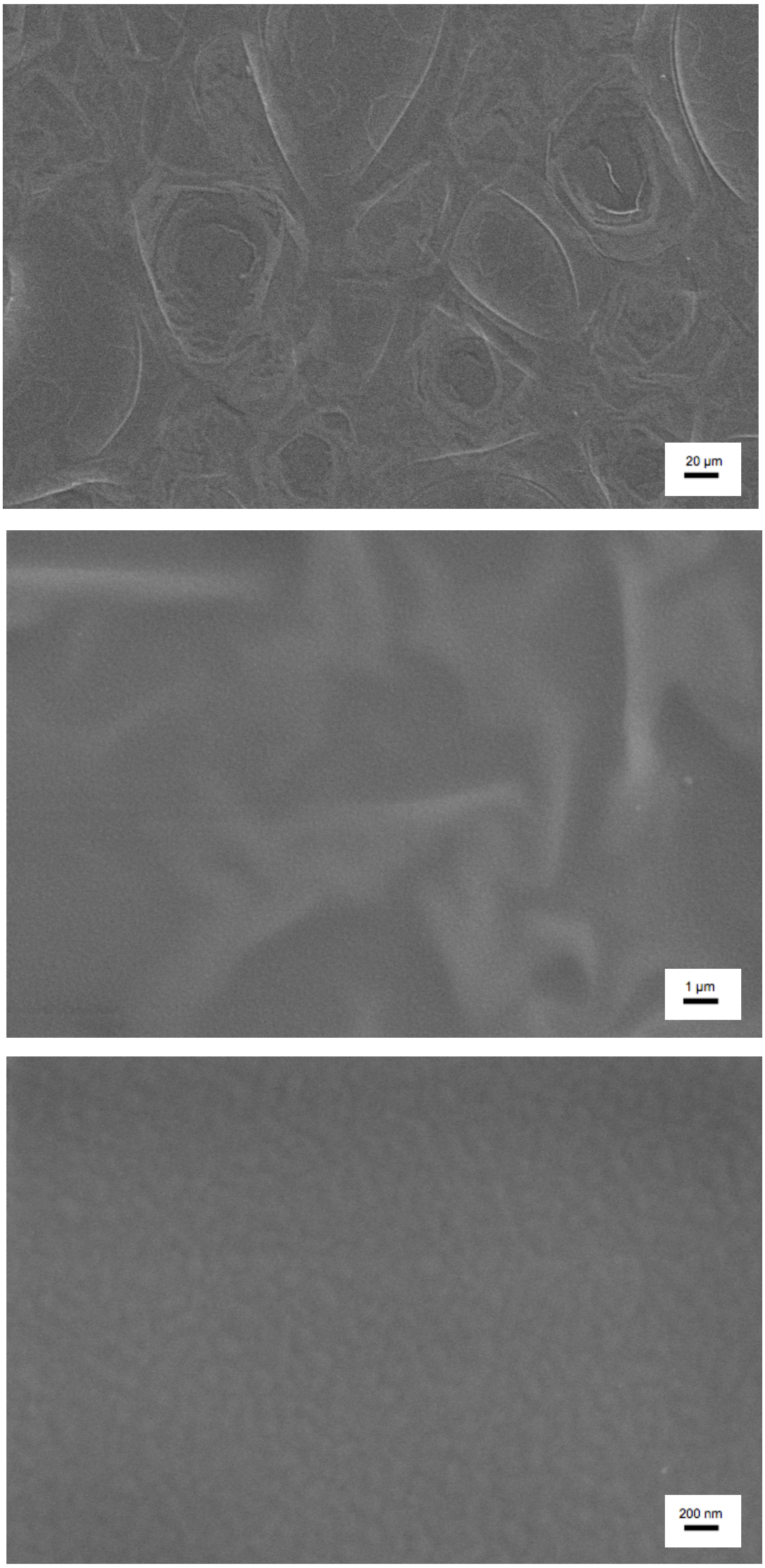

Figure 4.38: SEM images of the IZO40%-3-g-UVHT thin film.

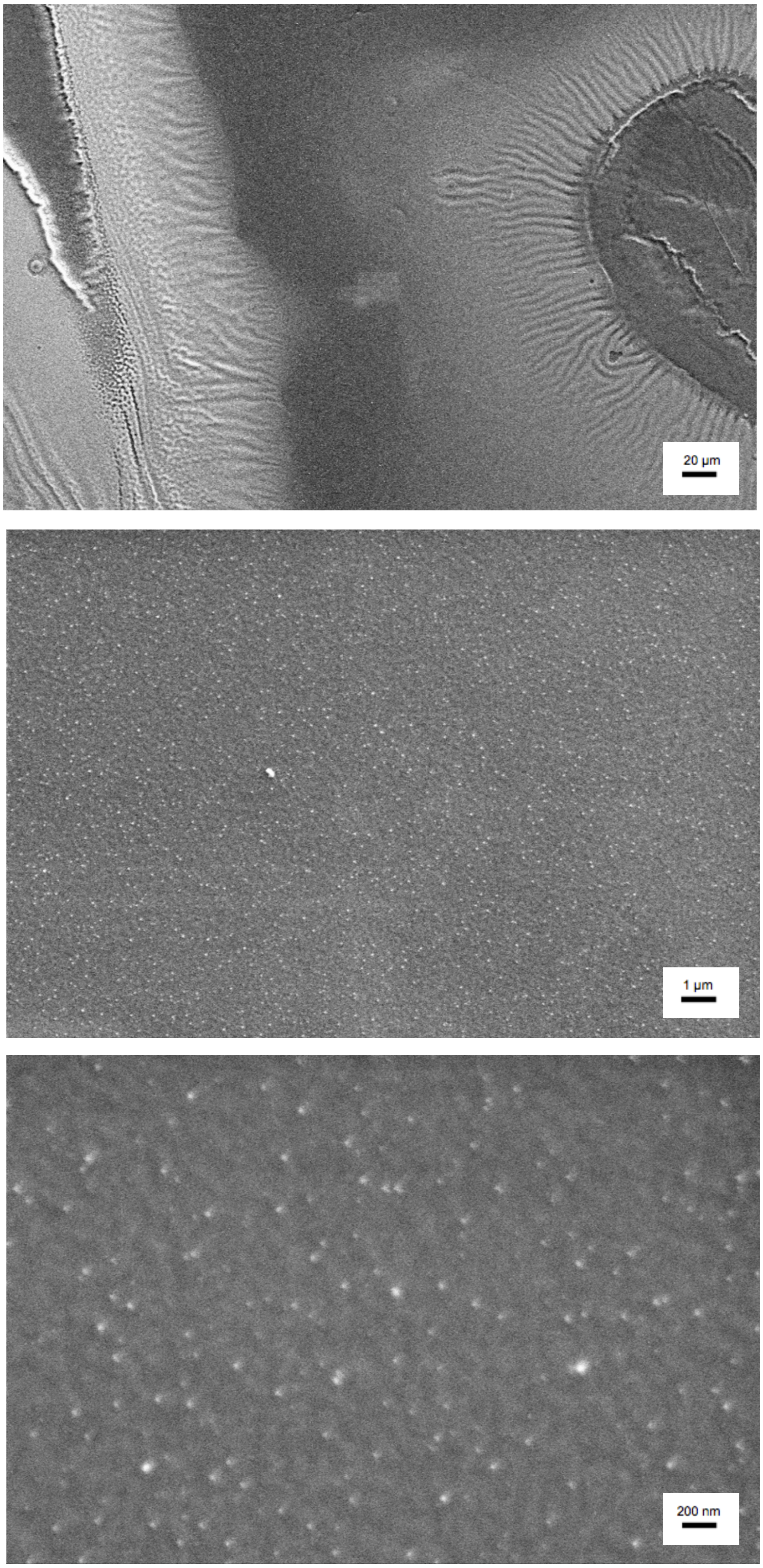

Figure 4.39: SEM images of thin film the IZO40%-3-Si-UVHT thin film.

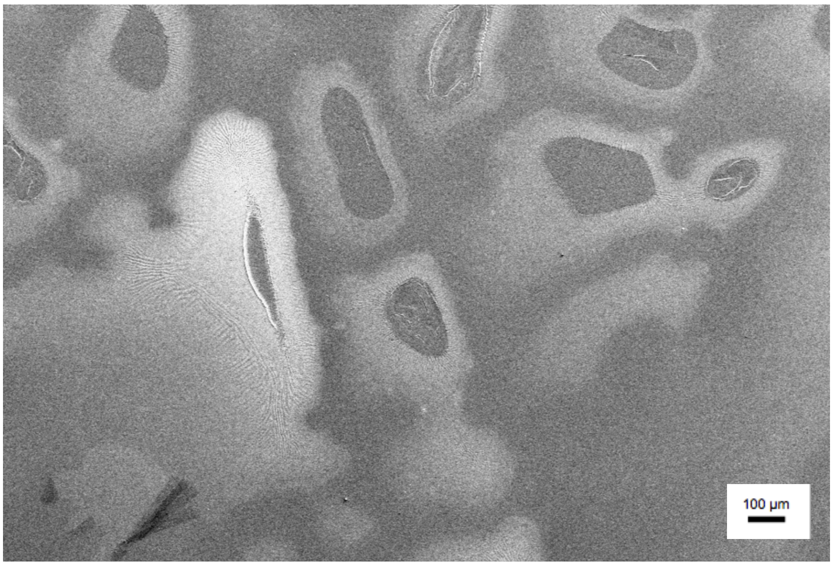

Figure 4.40: Lower magnification SEM image of the IZO40%-3-Si-UVHT thin film.

To study the roughness and topography of the thin films the characterization methods profilometer and AFM are used. The choice of thin films studied by these methods is based on the SEM images, where the thin films studied are the ones that stand out with regards to nano- or microstructure in a way that could cause a distinct topography on the surface.

4.5.4 Profilometer

Based on these considerations it is determined to study the thin films IZO40%-1-g-RTP, ITO10%-3-Si-UVHT, and IZO40%-3-Si-UVHT with the profilometer. Thin film ITO15%-1-g-RTP that appears to have a flat topography and homogenous morphology in the SEM, is measured to use as a reference. Representative scans for the different thin films are found in figures 4.41 to 4.44. Based on the scans the three roughness parameters average roughness (R_a), Root-Mean-Square ($R_q = R_{RMS}$), and maximum peak (R_p) are calculated and listed in Table 4.3. The values are average values of three scans, and are given together with standard deviations.

Table 4.3: The roughness parameters average roughness (R_a), Root-Mean-Square (R_q=R_{RMS}), and maximum peak (R_p) calculated based on profilometer scans.

Thin film	**R_a [nm]**	**R_q [nm]**	**R_p [nm]**
ITO15%-1-g-RTP	1.78 ± 0.23	2.27 ± 0.17	5.70 ± 0.35
IZO40%-1-g-RTP	1.88 ± 0.26	2.38 ± 0.35	7.66 ± 0.95
ITO10%-3-Si-UVHT	5.39 ± 0.97	8.69 ± 1.43	58.43 ± 3.49
IZO40%-3-Si-UVHT	6.93 ± 1.60	8.91 ± 1.90	24.03 ± 4.59

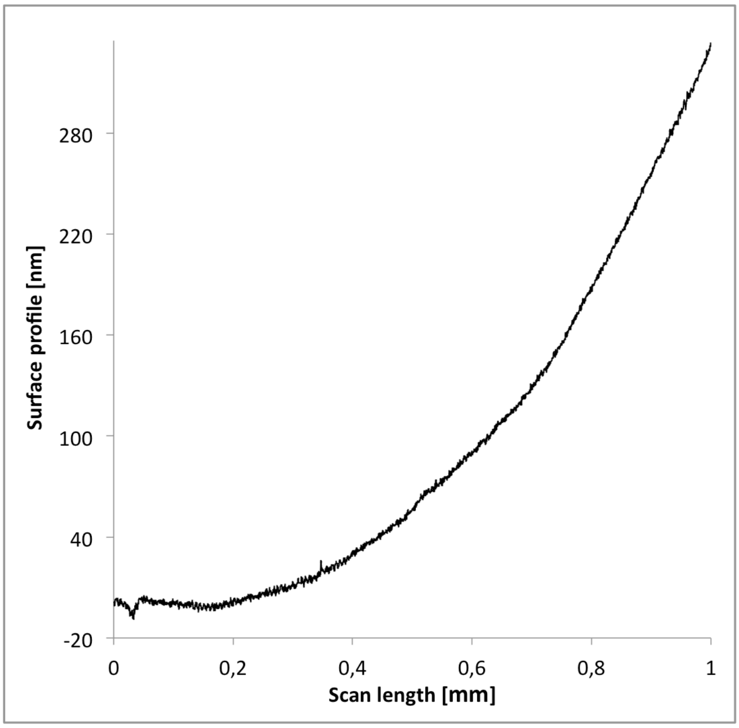

Figure 4.41: Representative profilometer scan for the ITO15%-1-g-RTP thin film with scan time 30 seconds and scan length 1 mm.

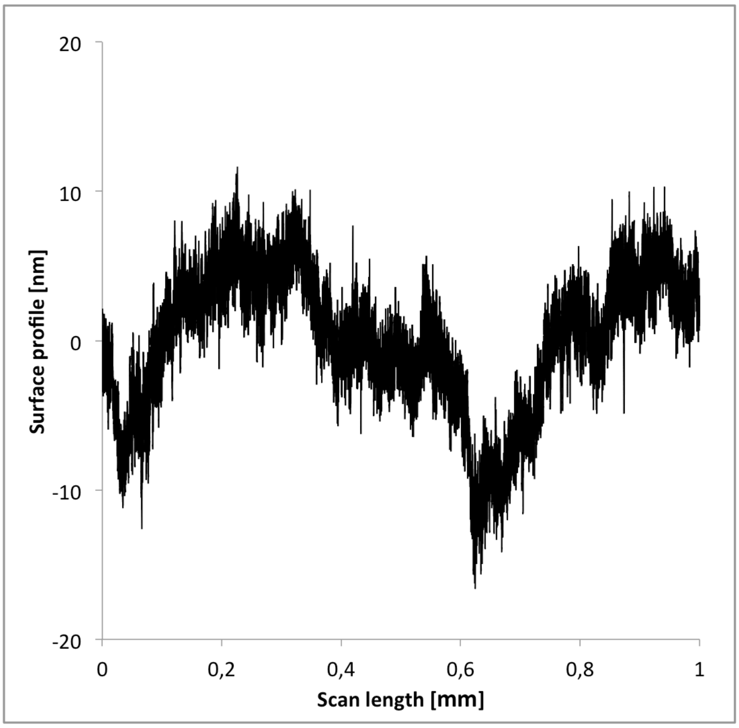

Figure 4.42: Representative profilometer scan for the IZO40%-1-g-RTP thin film with scan time 180 seconds and scan length 1 mm.

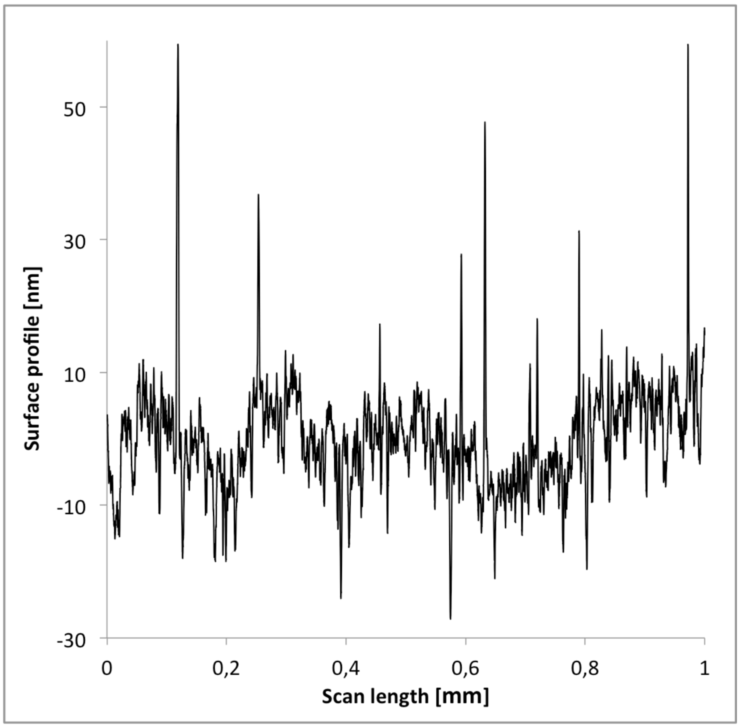

Figure 4.43: Representative profilometer scan for the ITO10%-3-Si-UVHT thin film with scan time 30 seconds and scan length 1 mm.

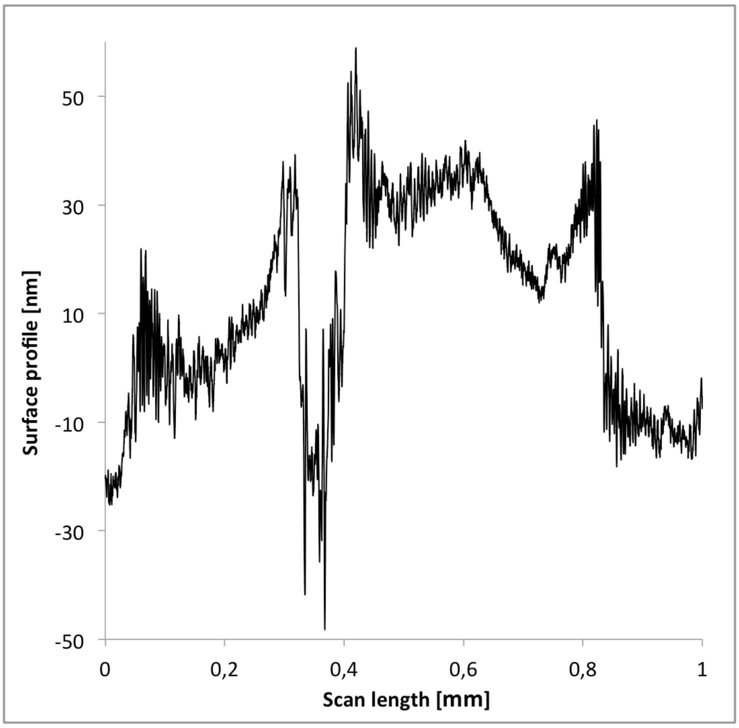

Figure 4.44: Representative profilometer scan for the IZO40%-3-Si-UVHT thin film with scan time 30 seconds and scan length 1 mm.

4.5.5 Atomic Force Microscopy

AFM images was obtained for the ITO15%-1-g-RTP, IZO40%-1-g-RTP, ITO10%-3-Si-UV, ITO10%-3-Si-UVHT, and IZO40%-3-Si-UVHT thin films, and are presented in figures 4.45 to 4.47. In the figures both an image of the surface from above and a topographic 3D-plot of the surface are displayed.

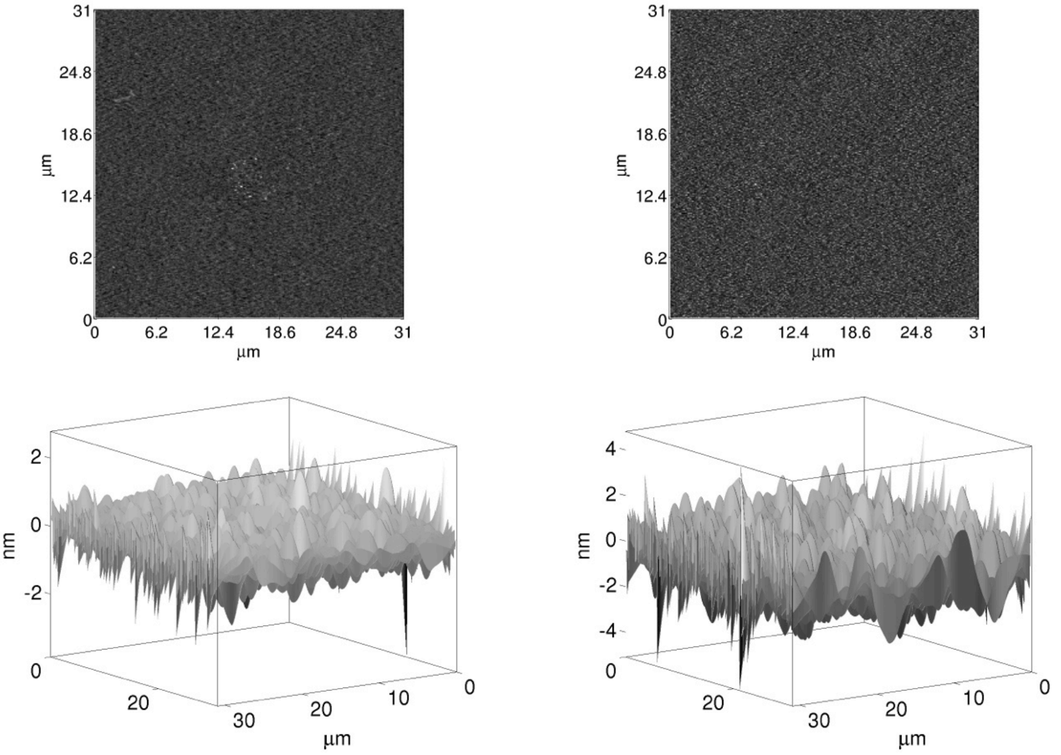

Figure 4.45: AFM images of the thermally cured thin films ITO15%-1-g-RTP and IZO40%-1-g-RTP to the left and right respectively. The upper image shows the surface from above, while the lower image display a topographic 3D-plot of the thin film surface. The AFM images were obtained by a third degree polynomial fit with a moving average filter.

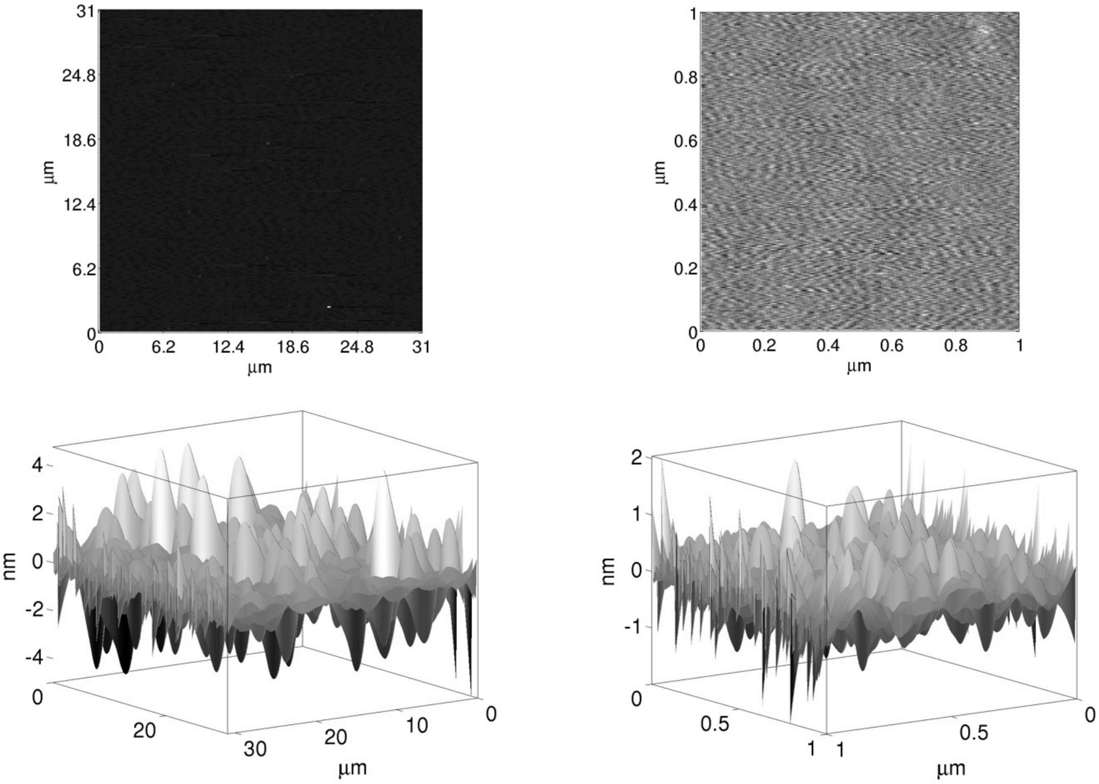

Figure 4.46: AFM images of the UV cured ITO10%-3-Si-UV thin film for a 31 × 31 μm^2 and 1 × 1 μm^2 area to the left and right respectively. The upper image shows the surface from above, while the lower image display a topographic 3D-plot of the thin film surface. The AFM images were obtained by a third degree polynomial fit with a moving average filter.

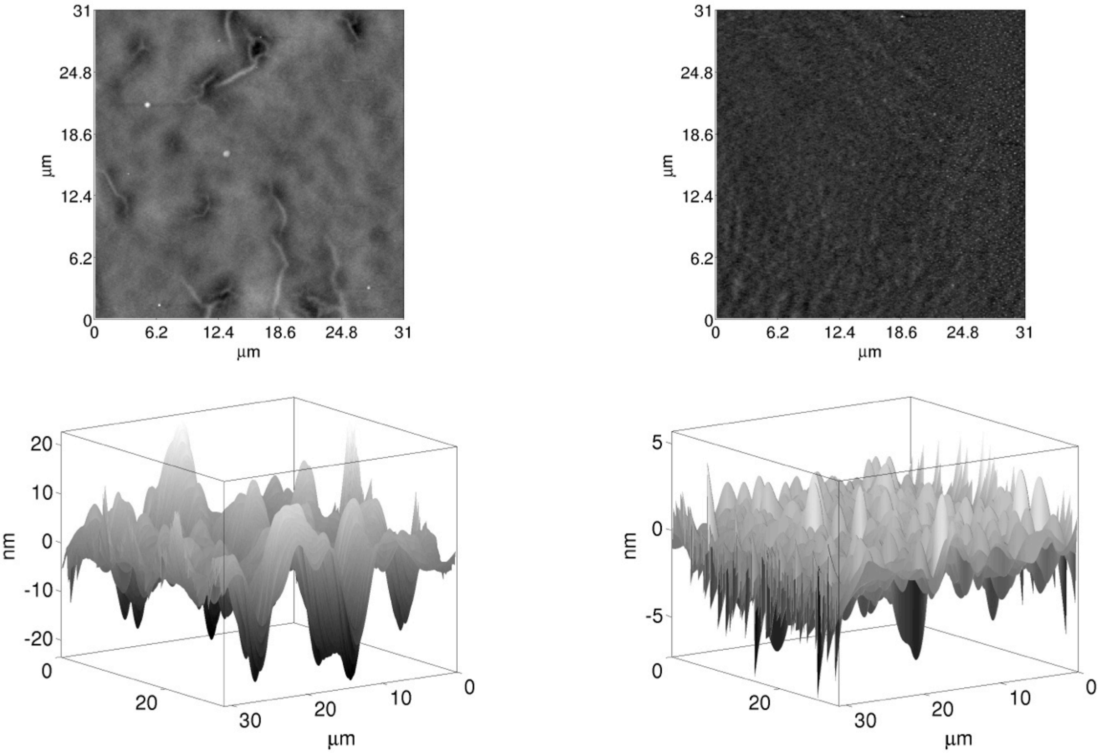

Figure 4.47: AFM images of the UVHT cured thin films ITO10%-3-Si-UVHT and IZO40%-3-Si-UVHT to the left and right respectively. The upper image shows the surface from above, while the lower image display a topographic 3D-plot of the thin film surface. The AFM images were obtained by a third degree polynomial fit with a moving average filter.

4.6 Energy Dispersive X-ray Spectroscopy

Based on the SEM images it was determined to study some of the thin films using EDS. From the SEM images some films are determined to be inhomogeneous with regards to morphology. These are: the thermally cured IZO thin film on glass (Figure 4.30), the UV cured ITO thin films (figures 4.32 and 4.33) and all the UVHT cured thin films (figures 4.36 to 4.40). One thin film from each of the three curing methods is analyzed using EDS, to determine if there are any compositional variations between the different regions of the thin films. Three EDS spectra are obtained for each region and the spectra are taken at different places on the thin film. Only a representative image of the regions is shown in figures 4.48, 4.50 and 4.52. In tables 4.4 to 4.6 average values for the elemental analysis of the three spectra are presented together with the standard deviation.

The IZO40%-1-g-RTP thin film is presented in Figure 4.48 showing the two different regions marked A and B where EDS spectra were obtained. Regions A are thought to be particles in a matrix B. In Figure 4.49 a typical EDS spectrum from the IZO40%-1-g-RTP thin film is shown. The thin film consists of In, Zn, and O, and the rest of the diffraction lines found in Figure 4.49 are from the substrate. The glass substrate is soda-lime glass, which contains oxides of Si, Na, Mg, Al, Ca, K, S, Fe, and Ti. All of these elements are marked in the EDS spectrum. For the elemental analysis given in Table 4.4 only O, Si, In, and Zn are included and the results indicate that there are no compositional variations between the two regions.

In Figure 4.50 the ITO10%-3-Si-UV thin film is seen showing the two different regions C and D analyzed by EDS. Regions C are thought to be holes in a matrix D. Figure 4.51 shows a typical EDS spectrum for this thin film. By looking at Table 4.5 no variation in composition is seen between the two regions.

Figure 4.52 shows the IZO40%-3-Si-UVHT thin film with the four different regions studied using EDS. A typical EDS spectrum from this thin film is found in Figure 4.53. From Table 4.6 a clear change in mol% with region is seen individually for each element, but the relationship between the different elements are not altered extensively with region. To show this, the relationship between zinc and indium is included in the table. Instead of indicating that there is a variation in composition between the different regions this instead reflects height changes in the thin film. Increased thickness is seen for the regions in the order E < H < F < G. The thinner the film, the more of the substrate is seen giving a higher mol% of Si and lower values for O, In, and Zn.

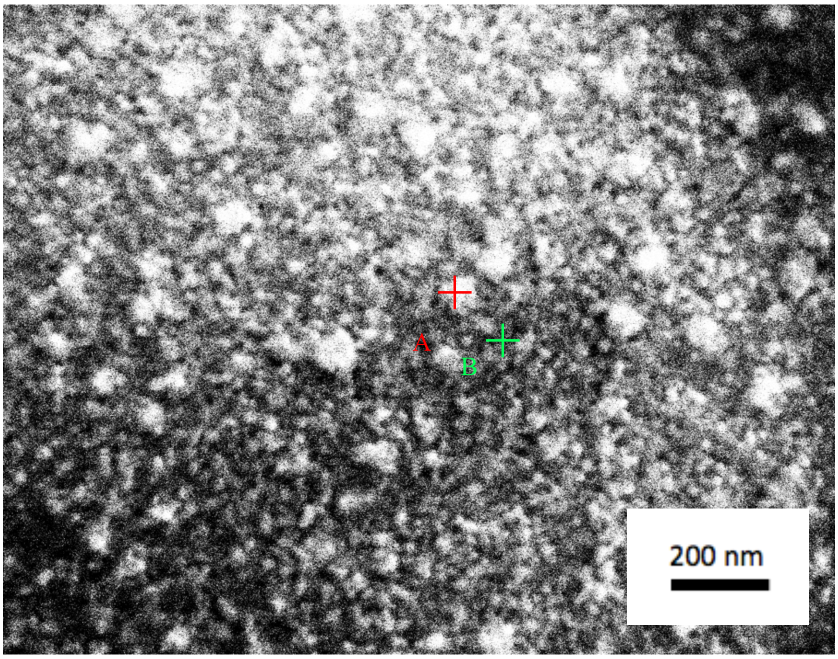

Figure 4.48: Image of the IZO40%-1-g-RTP thin film showing typical points A and B where the EDS spectra were obtained.

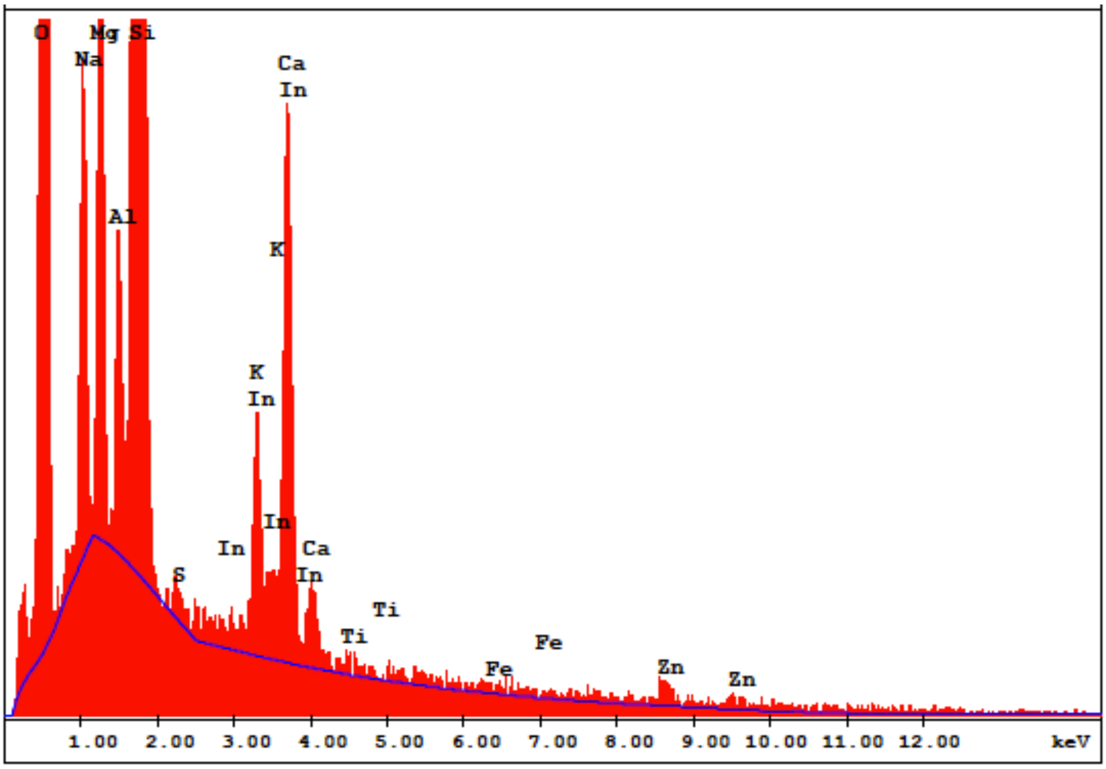

Figure 4.49: EDS spectrum for the IZO40%-1-g-RTP thin film. The spectrum is representative for all the spectra obtained for this thin film.

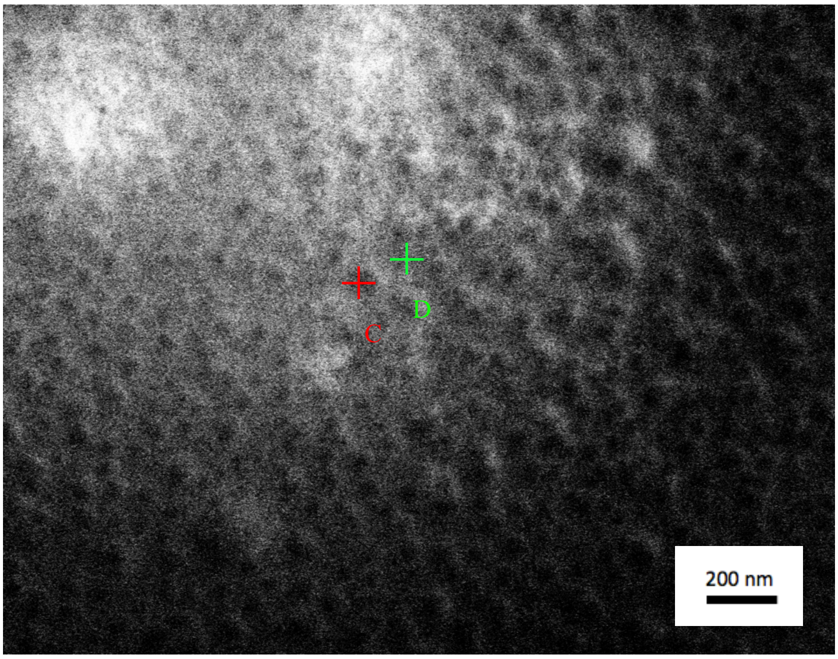

Figure 4.50: Image of the ITO10%-3-Si-UV thin film showing the C and D points where the EDS spectra were obtained.

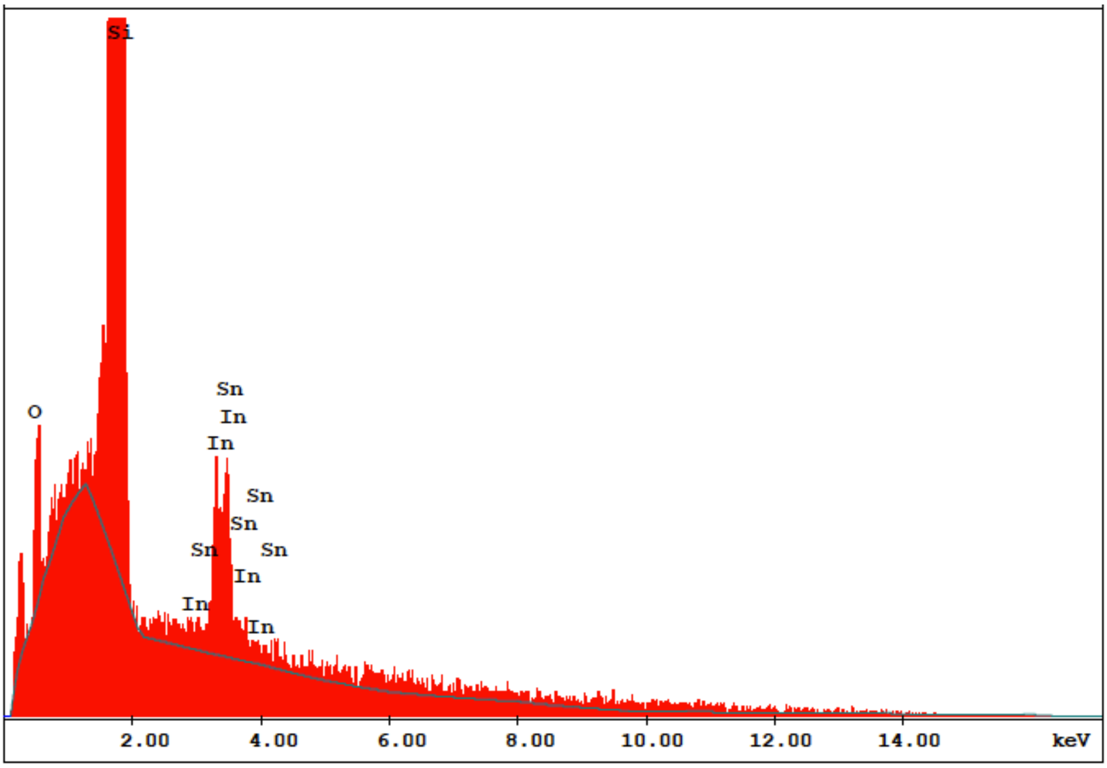

Figure 4.51: EDS spectrum for the ITO10%-3-Si-UV thin film. The spectrum is representative for all the spectra obtained for this thin film.

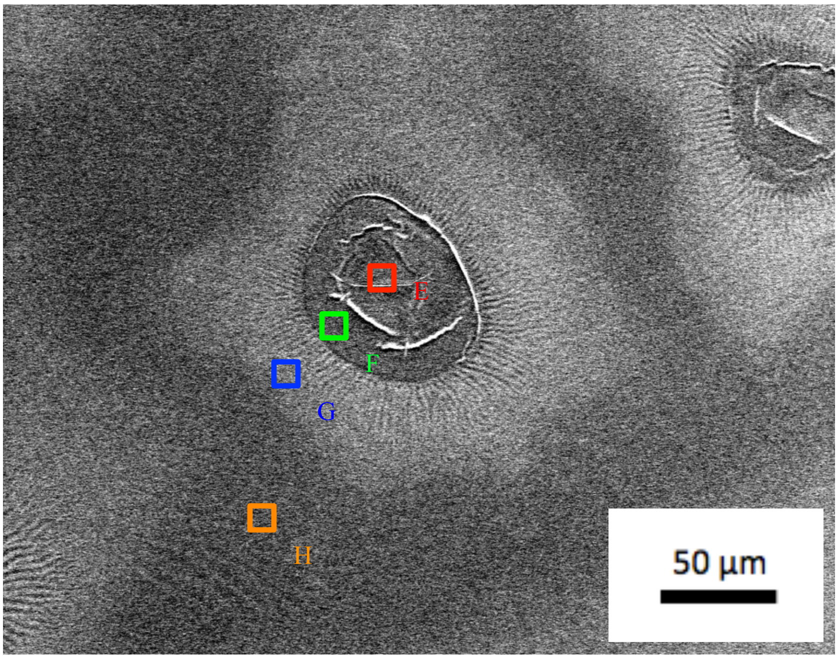

Figure 4.52: Image of the IZO40%-3-Si-UVHT thin film showing the E, F, G and H regions where the EDS spectra were obtained.

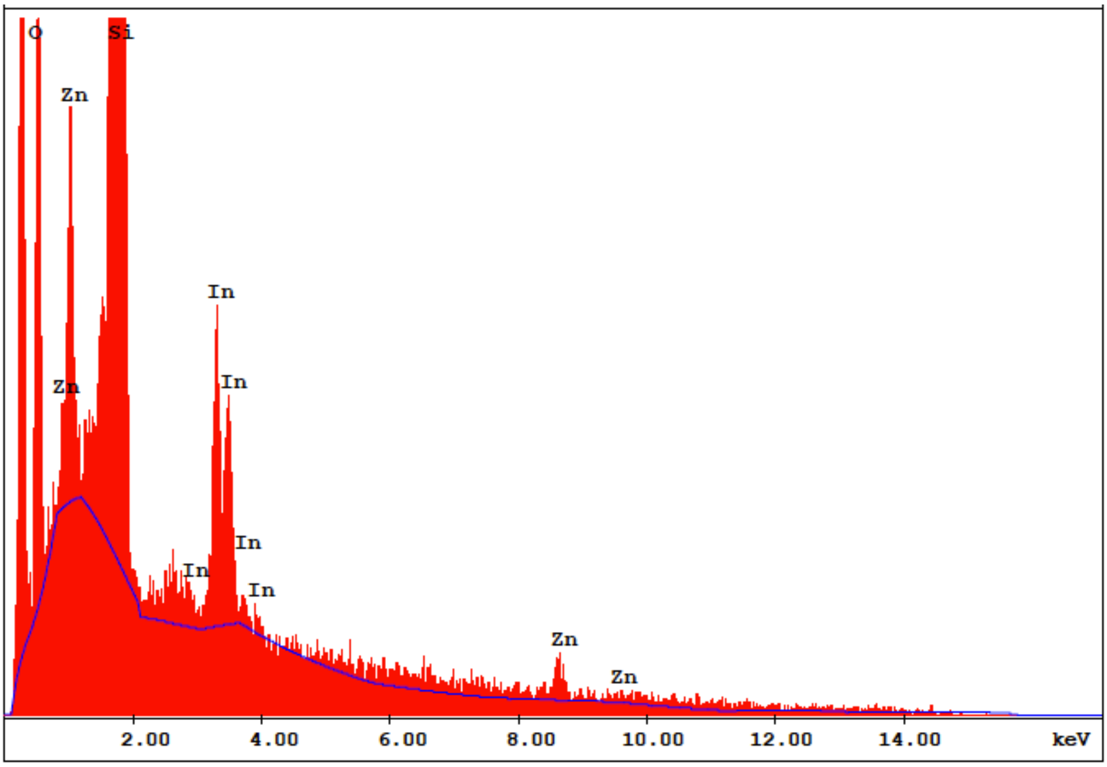

Figure 4.53: EDS spectrum for the IZO40%-3-Si-UVHT thin film. The spectrum is representative for all the spectrums obtained for this thin film.

Table 4.4: Elemental analysis for the IZO40%-1-g-RTP thin film from the points shown in Figure 4.48.

Region	mol% O	mol% Si	mol% In	mol% Zn	$\frac{\text{Zn}}{(\text{In+Zn})}$
A	58.59 ± 0.46	39.15 ± 0.44	1.10 ± 0.12	1.16 ± 0.22	0.51 ± 0.04
B	57.85 ±0.63	40.00 ± 0.62	1.00 ± 0.04	1.15 ± 0.11	0.53 ± 0.02

Table 4.5: Elemental analysis for the ITO10%-1-Si-UV thin film from the points shown in Figure 4.50.

Region	mol% O	mol% Si	mol% In	mol% Sn	$\frac{\text{Sn}}{(\text{In+Sn})}$
C	3.15 ± 0.04	95.27 ± 0.13	0.79 ± 0.07	0.80 ± 0.04	0.50 ± 0.02
D	3.28 ±0.07	95.09 ± 0.10	0.85 ± 0.04	0.78 ± 0.02	0.48 ± 0.01

Table 4.6: Elemental analysis for the IZO40%-3-Si-UVHT thin film from the regions shown in Figure 4.52.

Region	mol% O	mol% Si	mol% In	mol% Zn	$\frac{\text{Zn}}{(\text{In+Zn})}$
E	1.68 ± 0.01	97.45 ± 0.19	0.43 ± 0.05	0.43 ± 0.17	0.50 ± 0.09
F	6.63 ± 0.12	91.45 ± 0.16	0.94 ± 0.06	0.99 ± 0.11	0.51 ± 0.04
G	7.90 ± 0.22	89.73 ± 0.41	1.28 ± 0.08	1.09 ± 0.19	0.46 ± 0.03
H	4.98 ± 0.38	93.55 ± 0.41	0.70 ± 0.05	0.77 ± 0.03	0.53 ± 0.02

4.7 Optical Properties

The optical properties of the thin films were studied using spectrophotometry and ellipsometry. When obtaining the transmission spectra, only the thin films on glass substrates could be measured. Spectrophotometry is very quick and easy, and transmission spectra for all the thin films on glass were obtained including the two parallels of the In_2O_3-g-RTP thin film made in the specialization project [107]. For both methods a spectrum for the uncoated glass was obtained to correct the thin film transmission spectra by removing the contribution from the glass substrate. For spectrophotometry, optical transmission was obtained for the wavelengths 170 nm to 1100 nm. The ellipsometry is more complex, and a selection of thin films is characterized by this method. The ITO10%-3-g-RTP, ITO10%-3-Si-RTP, ITO15%-1-g-RTP, and IZO40%-2-Si-RTP thin films are defined as successful thin films and were analyzed to give representative results. Thin films IZO40%-1-g-RTP, ITO10%-3-Si-UVHT, and IZO40%-3-Si-UVHT have a deviating appearance, and are analyzed to see if they also have divergent optical properties. For ellipsometry, measurements were done at wavelengths 210 to 1700 nm. In addition to transmission spectra for the three thin films on glass substrates, thickness, roughness, refractive index and extinction coefficient of the thin films are direct results from the ellipsometry.

Even though ellipsometry measurements were done on the thin films mentioned above, it was not possible to model all the results in a satisfactory manner. For thin film IZO40%-2-Si-RTP it was not possible to make the model good enough, while for thin films ITO10%-3-Si-UVHT and IZO40%-3-Si-UVHT the measurements were not good enough to even make a model.

The transmission spectra for ellipsometry and spectrophotometry are plotted together in figures 4.54 to 4.59. Included are also the transmission spectra for the uncoated glass. The legends refer to thin film names and the spectra obtained through ellipsometry is marked with an (E) in the legend.

Small variations are seen between the different thin films with respect to absolute value and the shape of the transmission curves. However, it can be seen that a good accordance is found between the spectrophotometry and ellipsometry spectra verifying both the absolute value and the shape of the curves. All the thin films show a high optical transmission with an average of 88-97 % in the visible region. An exception is the ITO10%-3-g-RTP thin film that shows an average value of 86 % and 79 % for spectrophotometry and ellipsometry, respectively. The spectrum obtained from ellipsometry also diverges with respect to the shape of the curve. No distinct trend is found for the absolute transmission value depending on the different curing methods, compositions or solutions, but indications that a higher optical transmission in seen for the UV cured thin films is found. The difference in curve shape is more distinct between the different curing methods. As seen in Figure 4.59, the UV cured thin films obtain a more square shape while the UVHT cured thin films obtain a more round shape compared to the thermally cured thin films.

An absorption band edge is seen for the transmission spectra around 300 nm, giving low optical transmission in the UV region of the electromagnetic spectrum. The band gap, E_g, can be estimated from the transmission spectra via the absorption coefficient, α, as explained in the theory part “2.5.4 Ellipsometry”. The estimation of the band gap is found in Figure 4.60, and the values obtained are given in Table 4.7. The optical transmission remains high for all the transmission spectra, and is even increasing as the wavelengths move into the infrared region of the electromagnetic spectrum.

The refractive index, *n*, and the extinction coefficient, *k*, for the thin films measured by ellipsometry are presented in figures 4.61 to 4.64. These figures show how *n* and *k* varies with wavelength. The shapes of the curves for the ITO thin films look similar with a decrease in *n* and increase in *k* for large wavelengths. The *n* and *k* values for the IZO thin film seem to be more constant with wavelength, and only a slight decrease in *n* is seen for large wavelengths. Table 4.7 presents the average values of *n* and *k* in the visible region of the electromagnetic spectrum. It can be seen that the *n* values for the ITO thin films corresponds well with each other, while the *k* value of the ITO thin film on silicon substrate is lower. For the IZO thin film the *n* value is lower while the *k* value is higher compared to the ITO thin films.

Thickness and average roughness is also obtained through ellipsometry, and the values obtained are presented in Table 4.8 together with the mean square error of the calculated model. This number is explained in section “2.5.4 Ellipsometry” in the theory part.

A theoretical calculation of the thickness was also performed based on the weight and theoretical density of the thin films. The substrates had not been weighed in advance of the thin film deposition, so it had to be estimated. An average weight for the glass substrates was obtained by weighing eight similar uncoated glass substrates. The weight of the silicon substrates was determined theoretically based on the average thickness found in Table 3.4 in the experimental part and the theoretical density of silicon. The calculated values for the thin film thickness were not realistic or reliable, as both negative and positive thickness values of the same range were obtained. In addition a standard deviation much larger than the expected thickness was obtained. The substrates should have been weighted before deposition of the film, as too much uncertainty is introduced by estimating the substrate weight.

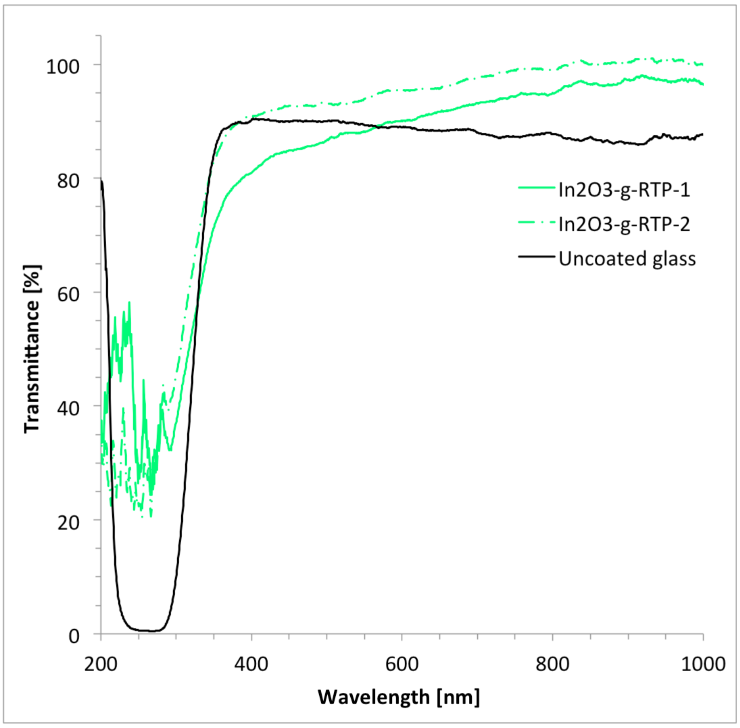

Figure 4.54: Optical transmittance for the two as prepared 3-layer In_2O_3 thin film parallels synthesized in the specialization project [107] plotted as a function of wavelength. The legends refer to thin film names. The transmission spectrum of uncoated glass is also included.

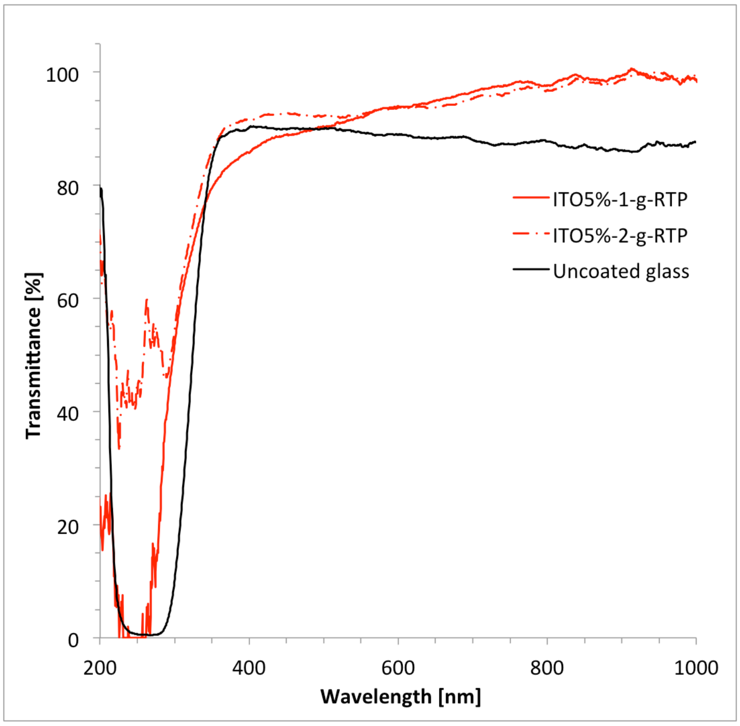

Figure 4.55: Optical transmittance for the as prepared 3-layer ITO5% thin films plotted as a function of wavelength. The legends refer to thin film names. The transmission spectrum of uncoated glass is also included.

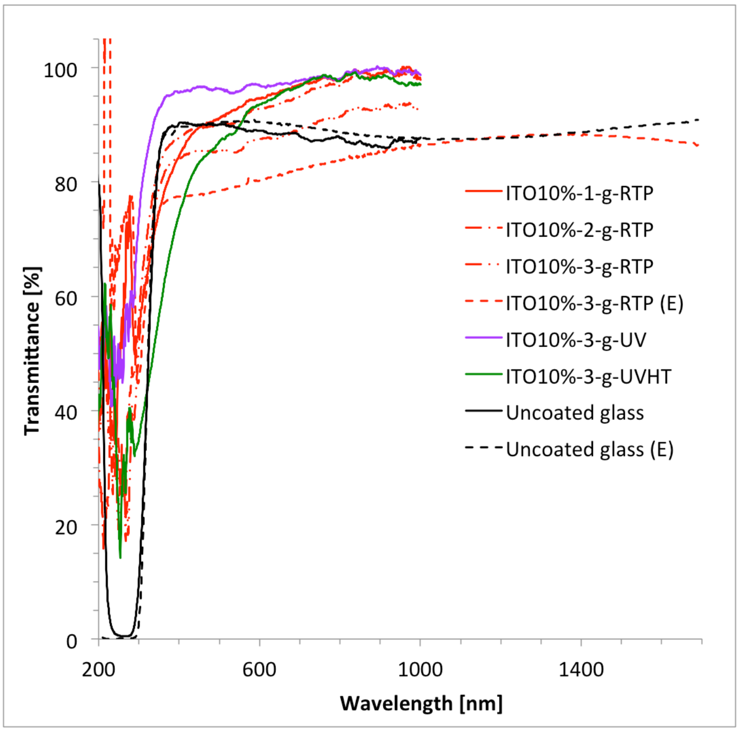

Figure 4.56: Optical transmittance for the as prepared 3-layer ITO10% thin films plotted as a function of wavelength. The legends refer to thin film names, and the transmission spectra obtained using ellipsometry is marked (E). The transmission spectra of uncoated glass are also included.

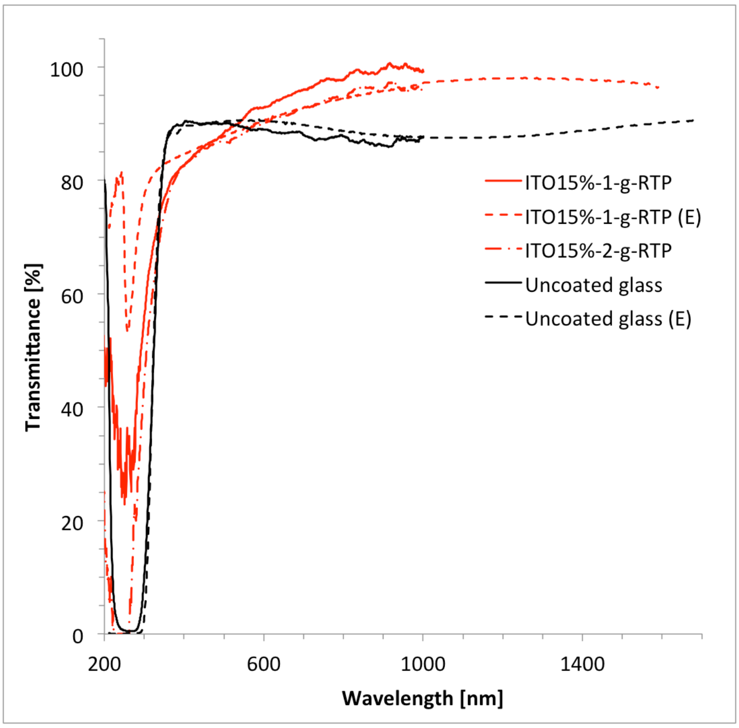

Figure 4.57: Optical transmittance for the as prepared 3-layer ITO15% thin films plotted as a function of wavelength. The legends refer to thin film names, and the transmission spectra obtained using ellipsometry is marked (E). The transmission spectra of uncoated glass are also included.

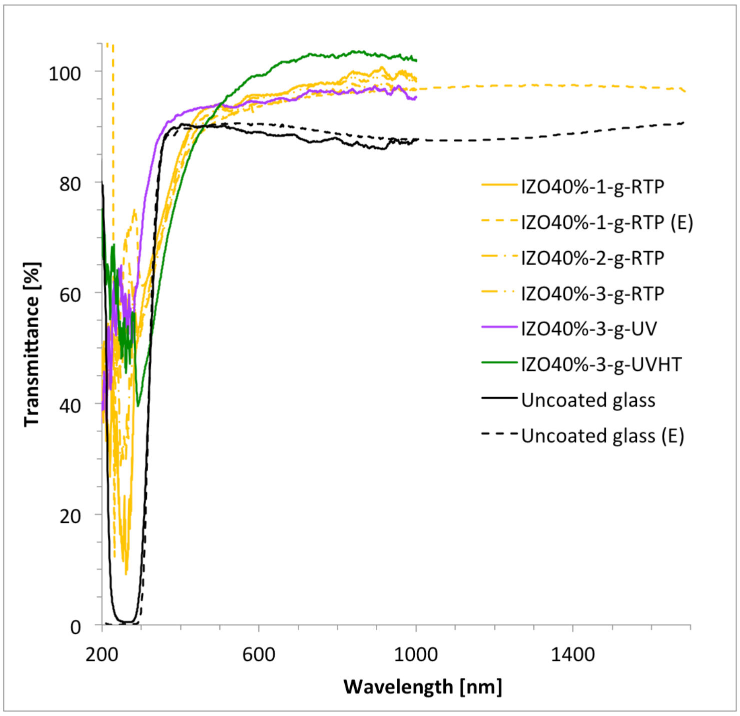

Figure 4.58: Optical transmittance for the as prepared 3-layer IZO40% thin films plotted as a function of wavelength. The legends refer to thin film names, and the transmission spectra obtained using ellipsometry is marked (E). The transmission spectra of uncoated glass are also included.

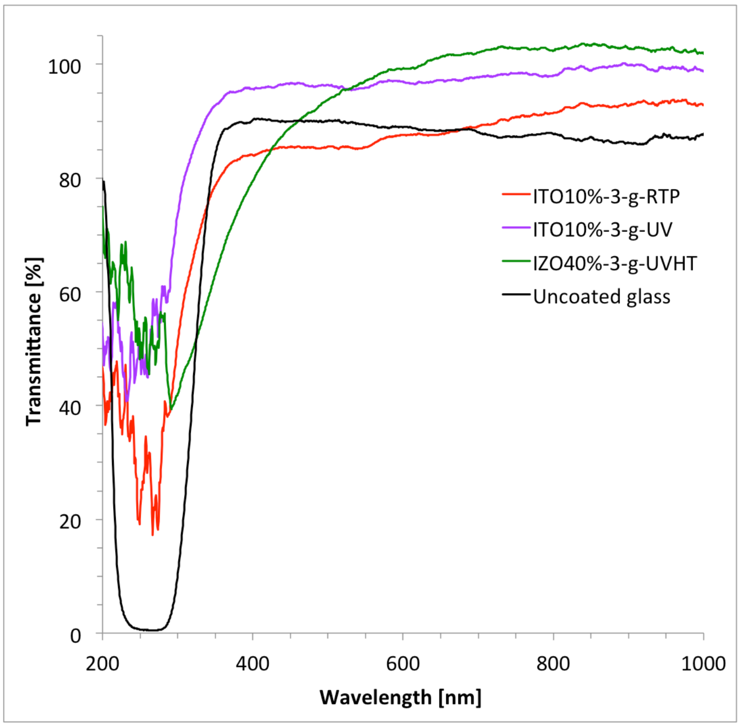

Figure 4.59: Optical transmittance plotted as a function of wavelength showing the different curve shapes for the three different curing methods. The legends refer to thin film names. The transmission spectrum of uncoated glass is also included.

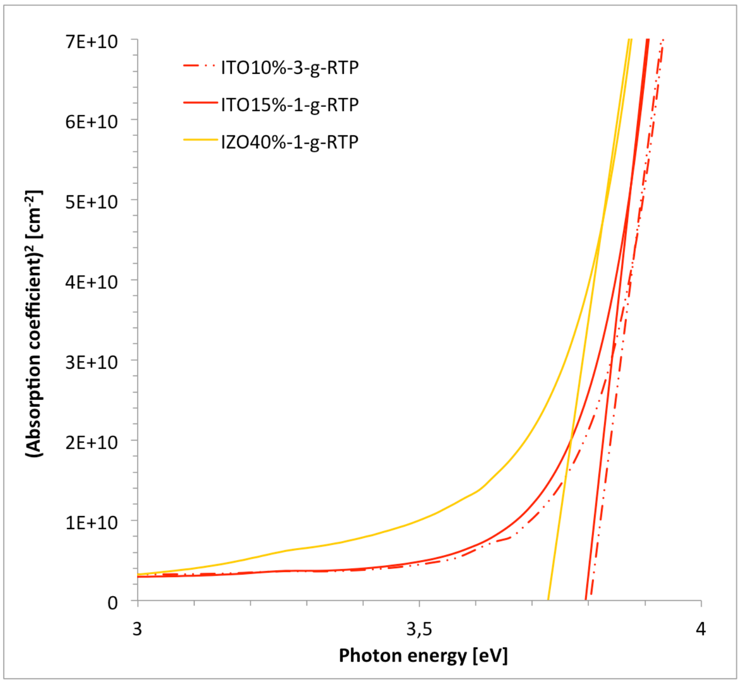

Figure 4.60: The absorption coefficient squared, α^2, plotted as a function of photon energy where the band gap, E_g, is determined by extrapolating the linear portion of α^2.

Table 4.7: Average values for the refractive index, *n*, and the extinction coefficient, *k*, in the visible region of the electromagnetic spectrum.

Thin film name	n	k	E_g [eV]
ITO10%-3-g-RTP	1.934	0.009	3.81 ± 0.01
ITO10%-3-Si-RTP	1.913	0.002	-
ITO15%-1-g-RTP	1.986	0.009	3.79 ± 0.01
IZO40%-1-g-RTP	1.857	0.012	3.73 ± 0.01

Table 4.8: Thin film thickness and average roughness, R_a, obtained from the ellipsometry measurements together with the mean square error of the calculated model.

Thin film name	Thickness [nm]	R_a [nm]	Mean-squared error
ITO10%-3-g-RTP	63.76	1.60	15
ITO10%-3-Si-RTP	60.58	0.40	21
ITO15%-1-g-RTP	52.74	2.86	11
IZO40%-1-g-RTP	48.50	0.50	10

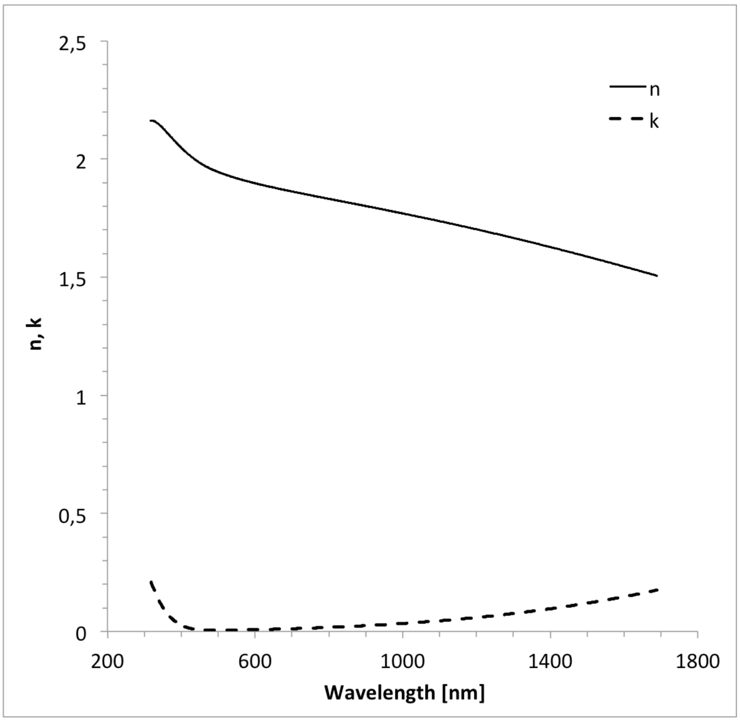

Figure 4.61: Refractive index, *n*, and extinction coefficient, *k*, for the ITO10%-3-g-RTP thin film plotted as a function of wavelength.

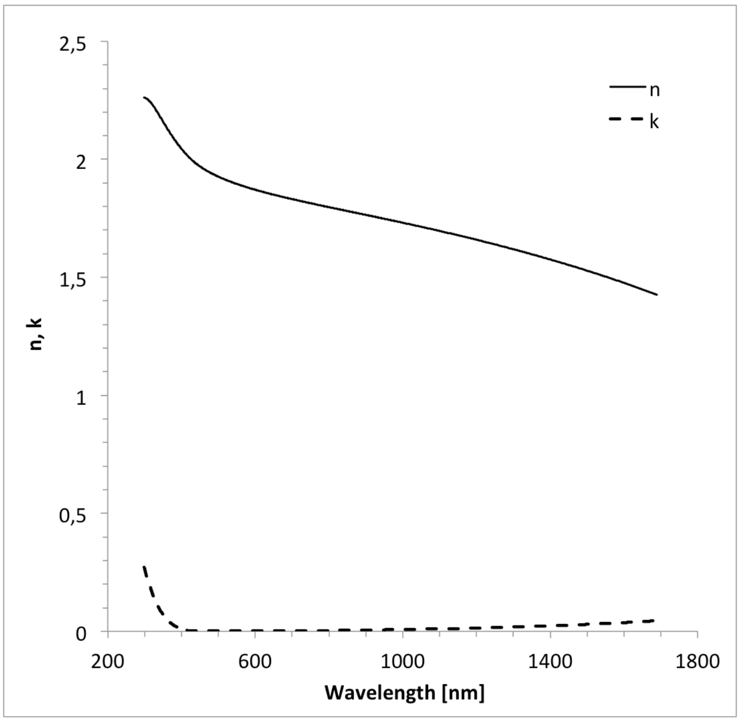

Figure 4.62: Refractive index, *n*, and extinction coefficient, *k*, for the ITO10%-3-Si-RTP thin film plotted as a function of wavelength.

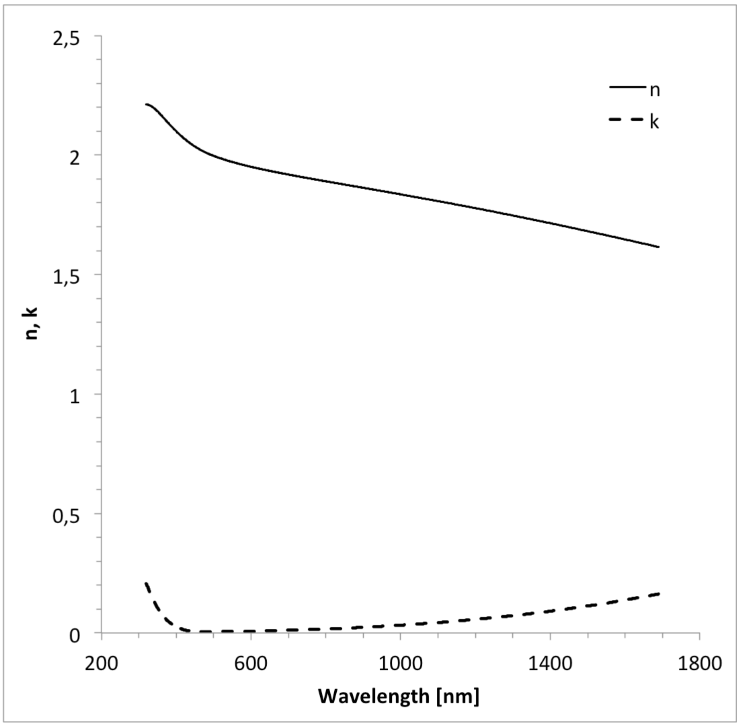

Figure 4.63 Refractive index, *n*, and extinction coefficient, *k*, for the ITO15%-1-g-RTP thin film plotted as a function of wavelength.

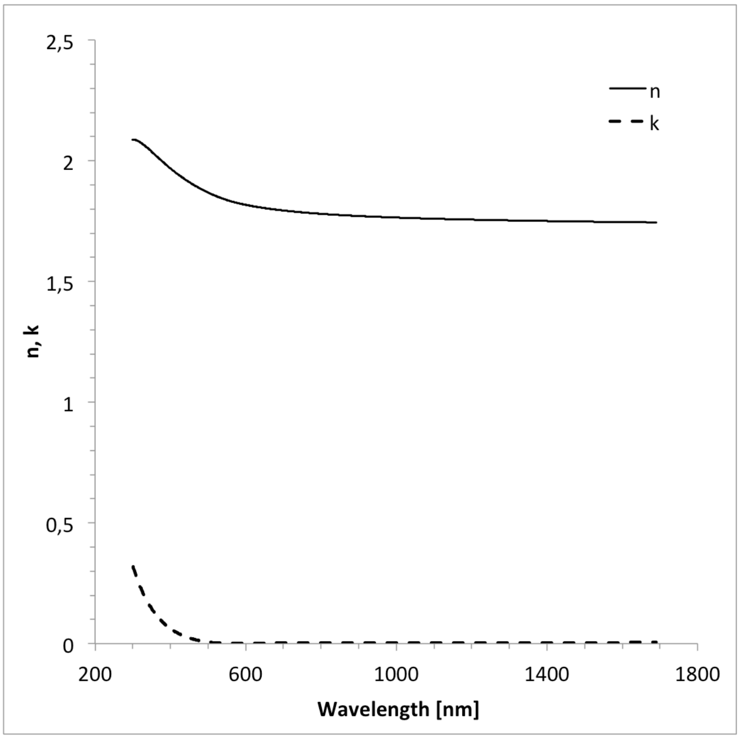

Figure 4.64: Refractive index, *n*, and extinction coefficient, *k*, for the IZO40%-1-g-RTP thin film plotted as a function of wavelength.

4.8 Electrical Resistivity

Electrical resistivity of the thin films is calculated based on the measurements from an in-house built van der Pauw apparatus and the thickness measurements from the ellipsometry. It was not possible to obtain measurements for the UV and UVHT cured thin films, thus only the resistivity of the thermally cured thin films is presented in figures 4.65 and 4.66.

Each thin film is measured two times, and if the deviation between the two runs is too high a third measurement is performed. The value that deviates most from the two others is discarded. The error bars in figures 4.65 and 4.66 reflect the deviation between the runs. Less than 16 % deviation is seen between the runs for Figure 4.65 and less than 24 % deviation between the runs for Figure 4.66. For the IZO40%-3-Si-RTP thin film, the readings varied so much that five runs was necessary to get a satisfying deviation between two runs. Thus, the error bars for this data point is misleading and the resistivity value is not to be trusted.

The thickness obtained for each of the ITO thin films found in Table 4.8 is used for the respective thin film when calculating the resistivity, while the average of the three values, 59 ± 6 nm, is used for the rest of the ITO thin films. This value is also used to recalculate the resistivity of the In_2O_3 thin film measured in the specialization project [107], giving a resistivity value of 1.4×10^{-2} Ω cm. The thickness found for the IZO40%-1-g-RTP thin film is used for all the IZO thin films.

In Figure 4.65 the electrical resistivity of the thermally cured ITO thin films for three different solutions and two different substrates is presented as a function of nominal doping level mol% Sn. The resistivity values re-plotted from the work of Frank and Köstlin [40] are not exact values, but are read off the graph for oxygen partial pressure of 10^{-2} bar. The literature values show the normal trend found for In_2O_3 doped with tin, which is a minimum resistivity value between 5 and 10 mol% Sn doping. An increase in resistivity is seen as the doping is increased above this optimal doping level. The original plot is found in Figure 2.13 section “2.2.2 Electrical Properties”.

It is clear that the resistivity of the In_2O_3 thin film is substantially lowered by tin doping as the resistivity is lowered from 1.4×10^{-2} Ω cm to 2.8×10^{-3} Ω cm and 2.2×10^{-3} Ω cm, which are the lowest resistivity values for the ITO thin films on glass and silicon substrates, respectively. The obtained resistivities have good accordance with the literature values found from Frank and Köstlin [40]. No coinciding trend with respect to resistivity as a function of doping level can be seen for the different datasets, and by only having three different concentrations of tin the foundation is not good enough to conclude on a trend or an optimal doping level for this synthesis. It is also hard to decide on which values that seems off.

The resistivities for the ITO thin films are in general found to be highly reproducibility. Some variation is seen between the resistivity for the different solution nr, and the variation is higher for the thin films on glass than for the thin films on silicon substrates. To quantify this, the standard deviation between the resistivity of the different solutions for each solution composition is calculated and the highest value for each substrate is presented. For glass the highest standard deviation between the different solutions is 9×10^{-4} Ω cm. For the thin films on silicon substrates the largest standard deviation is 9×10^{-5} Ω cm. The deviation between runs and the deviation between solutions introduces an uncertainty, which is higher than the change in resistivity with doping level making it unrealistic to predict a trend from these data.

A distinct difference in resistivity can be seen between the films deposited on glass and silicon substrates, as the thin films deposited on silicon lie in a lower value range.

In Figure 4.66 the resistivity for the IZO thin films deposited on two different substrates are plotted against solution nr. It is clear that doping In_2O_3 with zinc increases the resistivity. The resistivity of the pure In_2O_3 thin film is 1.4×10^{-2} Ω cm, while the lowest resistivity of the IZO thin films on glass and silicon substrate are 0.4 Ω cm and 0.1 Ω cm, respectively. An exception is the IZO40%-3-Si-RTP that has a resistivity of $1x10^{-3}$ Ω cm, but this value is as mentioned above not thought to be realistic.

A high reproducibility in resistivity values is seen for the IZO thin films on silicon substrates, while the reproducibility is low for the thin films on glass substrates. The variation in resistivity for the different solutions is quantified by calculating the standard deviation in resistivity for the different solutions for each substrate. For glass the standard deviation between the different solutions is 0.45 Ω cm, reflecting a large variation between the values. For silicon substrate the standard deviation is 0.006 Ω cm (if excluding the IZO40%-3-g-RTP thin film), indicating a good reproducibility. There seem to be a trend for the IZO thin films on glass substrate that the highest resistivity is found for the thin film made with solution nr 1 and that the resistivity decreases with higher solution nr.

Also for IZO thin films the resistivity is lower for the thin films on silicon substrate compared to the thin films on glass substrates.

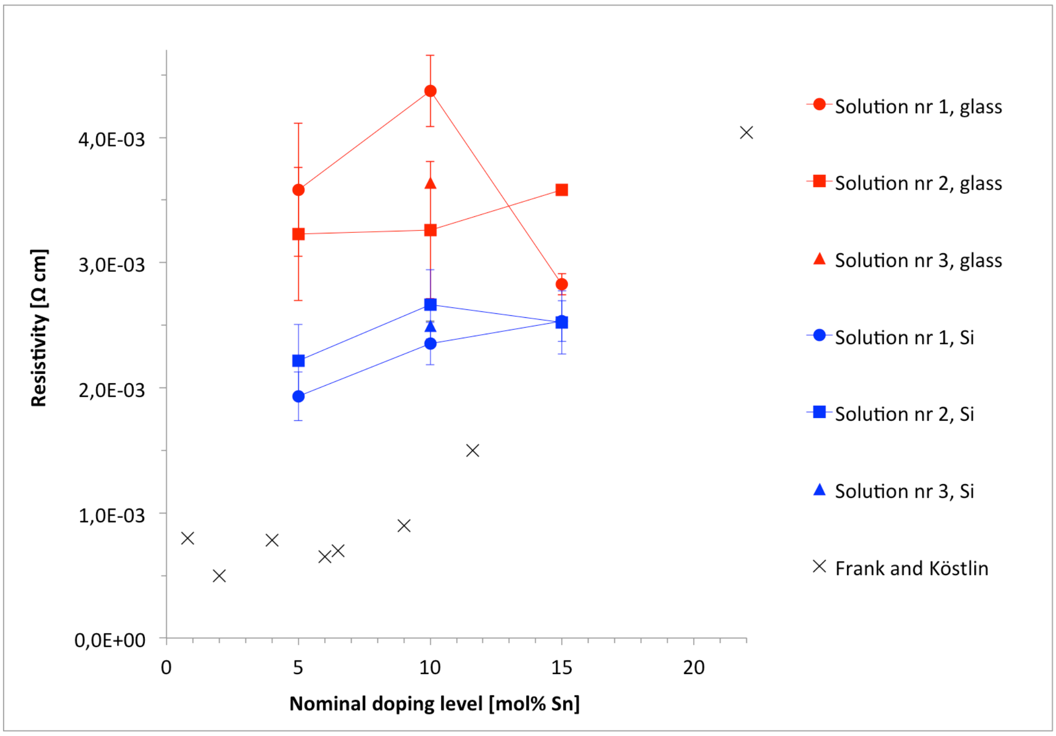

Figure 4.65: Resistivity for the thermally cured ITO thin films plotted as a function of nominal doping level mol% Sn. The legends refer to the solution nr and substrate for the thin film deposition. The bottom most legend refers to literature values re-plotted from the work by Frank and Köstlin [40].

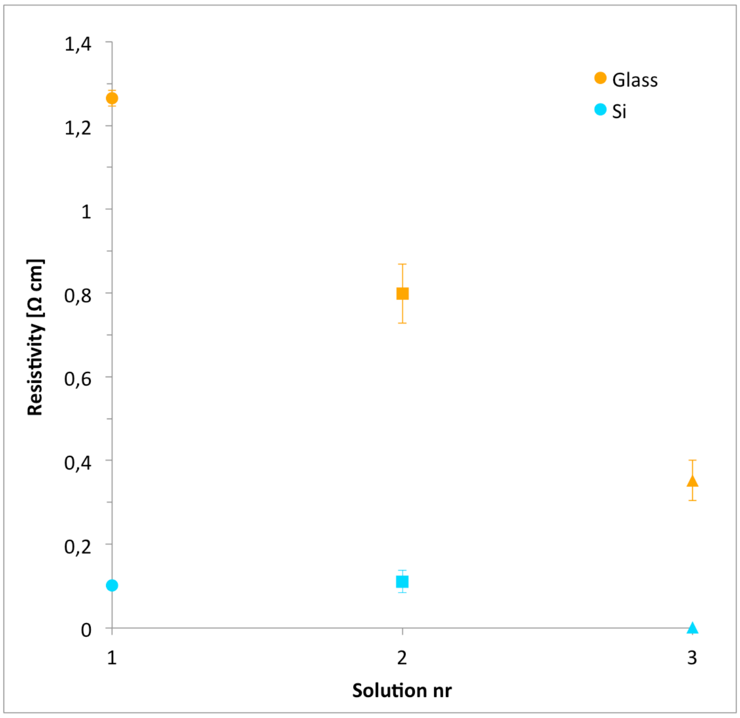

Figure 4.66: Resistivity for the thermally cured IZO thin films plotted as a function of solution nr. The legends refer to the substrate utilized for the thin film deposition.

5. Discussion

5.1 Precipitation During Synthesis and Quality of Precursor

Several others have utilized the modified aqueous Pechini method used in this thesis, and it is not the first time precipitation of SnO_2 has been observed in the ITO solutions [16, 84, 85]. Based on the study presented in "Appendix C Study of Precipitation and Precursor Quality" a few explanations to the formation of tin oxide are proposed. The indium nitrate standardized solution was found to be strongly acidic, and as tin oxide is only soluble in basic solutions it will precipitate out as tin oxide. Thus, it is possible that only a small amount of tin is soluble in the solutions and that the amount tin put in is irrelevant as long as it exceeds the solubility limit. Tin oxide may also form prior to synthesis in the precursor box or during the synthesis due to oxidation of the precursor itself as a result of contact with air. The synthesis is performed at ambient conditions.

It was shown by Otter [84] that a higher content of organics could prevent tin from precipitating out. This might indicate that the complexing properties of acetic acid are too weak. Acetic acid has only one carboxyl group, and normally a bi- or tridendate organic chelating agent as citric acid is utilized for obtaining satisfying complexing. In this experiment a 1.5 fold amount of organics was used compared to the number of moles cations, while Otter [84] concluded that a 20 fold amount of organics was necessary to avoid precipitation. Based on this it was proposed that a higher concentration of organics could delay or even prevent precipitation of tin oxide. It was also tried to switch complexing agent to citric acid, but a 20 fold amount of organics was still needed. Thus, for this synthesis citric acid is not a better complexing agent than acetic acid. The need for the large amount of organics could be due to the low pH of the indium nitrate standardized solution, which is thought to lower the solubility limit of tin in the solution.

If the tin concentration is lowered in the films due to the precipitate, the theoretical content will not conform to the experimental causing reproducibility issues. Thus, it is not recommended to use solutions where precipitation has occurred.

No conclusions could be made with regards to the present quality of the old precursor, but the extra diffraction lines found for the old precursor could indicate deterioration compared to the new precursor. Using a new box did not have any effect on the amount of precipitation, thus the hypothesis that the precursor oxidize extensively with time can be falsified.

5.2 Auger Electron Spectroscopy

Figure 4.1 shows that the amount of tin in the thin films increases with increasing nominal doping level. Through the elemental analysis it is found that the thin films contain a substantially lower level of tin doping than the nominal doping level. The actual doping level of tin in the thin films is 30-40 % of the nominal doping level. This makes it clear that the precipitation has a large impact on the stoichiometry of the films. The organics in the synthesis are added in a ratio that is dependent on the cation concentration. Since the sum of indium and tin cations is constant, the amount of organics is the same for the different solutions. Hence, the only difference between the solutions is that a lower amount of indium nitrate standardized solution is added for the higher nominal doping levels. This indicates that less standardized solution gives a higher solubility of tin. There could be a limited number of mole cations that is soluble in the solutions dictated by the amount of organics. Thus, if less indium cations are present a higher number of tin cations can be complexed. Another possible impact could be that a higher pH is obtained when less indium nitrate standardized solution is added, causing a higher concentration of tin to be soluble.

From the spectra it is found that the main part of the tin peak is separate from the indium peak, but some overlap of the peak areas is seen. A reference sample of known composition was also studied, giving convincing results that the main part of the tin peak can be distinguished. Even though the overlapping areas make the quantification more difficult, it is possible to calculate the contents of tin and indium separately. This is because the quantification is based on the peak height after differentiation of the spectrum. The peak height is dependent on the peak shape rater than relying on the area, thus the problem with the overlapping areas is avoided and the measurements can be trusted to reflect the actual content of tin in the thin films

A very mild sputtering that should take off less than 1 nm of the top surface was used to remove carbon on the thin film surface. Instead of obtaining better results for the sputtered thin films a decrease in the oxygen and tin content is seen, indicating that the thin films are sensitive to sputtering. The decrease in oxygen and tin could mean that these elements gather on the surface to a higher extent than indium, creating a non-stoichiometric layer. The different oxidation states that this would have caused could have been detected by X-ray photoelectron spectroscopy. When using sol-gel methods the different elements should be evenly distributed throughout the film, but there is always a chance that the surface layer is different from the bulk. The oxygen is lowered the same amount for all the films, while the lowering of the tin varies. Oxygen atoms could be associated with the carbon on the surface, thus removing the carbon would cause removal of oxygen. As the amount of carbon is constant for the different films, this could explain the constant lowering of the oxygen. A variation in the enrichment of tin on the surface between films could explain the difference in tin removal, but why a difference in enrichment between the films should occur is hard to explain. Auger electron spectroscopy measurements were only obtained for three samples because of a limited time frame. Both the effect of precipitation on the level of tin doping and the effect of sputtering should be studied in the continuation of this work, as there is not obtained enough data here to conclude on any trends with regards to these results.

In summary Auger electron spectroscopy shows that the content of tin in the thin films increases with increasing nominal composition, which indicates that less indium nitrate standardized solution added gives a higher solubility of tin. It is found that the thin films contain a substantially lower level of tin than the nominal doping level, making it clear that the precipitation has a large impact on the stoichiometry of the films. The thin films seem to be sensitive to sputtering, indicating a slight enrichment of tin at the surface.

5.3 Crystal Structure

It is apparent that the temperature of the thermal curing is above the crystallization temperature, as the thin films become crystalline. This is not the case for the UV and UVHT curing, which gives amorphous thin films.

Both the ITO and IZO thin films are found to obtain the cubic bixbyite structure of pure In_2O_3. It can be seen from figures 4.2 and 4.3 that the diffractograms fit well to the reference pattern of the In_2O_3 structure both with respect to the position, intensity, and shape of the peaks. The stable solid solubility of tin in In_2O_3 is only around 2 mol% [37], thus the thin films obtain a metastable solid solution. It has been found that a tin content as high as 20 mol% can be doped into In_2O_3 while still obtaining the bixbyite structure [34-36]. In the In_2O_3-ZnO phase diagram a number of homologous phases are found to appear when doping In_2O_3 with different amounts of zinc [38]. No stable solid solubility of zinc in In_2O_3 is seen, so also zinc obtains a metastable solid solution in In_2O_3. It is proposed that the limited solubility of zinc in In_2O_3 is due to the tetrahedral coordination favored by zinc, which is not readily available when zinc substitutes for indium to form a bixbyite solid solution. In literature a structure evolution with increasing zinc content from the bixbyite structure of In_2O_3 to the wurtzite structure of ZnO via intermediate homologous phases are found for In_2O_3 thin films doped with zinc [4, 28, 30, 31]. In addition, all literature sources found claim to have a directional growth independent of the deposition method. Even IZO films made using wet chemical methods are found to be directional. But, if one takes a closer look at the diffractogram in Figure 2.4 in the theory part section "2.1 Crystal Structure" it can be questioned if the thin films containing 20 and 33 mol% zinc can be called directional. My opinion is that they are not. By looking at the reference pattern of In_2O_3 in Figure 4.3 it can be seen that the diffraction lines that are considered to obtain the highest intensity for the In_2O_3 structure is clearly obtained in the 20 mol% Zn film. Weak diffraction lines can also be seen for the 33 mol% Zn film. Instead of having directional thin films, the lack of clear diffraction lines are caused by poor data giving a high noise to signal ratio in the diffractograms. Thus, it is thought that the results obtained in Figure 2.4 are similar to the results obtained in this thesis. To the best knowledge of the author, it is not known of any literature where such a high doping concentration of zinc has been doped into In_2O_3 while still retaining the pure bixbyite structure. Only the reference patterns of pure In_2O_3 and ZnO are included in Figure 4.3, but also the homologous phases are checked and excluded. If any secondary phases are present in these films the content must be very low, since no secondary phases can be spotted in the diffractogram. As discussed in the theory section "2.5.1 Gracing Incident X-ray Diffraction" the gracing incidence set-up is better for detecting small contents of other phases and contaminations than the conventional X-ray diffraction set-up. There could also be amorphous phases present, but if present the content must be low as the baseline of the thin films on silicon substrates are very flat and nice.

Variations in intensity are seen between the different diffractograms found in “Appendix D Pawley Refinement”, but they all show the same diffraction lines. There are no trends found with regards to the different compositions or solutions.

5.4 Lattice Parameter

In general, lattice parameter values that are off could be caused by poor data. Pawley refinement is based on X-ray diffractograms, and a poor diffractogram (high noise to signal ratio, incorrect peak shape, shift in the positions of the diffraction lines) can give lattice parameter values that are off. A poor diffractogram can be caused by bad sample preparation both with respect to height and position relative to the sample holder and inaccurate set-up of the instrument. The Pawley refinement is mainly based on the positions of the diffraction lines. For the gracing incidence X-ray diffraction set-up these are very stable between runs, as the diffraction lines are not easily shifted due to bad sample preparation or instrumental effects.

The ITO thin films on glass fits better with the reference values. As the reference values are for ITO thin films deposited by spray pyrolysis on glass, this is logic. The reference value given for In_2O_3 is based on the theoretical value found for a perfect unit cell of pure In_2O_3 [25, 42]. It was obtained by Sunde et al. [16] that the lattice parameter of ITO for a thin film is higher than that for powder and it was thought to be mainly because of strain in the lattice introduced by strain between the substrate and thin film. An increase from 10.130 Å to 10.153 Å was seen for powder and thin film, respectively. The increase in lattice parameter is on the same order as the increase seen between the reference value and the measured value for the In_2O_3 thin film in Figure 4.4. Sunde et al. obtained a lattice parameter for the pure In_2O_3 powder of 10.121 Å. The lattice parameter for the ITO thin film found by Sunde et al. is higher than the lattice parameter observed in this thesis. This is most likely due to a lower actual doping level in our films causing less stain in the lattice. The lattice parameter of the ITO thin films is generally higher than for the IZO films. To the best knowledge of the author there are not any literature that gives the lattice parameter of IZO with the cubic bixbyite structure. Several articles are found regarding the lattice parameter of IZO thin films obtaining the hexagonal structure of ZnO [38, 44]. The reason for the lack of lattice parameter values could be that all literature found show directional growth. At least for Pawley refinement, as many diffraction lines as possible should be present in the diffractogram to estimate a good approximation for the lattice parameter. Despite this, several factors makes it possible to predict that a contraction should be seen. Based only on the ionic radius a contraction of the In_2O_3 lattice is expected as the Zn^{2+} has a lower radius than In^{3+}. The Sn^{4+} ion is also smaller than the In^{3+}, but the expansion seen when doping with tin is caused by the high effective charge of Sn^{4+} that gives repulsion when a certain amount of In^{3+} is substituted by Sn^{4+}. No such repulsion (rather the opposite) should be seen when In^{3+} is replaced with Zn^{2+}, as the effective charge of Zn^{2+} is lower than for In^{3+}. In literature it is found that as the concentration of zinc increases the main diffraction line of the cubic In_2O_3 structure moves to higher 2θ indicating a decrease in the lattice parameter [28].

The lattice parameters for both IZO and ITO show good reproducibility. But, the variation seen is enough to introduce a large uncertainty in the trend with doping level seen for ITO. This is because the increase with doping level is found to be at the same order as the deviations between solutions. The same trend for the lattice parameter with the different solutions is seen for both substrates for the IZO thin films, which is surprising. Even though it was tried to execute all the process steps for making the thin films according to an identical protocol, the steps are most likely not performed in an identical manner. It is likely that the age of the sol could differ (maximum 2-3 hours). There are also small differences in the weight for the precursors and organics added in the synthesis as can be seen from "Appendix A Preparation of Solutions". It is also likely that the amount of deionized water and polyvinyl alcohol is not the exact same amount. Both the sol age and the concentration of the different species in the solutions can affect the viscosity of the sol and further affect the thickness of the spin coated films. Small variations in the pre-curing time at the hot plate and in the amount solution deposited for spin coating are likely. But, based on that the same trend is seen for both substrates the two last suggestions can be excluded as these varies individually for the thin films. Also, the pre-curing time does not matter as the thermally curing give crystalline films (complete decomposition of solvents and organics) and the amount of solution deposited does not affect the thickness as long as an excess amount is applied. Differences in thickness and stoichiometry are thought to be the most likely explanations for the trend. Both parameters substantially affects the crystal structure, hence also the lattice parameter. Measuring thickness, conductivity, and doping level might give more indications to what induces the trend. A limited number of thickness measurements, and conductivity measurements are found further down in the results part. For the resistivity values found in Figure 4.66 the same trend is seen for the thin films on silicon substrate, while for the thin films on glass substrate the value for solution nr 1 does not fit with the trend. Still, this could indicate that the trend for the lattice parameter is caused by a difference in resistivity, which is highly affected by the doping concentration. This could have been clarified by measuring the doping level and thickness of the different films. It would also have been interesting to obtain the crystallite size for the different films, which could have been done by using transmission electron microscopy. From these images it would also have been possible to see each layer of the thin film, which could have been useful for studying differences between the films.

A clear dependence of lattice parameter on the substrate is seen for both IZO and ITO. This is most likely due to the different structure of the substrates, as glass is amorphous while silicon is crystalline. It can be seen that the ITO and IZO lattice parameter for films deposited on silicon substrates are of similar values, this indicates that the silicon substrate to a degree dictates the obtained lattice parameter. The silicon substrate is single crystalline and exhibits a face-centered cubic structure known as the diamond lattice. Crystalline silicon has a lattice parameter of 5.43 Å [108]. By multiplying this value by two we get 10.862 Å. So even though the obtained lattice is far from the lattice parameter of silicon, the silicon substrate seems to manipulate the thin films into having a lattice parameter of about 10.1 Å. It could also be seen from the diffractogram that a higher crystallinity of the films was obtained for the thin films deposited onto silicon substrates compared to the films on glass. The degree of crystallinity will also affect the lattice parameter.

5.5 Morphology

The discussion for the different sections in the result part “4.5 Morphology” are gathered into one because it is good to use these methods as a complement to each other when studying the trends of morphology. By studying the samples with the naked eye, the thin films that are non-homogenous due to problems with the thin film deposition can be spotted. For the optical light microscopy and SEM inhomogeneity associated with morphology at the micro- and nanometer scale can be detected. Using a profilometer and AFM information about the roughness and topography of the thin films can be obtained. An example is the UV cured IZO thin film. By studying the film using SEM it looks homogenous at the nanometer scale, but already with the eye it can be seen that this film is not homogeneously distributed across the substrate. The problem with SEM is that only a small region is studied at the time, and the thin film can look homogenous in one spot without being homogenous with respect to a larger area. Sometimes it is also experienced that a film, which looks inhomogeneous at low magnification in the optical light microscopy actually is homogenous when studied at low magnifications in the SEM. It is experienced that the light can induce what looks like flaws on the sample surface that are not actually there. This is thought to be the case for the thin film shown in Figure 4.17 as explained in “Appendix E Morphology”.

From Figure 4.6 in the results part it can be seen that the thermally and UV cured thin films appear transparent for the naked eye, hence no parts of the visible region is absorbed by the film. The slightly yellow color of the UVHT cured films therefore indicates that these films partially absorb the short wavelength region of visible light. The thermally cured thin films have a black contour around the edges, and for the IZO thin films seen in Figure 4.7 this extends inwards from the edges showing what looks like a typical spin coating pattern. The pattern is especially clear for thin film c). It is assumed that a thicker outer region is found around a thinner homogenous central area. Due to the thicker film around the edges it is likely that the thin films are only partly cured between each deposition, giving these areas a black color. The effect is only seen for the IZO thin films, and could be explained by the higher cation concentration in the IZO solutions as precipitation is avoided. A higher cation concentration can raise the viscosity of the solution giving thicker spin coated films. As the thin films are polycrystalline, they are transparent because they are very thin. In a polycrystalline film, several crystal grains of different orientation will lie on top of each other. If enough such crystals are placed on top of each other the light will not be able to pass through the film making it non-transparent. This is not likely to be the reason here, as only three layers are deposited. When the thin films are deposited on silicon substrates small differences in film thickness give variation in color (interference effect) revealing the spin coating pattern. Most of the thin films show the same spin coating pattern as in Figure 4.7. The defects in the homogenous regions that appear as light spots in figures 4.8 and 4.11 have the same color as the substrate and could be holes in the films. These defects were not investigated further, but could be caused by air bubbles made by the syringe filter during deposition of the solution. This was avoided to the best extent, but it can have been overlooked for these two thin films. Spin coating seemed to give a homogenous central region with respect to both thickness and morphology for most of the thin films, but the solutions showed better wetting of the glass substrates than the silicon substrates. This was not a problem for the thermally cured thin films, except for IZO40%-3-Si-RTP seen in Figure 4.11. For the UV and UVHT cured thin films the first deposited layer looked good with a homogenous central region, while the deposition of the second and third layers were problematic giving non-homogenous films. This is most likely due to an incomplete decomposition of the organics in the thin films between depositions. An exception is the ITO10%-3-Si-UVHT thin film, which retained its spin coating pattern throughout the deposition procedure.

When comparing the thin films cured using different methods by looking at the SEM images in figures 4.29 to 4.40, the thermally treated films in general looks homogenous even at nanoscale except for the thin film in Figure 4.30 were there seems to be some particle shaped features of varying size on the surface. This agrees with the observations from the appearance study and the optical light microscopy. By comparing the SEM images obtained for the thermally cured films with literature, the thin films are found to look similar to the sol-gel derived ITO thin films obtained by Sunde et al. [16]. Also the IZO thin films prepared using pulsed laser deposition by Naghavi et al. [62] showed an equivalent morphology. When the UV cured thin films are studied at nanometer scale (figures 4.32 to 4.35) the IZO films look homogenous while there seem to be circular indentations in the surface of the ITO films. No clear effect of the substrate is seen. From appearance studies and the optical light microscopy, the thin films looks homogenous on glass substrates and non-homogenous on silicon substrates. Considering the AFM images of IZO40%-1-g-RTP and ITO10%-3-Si-UV in Figure 4.45 and 4.46 respectively, it could look as if an overweight of "hills" are present on the IZO40%-1-g-RTP surface while an overweight of "valleys" are seen for the ITO10%-3-Si-UV surface. This could indicate that particles are present on the IZO40%-1-g-RTP thin film, while indentations are seen in the ITO10%-3-Si-UV thin film. But as "hills and valleys" appearance are found in both images, it is impossible to determine if particles/indentations are actually present. For the ITO10%-3-Si-UV thin film a scan of a smaller area of 1×1 μm^2 was obtained in addition to the standard area of 31×31 μm^2. This was mainly done to see if a smaller scan-area could give a higher degree of clarity with regards to the possible indentations in the surface. The small scan area did not give any new information on the topography as it only shows a lower roughness, and the AFM image of the standard scan area seen in Figure 4.46 was used to compare with the other samples. For all the UVHT cured films the optical light microscopy and the SEM images indicate non-homogenous films. For the IZO40%-3-Si-UVHT thin films this can even be spotted with the naked eye. The AFM is able to detect the features seen in the SEM images in Figure 4.37 for the ITO10%-3-Si-UVHT thin films. Based on the AFM images in Figure 4.47 it can be determined that the features seen in the SEM are actually ridges on the surface. When looking at the surface from above dark holes are seen close to the white features at several places. These might be indentations in the thin film, but they could also be due to the tip being unable to reach the actual surface near the elevated features. For IZO40%-3-Si-UVHT the profilometer scan seen in Figure 4.44 is thought to reproduce the profile of the features seen in the SEM image in Figure 4.39. The features are found to be in the 100 μm scale for both the profilometer scan and the SEM image. These features are not detected with the AFM. The AFM images in Figure 4.47 show a lower roughness for the IZO40%-3-Si-UVHT thin film than the ITO10%-3-Si-UVHT thin film. Both from SEM images and the profilometer it is found that this is not likely to be the case. It is concluded that the AFM is not suitable to study the topography of the IZO40%-3-Si-UVHT thin film because the surface features are too large.

The profilometer scan for thin film ITO15%-1-g-RTP is given in Figure 4.41. From this figure it looks as if the thin film has a steep increase in film thickness with scan length. This increase in not thought to be realistic, but thought to be an instrumental effect. Scans supporting this statement together with argumentation for why this is so, is found in "Appendix F Profilometer Instrumental Effect". Based on the appendix, it is expected that long scan times (longer than 6 minutes) are needed to get a realistic scan profile for the ITO15%-1-g-RTP thin film. It was not prioritized to use extended amount of time on this, and the 30 seconds scans are used to calculate the roughness parameters. The roughness parameter values for the short scan are found to be within 70 % of the longer scan values of 6 minutes, which is thought to be okay as variations of the same order are seen between the three scans of the short scan time. The scan profiles found in figures 4.42 and 4.43 for the IZO40%-1-g-RTP and ITO10%-3-Si-UVHT thin films respectively are thought to reflect the actual profile of the thin films. From the profilometer scans no height changes that match the surface features seen in the SEM images of these thin films in figures 4.30 and 4.37, respectively can be found. For the profilometer the resolution in the vertical direction is in Å, while the resolution in the horizontal direction is in µm. By considering this and the size of the features, which are of nanometer scale, it is not strange that these features are not possible to detect by the profilometer. The instrumental effect seen for the profilometer only showed up for the thin films on glass substrates, and the profilometer did not have any trouble with reproducing the profiles of the thin films on silicon substrates. Two possible explanations are suggested for why this is. First, the thin films on glass were thermally cured while the thin films on silicon substrate were UVHT cured. A higher roughness that is easier to detect for the profilometer is present for the UVHT cured thin films. Another reason could be that the profilometer stylus tip interacts better with the thin films on silicon substrate, due to the conductive properties of silicon compared to the non-conductive glass substrate. It is difficult to quantify the roughness of the thin films by only studying the profilometer scans. A better indication of the roughness is found by looking at the roughness parameters listed in Table 4.3. A distinction in roughness parameter values can be seen between the thermally cured and the UVHT cured thin films. The thermally cured thin films show substantially lower R_a, R_q and R_p values than the UVHT cured thin films. Based on the SEM images in figures 4.29, 4.30, 4.37, and 4.39 this seems realistic, as the thermally cured thin films look more flat and homogenous than the UVHT cured thin films. This is also in good accordance with the AFM results in Figure 4.45 and 4.47. The thermally cured thin films show similar R_a and R_q values, as do the UVHT cured thin films. For the thermally cured thin films the R_p values are also in the same range, whereas for the UVHT cured thin films the R_p values are different. It is likely that the R_p values differ substantially across the UVHT cured thin films, as the surface features seen in the SEM images in Figure 4.37 and 4.39 most likely vary in size and shape. Therefore the R_p value for the UVHT cured thin films in Table 4.3 might not be representative for the entire thin film.

From figures 4.8 to 4.11 a distinction in color can be seen between the thermally cured ITO and IZO thin films on silicon substrates. The ITO thin films attain a more orange color than IZO thin films, which attains a yellow tone. As no color difference is seen between the thermally cured ITO and IZO thin films on glass substrates in figures 4.6 and 4.7, the color difference is most likely due to a difference in thickness.

Small variations in color can be seen between the thin films of different solutions, and this could also be due to small variations in film thickness. Based on the optical light microscopy images the IZO40%-1-g-RTP thin film was thought to look the same as ITO15%-1-g-RTP. From the SEM images in figure 4.29 and 4.30 it is clear that these thin films do not look the same. It can be seen from the profilometer in Table 4.3 that slightly higher R_a and R_q values are seen for the IZO thin films compared to the ITO thin films. This is also in accordance to the AFM images in Figure 4.45. By studying the thin films in the optical light microscope ITO10%-3-g-UV and IZO40%-3-g-UV was thought to look the same as ITO15%-1-g-RTP. By comparing the SEM images in figures 4.29, 4.32 and 4.34 it is seen that this is not the case. The UV cured ITO and IZO thin films look similar to each other in the optical light microscope for both substrates, but by studying the films in the SEM it is found that the they obtain a different morphology. In the optical light microscope the microstructure of the two films ITO10%-3-g-UVHT and IZO40%-3-g-UVHT in figures 4.19 and 4.20, respectively looks approximately the same, but from the SEM images the morphology is found to be rather different. However, there is accordance between the SEM and optical light microscopy findings that the features on the ITO thin film is smaller than the features on the IZO thin film. The only case where the ITO and IZO thin films look similar based on the SEM images is for the thermally cured films on silicon substrate. For the lattice parameter it was seen that the ITO and IZO crystalline films on silicon substrate had the same lattice parameter, whereas for the films on glass substrates a distinct difference was seen. These results are in accordance with morphology, indicating that the silicon substrate impacts both the lattice parameter and the morphology. The morphology of the thermally cured ITO films is not altered with substrate, whereas the morphology for IZO is altered with substrate. For the UV curing only a small difference is seen between the ITO thin films on different substrates and no difference is seen for the IZO thin films. The UVHT curing gives different morphology for all the thin films made. Thus for both the UV and UVHT curing, more thin films should be made to see if the morphologies obtained are representative.

It is proposed to use the SEM, profilometer and AFM to complement each other when determining on the relative surface roughness of the different thin films. Based on this it can be determined that an increase in roughness for the different curing methods in the order thermal curing < UV curing < UVHT curing is seen. It is also found that the IZO thin films are rougher than the ITO thin films. The effect of substrate on the roughness was not studied. In sum it is found that curing method, composition and substrate affects the morphology of the thin films. The morphology of the thermally cured thin films is most homogenous, while the UVHT cured films are the least homogenous. Too few thin films are studied to conclude on how composition and substrate affects the morphology.

It is not strange that the morphology of the thin films changes with curing method, as the mechanisms of thermal and UV curing is quite different. In the UV curing high energy radiation is used to break the chemical bonds, whereas for thermal curing it is the increased vibration of the atoms that causes bond cleavage when the temperature gets high enough. For the UVHT curing method, a combination of these to mechanisms will be present. The effect of these different curing methods are also seen from the diffraction spectra as the thermally cured films obtain a crystalline structure while the UV and UVHT cured thin films obtain an amorphous structure. The curing methods are also found to affect the wetting substantially, where poor wetting give less homogenous films.

Difference in composition (doping level and doping specie) is seen to affect the lattice parameter and is also likely to affect the morphology. The composition will affect the stoichiometry and structure in the films, which again affects morphology. Compositional differences can also affect the thickness the thin film.

The substrate affect the morphology in some cases, and it is the difference in structure between the two substrates that is most likely to cause the effect. It was found that changing the substrate altered the lattice parameter of the crystal structure, and different wetting of the different substrates is also observed.

5.6 Energy Dispersive X-ray Spectroscopy

Even though no variation in composition is seen between the different regions for any of the thin films, this might not be the real case. From the elemental analysis it can be seen that the signal from the substrate is very high compared to the signal from the thin films. This is due to the emission depth of the EDS signal, which was introduced in the theory part section “2.5.2 Scanning Electron Microscopy”. For the IZO40%-1-g-RTP and the ITO10%-3-Si-UV thin films the features on the surface are very small and possibly even overlapping. For IZO40%-1-g-RTP there seems to be small white particles everywhere, only some is bigger than others. The same seems to apply for the dark holes seen in the ITO10%-3-Si-UV thin film. Conclusively it is difficult to see if there actually is a homogenous matrix area between the features. Because the different regions where EDS is obtained from are so small the signal might be emitted from an area that is larger than the feature. Even though the EDS spectra are taken at what seems to be different areas, the areas might get smeared into each other due to the small size of the features and because EDS is not a surface sensitive technique. The resulting elemental analysis will then not show a variation in composition between the different regions, even though there might be a compositional variation present. Hence a variation in composition between the different regions cannot be excluded. For the IZO40%-3-Si-UVHT thin film this should not be a problem, as the different areas where EDS spectra are obtained are larger homogenous regions. Therefore it is thought that the result, which indicates no variation in composition between the different regions, but instead a difference in film thickness, is valid. These variations in height also fit with the results found for this thin film using a profilometer.

To get the most accurate elemental analysis, some corrections need to be done to the spectrum before quantification. First the background is subtracted. The estimated background model is seen in the EDS spectra in figures 4.49, 4.51 and 4.53 as a dark line. The software estimates a best possible model, but the model will never fit 100 % with the actual background. This introduces some inaccuracy into the results, which is further corrected for by the ZAF corrections.

For both the IZO40%-1-g-RTP and IZO4%-3-Si-UVHT thin film the indium diffraction line is higher than the zinc diffraction line in the EDS spectra. Thus, a higher than expected mol% of Zn compared to the mol% of In is seen in the elemental analysis. From the elemental analysis it is found that the mol% of In and Zn are of similar value. Even though it seems illogic, this is found to occur due to the corrections. When doing the quantification, the ZAF corrections will try to compensate back the possible inaccuracy of the background correction. So, after ZAF corrections the mol% Zn value is higher than what is expected by only taking the spectra into account.

When doing the elemental analysis for the thin films the silicon diffraction line is included. Because silicon is the main diffraction line, and because it is not a light element, excluding this diffraction line changes the mol% of the different elements, and also the relationship between them considerably. The other elements introduced into the spectra by the substrate are either light elements or have a low intensity diffraction line, thus excluding these does not affect the elemental analysis substantially.

A large amount of the signal detected during EDS is from silicon. The stronger a signal is the more likely is it that two signals of the same energy hit the detector simultaneously. Thus, the diffraction line seen at the energy 3.478 keV is thought to be the double peak of silicon also called the sum peak. This peak arises when two Si K_α signals of the energy 1.739 keV hits the detector at the same time. The detector registers one signal with the energy 3.478 keV.

As mentioned in the theory part "2.5.2 Scanning Electron Microscopy" the energy resolution of the EDS is 0.124 keV. For the IZO40%-1-g-RTP thin film the Zn L_α diffraction line at 1.012 keV is not included in the elemental analysis as it overlaps with the Na K_α diffraction line at 1.041 keV. No such overlap is seen for the IZO40%-3-Si-UVHT thin film in Figure 4.53, and the Zn L_α diffraction line is included in the elemental analysis. However including or excluding the Zn L_α diffraction line does not have a substantial effect on the results from the elemental analysis.

The results from the elemental analysis for the ITO10%-3-Si-UV thin film found in Table 4.5 show a doping level of 50 mol% Sn. The nominal doping level is 10 mol% Sn and the actual doping level is considered to be even lower. For the EDS spectrum it can be seen that the Sn L_α signal with an energy of 3.443 keV overlaps with the double peak of silicon with energy 3.478 keV. This causes a substantially higher doping level of tin than the actual level to be obtained in the elemental analysis. The In L_α diffraction line at 3.286 keV is also close in energy to the silicon double peak, but has an energy 0.192 keV lower. It can be seen from the spectra in Figure 4.51 that the detector is able to separate this signal from the double peak of silicon, giving a separate diffraction line for indium.

5.7 Optical Properties

Correction of the thin film spectrum was obtained by dividing it on the glass spectrum, thus if the glass has a transmission of 90 % the thin film spectrum is enhanced by 10 % by dividing the spectrum by 0.9. From the transmission spectra it can be seen that the glass substrate also has an absorption band edge around 300 nm. As the glass substrate fully extinguishes radiation below this wavelength, the values obtained for the thin films cannot be trusted below around 300 nm. A small value would give a large outcome when corrected as the thin film spectra are divided by values close to zero in this region. This causes the strange behavior of the thin film transmission spectra of the thin films below 300 nm. The correction also causes some of the thin films to obtain transmission slightly above 100 %. This is only seen for the thin films obtained by spectrophotometry and is likely to be caused by the decrease seen for the glass substrate above 600 nm as it can be seen that the shape of the glass substrate curve is mirrored by the thin film curve. For spectrophotometry there is also large uncertainties in the measurements obtained for wavelengths below 200 nm and above 1000 nm, thus these values are excluded.

Of the thin films that were supposed to be characterized by ellipsometry, models for 3 out of 3 thin films on glass substrates while only 1 out of 4 of the thin films on silicon substrates could be obtained. This could give an indication that good ellipsometry measurements are easier to obtain for thin films on glass substrates than on silicon substrates. A higher contrast between the refractive indexes of thin film and substrate give better measurements. The average refractive index in the visible region of the specific glass and silicon substrates used for these thin films are 1.5 and 4.3 respectively. As seen from Table 4.7 in the result part the refractive indexes of the films have an average in the visible region of 1.9-2.0, meaning that it should be easier to obtain good measurements for the thin films on silicon compared to thin films on glass substrates. The ellipsometry measurements for the thin films on glass substrates have one advantage; a transmission spectrum is obtained for these thin films. The transmission spectrum is used as an input parameter when making the models for the ellipsometry measurements, eliminating some uncertainty in the model and making the modeling easier. To get a best possible measurement, the surface should be as flat as possible. Wetting of the substrate can definitely affect the roughness of the thin film surface. In some cases, especially for the UV and UVHT cured thin, the solution wets the glass better than it wets the silicon substrate. It is likely that the UVHT cured thin films could not be measured by ellipsometry because of a too high roughness. Roughness parameters for these thin films are found in Table 4.3 in the results part. From the SEM images in figure 4.37 and 4.39 the morphology is found to be inhomogeneous. Based on this it can be concluded that these thin films are not suitable for ellipsometry measurements. The IZO40%-2-Si-RTP are not found to stand out in any of the above results, and it is not possible to conclude on why this sample could not be measured by ellipsometry. It cannot be determined that it is easier to obtain ellipsometry measurements for thin films on glass substrates. Only one out of two thin films on silicon substrates that should be suitable for ellipsometry measurements was impossible to measure. To clarify this, measurements of more samples must be performed. Time limitations made it impossible to perform more ellipsometry measurements in this thesis.

The transmission spectra show that no distinct trend is found for the absolute transmission value depending on curing method, thin film composition or solution. The thin films are only made by three depositions trends might have emerged with a thicker film. It is often seen in literature that altering a variety of different parameters does not alter the optical transparency. Kim et al. [6] showed that the optical transparency did not change substantially with composition or thermal curing temperature for sol-gel derived IZO thin films. Optical transmission properties of TCOs are among other parameters related to film thickness, densification and surface morphology. All the thin films (excluding ITO10%-3-g-RTP) obtain a high optical transparent, which is expected as only three layers were deposited giving a very thin film. The dependency of the optical transparency on film thickness is discussed in theory section "2.2 Optoelectronic Properties". There are indications that higher transmission values are seen for the UV cured films, but more UV and UVHT cured thin films should be obtained to get a clear trend on how curing method affects the absolute values. For the UVHT cured thin films some absorption of the high-energy radiation in the visible region is seen. This was not studied further, and it is not known what causes this absorption in the thin film. The ITO10%-3-g-RTP thin film stands out for both the spectrophotometry and ellipsometry by obtaining a lower transmission value and also a different shape for the ellipsometry measurements. It can be seen that this thin film also has a lower lattice parameter than the other thin films of the same composition. No information about the morphology was obtained, and the resistivity found in Figure 4.65 is in good accordance with the other thin films. Based on this no conclusion can be made, but it is decided to disregard this result as both the spectrophotometry and the ellipsometry show low optical transmission. No transmission spectra could be obtained for the thin films on silicon substrates, thus a comparison of the substrates is impossible. If only concentrating on the curve shape no trend is seen with respect to thin film composition or the different solutions. However for the curing methods, the curve shapes look distinctly different. Especially the shape of the UVHT cured thin film curves stand out, and the round shape makes it difficult to define the absorption band edge for these spectra. From the other results, the different curing methods have been found to impact the surface morphology, resistivity and structure. It is also likely that the curing method impacts film thickness and densification. Both the absolute values and the shape of the transmission curves fit well with literature as can be seen by comparing the results obtained in this thesis with the results presented in figures 2.11 and 2.12 in the literature section "2.2.1 Optical Properties"

Due to problems with the modeling of some of the ellipsometry measurements, results for a very limited selection of thin films are obtained. Due to this, no comparison of the different curing methods is possible and comparisons of the different compositions, solutions and substrates are based on few observations.

The obtained band gap values of 3.8 eV for ITO and 3.7 eV fit good with values obtained in literature [49-51]. This also fits good with the observation that IZO thin films are known to have a smaller band gap than ITO thin films [28].

As described in theory section "2.5.4 Ellipsometry" the extinction coefficient, *k*, tells something about how long into the material electromagnetic radiation will travel. A high transmittance in the visible region is seen for the films even though $k \neq 0$, this is because the films are very thin compared to the wavelength of visible light. The average values in the visible region of the electromagnetic spectrum for the refractive index, *n*, and the extinction coefficient, *k*, are seen in Table 4.7. The IZO thin film has a bit lower *n* and larger *k* than the ITO thin films. Also from the *n* and *k* plots in figures 4.61 to 4.64, a difference between the dependence of *n* and *k* on wavelength is seen for ITO and IZO. This indicates that there are differences in the optical properties for IZO and ITO thin films. The optical properties does not seem to be much affected by the different doping levels in ITO or the different solutions. A lower *k* is seen for the thin film on silicon substrates, but values for more thin films needs to be obtained to determine if this is a trend. The *n* and *k* values and the shape of their curves for both ITO and IZO are found to correspond good with literature [22, 109].

In Table 4.8 thickness and average roughness of the thin films obtained from the ellipsometry measurements are presented. The parameters that affects the thickness most, is sol age, concentration of precursors, viscosity, spin coating parameters, number of deposited layers, and wetting. The spin coating parameters and number of deposited layers are held constant for all films, hence this should not be the reason for observed differences in film thickness. The thin films ITO10%-3-g-RTP and ITO10%-3-Si-RTP have similar film thicknesses, but a slightly lower thickness is seen for the thin film on silicon substrate. The only difference between the films is the substrate, which excludes solution related explanations like sol age, precursor concentration and viscosity. Differences in wetting for the glass and silicon substrates are therefore most likely to cause the different film thicknesses. The lattice parameter is smaller for ITO thin films on silicon substrate compared to on glass, and if it is assumed that a higher lattice parameter gives a thicker film, this could also give a small contribution in the same direction. A difference is also seen in the roughness, as the thin film on silicon substrate has a lower value than the thin film on glass. Both thin films are thought to be homogenous and flat and when comparing to the average roughness found for similar films using a profilometer, ITO10%-3-g-RTP corresponds well in value. A higher uncertainty is associated with the values for the ITO10%-3-Si-RTP thin film due to the higher mean square error. The mean square error should preferably be 10 or lower, but values with a higher mean square error still gives a good indication of the actual values. ITO15%-1-g-RTP shows a thickness ~10 nm lower than ITO10%-3-g-RTP. Due to the low mean square error, the values for both thin films are thought to be realistic. By only considering the lattice parameters in Figure 4.4 this is opposite of what is expected, since the lattice parameter of ITO15%-1-g-RTP is way larger than the lattice parameter of ITO10%-3-g-RTP. This indicates that a parameter that influences the thickness more than the lattice parameter causes the change in thickness. The thin films are made from different solutions and compositions, and explanations for the difference in thickness can be variation in sol age, precursor concentration and viscosity. The average roughness value found for ITO15%-1-g-RTP through the profilometer is 1.78 ± 0.23 nm, which is ~1 nm lower than the average roughness of 2.86 nm found from ellipsometry. The thinnest film is found for IZO40%-1-g-RTP. This is logic if only based on the lattice parameter value, which is much lower for the IZO40%-1-g-RTP than any of the ITO thin films. But, the lattice parameter itself cannot cause such a lowering of film thickness. Additional factors like shorter sol age, lower precursor concentration, and lower viscosity could be main contributors. The viscosity is prone to change due to the different precursor, and the precursor concentration is likely to be higher since no precipitation is observed. The sol-age should be similar, but small variations are possible. A higher precursor concentration gives thicker films. Despite this a thinner film is seen, and a lower viscosity is likely to be the reason. The average roughness for the IZO40%-1-g-RTP found using the profilometer is 1.88 ± 0.26 nm, which is ~1 nm higher than the average roughness value of 0.50 nm found by ellipsometry. A deviation in roughness of 1 nm between the two separate characterization techniques is thought to be satisfying as the values are in the same range. From the profilometer the roughness for ITO15%-1-g-RTP and IZO40%-1-g-RTP are similar, but the roughness of IZO40%-1-g-RTP is a bit higher. For the ellipsometer, the roughness of IZO40%-1-g-RTP is lower. This is not expected based on the SEM and AFM images, where IZO40%-1-g-RTP seems to be rougher than ITO15%-1-g-RTP at nanoscale.

The ellipsometry results are very precise, but it is difficult to determine its accuracy. If questionable results are obtained the ellipsometric results should be corroborated with data from other techniques such as Rutherford back scattering, transmission electron microscopy and atomic force microscopy. Even though the transmittance and roughness found using ellipsometry are confirmed by other methods, the film thickness should also have been obtained by another method. Transmission electron microscopy or a stylus method would have been good choices. In addition, being able to obtain thickness measurements by using a reflectometer would have been neat. This method is based on the same principles as ellipsometry, which is discussed in theory section “2.5.4 Ellipsometry”, but is way quicker. The problem is that there is not made a good model for ITO and IZO thin films for the reflectometer, but this could have been done based on the information obtained from the ellipsometer and the transmission electron microscopy. If it had been time to do this, all the thin films could have easily been measured within a few hours.

In the work by Sunde et al. [16] a model for the thickness of ITO thin films made through the same procedure as in this thesis was developed. Each layer was approximated to give an increase in thickness of 17 ± 1 nm, giving a film thickness of ~51 nm for three layers. In the specialization project [107] a film thickness of 150 nm was determined based on a SEM image. It is questioned weather this is a real value. Based on the results in this master thesis, and the results obtained from Sunde et al. it is concluded that 150 nm is not a realistic value, at least for the thermally thin films. To study the cross section of the thin film in the SEM, the thin film was broken in two using bare hands. It is not given that the thin film breaks along the edge of the substrate when a cross section is obtained in such a manner. Since the thin film was UV cured and non-conductive, carbon was sputtered onto the surface before studying it in the SEM, thus it could have been the carbon layer that was depicted. One argument that supports a film thickness of 150 nm is the difference in curing method. A UV cured film could be substantially thicker due to incomplete densification of the film/decomposition of the organics. Since no measurements of the thin film thickness was obtained for the UV cured thin films, no conclusion can be drawn with respect to this discussion.

No well-documented trends for thickness are seen with regards to curing method, thin film composition, different solutions or different substrates. It is only assumed that the thermally cured IZO films actually are thinner than the ITO films.

5.8 Electrical Resistivity

Two or more van der Pauw measurements are performed on the thin films to check the reproducibility of the measurements. Scratching of the films during measurement is observed. This could have affected the second and third runs, by giving lower readings. There is not seen any such trend, as second and third runs both show higher and lower resistivity values than the first run.

The average thickness of the ITO thin films is based on three thickness measurements. Assuming that the rest of the ITO thin films obtain a thickness close to this value is the best assumption that could be made with the time aspect of this master thesis. Ideally all the films should have been measured, or at least one thin film for each parameter. Especially the UV and UVHT cured thin films are likely to have a different thickness, but as no van der Pauw measurements could be obtained for these thin films this is not a problem for this section. The resistivity obtained for the In_2O_3 thin film in the specialization project was calculated based on a thicker thin film of 150 nm, thus causing a higher value of 3.6×10^{-2} Ω cm [107]. The thickness measured by the ellipsometry is thought to be much more reliable, and the thickness found in the specialization project is discarded.

Frank and Köstlin [40] reported the dependence of resistivity on the doping level of tin for In_2O_3 thin films, but they also studied the effect of the oxygen partial pressure during synthesis. When re-plotting the literature values from Frank and Köstlin, the values obtained having an oxygen partial pressure of 10^{-2} bar was used. This is thought to be closest to the oxygen partial pressure during curing for the thin films synthesized in this master thesis. The rapid thermal process furnace has a highest possible theoretical vacuum of 10^{-6} bar, but in practice vacuum it is around 5×10^{-5} bar. By also including the effect from the nitrogen gas used, which causes a higher oxygen partial pressure, an oxygen partial pressure of 10^{-2} bar is thought to be closer to the actual curing parameters than 10^{-6} bar.

As already mentioned, it is not possible to measure the UV and UVHT cured thin films with the van der Pauw apparatus, thus no resistivity value is obtained. The approximate detection limit of the van der Pauw is at the order of 10^{2} Ω cm. Thus the van der Pauw can be used to measure conductive materials, but cannot be used for all semiconducting materials. From this we know that the UV and UVHT cured films are not conductive, but it cannot be determine whether they are semiconducting or insulating. Considering this, it might be an idea to do Hall measurements instead of van der Pauw measurements. From the section “4.5 Morphology” it is concluded that the UV and UVHT cured films are inhomogeneous. This might deteriorate the conductivity, but could not be the only reason as no measurements could be obtained for the morphologically homogenous UV cured IZO thin films. The high resistivity for these films could suggest that some of the organics added in the synthesis is still present. Having organics present will lower the conductivity substantially. The energy available during the UV and UVHT curing might not be enough to decompose all the organic material. Kim et al. [12] synthesized sol-gel derived In_2O_3 and IZO by photochemical activation with properties equal to a thermally cured thin film at 350 °C. They found that in addition to the energy from the UV lamp, the thermal energy accumulated was an important energy contributor. The solvent used in the synthesis has a boiling point of 124 °C, and they reached a temperature of 150 °C during UV curing. The boiling point for the organics used in this synthesis; acetic acid, ethylene glycol and polyvinyl alcohol is T_b= 117.9 °C, T_b= 198 °C, and T_b= 230 °C, respectively [39]. It can be seen from figures 3.7 and 3.8 in the experimental part that the boiling point of the organics used in this synthesis are above the heat reached in the system. The temperatures reached for the UV curing is about 48 °C, and for the UVHT curing it is 150 °C. Also for the UV cured In_2O_3 thin films synthesized in the specialization project [107], where the curing temperature reached 43 °C, it was impossible to measure the resistivity of the thin films by using the van der Pauw apparatus. It can be seen that a temperature of ~10 °C higher was reached in the modified UV set-up compared to the original after 2 hours UV curing. This could indicate that the efficiency of the UV curing is also raised, but as the UV and UVHT cured films are still non-conductive the raise in temperature and efficiency is not enough. Thus, it is proposed that a temperature above the boiling points of the organics/solvents is necessary to obtain complete decomposition and densification of the thin films. It is not thought safe for the environment, or sustainable for the apparatus to raise the curing temperature above 150 °C. Thus two options are possible: do a higher pre-curing heat treatment step or tailor the synthesis for UV curing. The synthesis used in this thesis is optimized for thermal curing of ITO thin films, and was chosen due to the good results obtained combined with the environmental friendly synthesis. When tailoring the synthesis for photochemical activation one should choose low boiling point solvents and organics that are easily decomposed by photochemical activation. In other literature found regarding photochemical activation of thin films they aim at producing crystalline films, but instead often obtain crystalline metal particles in a porous film [88, 89]. No formation of metal particles was found to occur here.

When comparing the resistivities obtained for the thermally cured thin films of different compositions an increasing in resistivity is seen in the order ITO < In_2O_3< IZO. As already introduced in the results part it could not be determined anything with regards to which of the ITO compositions that showed the lowest resistivity. The problems with getting a coinciding trend for the different datasets is most likely due to the problem with precipitation, as the precipitation gives a large uncertainty with respect to the actual doping level of the film. The resistivity for the ITO thin films are on the same order as the values obtained by Sunde et al. [16], and are also in good accordance with other values obtained for sol-gel derived thin films [58, 59]. This value is thought to be low when considering the environmental friendly synthesis and the short thermal curing at a moderate temperature. The values obtained in this thesis are especially low considering the non-optimal actual tin concentration of the films. A lower resistivity is normally seen when doping In_2O_3 with zinc [8]. The author is unsure why such a high resistivity is obtained for the IZO thin films. In general, the crystallization temperature of IZO is known to be higher than ITO as reported in section “2.1 Crystal Structure”. Since the thermal curing method is optimized for ITO, the curing step is most likely not optimal for IZO. It might be necessary to use higher curing temperatures, and longer curing times to get lower resistivities for IZO. It is also possible that the synthesis has to be specifically optimized for IZO.

Even though the deviations for the ITO thin films are too large to conclude on a resistivity trend with respect to the level of tin doping, the lowest resistivity value for each substrate is quite representative for the other values. For the IZO thin films on glass a too large variation is seen between the different solutions making it difficult to conclude on a representative resistivity value, thus it is determined to give the lowest value. In addition, a decrease in resistivity is seen for increasing solution number. The thin films of the different solutions are made following the same procedure, and should in theory give the same resistivities. There is nothing that suggests that the resistivity should decrease with a higher solution nr. Also in section "5.4 Lattice Parameter" a trend with solution nr is seen and many of the proposed reasons listed in this section also applies here. For the resistivity, this phenomenon is not seen for the thin films on silicon substrates. If we consider the different wetting observed for the two substrates, it should have been silicon substrates that obtained the non-reproducible results, as the wetting of glass was better than the wetting of the silicon substrates. The methods proposed to understand the trend seen for the lattice parameter would also have given a clearer view of the resistivity trend, especially the film thickness.

As mentioned in the result part, the readings for the IZO40%-3-Si-RTP thin film varied so much that it was difficult to obtain reproducible readings. Thus, it was determined to disregard the obtained resistivity value. By comparing to the results found from the other characterization methods, more arguments for why the results from this thin film should be discarded could be obtained. For the lattice parameter values in Figure 4.5 this data point stands out as being off compared to the other values. Based on the image of the thin film found in Figure 4.11 and the optical light microscopy image in Figure 4.24 the thin film look non-homogenous, especially with regards to thickness. This might be the reason for the unstable readings. The two lowest readings are used for the plot. This reading could be realistic at some points of the thin film where the thin film is very thick. By using a lower thickness than the real to calculate the resistivity, a lower than actual resistivity is obtained. By looking at the SEM image of the thin film in Figure E.7 in "Appendix E Morphology" the thin film look similar to the other thin films. Also for the optical properties, the thin film conforms to the values found for the other thin films.

For all the thermally cured thin films, a lower resistivity is seen for the thin films deposited on a silicon substrate. One obvious factor, is the lower resistivity of the silicon substrate compared to the glass substrate, which are a semiconductor and an insulator respectively. Another factor that could lower the resistivity is that the thin films crystallize better on the single-crystalline silicon substrate compared to the amorphous glass substrate, as can be seen from the diffractograms in Figure 4.2. The substrate also affects the lattice parameter of the crystal structure. It could also be that the low resistivity of the silicon substrate affects the van der Pauw measurements to an extent large enough to make the resistivity values for the different solutions more alike than the resistivity values for the different solutions on glass. The resistivity results for the thin films on silicon substrates seem to be more reproducible, but this might not be the case if it is actually the resistivity of the silicon substrate that influences the resistivity of the thin film. But, also for the lattice parameter the thin films on silicon substrates tend to lie closer to each other in value. The different IZO solutions studied in the SEM also look more similar for the thin films on silicon compared to the ones on glass substrate. This could either indicate that the thin film properties (or at least lattice parameter, morphology and resistivity) are more reproducible for the thin films on silicon substrates, or that the crystalline structure of the silicon substrate to a larger degree dictates these properties.

6. Conclusions

ITO and IZO thin films were prepared by spin coating a sol synthesized by an environmental friendly Pechini method onto glass and silicon substrates. A UV curing method was investigated as an alternative to the conventional thermal curing method. The thin films cured by the different methods were compared with respect to structure, morphology, optical properties, and electrical properties.

Precipitation of SnO_2 was observed in the ITO solutions during synthesis. The amount of precipitate was constant over time, and when removed no new precipitate was seen. The precipitation is proposed to occur due to the low pH of the indium nitrate standardized solution of 1.17, which is likely to cause a low solubility limit of tin in the solutions.

From Auger electron spectroscopy it is found that the amount of tin in the thin films increases with increasing nominal doping levels. Elemental analysis of the spectra shows that the thin films contain a substantially lower level of tin doping than the nominal doping level. This indicates that the precipitation affects the doping level of the films substantially. It was also observed that the surface stoichiometry of the thin films seemed to be sensitive to ion sputtering.

The thermally cured ITO and IZO thin films obtained a non-directional phase pure cubic bixbyite crystal structure. This indicates a metastable solid solution of tin and zinc in both the ITO and IZO thin films. To the best knowledge of the author, it is not known of any literature where such a high doping concentration as 40 % zinc has been doped into In_2O_3, while still retaining the pure bixbyite structure. It was found that the crystalline thin films deposited on silicon substrates obtained a higher crystallinity than the thin films deposited onto glass substrates. For the UV and UVHT cured samples an amorphous structure was obtained.

The absolute value and trend with increased level of tin doping for the lattice parameter of the ITO thin films are found to correlate well with values found in literature. Generally, the lattice parameter of the ITO thin films is found to be higher than for the IZO films. A clear dependence of lattice parameter on the substrate is seen for both IZO and ITO, as the lattice parameter decrease for ITO while it increase for IZO when the thin film is deposited onto a silicon substrate instead of a glass substrate. Thus, the lattice parameter of ITO and IZO are of similar values when deposited onto silicon substrates. This indicates that the silicon substrate to a degree dictates the value of the lattice parameter. The higher crystallinity seen for the thin films deposited onto silicon substrates compared to the films on glass will also affect the lattice parameter. For both the ITO and IZO thin films a high reproducibility is seen with respect to lattice parameter.

Already with the naked eye, a difference in morphology between the different curing methods can be detected. By summing up the results from the morphology study, the following general conclusion can be made. The morphology shows an increasing inhomogeneity and roughness with respect to curing methods in the following order thermal curing < UV curing < UVHT curing. A slightly higher roughness was found for the IZO thin films compared to the ITO thin films. For the thermally and UV cured thin films, no finite conclusion could be made to whether the features seen on the surface of the thin films were caused by compositional or height differences. However, for the UVHT curing method the features were determined to be height differences and not compositional differences. The solutions were found to wet glass substrates better than silicon substrates. Wetting problems were especially seen for the second and third deposited layer for the UV and UVHT cured thin films on silicon substrate. This is most likely due to an incomplete decomposition of organics between the deposited layers. In sum it was found that the curing method, composition and substrate could affect the thin film morphology. A higher amount of UV and UVHT cured thin films should be synthesized to evaluate if the results obtained are valid trends.

The thin films show a high optical transparency with an average of 88-97 % in the visible region, and good reproducibility was observed. The absolute value and the shape of the curves were verified both by doing two characterization methods and by comparing to literature. No clear trend could be seen with regards to the effect of the different curing methods on the absolute value of the transparency, whereas an evident trend was seen for the curve shape. Both thermally and UV cured thin films showed an absorption band edge around 300 nm. This was more difficult to determine for the UVHT cured thin films, which seemed to absorb some of the high energy radiation of visible light. No dependence of the transparency on composition or different solutions was found. The band gap of ITO was determined to be 3.8 eV, while the band gap of IZO was determined to be 3.7 eV. These values are in good accordance with the literature values found, and also fit with the general perception that IZO obtains a smaller band gap than ITO. The optical constants refractive index, n, and extinction coefficient, k, were also found to agree with literature. Thus, the optical properties obtained are typical for TCO thin films. Differences in the optical properties between ITO and IZO were observed. No well-documented values for the thin film thickness were obtained in this thesis.

For the thermally cured ITO thin films the lowest resistivity values obtained on glass and silicon substrates are 2.8×10^{-3} Ω cm and 2.2×10^{-3} Ω cm, respectively, which coincide good with literature values of sol-gel derived ITO thin films. For the thermally cured IZO thin films the lowest resistivity values obtained on glass and silicon substrates are 0.4 Ω cm and 0.1 Ω cm, respectively. The lower resistivity obtained for the thin films deposited onto silicon substrates are due to the lower resistivity of silicon, which is a semiconductor compared to glass that is an insulator. When comparing the resistivities obtained for the thermally cured thin films of different compositions an increasing in resistivity is seen in the order ITO < In_2O_3 < IZO. No conclusion could be made regarding why the IZO films obtains higher resistivity than the pure In_2O_3 thin films, but it is proposed to be linked to that the procedure is optimized for synthesizing thermally cured ITO thin films. Good reproducibility is found for all the thin films except the IZO thin films on glass. No conclusions could be drawn regarding why these films show a low reproducibility. It was not possible to obtain resistivity measurements for the UV and UVHT cured thin films, indicating that these films are non-conducting. This is most likely due to incomplete decomposition of organics in the thin films.

7. Further work

Numerous ideas for further work were proposed throughout the discussion for specific cases, so in this part a more general approach is given.

Problems with precipitation were seen during the solution synthesis. To conclude on the impact of this, a more thoroughly study has to be performed. A sample of known composition could be studied to see if the composition is reproduced by analysis using Auger electron spectroscopy. In addition, the results from the Auger electron spectroscopy should be validated by comparing them to measurements performed using the X-ray photoelectron spectroscopy. More films need to be studied to see if the results are reproducible with respect to both the tin content and the effect of sputtering. It would also have been nice to do different areas of the film to see if the same results are obtained across the surface.

In general more UV and UVHT cured films should be made to see if the results obtained in this master thesis for morphology, roughness and optical properties are reproducible. Hall measurements of the thin films should also be performed to be able to see the effect of the different UV parameters on the electrical properties as well. In addition to the room temperature and 150 °C UV curing, studying the effect of higher pre-curing temperatures would be interesting.

As the UV and UVHT cured films could not be measured using the ellipsometer, refractive index, extinction coefficient, band gap and film thickness could not be obtained. Further work should aim at finding a way to do ellipsometry measurements on these films, as this would give valuable information about the difference in the optical properties of the thermally and UV cured films. In addition to doing ellipsometry measurements, transmission electron microscopy should be done to verify the thickness and also study differences in crystallite size. Preferably, enough film thickness measurements should be performed to see a trend for each parameter. By making a good model for the films on the reflectometer utilizing the optical constants and thickness measurements obtained from the ellipsometer a quick and reliable way of measuring the film thickness could be obtained.

The main properties that the UV and UVHT cured thin films lack are a homogenous morphology and measureable electrical conductivity. To solve this, a deeper understanding of the mechanisms of photochemical activation could be of help. It would have been interesting to study the chemical bonds in the UV and UVHT cured thin films and compare them to the chemical bonds seen in the thermally cured thin films. A study of the change in chemical bonds with time and temperature of the UV irradiation could also provide useful information. One method for studying the chemical bonds of the thin films is by Fourier transform infrared spectroscopy. Also X-ray photoelectron spectroscopy can give important information for understanding the chemical aspects of the films.

Incomplete decomposition of organics is thought to be the main reason for the non-measureable conductivity for the UV and UVHT cured thin films. Optimizing the synthesis for UV curing is thought to be the best suggestion for obtaining complete decomposition of the organics. When altering the synthesis it is proposed to use low boiling point organics/solvents that are known to easily decompose when exposed to UV radiation. The synthesis should be tailored to include precursors and solvents where UV-absorbing species or groups that generate hydroxyl radicals are present. It can already at solution stage, be determined if the solution is suitable for UV curing by obtaining ultraviolet–visible absorption spectra of the precursor solutions. 2-methoxyethanol is used as a solvent in a number of articles concerning sol-gel derived thin films for both conventional and low temperature curing methods [8, 12, 32]. This could be a suitable solvent with respect to a low boiling point and good absorption of UV light, but it is not too good with respect to HSE. Getting rid of the organics is thought to be the key element for obtaining conductive thin films by photochemical activation. Hence, when optimizing the synthesis a method for determining the content of organic material in the thin films should be developed. By fitting a mass spectrometer on the gas outlet of the UV set-up the weight loss during UV irradiation could be monitored. Also a study of chemical bonds and binding states by Fourier transform infrared spectroscopy and X-ray photoelectron spectroscopy could help determining if any organics are left in the thin films.

References

1. Ginley, D., *Handbook of transparent conductors.* 1st ed. 2011, New York: Springer.
2. Lewis, B.G. and D.C. Paine, *Applications and processing of transparent conducting oxides.* MRS Bull., 2000. **25**(8): p. 22-27.
3. *The future of ITO: Transparent conductor and ITO replacement markets.* 2008: NanoMarkets.
4. Wang, A., et al., *Charge transport, optical transparency, microstructure, and processing relationships in transparent conductive indium–zinc oxide films grown by low-pressure metal-organic chemical vapor deposition.* Applied Physics Letters, 1998. **73**(3): p. 327-329.
5. Yaglioglu, B., et al., *A study of amorphous and crystalline phases in In2O3–10 wt.% ZnO thin films deposited by DC magnetron sputtering.* Thin Solid Films, 2006. **496**(1): p. 89-94.
6. Kim, C.-H., J.-H. Lee, and B.-O. Park, *Preparation and Characterization of IZO Transparent Conducting Films by the Sol-gel Method.* Materials Science Forum, 2004. **449-452**: p. 469-472.
7. Li, X., et al., *Sol–gel processed indium zinc oxide thin film and transparent thin-film transistors.* Journal of Sol-Gel Science and Technology, 2013. **65**(2): p. 130-134.
8. Lee, S.-Y. and B.-O. Park, *Electrical and optical properties of In2O3-ZnO thin films prepared by sol-gel method.* Thin Solid Films, 2005. **484**(1-2): p. 184-187.
9. Bel Hadj Tahar, R., et al., *Tin doped indium oxide thin films: Electrical properties.* J. Appl. Phys., 1998. **83**(5): p. 2631-2645.
10. Han, S.-Y., G.S. Herman, and C.-h. Chang, *Low-Temperature, High-Performance, Solution-Processed Indium Oxide Thin-Film Transistors.* J. Am. Chem. Soc., 2011. **133**(14): p. 5166-5169.
11. Adamopoulos, G., et al., *High-Mobility Low-Voltage ZnO and Li-Doped ZnO Transistors Based on ZrO2 High-k Dielectric Grown by Spray Pyrolysis in Ambient Air.* Adv. Mater. (Weinheim, Ger.), 2011. **23**(16): p. 1894-1898.
12. Kim, Y.-H., et al., *Flexible metal-oxide devices made by room-temperature photochemical activation of sol-gel films.* Nature (London, U. K.), 2012. **489**(7414): p. 128-132.
13. Kim, H.S., et al., *Low-Temperature Solution-Processed Amorphous Indium Tin Oxide Field-Effect Transistors.* J. Am. Chem. Soc., 2009. **131**(31): p. 10826-10827.
14. Nomura, K., et al., *Room-temperature fabrication of transparent flexible thin-film transistors using amorphous oxide semiconductors.* Nature (London, U. K.), 2004. **432**(7016): p. 488-492.
15. Van de Leest, R.E., *UV photo-annealing of thin sol-gel films.* Appl. Surf. Sci., 1995. **86**(1-4): p. 278-85.

16. Sunde, T.O.L., et al., *Transparent and conducting ITO thin films by spin coating of an aqueous precursor solution.* J. Mater. Chem., 2012. **22**(31): p. 15740-15749.
17. Yates, H.M., et al., *The development of high performance SnO2:F as TCOs for thin film silicon solar cells.* Surf. Coat. Technol., 2012. **213**: p. 167-174.
18. Liu, H.-Y., et al., *Transparent conducting oxides for electrode applications in light emitting and absorbing devices.* Superlattices Microstruct., 2010. **48**(5): p. 458-484.
19. Ferry, V.E., et al., *Light trapping in ultrathin plasmonic solar cells.* Opt. Express, 2010. **18**(S2): p. A237-A245.
20. Morris, J., et al., *Absorption enhancement in hydrogenated amorphous silicon-based solar cells.* J. Appl. Phys., 1990. **67**(2): p. 1079-87.
21. Markvart, T., *Solar electricity*. 2nd ed. 2009: John Wiley & sons, LTD.
22. Jung, Y.S., et al., *Influence of DC magnetron sputtering parameters on the properties of amorphous indium zinc oxide thin film.* Thin Solid Films, 2003. **445**(1): p. 63-71.
23. Gonçalves, G., et al., *Influence of post-annealing temperature on the properties exhibited by ITO, IZO and GZO thin films.* Thin Solid Films, 2007. **515**(24): p. 8562-8566.
24. Yaglioglu, B., H.-Y. Yeom, and D.C. Paine, *Crystallization of amorphous In2O3-10 wt. % ZnO thin films annealed in air.* Appl. Phys. Lett., 2005. **86**(26): p. 261908/1-261908/3.
25. Gonzalez, G.B., et al., *Defect structure studies of bulk and nano-indium-tin oxide.* J. Appl. Phys., 2004. **96**(7): p. 3912-3920.
26. Shigesato, Y., *"In-based TCOs." Ch. 5 in "Handbook of Transparent Conductors."*. 2011, New York: Springer.
27. Flickyngerova, S., et al., *Structural and optical properties of sputtered ZnO thin films.* Applied Surface Science, 2008. **254**(12): p. 3643-3647.
28. Naghavi, N., et al., *Structural and physical characterisation of transparent conducting pulsed laser deposited InO-ZnO thin films.* Journal of Materials Chemistry, 2000. **10**(10): p. 2315-2319.
29. Mikawa, M., et al., *Characterization of ZnO–In2O3 transparent conducting films by pulsed laser deposition.* Materials Research Bulletin, 2005. **40**(6): p. 1052-1058.
30. Taylor, M.P., et al., *The Remarkable Thermal Stability of Amorphous In-Zn-O Transparent Conductors.* Advanced Functional Materials, 2008. **18**(20): p. 3169-3178.
31. Luna-Arredondo, E.J., et al., *Indium-doped ZnO thin films deposited by the sol–gel technique.* Thin Solid Films, 2005. **490**(2): p. 132-136.
32. Tsay, C.-Y. and T.-T. Huang, *Characterization of low-temperature solution-processed indium–zinc oxide semiconductor thin films by KrF excimer laser annealing.* Ceramics International, 2014. **40**(6): p. 8287-8292.
33. Koo, C.Y., et al., *Low Temperature Solution-Processed InZnO Thin-Film Transistors.* Journal of The Electrochemical Society, 2010. **157**(4): p. J111-J115.
34. Heward, W.J. and D.J. Swenson, *Phase equilibria in the pseudo-binary In2O3-SnO2 system.* J. Mater. Sci., 2007. **42**(17): p. 7135-7140.
35. Alam, M.J. and D.C. Cameron, *Optical and electrical properties of transparent conductive ITO thin films deposited by sol-gel process.* Thin Solid Films, 2000. **377-378**: p. 455-459.

36. Park, Y.-G., et al., *Phase transformation behavior of nanocrystalline ITO powders during heat-treatment: oxygen partial pressure effect.* J. Electroceram., 2004. **13**(1/2/3): p. 851-855.
37. González, G.B., et al., *Determination of the Solubility of Tin in Indium Oxide Using In Situ and Ex Situ X-Ray Diffraction.* Journal of the American Ceramic Society, 2012. **95**(2): p. 809-815.
38. Moriga, T., et al., *Phase Relationships and Physical Properties of Homologous Compounds in the Zinc Oxide-Indium Oxide System.* Journal of the American Ceramic Society, 1998. **81**(5): p. 1310-1316.
39. Aylward, G., *SI Chemical Data*. 5th ed. 2002, Milton: John Wiley & Sons Australia.
40. Frank, G. and H. Koestlin, *Electrical properties and defect model of tin-doped indium oxide layers.* Appl. Phys., [Part] A, 1982. **A27**(4): p. 197-206.
41. Fan, J.C.C. and J.B. Goodenough, *X-ray photoemission spectroscopy studies of Sn-doped indium-oxide films.* Journal of Applied Physics, 1977. **48**(8): p. 3524-3531.
42. Hamberg, I. and C.G. Granqvist, *Evaporated tin-doped indium oxide films: basic optical properties and applications to energy-efficient windows.* J. Appl. Phys., 1986. **60**(11): p. R123-R159.
43. Chopra, K.L., S. Major, and D.K. Pandya, *Transparent conductors - a status review.* Thin Solid Films, 1983. **102**(1): p. 1-46.
44. Ilican, S., et al., *Polycrystalline indium-doped ZnO thin films: preparation and characterization.* J. Optoelectron. Adv. Mater., 2008. **10**(10): p. 2592-2598.
45. Hamberg, I., et al., *Band-gap widening in heavily tin-doped indium oxide.* Phys. Rev. B Condens. Matter, 1984. **30**(6): p. 3240-9.
46. Perry, C.C., J.K. McGiveron, and P.G. Harrison, *Aqueous sol-gel routes to conducting films of indium oxide and indium-tin-oxide.* Proc. SPIE-Int. Soc. Opt. Eng., 2000. **3943**(Sol-Gel Optics V): p. 270-279.
47. Koestlin, H., R. Jost, and W. Lems, *Optical and electrical properties of doped indium(III) oxide films.* Phys. Status Solidi A, 1975. **29**(1): p. 87-93.
48. Walsh, A., et al., *Nature of the Band Gap of In2O3 Revealed by First-Principles Calculations and X-Ray Spectroscopy.* Phys. Rev. Lett., 2008. **100**(16): p. 167402/1-167402/4.
49. Ambrosini, A., et al., *Electrical, Optical, and Structural Properties of Tin-Doped In2O3–M2O3 Solid Solutions (M=Y, Sc).* Journal of Solid State Chemistry, 2000. **153**(1): p. 41-47.
50. Odaka, H., et al., *Electronic structure analyses of Sn-doped In2O3.* Jpn. J. Appl. Phys., Part 1, 2001. **40**(5A): p. 3231-3235.
51. Ito, N., et al., *Electrical and optical properties of amorphous indium zinc oxide films.* Thin Solid Films, 2006. **496**(1): p. 99-103.
52. Noguchi, S. and H. Sakata, *Electrical properties of undoped indium oxide films prepared by reactive evaporation.* J. Phys. D, 1980. **13**(6): p. 1129-33.
53. Pan, C.A. and T.P. Ma, *High-quality transparent conductive indium oxide films prepared by thermal evaporation.* Appl. Phys. Lett., 1980. **37**(2): p. 163-5.
54. Robertson, J., *"Electronic Structure of Transparent Conducting Oxides" Ch. 2*, in *"Handbook of Transparent Conductors"*. 2011, Springer: New York.
55. Bellingham, J.R., W.A. Phillips, and C.J. Adkins, *Amorphous indium oxide.* Thin Solid Films, 1991. **195**(1-2): p. 23-31.

56. Mizuhashi, M., *Electrical properties of vacuum-deposited indium oxide and indium tin oxide films.* Thin Solid Films, 1980. **70**(1): p. 91-100.
57. Tuna, O., et al., *High quality ITO thin films grown by DC and RF sputtering without oxygen.* J. Phys. D: Appl. Phys., 2010. **43**: p. 055402.
58. Mottern, M.L., et al., *Textured indium tin oxide thin films by chemical solution deposition and rapid thermal processing.* Thin Solid Films, 2007. **515**(7-8): p. 3918-3926.
59. Al-Dahoudi, N. and M.A. Aegerter, *Comparative study of transparent conductive In2O3:Sn (ITO) coatings made using a sol and a nanoparticle suspension.* Thin Solid Films, 2006. **502**(1-2): p. 193-197.
60. Bellingham, J.R., A.P. Mackenzie, and W.A. Phillips, *Precise measurements of oxygen content: oxygen vacancies in transparent conducting indium oxide films.* Appl. Phys. Lett., 1991. **58**(22): p. 2506-8.
61. De Wit, J.H.W., *Structural aspects and defect chemistry in indium oxide (In2O3).* J. Solid State Chem., 1977. **20**(2): p. 143-8.
62. Naghavi, N., et al., *Characterization of indium zinc oxide thin films prepared by pulsed laser deposition using a Zn3In2O6 target.* Thin Solid Films, 2000. **360**(1–2): p. 233-240.
63. Kim, M.-G., et al., *Low-temperature fabrication of high-performance metal oxide thin-film electronics via combustion processing.* Nat. Mater., 2011. **10**(5): p. 382-388.
64. Sigmund, P., *Theory of sputtering. I. Sputtering yield of amorphous and polycrystalline targets.* Phys. Rev., 1969. **184**(2): p. 383-416.
65. Hecht, D.S. and R.B. Kaner, *Solution-processed transparent electrodes.* MRS Bull., 2011. **36**(10): p. 749-755.
66. Legnani, C., et al., *Indium tin oxide films prepared via wet chemical route.* Thin Solid Films, 2007. **516**(2-4): p. 193-197.
67. Bel Hadj Tahar, R., et al., *Optical, structural, and electrical properties of indium oxide thin films prepared by the sol-gel method.* J. Appl. Phys., 1997. **82**(2): p. 865-870.
68. Manifacier, J.C., J.P. Fillard, and J.M. Bind, *Deposition of indium oxide-stannic oxide layers on glass substrates using a spraying method.* Thin Solid Films, 1981. **77**(1-2-3): p. 67-80.
69. Ramaiah, K.S., et al., *Optical, structural and electrical properties of tin doped indium oxide thin films prepared by spray-pyrolysis technique.* Semicond. Sci. Technol., 2000. **15**(7): p. 676-683.
70. Moses Ezhil Raj, A., et al., *Growth mechanism and optoelectronic properties of nanocrystalline In2O3 films prepared by chemical spray pyrolysis of metal-organic precursor.* Phys. B (Amsterdam, Neth.), 2008. **403**(4): p. 544-554.
71. Nishio, K., T. Sei, and T. Tsuchiya, *Preparation and electrical properties of ITO thin films by dip-coating process.* J. Mater. Sci., 1996. **31**(7): p. 1761-6.
72. Zhang, X., et al., *Deposition of transparent conductive mesoporous indium tin oxide thin films by a dip coating process.* Mater. Res. Bull., 2008. **43**(4): p. 1016-1022.
73. Lawrence, C.J., *The mechanics of spin coating of polymer films.* Phys. Fluids, 1988. **31**(10): p. 2786-95.
74. Schubert, D.W. and T. Dunkel, *Spin coating from a molecular point of view: its concentration regimes, influence of molar mass and distribution.* Mater. Res. Innovations, 2003. **7**(5): p. 314-321.

75. Kakihana, M. and M. Yoshimura, *Synthesis and Characteristics of Complex Multicomponent Oxides Prepared by Polymer Complex Method.* Bull. Chem. Soc. Jpn., 1999. **72**(7): p. 1427-1443.
76. Brinker, C.J. and G.W. Scherer, *Sol-Gel Science: The Physics and Chemistry of Sol-Gel Processing*. 1990, San Diego: Academic Press, Inc.
77. Schaefer, D.W., *Polymers, Fractals, and Ceramic Materials.* Science, 1989. **243**(4894): p. 1023.
78. Srolovitz, D.J. and S.A. Safran, *Capillary instabilities in thin films. I. Energetics.* J. Appl. Phys., 1986. **60**(1): p. 247-54.
79. Rahman, M.N., *Ceramic processing and sintering*. 2 ed. 2003, USA: Marcel Dekker, Inc.
80. Kim, S.-S., et al., *Transparent conductive ITO thin films through the sol-gel process using metal salts.* Thin Solid Films, 1999. **347**(1,2): p. 155-160.
81. Cushing, B.L., V.L. Kolesnichenko, and C.J. O'Connor, *Recent Advances in the Liquid-Phase Syntheses of Inorganic Nanoparticles.* Chem. Rev. (Washington, DC, U. S.), 2004. **104**(9): p. 3893-3946.
82. Pechini, M., *Method of preparing lead and alkaline earth titanates and niobates and coating method using the same to form a capacitor.* US Patent 3330697, 11th July, 1967.
83. Lee, H., et al., *A novel approach to preparing nano-size Co3O4-coated Ni powder by the Pechini method for MCFC cathodes.* J. Mater. Chem., 2003. **13**(10): p. 2626-2632.
84. Otter, B.R., *Chemical Solution Deposition of Transparent Conducting Oxide Thin Films*, in *Department of Material Science and Engineering*. 2011, NTNU.
85. Skjervø, S.H., *Terbium Doped ITO Thin Films Prepared by an Aqueous Sol-Gel Method*, in *Department of Materials Science and Engineering*. 2013, NTNU.
86. Quéré, D., *Non-sticking drops.* Reports on Progress in Physics 2005. **68**(11): p. 2495–2532.
87. Drobny, J.G., *Radiation Technology for Polymers*. 2nd ed. 2010: Taylor & Francis Group.
88. Asakuma, N., et al., *Crystallization and Reduction of Sol-Gel-Derived Zinc Oxide Films by Irradiation with Ultraviolet Lamp.* J. Sol-Gel Sci. Technol., 2003. **26**(1/2/3): p. 181-184.
89. Imai, H., A. Tominaga, and H. Hirashima, *Ultraviolet-reduced reduction and crystallization of indium oxide films.* J. Appl. Phys., 1999. **85**(1): p. 203-207.
90. Ohishi, T., S. Maekawa, and A. Katoh, *Synthesis and properties of tantalum oxide films prepared by the sol-gel method using photo-irradiation.* J. Non-Cryst. Solids, 1992. **147-148**: p. 493-8.
91. Nishizawa, K., et al., *Photo-assisted crystallization of zirconia thin films and their electrical evaluation.* Thin Solid Films, 2007. **515**(7-8): p. 4004-4010.
92. Hirai, S., K. Shimakage, and M. Sekiguchi, *Zirconium oxide coating on anodized aluminum by the sol-gel process combined with ultraviolet irradiation at ambient temperature.* J. Am. Ceram. Soc., 1999. **82**(8): p. 2011-2016.
93. Calzada, M.L., et al., *Photo-sensitive sol-gel solutions for the low-temperature UV-assisted processing of PbTiO3 based ferroelectric thin films.* J. Mater. Chem., 2003. **13**(6): p. 1451-1457.

94. Imai, H., et al., *Significant densification of sol-gel derived amorphous silica films by vacuum ultraviolet irradiation.* J. Appl. Phys., 1996. **79**(11): p. 8304-8309.
95. Wypych, G., *Handbook of UV Degradation and Stabilization*. 1st ed. 2011, Toronto: ChemTec Publishing.
96. Graef, M.D. and M. McHenry, *Structure of Materials - An Introduction to Crystallography, Diffraction and Symmetry*. 1st ed. 2007, UK: Cambridge University Press. 275.
97. Huang, T.C. and P.K. Predecki, *Grazing-incidence x-ray technique for surface, interface, and thin-film analysis.* Adv. X-Ray Anal., 1998. **40**: p. 56-67.
98. Dutta, P., *Grazing incidence x-ray diffraction.* Curr. Sci., 2000. **78**(12): p. 1478-1483.
99. Pecharsky, V.K., *Fundamentals of Powder Diffraction and Sructural Characterization of Materials*. 2. ed. 2009, USA: Springer.
100. *D8 ADVANCE Series 2 X-ray Diffractometer USER´S MANUAL VOL. II.* BRUKER. 2004, Karlsruhe, West Germany.
101. Hjelen, J., *Scanning elektron-mikroskopi*, in *Metallurgisk institutt*. 1989, NTH: Trondheim.
102. Adams, T., C. Grant, and H. Watson, *A Simple Algorithm to Relate Measured Surface Roughness to Equivalent Sand-grain Roughness.* International Journal of Mechanical Engineering and Mechanics, 2012. **1**(1): p. 66-71.
103. Haugstad, G., *Atomic force microscopy: understanding basic modes and advanced applications*. 2012: John Wiley & Sons. p. 1-90.
104. *Guide to Using WVASE32G*. J. A. Woollam Co. Inc. 2010, Nebraska, USA.
105. *AvaSpec Operating Manual version 3.0*, Avantes, Editor. 2010, Heco Laboratorieutstyr AS: Oslo.
106. Pauw, L.J.V.D., *A method of measuring resistivity and Hall coefficient on lamellae of arbitrary shape.* Philips Technical Review, 1958. **20**: p. 220-224.
107. Haugesten, L.H., *Alternative methods for curing of TCO thin films, Specialization Project*, in *Department of Materials Science and Engineering*. 2013, NTNU: Trondheim.
108. Adams, T.M. and R.A. Layton, *Introductory MEMS - Fabrication and Applications*. 2010, USA: Springer.
109. Wu, W.-F. and B.-S. Chiou, *Deposition of indium tin oxide films on polycarbonate substrates by radio-frequency magnetron sputtering.* Thin Solid Films, 1997. **298**(1,2): p. 221-227.

Appendix A Preparation of Solutions

Ten solutions of four different compositions were made in total. The different compositions are In_2O_3 doped with 5, 10 and 15 mol% Sn and 40 mol% Zn denoted ITO5%, ITO10%, ITO15% and IZO40% respectively. The actual weight of chemicals used in each solution is listed in tables A.1 and A.2. The wanted cation concentration was 0.4 M for all the solutions. For solution nr 1 and nr 3 the amount of solution made was 10 ml, while for solution nr 2 20 ml was made.

Table A.1: The actual weight of chemicals used in the different ITO solutions.

Thin film composition	**Solution nr**	**Weight [g]**			
		$In(NO_3)_3 \cdot xH_2O$	$Sn(CH_3COO)_2$	CH_3COOH	$C_2H_4(OH)_2$
ITO5%	1	4.9885	0.0470	0.3637	0.3846
	2	9.9996	0.0961	0.7317	0.7450
ITO10%	1	4.7340	0.0936	0.3707	0.3910
	2	9.4866	0.1886	0.7274	0.7479
	3	4.7342	0.0950	0.3624	0.3755
ITO 15%	1	4.4851	0.1415	0.3620	0.3682
	2	8.9425	0.2838	0.7284	0.7462

Table A.2: The actual weight of chemicals used in the different IZO solutions.

Thin film composition	**Solution nr**	**Weight [g]**			
		$In(NO_3)_3 \cdot xH_2O$	$Zn(CH_3COO)_2 \cdot 2H_2O$	CH_3COOH	$C_2H_4(OH)_2$
IZO 40%	1	3.1575	0.3528	0.3624	0.3882
	2	6.3124	0.7057	0.7248	0.7568
	3	3.1633	0.3526	0.3608	0.3766

Appendix B Thin Film Library

In this master thesis a number of thin films are discussed and compared. To make it easier to keep track of the different thin films, a thin film library is provided in Table B.1 as an additional overview to complement the one given in Table 3.3 in the experimental section “3.1.2 Parameters”. The different curing methods are rapid thermal process (RTP) furnace, UV curing at room temperature and UV curing at 150 °C (UVHT).

Gracing incidence X-ray diffraction, conductivity measurements and optical light microscopy were done for all the thin films. Pauley refinement was done for all the crystalline thin films and spectrophotometry was done for all the thin films on glass substrates. The characterization methods that were for specific thin films are included in Table B.1. The abbreviations used in the table are as follows:

AES	Auger Electron Spectroscopy
E	Ellipsometry
SEM	Scanning Electron Microscopy
EDS	Energy Dispersive X-ray Spectroscopy
AFM	Atomic Force Microscopy
P	Profilometer

Table B.1: A thin film library giving an overview of synthesis parameters for the thin films and characterization methods performed on each thin film.

Thin film composition	Solution number	Substrate	Curing method	Thin film name	Characterization
ITO (5 mol% Sn)	1	Glass	RTP	ITO5%-1-g-RTP	
	2	Glass	RTP	ITO5%-2-g-RTP	
	1	Si wafer	RTP	ITO5%-1-Si-RTP	
	2	Si wafer	RTP	ITO5%-2-Si-RTP	AES
ITO (10 mol% Sn)	1	Glass	RTP	ITO10%-1-g-RTP	
	2	Glass	RTP	ITO10%-2-g-RTP	
	3	Glass	RTP	ITO10%-3-g-RTP	E
	3	Glass	UV	ITO10%-3-g-UV	SEM
	3	Glass	UVHT	ITO10%-3-g-UVHT	SEM
	1	Si wafer	RTP	ITO10%-1-Si-RTP	
	2	Si wafer	RTP	ITO10%-2-Si-RTP	AES
	3	Si wafer	RTP	ITO10%-3-Si-RTP	E
	3	Si wafer	UV	ITO10%-3-Si-UV	SEM, EDS, AFM
	3	Si wafer	UVHT	ITO10%-3-Si-UVHT	E, SEM, AFM, P
ITO (15 mol% Sn)	1	Glass	RTP	ITO15%-1-g-RTP	E, SEM, AFM, P
	2	Glass	RTP	ITO15%-2-g-RTP	
	1	Si wafer	RTP	ITO15%-1-Si-RTP	SEM
	2	Si wafer	RTP	ITO15%-2-Si-RTP	AES
IZO (40 mol% Zn)	1	Glass	RTP	IZO40%-1-g-RTP	SEM, EDS, P, E, AFM
	2	Glass	RTP	IZO40%-2-g-RTP	SEM
	3	Glass	RTP	IZO40%-3-g-RTP	SEM
	3	Glass	UV	IZO40%-3-g-UV	SEM
	3	Glass	UVHT	IZO40%-3-g-UVHT	SEM
	1	Si wafer	RTP	IZO40%-1-Si-RTP	SEM
	2	Si wafer	RTP	IZO40%-2-Si-RTP	E, SEM
	3	Si wafer	RTP	IZO40%-3-Si-RTP	SEM
	3	Si wafer	UV	IZO40%-3-Si-UV	SEM
	3	Si wafer	UVHT	IZO40%-3-Si-UVHT	E, SEM, EDS, AFM, P

Appendix C Study of Precipitation and Precursor Quality

C.1 Precipitation

The synthesis presented in the experimental part was utilized for making all the solutions. The IZO solutions became transparent during the steps of the synthesis, while the ITO solutions remained turbid. A higher tin content made the solutions more opaque as can be seen in Figure C.1. In the figure solutions nr 1 are depicted, but they are representative for solutions nr 2 and nr 3. For explanation on the different solution nr, see the experimental section "3.1.2 Parameters". The photograph was taken directly after synthesis.

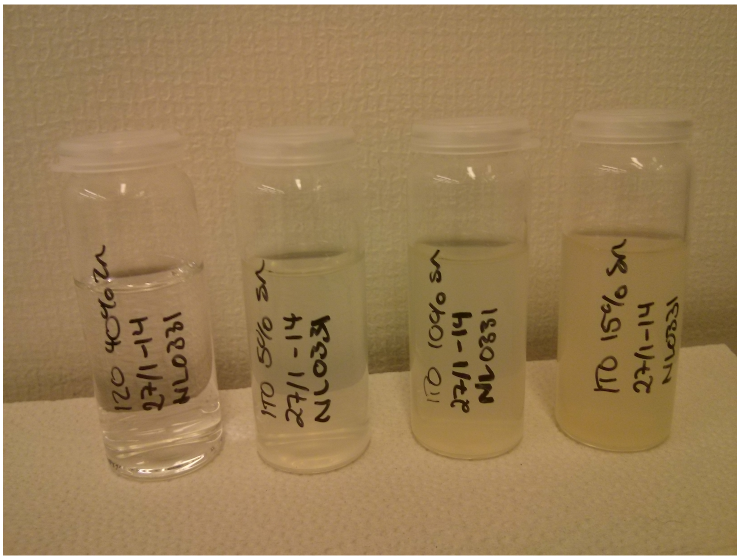

Figure C.1: A photograph of the four different solutions directly after synthesis. From the left the IZO40%, ITO5%, ITO10%, and ITO15% solution nr 1 are seen.

After less than 1 hour a thin layer of light yellow precipitate was visible at the bottom of the ITO solutions as shown in figures C.2 and C.3. Amount of precipitate was proportional to level of tin doping, and more precipitated out in the more concentrated solution. Thus it seems, that the solubility limit of tin in the solution was reached. When making the films the transparent top part of the ITO solutions was used. The precipitation was not removed from the solutions before making the films as it could be in equilibrium with the solution. Removing the precipitation would then cause more to precipitate out, lowering the percentage of tin doping in the films even more. The IZO solutions were still transparent during the thin film synthesis.

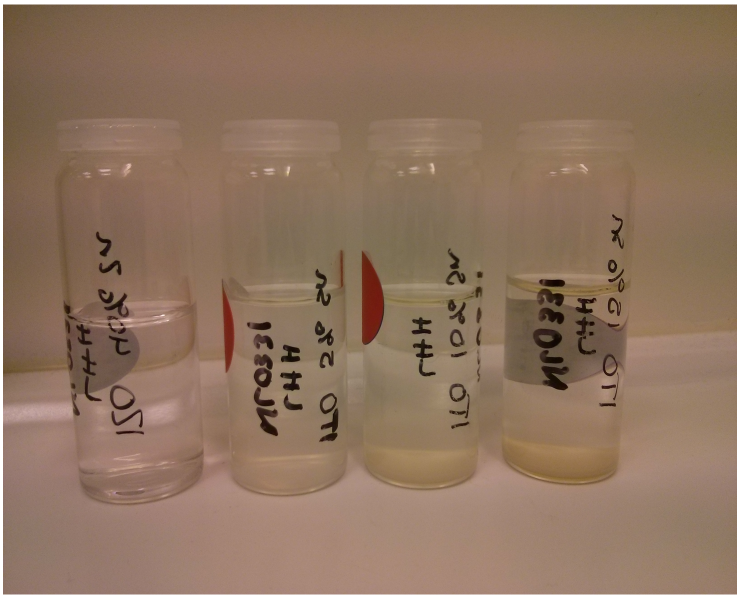

Figure C.2: A light yellow precipitate could be seen at the bottom of the ITO solutions less than 1 hour after the solution synthesis. From the left the IZO40%, ITO5%, ITO10%, and ITO15% solution nr 1 are seen.

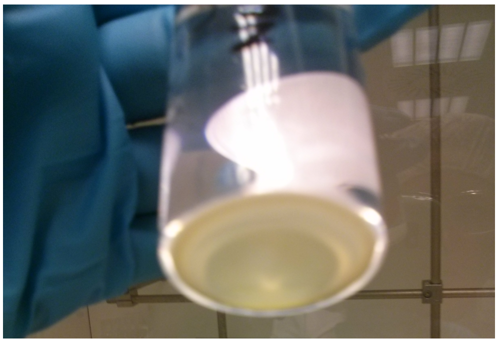

Figure C.3: Close-up of the precipitate in the ITO15% solution.

A visual study of the solutions was performed when the solution age of solutions nr 1 was 70 days, solutions nr 2 was 64 days and solutions nr 3 was 8 days. A photograph of solutions nr 1 is seen in Figure C.4. For all the ITO solutions the amount of precipitate seemed to be constant with time, but it looked as if the precipitate had crystallized. For solutions nr 2, where the precipitate had been removed at a solution age of 10 days, no new precipitate could be seen. This indicates that there was no equilibrium between the precipitate and solution that would cause new precipitate to appear after removal.

In addition to the crystallization of the precipitate, uniformly distributed small crystals had formed in all the solutions, including the IZO solutions. This gave the ITO solutions an opaque look while the IZO solutions remained transparent, as the amount of crystals here were way less than the amount of crystals in the ITO solutions. For the ITO solutions, the crystals in the solution look similar to the crystallized precipitate. The crystals were easily visible for the naked eye, but it was not possible to photograph them by using a standard camera.

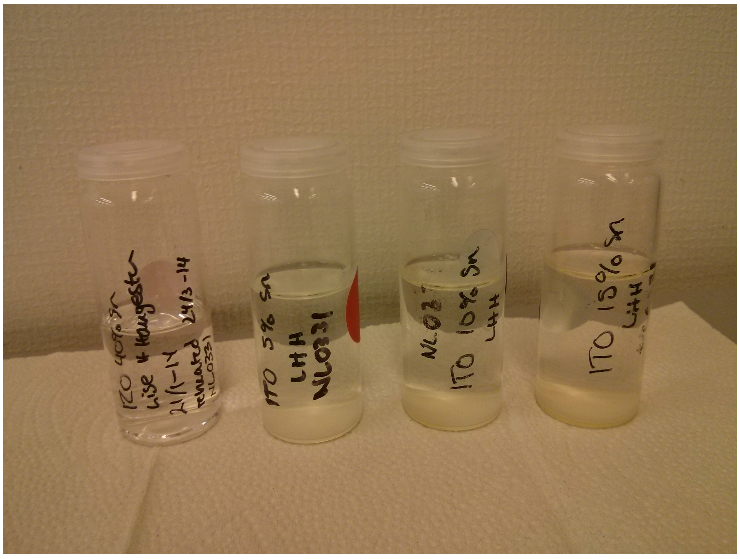

Figure C.4: From the left the IZO40%, ITO5%, ITO10%, and ITO15% solution nr 1 are seen, all with a solution age of 70 days.

The precipitation was considered to be SnO_2, but it was decided to study this closer. To separate out the precipitate from the solution it was attempted to filter the ITO5% solution using a nuclepore filter with 0.1 μm pores on top of a glass microfiber filter with particle retention of 0.7 μm. This turned out to be impossible as the solution clogged the filter and foamed extensivly. The solution ended up being filtered only through the glass microfiber filter. Based on this it was decided to decant the ITO10% and ITO15% solutions. The precipitation in the vials and on the filter was dried in room temperature for 3 days. When this did not yield any effect, the precipitation was dried in an oven at 80 ºC for 6 hours. A temperature of 80 ºC was used to avoid melting of the nuclepore filter. In Figure C.5 the dried precipitation from the ITO10% and ITO15% solutions is depicted showing a yellow powder. The study was only done for solution nr 2.

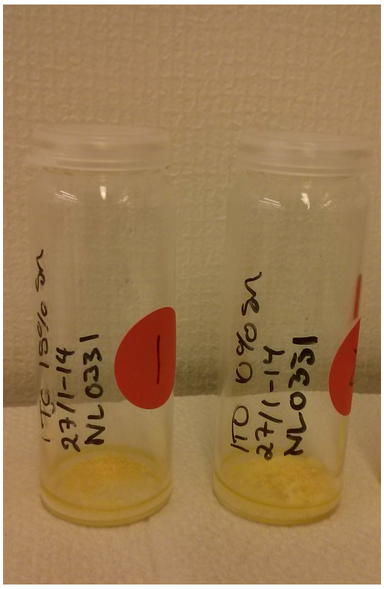

Figure C.5: The precipitate was a yellow powder after drying. The vial to the left and right contains the precipitation from the ITO15% and ITO10% solution respectively.

X-ray diffraction was used to determine the structure of the precipitate. The powders were dispersed in isopropanol and distributed on a holder with an integrated single crystal silicon wafer. Figure C.6 shows the full diffractogram for the precipitate from the ITO10% solution, while Figure C.8 shows the equivalent diffractogram for the ITO15% solution. Figure C.7 and Figure C.9 show close-up diffractograms of the 20° to 40° 2θ region of the diffractograms for the precipitate from the ITO10% and ITO15% solutions respectively. A Bruker D8 Focus X-Ray Diffractometer with $CuK\alpha_1$ radiation in the θ-2θ mode and a scanning time of 60 minutes was used for all the diffractograms in this appendix.

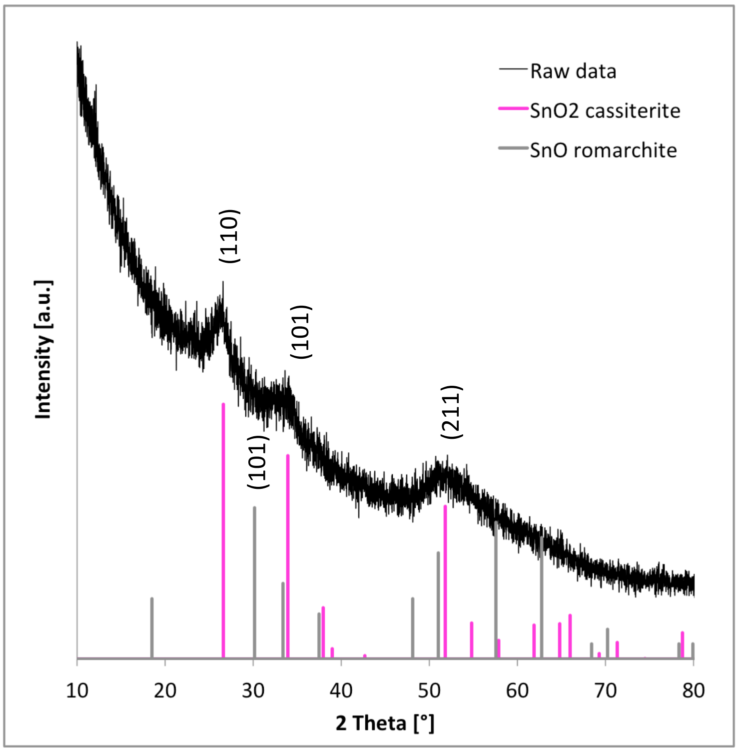

Figure C.6: Full diffractogram for the precipitate from the ITO10% solution together with reference patterns for the SnO_2 cassiterite and SnO romarchite crystal structure.

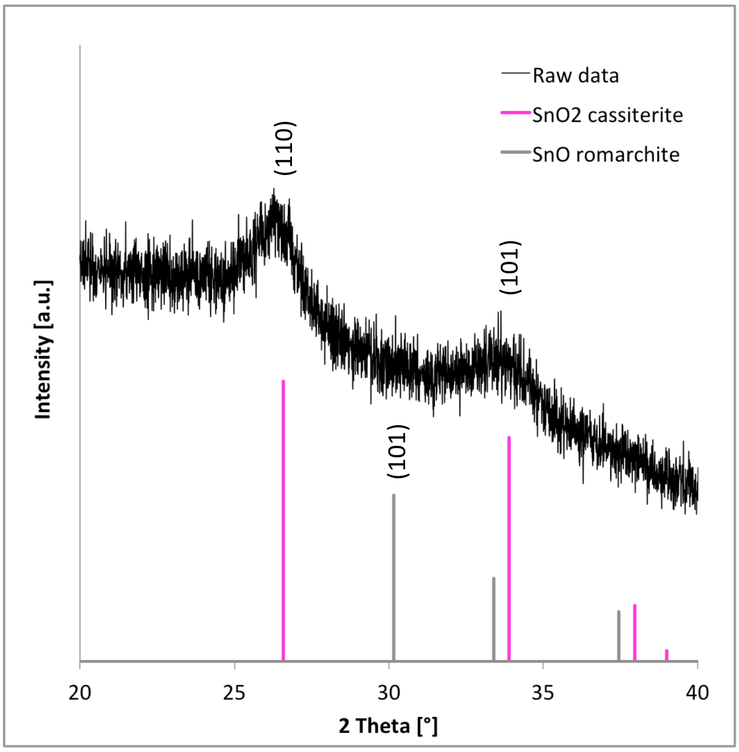

Figure C.7: A diffractogram of the 20º to 40º 2θ region for the precipitate from the ITO10% solution together with reference patterns for the SnO_2 cassiterite and SnO romarchite crystal structure.

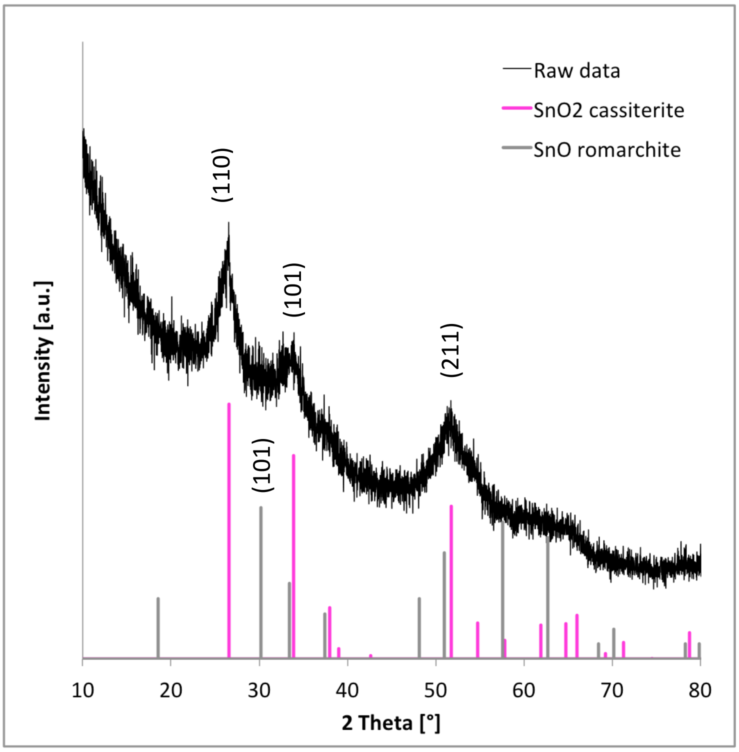

Figure C.8: Full diffractogram for the precipitate from the ITO15% solution together with reference patterns for the SnO_2 cassiterite and SnO romarchite crystal structure.

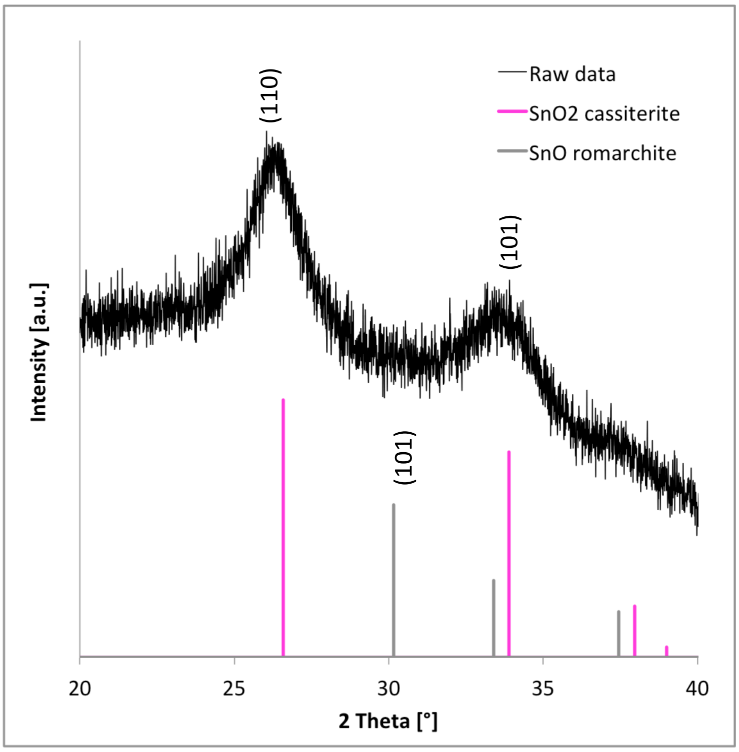

Figure C.9: Diffractogram of the 20º to 40º 2θ region for the precipitate from the ITO15% solution together with reference patterns for the SnO_2 cassiterite and SnO romarchite crystal structure.

From these diffractograms it can be determined that the precipitate is SnO_2 and that SnO is not present. By only looking at the full diffractograms it was not possible to exclude SnO, which has its main peak along the (101) crystal plane, due to a too high background noise. For the close-up diffractograms smaller step size was used and longer time was spent at each step, thus it can clearly be seen that there is no SnO structured phase present.

The number of moles tin precipitated was determined based on the weight of the precipitate and the X-ray diffraction results above. Compared to the number of moles tin put in, the calculations showed that more tin had precipitated out than the amount of tin put in. These results are obviously misleading, and are most likely caused by the presence of water in the powders. To evaporate the water, the powders should have been heated to above 100 ºC and weighed again. This could not be done as the powders had already been rinsed out to obtain the weight of the empty vials. The weight of the vials should have been obtained in advance of the solution synthesis, but this was not thought of at the present. Thus when the results was obtained it was realized that the powder should not have been rinsed out, but kept in the event that further analysis was necessary. The attempt to determine the actual concentration of tin in the remaining solutions after removing the precipitation therefore failed.

Through the study of the precipitation two possible explanations for the formation of SnO_2 was found. The pH of the indium nitrate standardized solution was measured, and a resulting pH = 1.17 was found. It is known that SnO_2 precipitates out in acidic solutions. Thus, it is possible that only a small concentration of tin is soluble in the solution and that the amount tin put in is irrelevant as long as it exceeds the solubility limit. It is also likely that SnO_2 has formed due to oxidation of the tin (II) acetate precursor. SnO_2 may have formed due to contact between oxygen in the air and the tin (II) acetate precursor in the opened box. It can also have formed during synthesis, as the synthesis was performed in ambient conditions in a fume hood.

C.2 Study of Precursor

A further study of the precursor was performed based on the discussion in the above section. The goal was to determine the present quality of the precursor, as the box had been open for a while and it had also been used in different projects.

Thermogravimetrical analysis (TGA, Netzsch, STA 449 C) was used to study if the tin (II) acetate precursor had oxidized in the box and to what extent. Figure C.10 shows the thermogravimetrical analysis curve obtained using a heating and cooling rate of 10 ºC/min and a peak temperature of 1000 ºC. The total weight loss is 64 %. By calculating the ideal weight loss when tin (II) acetate ($Sn(CH_3COO)_2$) oxidize to tin oxide (SnO_2) a weight loss of 36 % is expected. A much higher weight loss is seen here. This does not support the theory that the precursor has oxidized substantially, but oxidation of the precursor cannot be excluded. The problem is that the starting composition is unknown. It is likely that some water has bonded to the tin (II) acetate as tin (II) acetate is easily hydrated, even though tin (II) acetate is not suppose to have any crystal water. If it is assumed that the extra weight loss of 28 % is caused by water, this will correspond to 1.5 water molecules. But, if some tin (II) acetate actually has oxidized already more water could be present. By starting at 36 % at the relative mass and adding the weight gain of the organics the relative mass ends up at 72 % of the relative mass. This corresponds to 200 ºC on the x-axis in Figure C.10. It is mainly organics that are being decomposed above 200 °C and most of the water evaporates below. Differential scanning calorimetry (DSC) was also performed and the large exothermic peak at ~ 350 ºC could correspond to the combustion of organics. The endothermic peaks can correspond to evaporation of water.

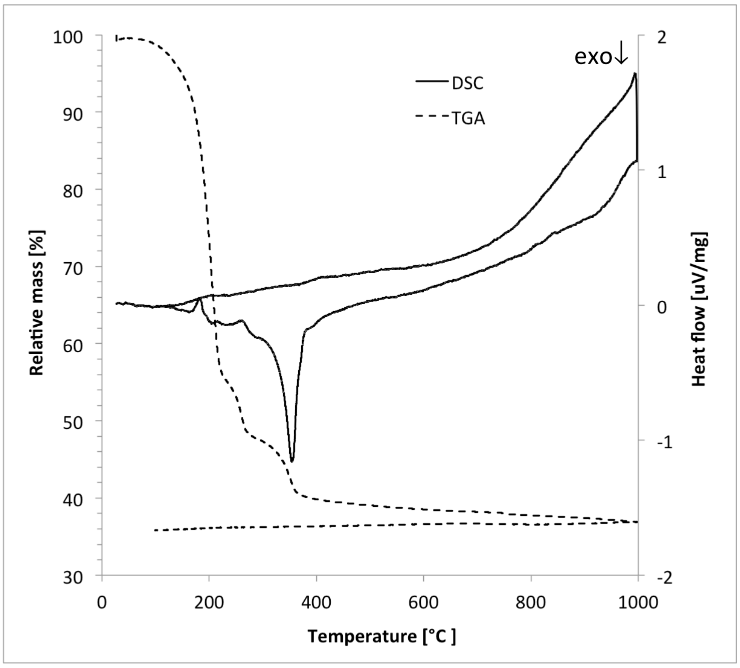

Figure C.10: Thermogravimetrical analysis (TGA) and differential scanning calorimetry (DSC) curves for the tin (II) acetate precursor.

Thermogravimetrical analysis and differential scanning calorimetry was also performed on the zinc acetate dihydrate precursor for comparison, but this chemical combusted in an extreme matter throwing material out of the crucible. These results could thus not be used, and it was decided not to study this precursor further as the IZO solutions had the wanted apperance.

It was desired to do X-ray diffraction on the oxidized product from the thermogravimetrical analysis, but the amount of powder was too little. Instead, a simulation of the thermogravimetrical analysis experiment was perfomed in a calcination furnace using a solution of tin (II) acetate precursor in deionized water. The reason for tin (II) acetate being dissolved in deionized water was because rest of the tin (II) acetate precursor had been used up in a test were it was solved in deionzied water. As the test was a failure some of it was used in this simulation instead. The heating program for the simualtion consisted of four steps. First step was heating from room temperature to 100 ºC at a rate of 50 ºC/h. Then the temperature was held at this value for 3 hours to evaporate the water. Third step was heating with a rate of 200 ºC/h to the peak temperature of 800 ºC. The last step was cooling at a rate of 200 ºC/h until room temperature was reached. The heating program is shown in Figure C.11. The peak temperature of 800 ºC was chosen based on the thermogravimetrical analysis curve. From the thermogravimetrical analysis curve it is seen that the oxidation of the tin (II) acetate is complete well before 1000 ºC, so it is satisfying to use 800 ºC as the peak temperature.

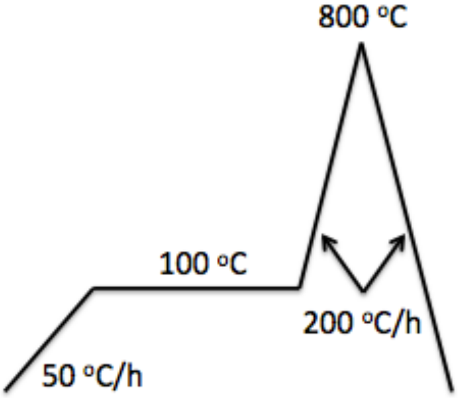

Figure C.11: Heating program for oxidation of the tin (II) acetate precursor.

The photograph in Figure C.12 shows the resulting powder after heating the tin (II) acetate precursor. The appearance of the powder is white to light yellow.

Figure C.12: Photograph showing the resulting powder after heating the tin (II) acetate precursor to 800 ºC in a calcination furnace.

The powder from the oxidized precursor was studied using X-ray diffraction. A sample holder was filled with the powder in such a manner that the powder had a plane surface in the same height level as the edge of the sample holder. The resulting diffractograms are shown in Figure C.13 and C.14, were the first one is from 10º to 80º 2θ and the second is from 20º to 40º 2θ. The peaks correspond to SnO_2 except for the two peaks marked with an asterisk.

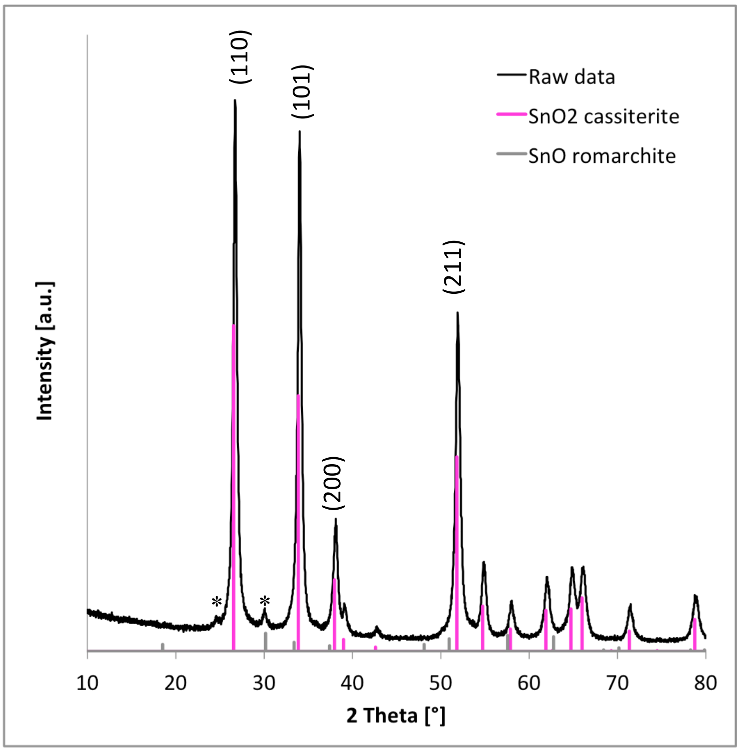

Figure C.13: Diffractogram for the tin (II) acetate precursor oxidized at 800 ºC together with reference patterns for the SnO_2 cassiterite and SnO romarchite crystal structure.

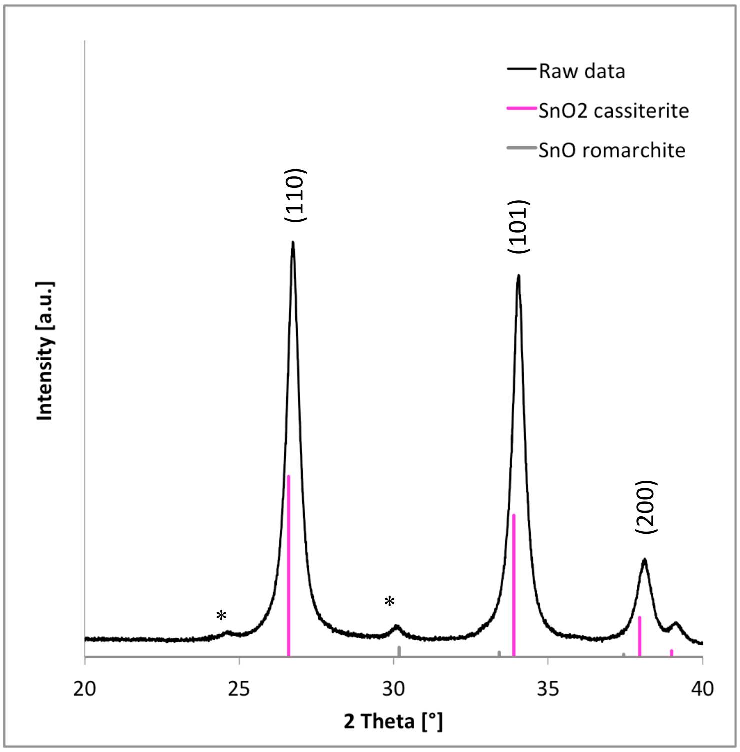

Figure C.14: Diffractogram from 20º to 40º 2θ for the tin (II) acetate precursor oxidized at 800 ºC together with reference patterns for the SnO_2 cassiterite and SnO romarchite crystal structure.

The peaks marked with an asterisk might be due to a contamination. This was further investigated by utilizing an energy dispersive X-ray spectrometer (EDS, Oxford Instruments Aztec Automate system, with an 80 mm^2 X-Max detector) mounted on a SEM (Hitachi S-3400N). Three different areas of the powder were scanned to quantify the composition of the powder. The EDS spectrum from the oxidized precursor is given in Figure C.15. Signals from O, Sn, N and Cl can be seen, and by calculating an average value of the three spectra the mol% for the different chemical elements are 57.9, 40.0, 2.6, and 0.4 respectively.

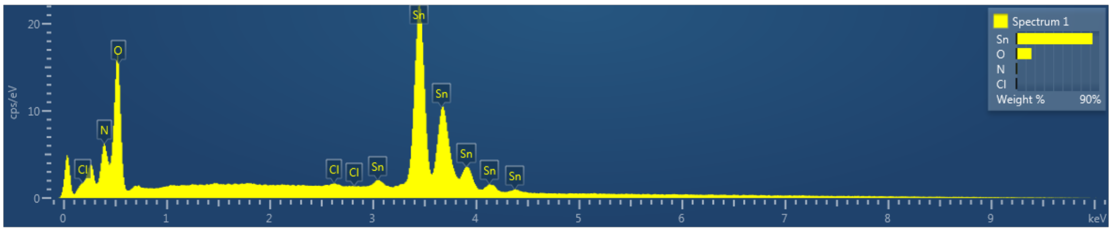

Figure C.15: EDS spectrum of the oxidized tin (II) acetate precursor.

When including O, Sn, N, and Cl in the matching search for the X-ray diffraction spectrum using the software by Bruker, Diffrac.Suite EVA V3.1 it was found that the main peak of the ClO_3 structure could match the first peak. The intensity of the main peak is low and the rest of the peaks for the ClO_3 structure could not be detected making it impossible to confirm or exclude the presence of the structure. If this structure is present it is only in small amounts, which also conforms to the EDS results. SnO and $N_{0.5}O_{0.5}$ were the only structures to fit the second peak. Thus, as no other metallic cation is present we cannot conclude that the precursor is contaminated. The nitrogen is most likely introduced from the air. The chloride is a bit hard to explain, but it could originate from a tin-chloride compound even though such compounds should have evaporated below 800 ºC.

Even though it could not be proved that the precursor was of bad quality (that it had oxidized in the box or that there were contaminations present) a new box of the same precursor was opened and used to make solution nr 3 directly after opening.

The last part of this study was to do X-ray diffraction on the new tin (II) acetate precursor to compare with the results from the old precursor. The new precursor was oxidized in a calcination furnace directly after opening of the box using the same heating program as for the old precursor, which is found in Figure C.11. The only difference was that the holding time at 100 ºC was 0.5 hours instead of 3 hours, as the precursor was not dispersed in deionized water. The resulting powder together with the untreated tin (II) acetate precursor can be seen in Figure C.16. The new tin (II) acetate precursor has the same appearance as the old, both in untreated and oxidized state. The untreated tin (II) acetate has a white color, while the oxidized powder has a white to light yellow color.

Figure C.16: Photograph of the new tin (II) acetate precursor. The untreated tin (II) acetate is to the left, while the tin (II) acetate heat treated at 800 ºC in a calcination furnace is seen to the right.

Figure C.17 shows the resulting diffractogram for the oxidized powder from the new precursor. Due to a small amount of resulting powder, the powder was dispersed in isopropanol and distributed on a holder with an integrated single crystal silicon wafer for the X-ray diffraction. Based on the diffractogram the oxidized powder is identified to be SnO_2. By comparing the diffractogram for the new and old precursor (Figure C.17 and C.13) all of the peaks match except for the two peaks with the asterisk. These two peaks are not seen in the new precursor. This indicate that there is a difference between the two precursors, and strengthens the hypothesis of the old precursor having a lower quality. The unknown peaks could also be caused by the dissolution of the old precursor in deionized water and the use of this solution in another test. For example the beaker used may not have been perfectly clean, which could have introduced impurities causing the unknown peaks. The same amount of precipitate is seen in solutions nr 3 of ITO made from the new precursor. This falsifies the hypothesis that oxidation of the precursor increases with time.

X-ray diffraction was also run on the new tin (II) acetate precursor before oxidation. The diffractogram can be seen in Figure C.18, and analysis shows that the diffractogram is consistent with the tin (II) acetate structure. Due to the large number of peaks it is difficult to spot potential peaks caused by a contamination. In addition no diffractogram was obtained for the old precursor such that a comparison could be made, as there were no more of the old precursor left when this was thought of. For the peaks marked with an asterisk in Figure C.18, the small double peak is not real, but is caused by an instrumental effect. For the first and third peak marked with an asterisk in the diffractogram the intensity relationship between the real and imaginary peak is out of balance, as the imaginary peak has a too high intensity. Why this is so, is hard to explain and will not be discussed further.

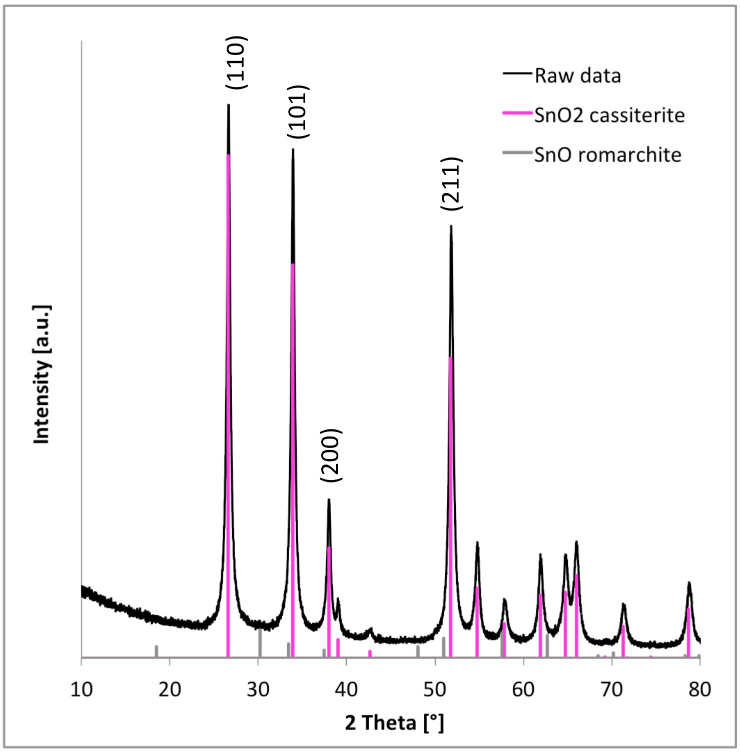

Figure C17: Diffractogram for the new tin (II) acetate precursor oxidized at 800 °C together with reference patterns for the SnO_2 cassiterite and SnO romarchite crystal structure.

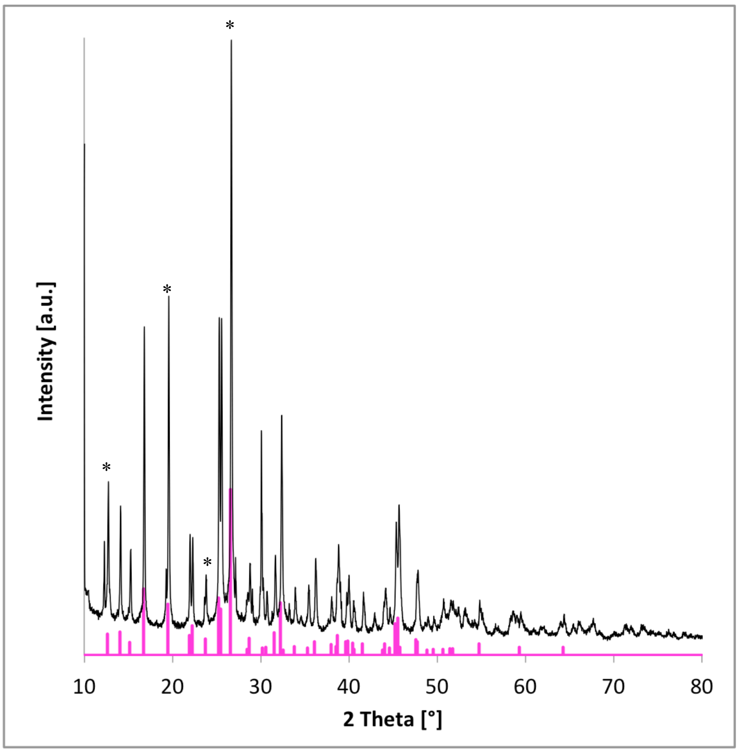

Figure C.18: Diffractogram for the tin (II) acetate precursor (black) together with the reference pattern for the tin (II) acetate structure (pink).

In conclusions, the precipitation was determined to be SnO_2, but it could not be determined what the cause of the precipitation was (see also section “4.1 Precipitation During Synthesis and Quality of Precursor” and “5.1 Precipitation During Synthesis and Quality of Precursor” in the results and discussion parts respectively). It could either be due to oxidation of the precursor in the box/during synthesis or due to a low solubility of tin in the solution.

Indications of a lower quality for the old precursor were found, but it could not be concluded on a specific contamination. It could not be determined whether the precursor had oxidized in the box or not, but it was found that the precursor did not oxidize an extended amount with time.

Appendix D Pawley Refinement

Pawley refinement was used to extract information about the lattice parameter of the cubic bixbyite crystal structure that was obtained for all the thermally cured thin films. More on the bixbyite crystal structure is found in the theory section “2.1 Crystal Structure”. The lattice parameter calculations are based mainly on the peak positions in the diffractograms and not on the intensity of the peaks. The refinement was performed using a hkl-phase and the space group Ia3, number 206. The software used for the refinement was Diffrac.Suite Topas 4.2 by Bruker.

The refinement parameters for the thin films are listed in Table D.1, where R_{wp} is a measure of how good the calculated values fit with the raw data. This value should be as low as possible, but a value around 10 is generally thought to be good. During the refinement the calculated values are fitted to the raw data through an iteration process, and the process stops when the lowest possible R_{wp} is obtained. The error listed in Table D.1 is only statistical, and it is the difference between the last and second last R_{wp} value in the iteration process. Thus, this error value does not include errors in sample preparation. For thin films, errors induced from sample preparation are mainly related to the placement of the sample. For a perfect sample preparation, the thin film should be placed in the center with the surface parallel to and at the same height as the sample holder. The In_2O_3 thin film listed in Table D.1 was made in the specialization project [107].

The difference between the calculated values and the raw data is given as the misfit function in figures D.1 to D.21. Flat parts of the misfit function are parts of the diffractogram that is excluded in the refinement. These parts are not considered to reflect the sample, but are regarded as instrumental effects. The peaks seen in the area 54-57° 2θ, which are only observed for the thin films on silicon substrates, are thought to be caused by an interaction between the instrument and the silicon substrate (the same effect has been observed by others with thin films on silicon substrates on this instrument). The peak positions show the peaks of the In_2O_3 bixbyite crystal structure, in which the refinement calculations are based on.

Table D.1: Pauley refinement parameters for the In_2O_3, ITO and IZO thin films.

Thin film name	Lattice parameter [Å]	R_{wp}	Error
In_2O_3-g-RTP	10.1269799	9.907	0.0009989
ITO5%-1-g-RTP	10.1273174	5.400	0.0007882
ITO5%-2-g-RTP	10.1193697	12.555	0.0020286
ITO5%-1-Si-RTP	10.1059180	12.250	0.0005094
ITO5%-2-Si-RTP	10.1061754	9.750	0.0005886
ITO10%-1-g-RTP	10.1315484	5.567	0.0010971
ITO10%-2-g-RTP	10.1326999	6.429	0.0007504
ITO10%-3-g-RTP	10.1236660	9.502	0.0011366
ITO10%-1-Si-RTP	10.1066469	12.364	0.0005483
ITO10%-2-Si-RTP	10.1090382	21.275	0.0014042
ITO10%-3-Si-RTP	10.1093112	16.520	0.0009324
ITO15%-1-g-RTP	10.1322523	5.112	0.0007869
ITO15%-2-g-RTP	10.1289915	8.700	0.0010828
ITO15%-1-Si-RTP	10.1148347	11.443	0.0005084
ITO15%-2-Si-RTP	10.1127949	10.844	0.0006294
IZO40%-1-g-RTP	10.0875083	4.836	0.0037767
IZO40%-2-g-RTP	10.0907425	6.441	0.0011782
IZO40%-3-g-RTP	10.0842993	9.407	0.0022551
IZO40%-1-Si-RTP	10.0988249	11.306	0.0005822
IZO40%-2-Si-RTP	10.1018403	9.989	0.0008957
IZO40%-3-Si-RTP	10.0821419	20.303	0.0015600

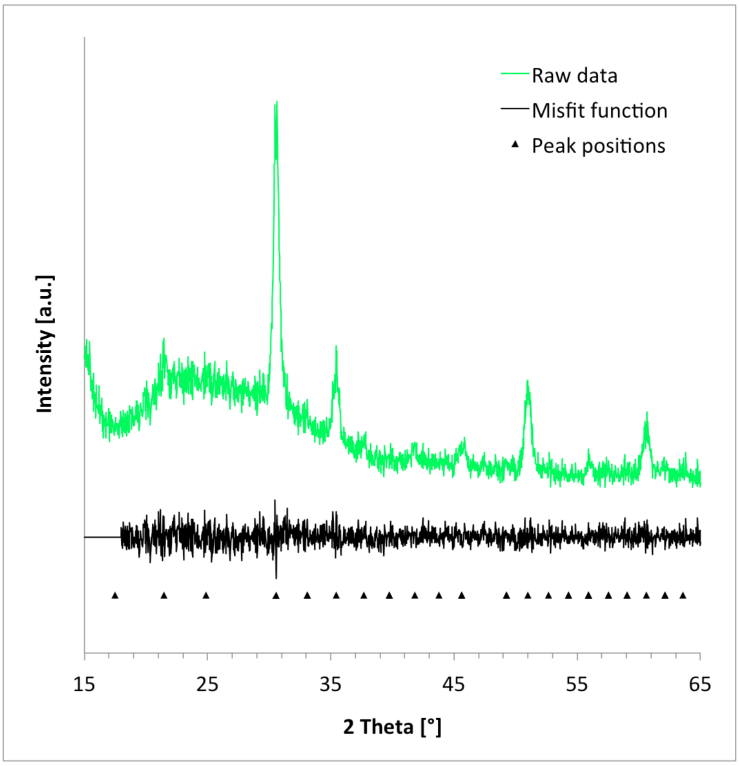

Figure D.1: The In_2O_3-g-RTP thin film made in the specialization project [107]. This diffractogram was obtained in the master thesis.

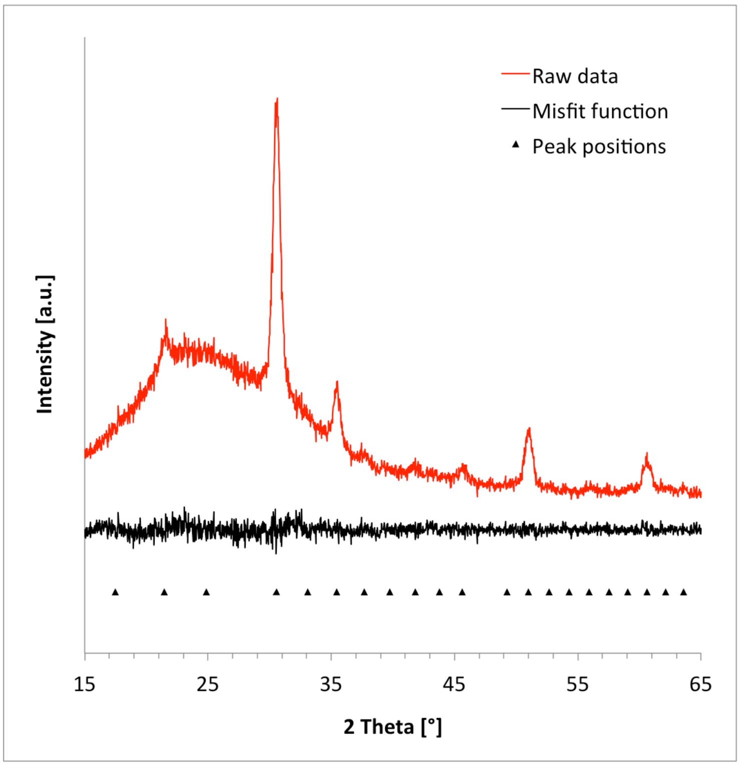

Figure D.2: The ITO5%-1-g-RTP thin film.

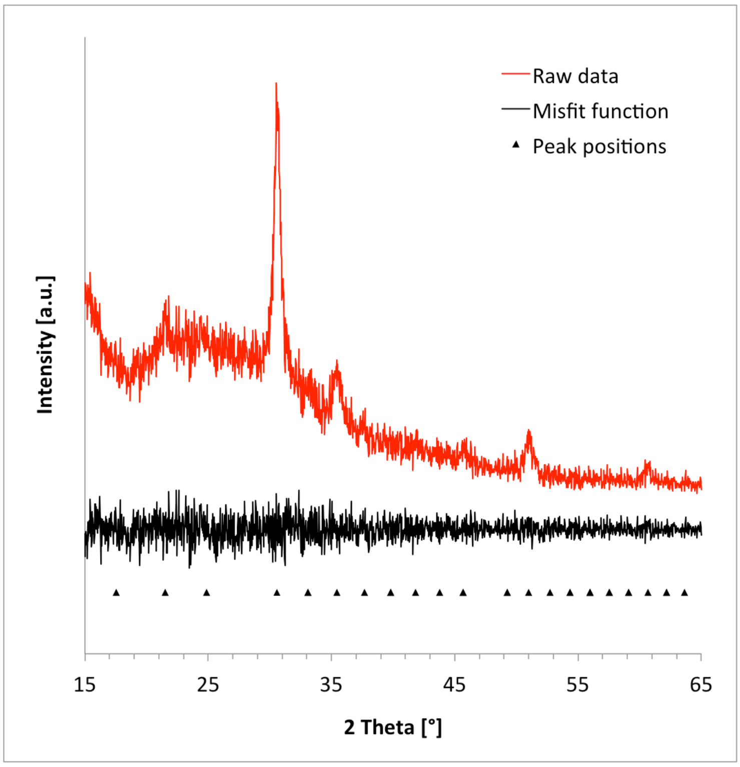

Figure D.3: The ITO5%-2-g-RTP thin film.

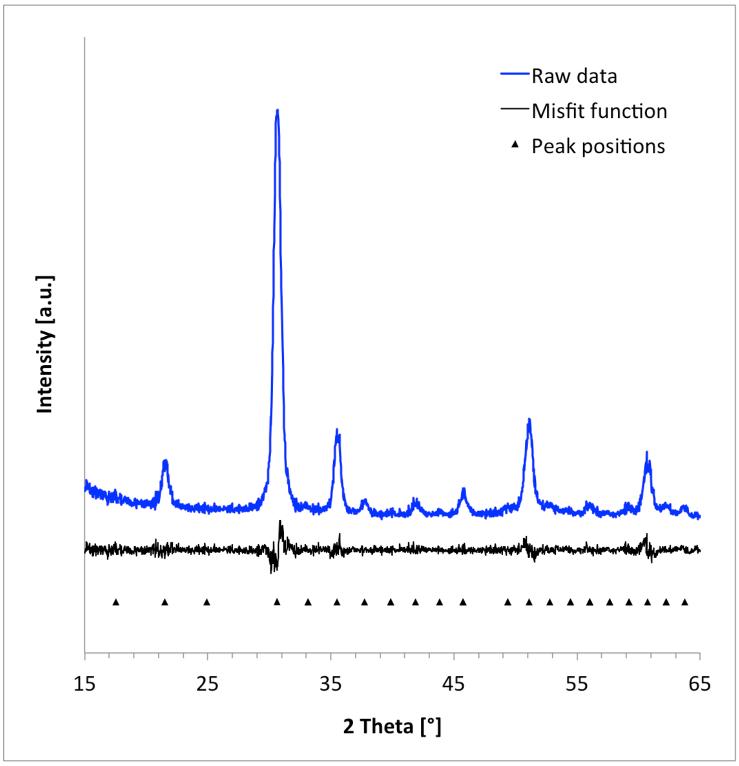

Figure D.4: The ITO5%-1-Si-RTP thin film.

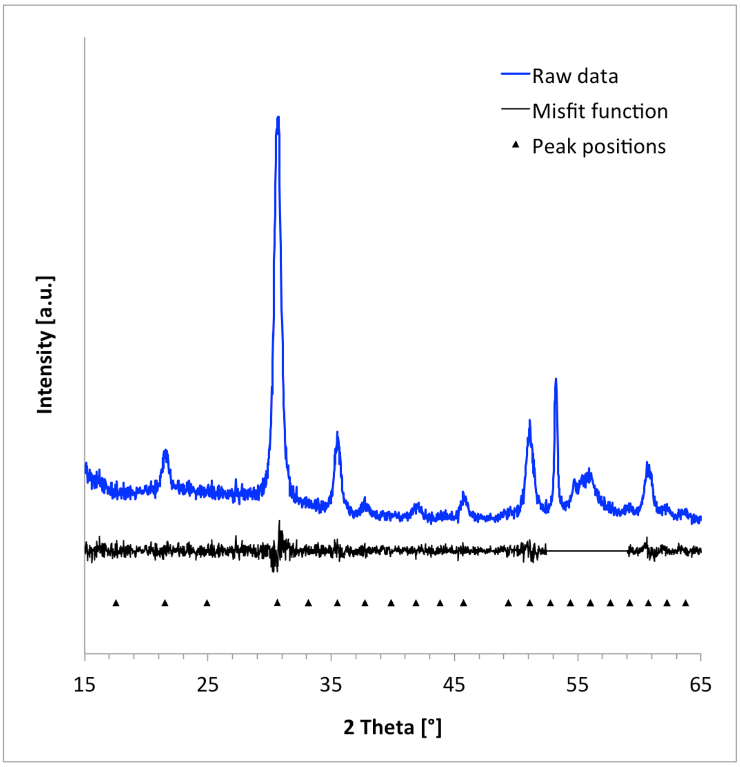

Figure D.5: The ITO5%-2-Si-RTP thin film.

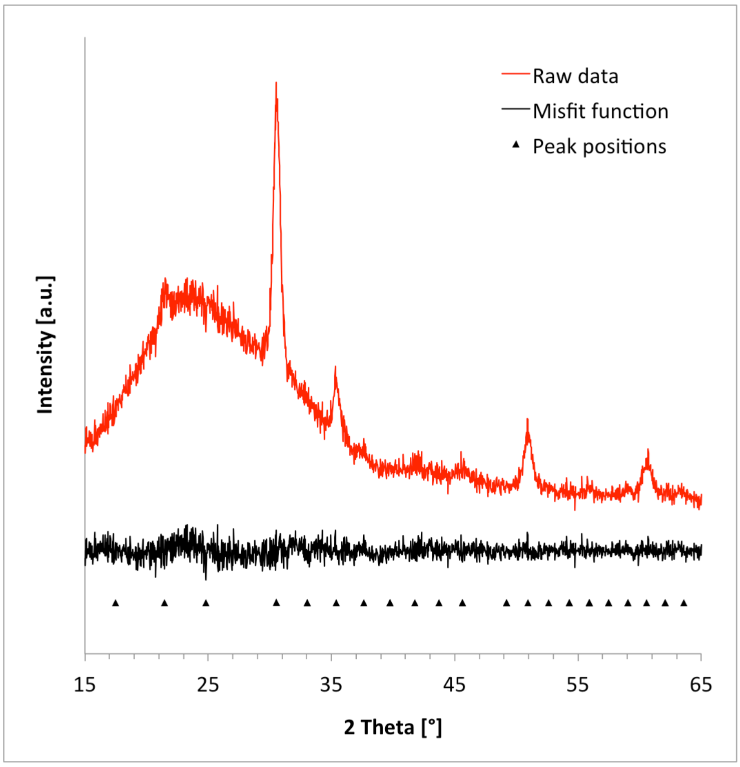

Figure D.6: The ITO10%-1-g-RTP thin film.

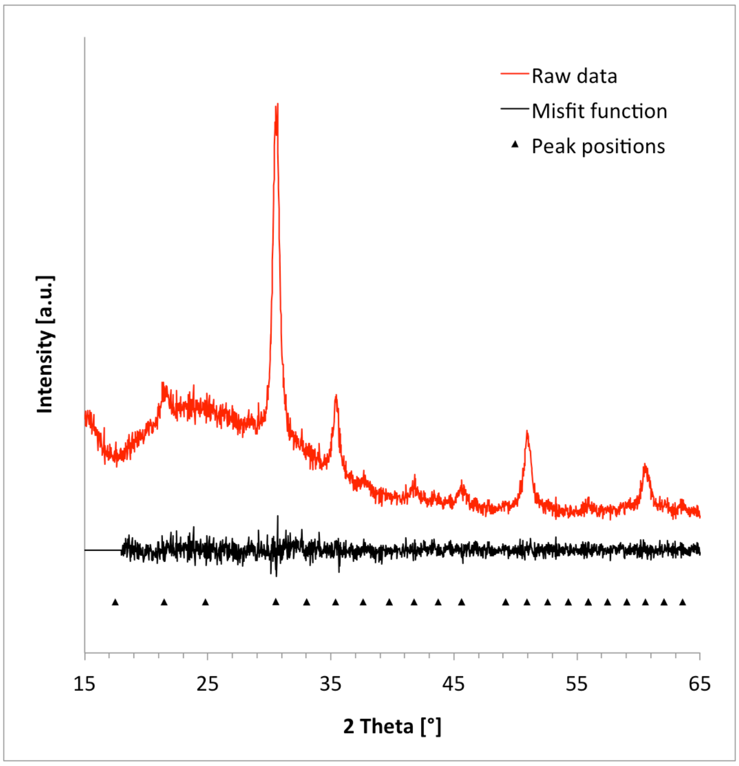

Figure D.7: The ITO10%-2-g-RTP thin film.

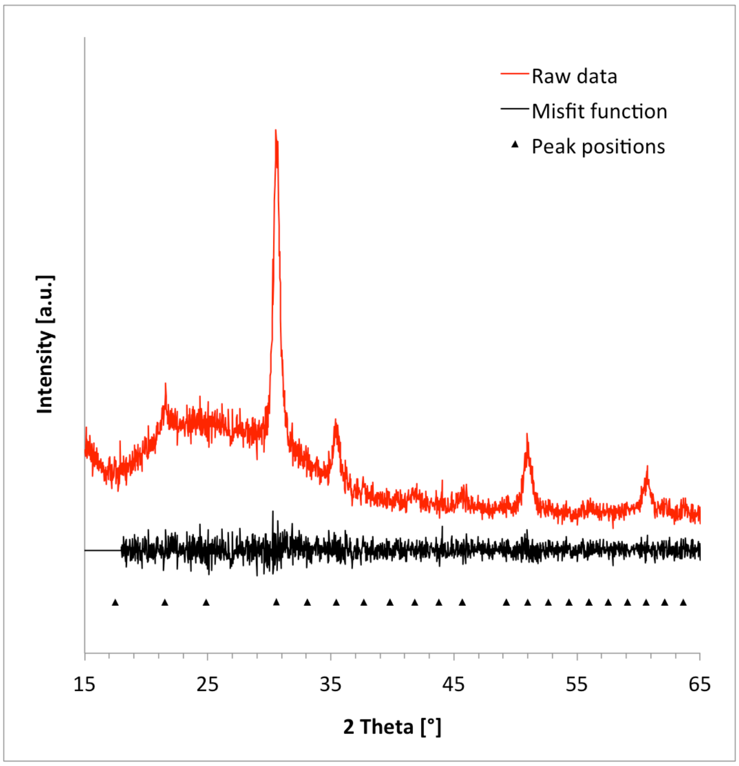

Figure D.8: The ITO10%-3-g-RTP thin film.

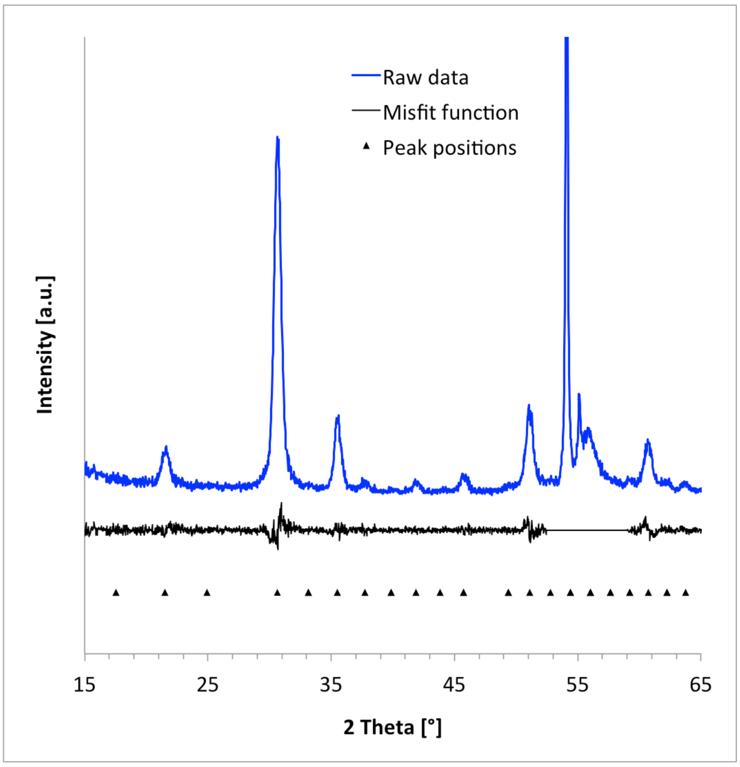

Figure D.9: The ITO10%-1-Si-RTP thin film.

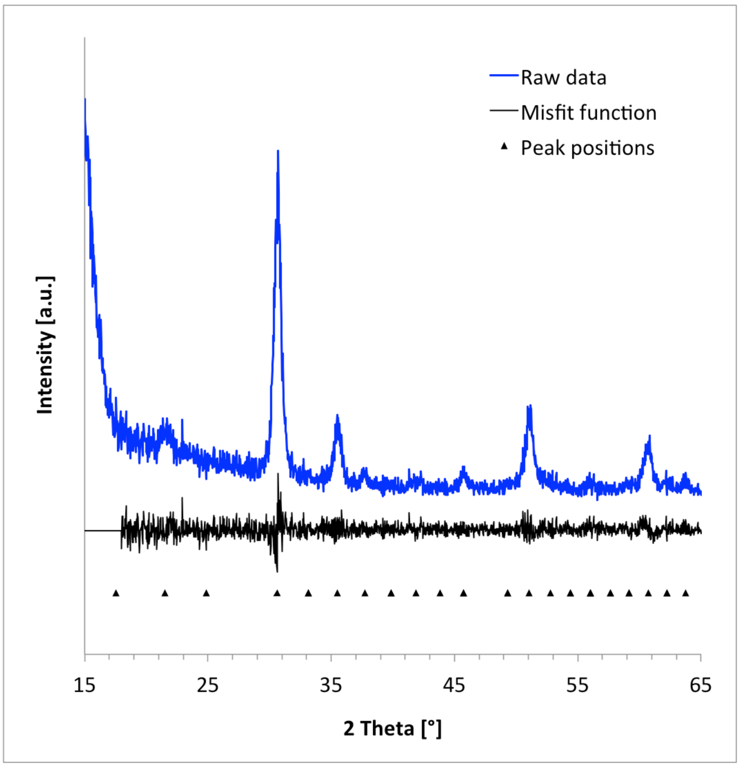

Figure D.10: The ITO10%-2-Si-RTP thin film.

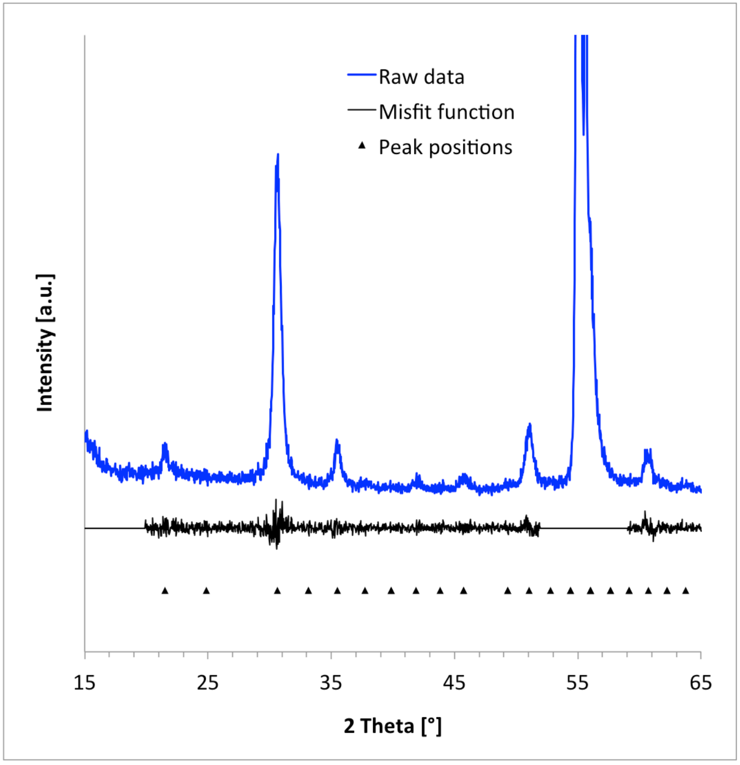

Figure D.11: The ITO10%-3-Si-RTP thin film.

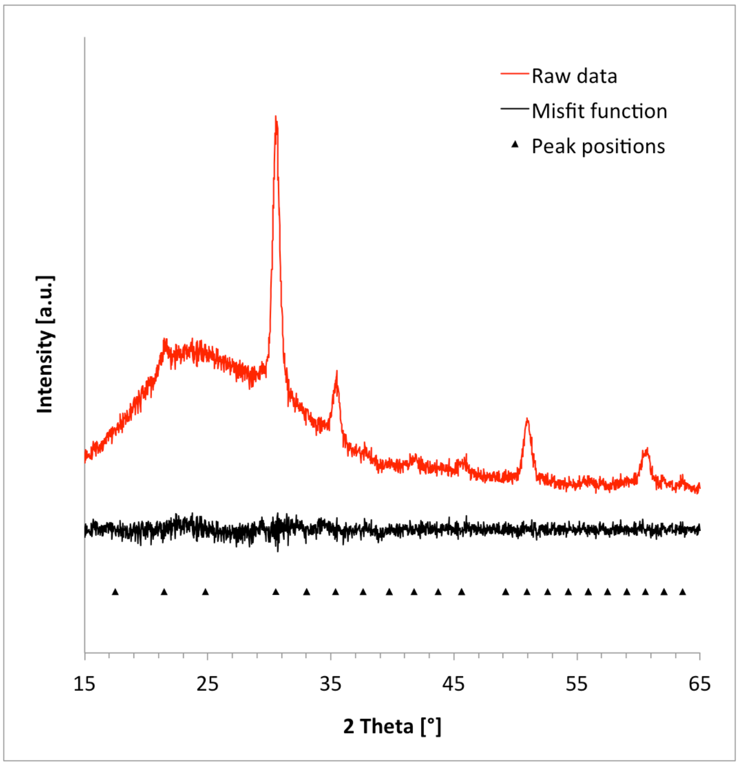

Figure D.12: The ITO15%-1-g-RTP thin film.

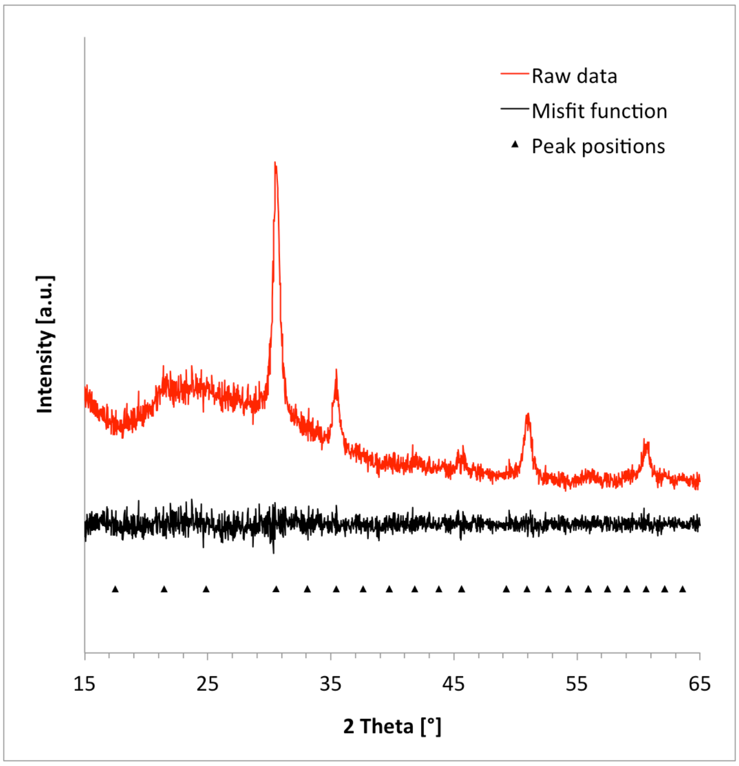

Figure D.13: The ITO15%-2-g-RTP thin film.

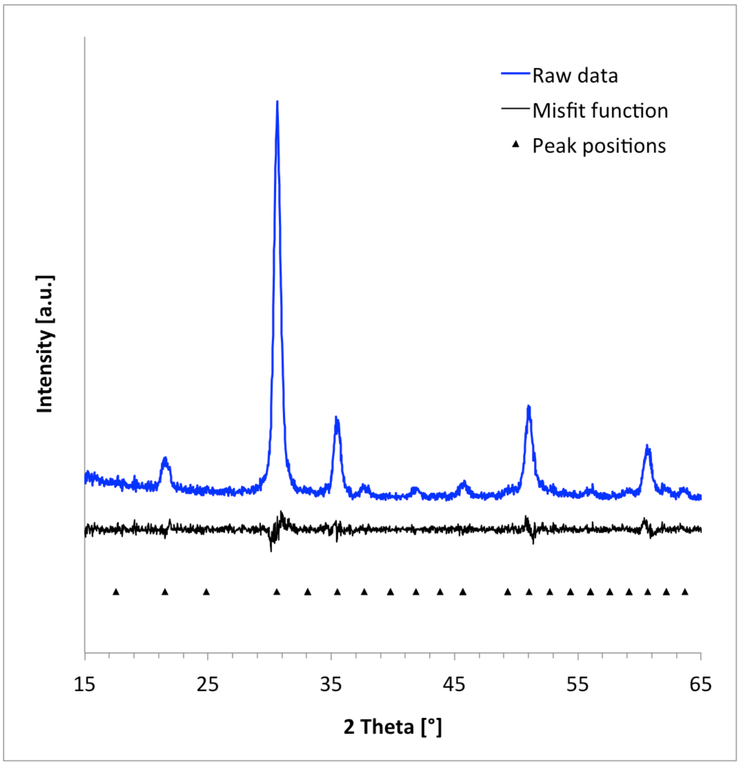

Figure D.14: The ITO15%-1-Si-RTP thin film.

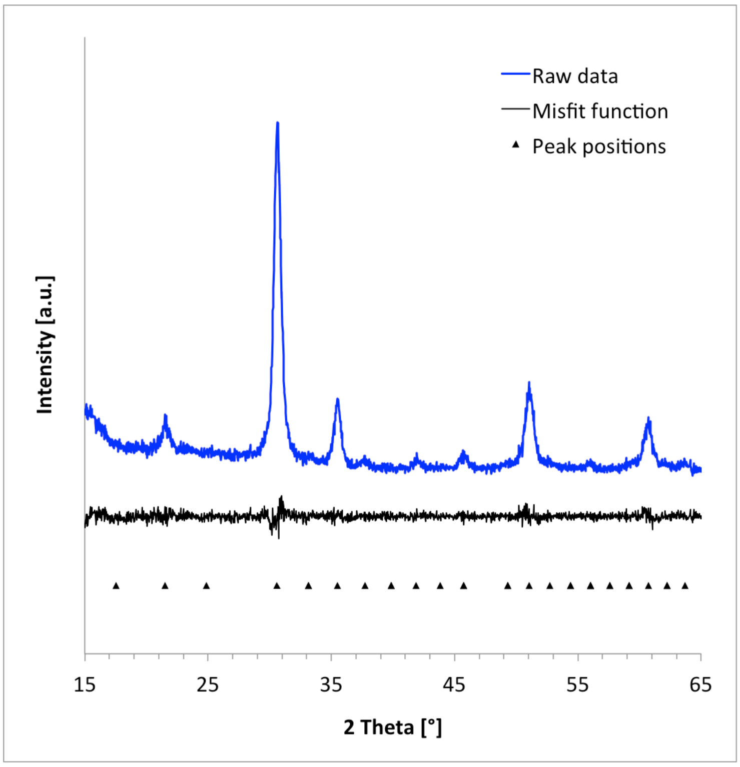

Figure D.15: The ITO15%-2-Si-RTP thin film.

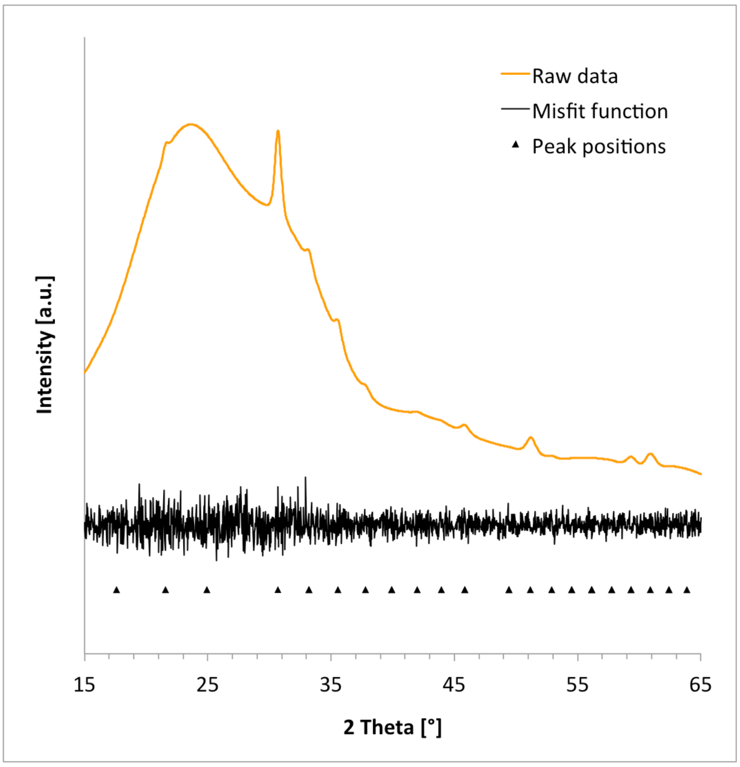

Figure D.16: The IZO40%-1-g-RTP thin film.

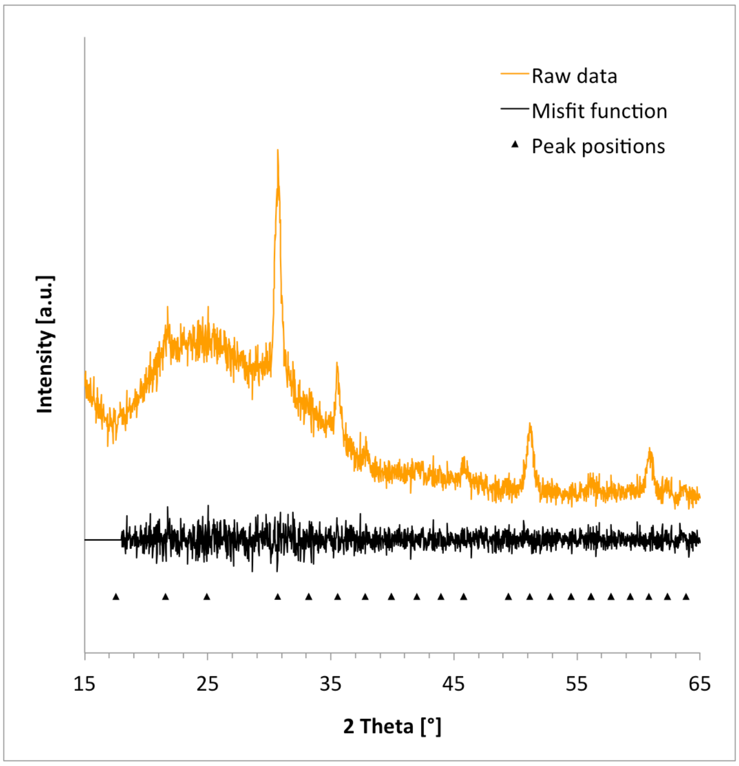

Figure D.17: The IZO40%-2-g-RTP thin film.

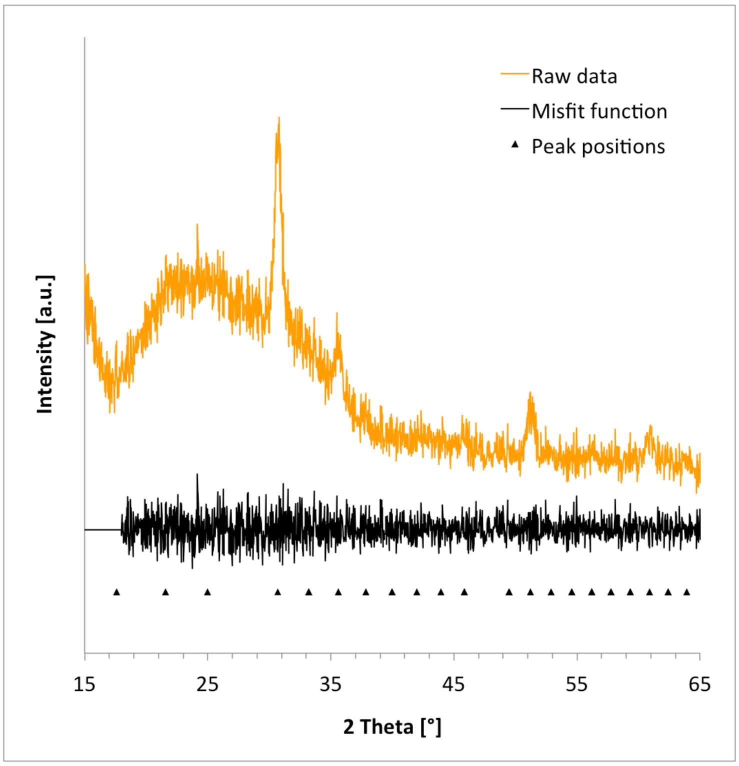

Figure D.18: The IZO40%-3-g-RTP thin film.

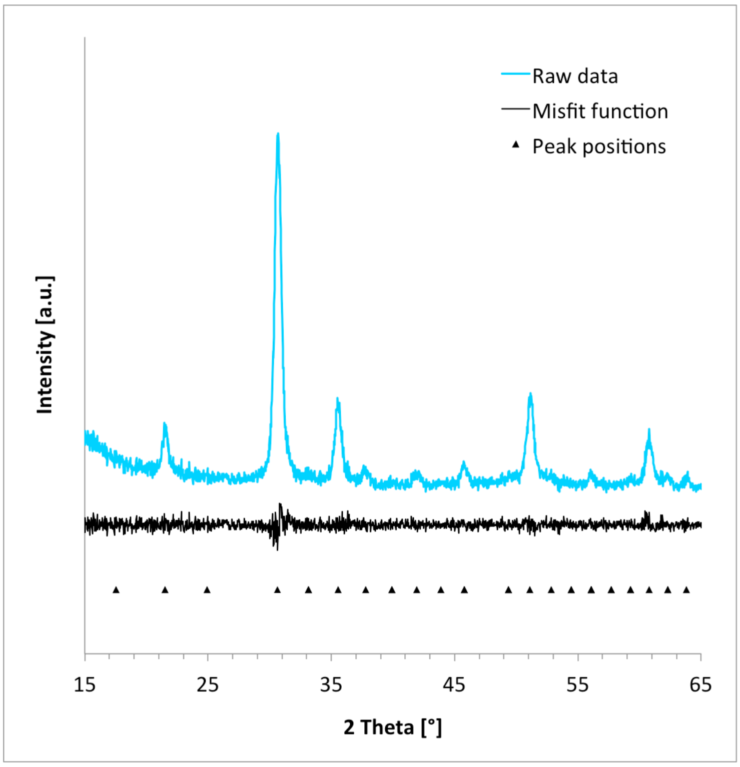

Figure D.19: The IZO40%-1-Si-RTP thin film.

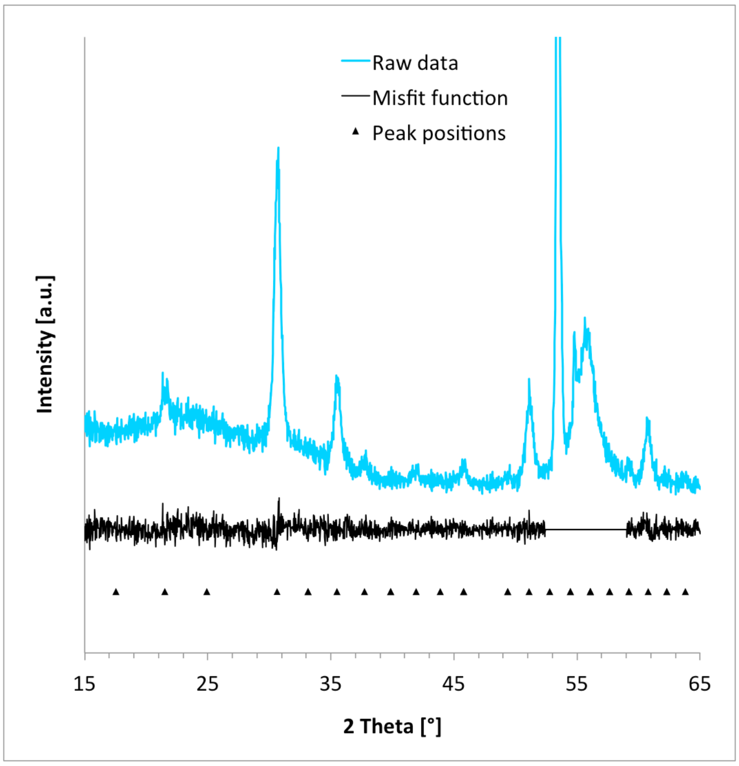

Figure D.20: The IZO40%-2-Si-RTP thin film.

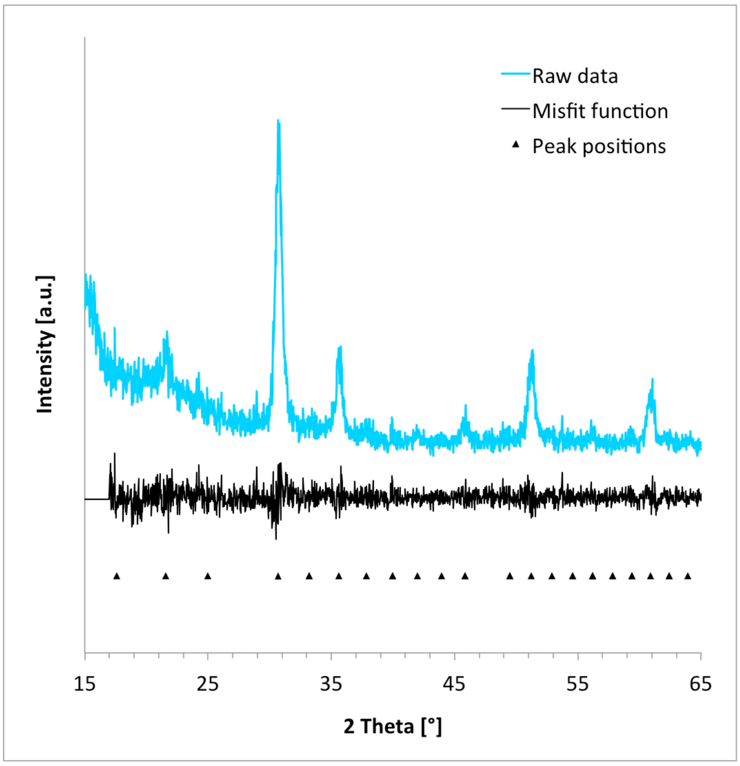

Figure D.21: The IZO40%-3-Si-RTP thin film.

Appendix E Morphology

Two different morphologies are found for the thermally cured IZO thin films. The one that was thought to be the most representative was chosen for the result part. By comparing Figure 4.30 in the result section “4.5 Morphology” with figures E.2 and E.3 it can be seen that Figure E.3 shows a different morphology. Since figures 4.30 and E.2 gave the same morphology the inhomogeneity seen in the optical light microscope in Figure 4.17 are not thought to be real, but caused by an instrumental effect. Since two out of three samples gave the same morphology in the SEM, and as the thin film in E.3 looks inhomogeneous across the sample in the optical light microscope (can be seen form Figure 4.18) the morphology in Figure 4.30 and E.2 was chosen to be the representative.

The thermally cured ITO and IZO thin films on silicon substrate in Figure 4.31 and figures E.4 to E.7 are thought to be morphologically similar even though small variations are seen. This is based on how much variation that is seen in the structure of one thin film, which is illustrated by figures E.5 and E.6 where high magnification images for both points in Figure E.1 are presented. Thus, also the thermally cured IZO thin films on silicon substrates look the same for the three different solutions.

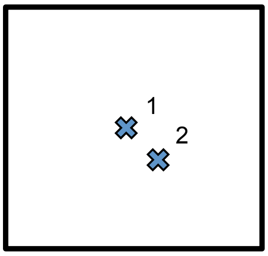

Figure E.1: A schematic illustrating where on the thin films the high magnification SEM images are taken.

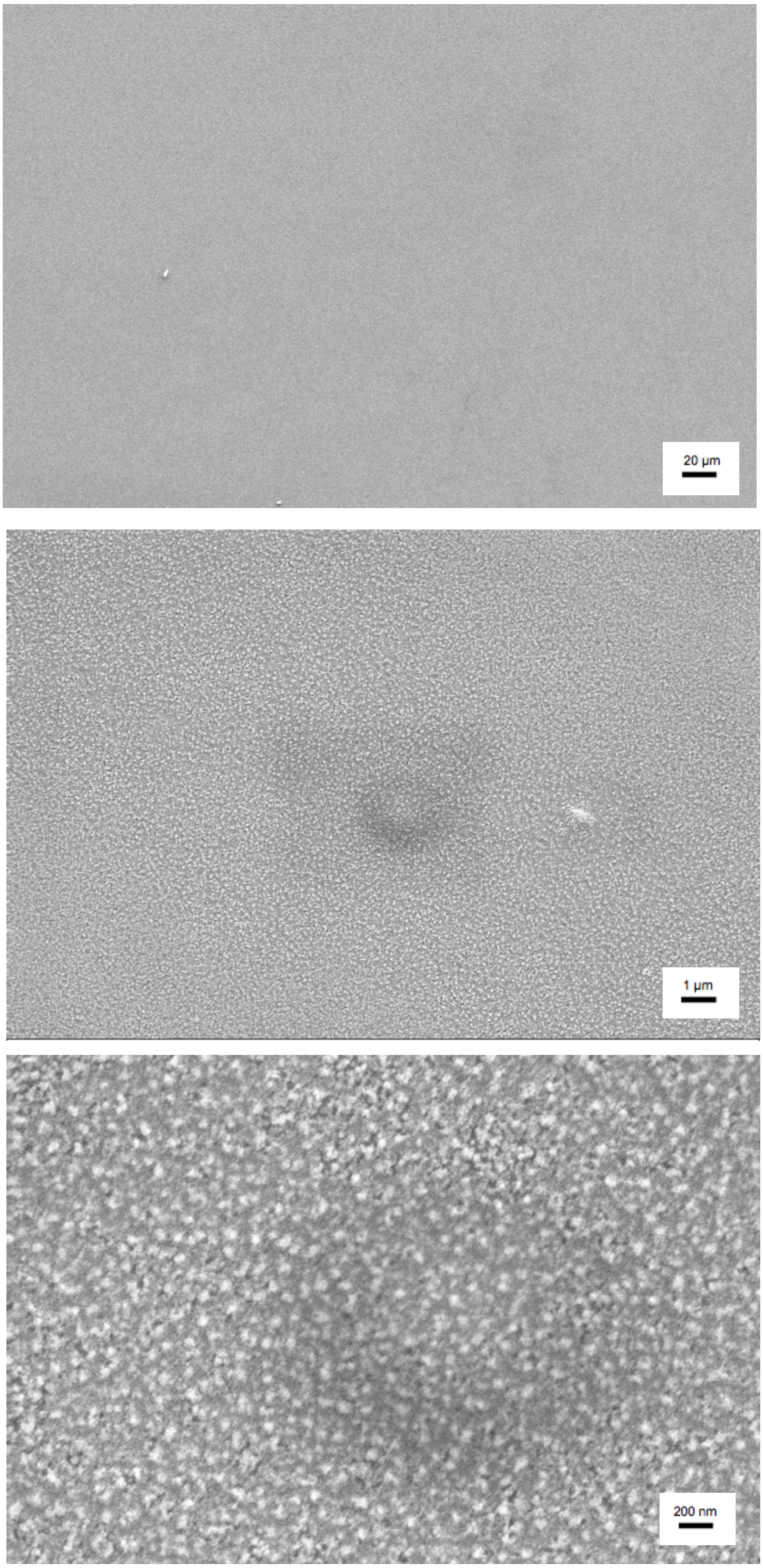

Figure E.2: SEM images of the IZO40%-2-g-RTP thin film. A square with a circle inside is seen in the center of the middle image. This is not a feature in the thin film, but a beam damage effect. The lower image shows the same beam damage, only zoomed in.

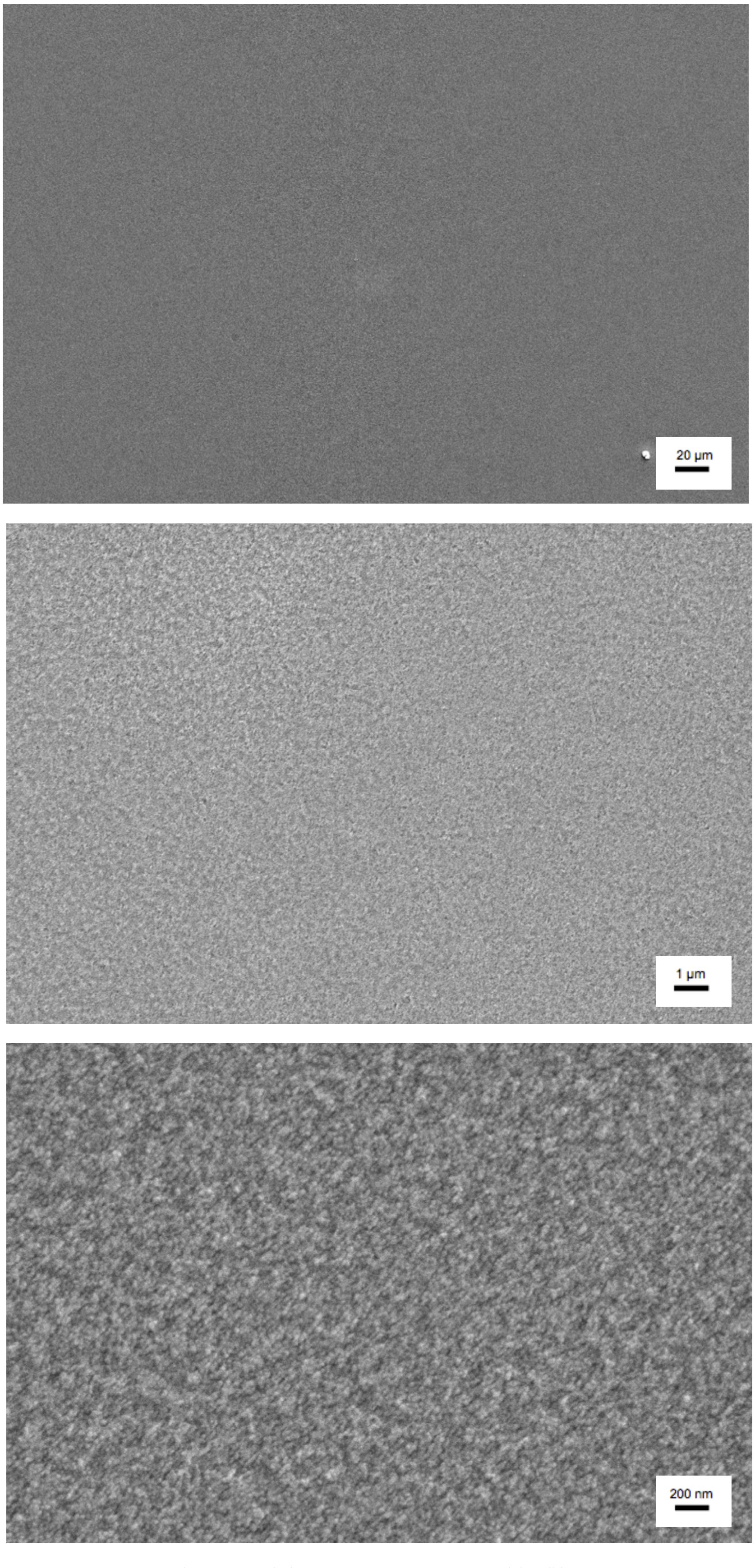

Figure E.3: SEM images of the IZO40%-3-g-RTP thin film.

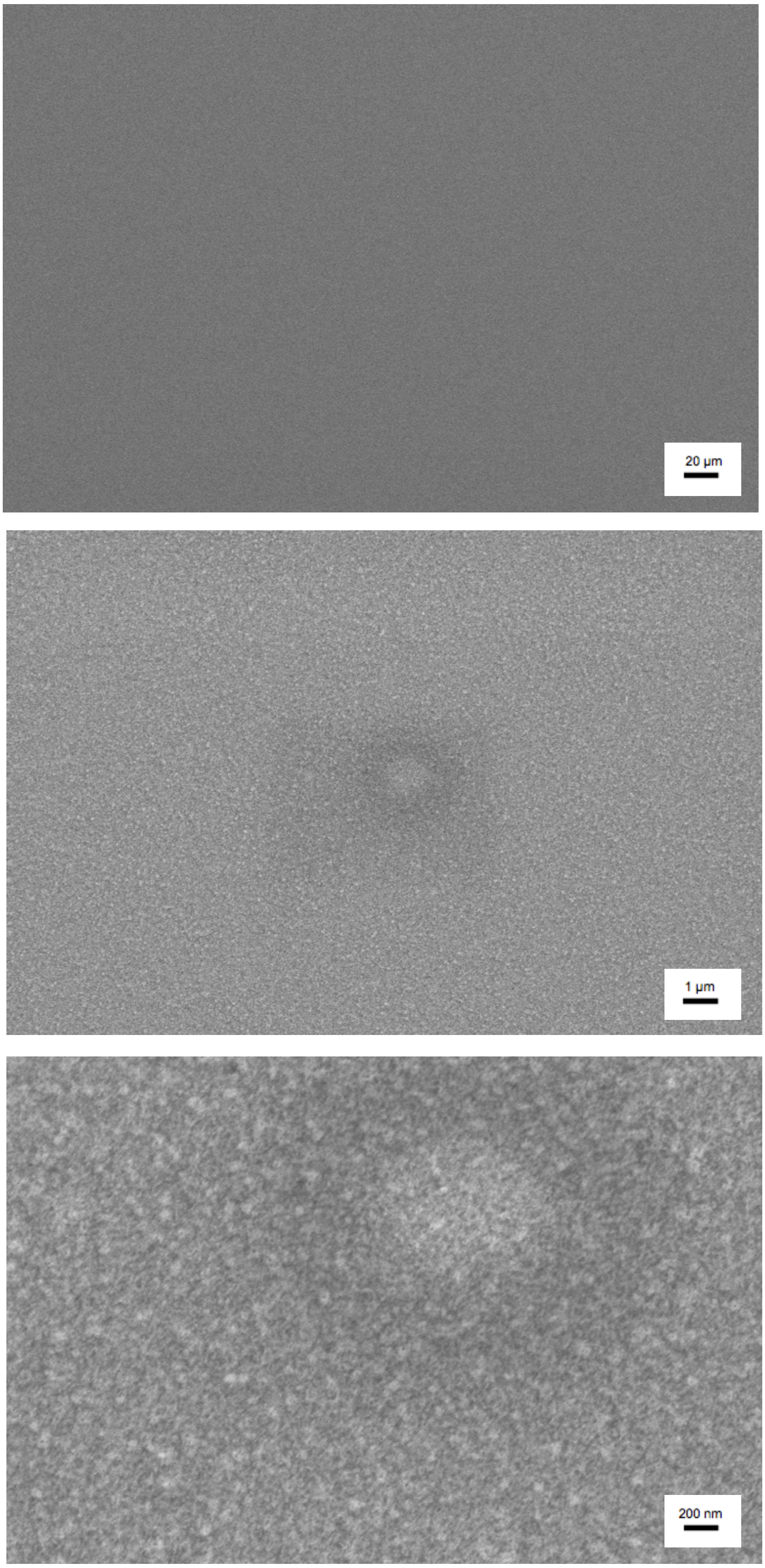

Figure E.4: SEM images of the IZO40%-1-Si-RTP thin film. A square with a circle inside is seen in the center of the middle image. This is not a feature in the thin film, but a beam damage effect. The lower image shows the same beam damage, only zoomed in.

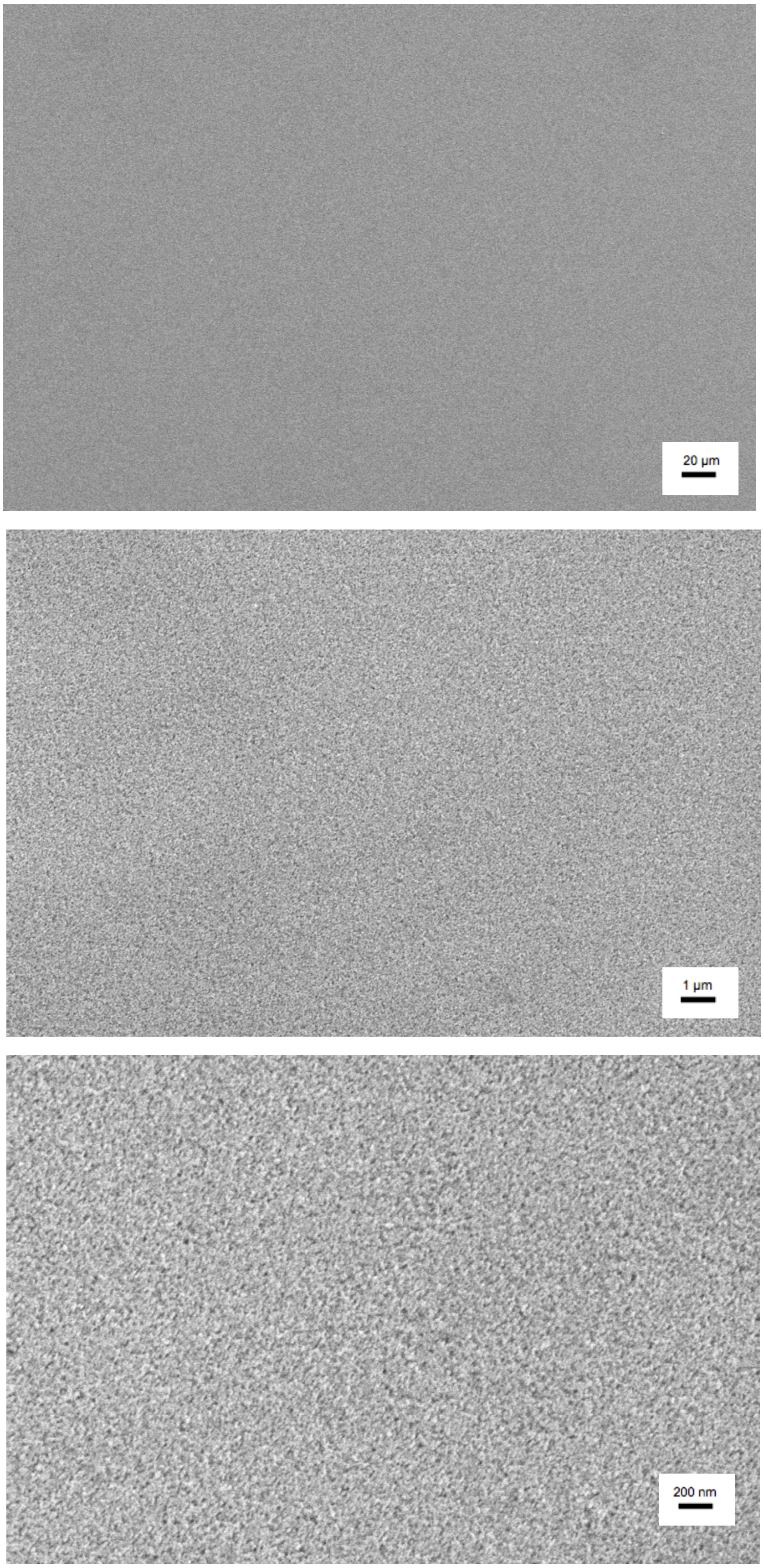

Figure E.5: SEM images of the IZO40%-2-Si-RTP thin film. The high magnification images are taken at point 1 in Figure E.1.

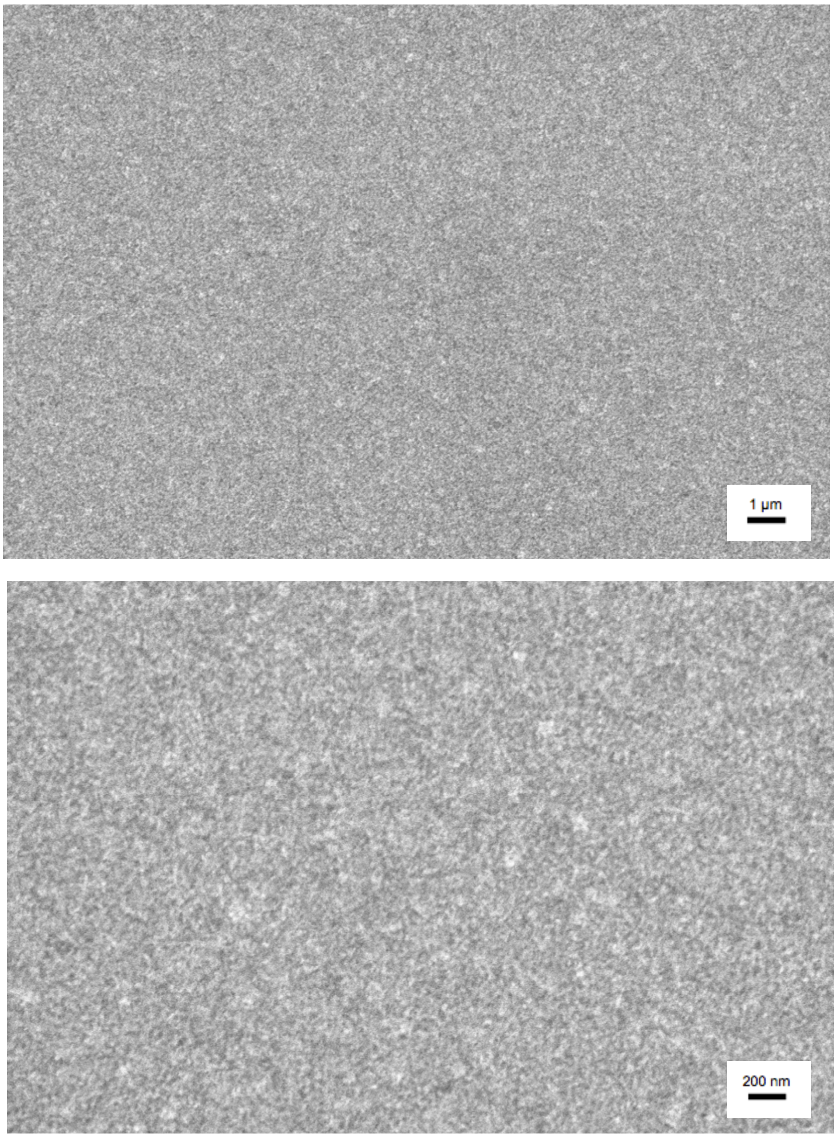

Figure E.6: SEM images of the IZO40%-2-Si-RTP thin films. The images are taken at point 2 in Figure E.1.

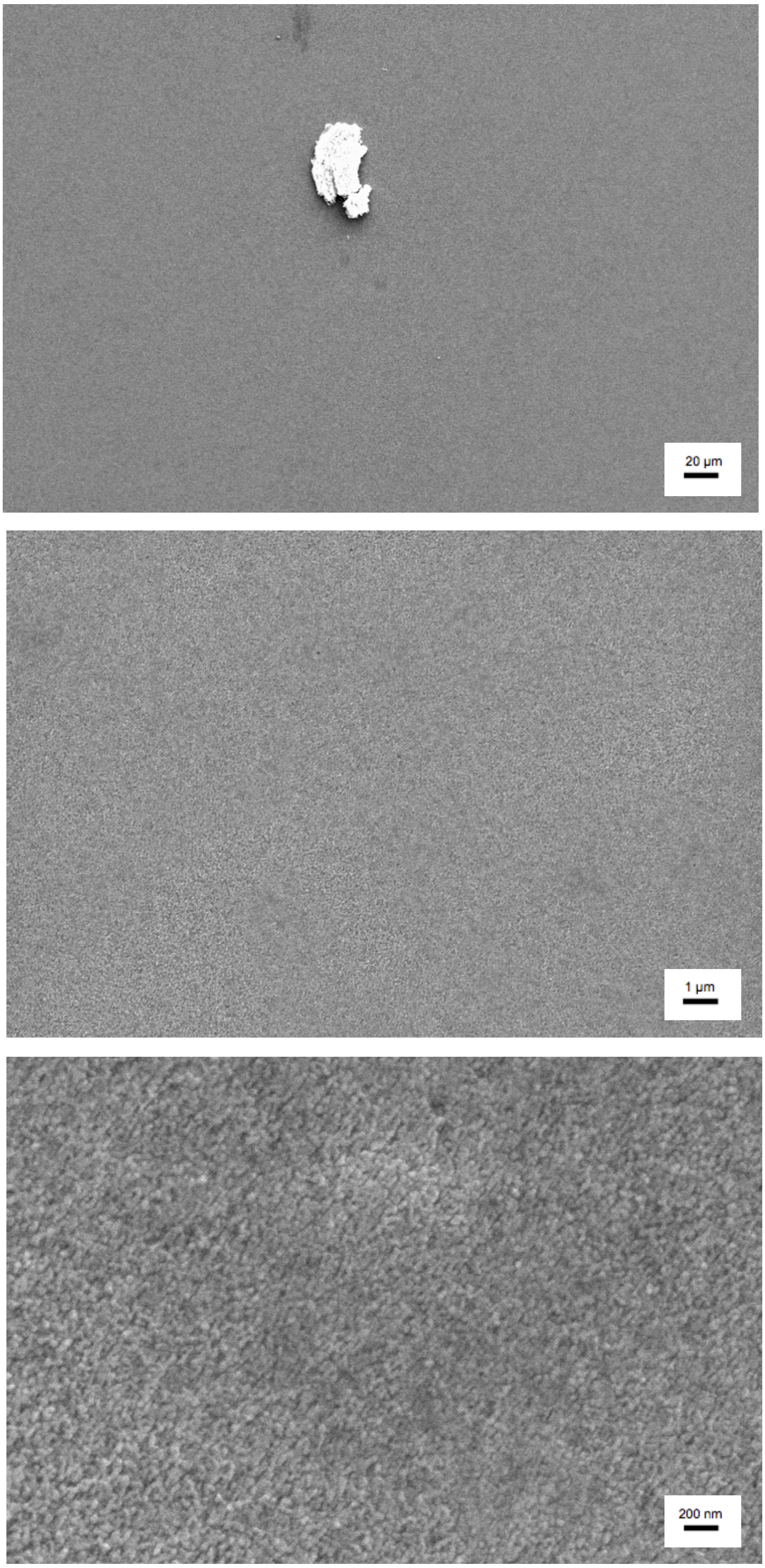

Figure E.7: SEM images of the IZO40%-3-Si-RTP thin film.

Appendix F Profilometer Instrumental Effect

When doing the profilometer scans a steep increase in height with scan length was seen for some of the thin films. This is thought to be an instrumental effect as also discussed in section “5.5 Morphology”.

This effect is seen in Figure 4.41 in section “4.5.4 Profilometer”. Figure E.1 shows a longer scan time of the same scan length as shown in Figure 4.41, while Figure E.2 shows a shorter scan time for the same scan length as shown in Figure 4.42. For the thin film in figures E.2 and 4.42 it can be seen that an increase from 30 to 180 seconds for the scan time was enough to get a realistic profile. For the thin film in Figure E.1, the 360 second scan look quite similar to the 30 second scan in Figure E.2, and based on this it is expected that a further increase in scan time for the thin film in Figure E.1 would give a realistic profile. As already mentioned in the discussion part, the roughness parameters are not affected extensively by the different scan times, thus the roughness parameters obtained for ITO15%-1-g-RTP can still be trusted even though a realistic profile is not obtained. That the steep increase with scan length disappears for longer scan times indicate that this is an instrumental effect. Another argument is that this profile is seen regardless of the direction on the surface in which the scan is obtained. It was also tried to change the force from the stylus on the thin film from 3 mg to 1 mg, but no change was observed. A higher force gives better resolution, but can damage the surface of soft samples.

In figures E.3 and E.4 longer scan lengths from the middle to the edge and across the diagonal of the sample was obtained respectively. From the middle to the edge of the sample an increase in thickness is expected, but the large increase shown in Figure E.3 is unrealistic. Be aware that the scan profile for figures E.3 and E.4 is given in µm and not nm as the other profilometer scans. Since the scan in Figure E.4 is obtained across the entire diagonal of the sample, it would be expected to see a symmetrical profile where the thickness first decreases and then increase. Instead a large overweight of increase is seen, and also here the increase is unrealistically large. It is seen from figures E.3 and E.4 that the effect gets worse with longer scan lengths.

Based on the figures in this appendix and in section 4.5.4 it is concluded that the large increase with scan length is an instrumental effect. It was found that the scan time and scan length were the only parameters that affected the instrumental effect. To get rid of this effect, one should increase the scan time and decrease the scan length.

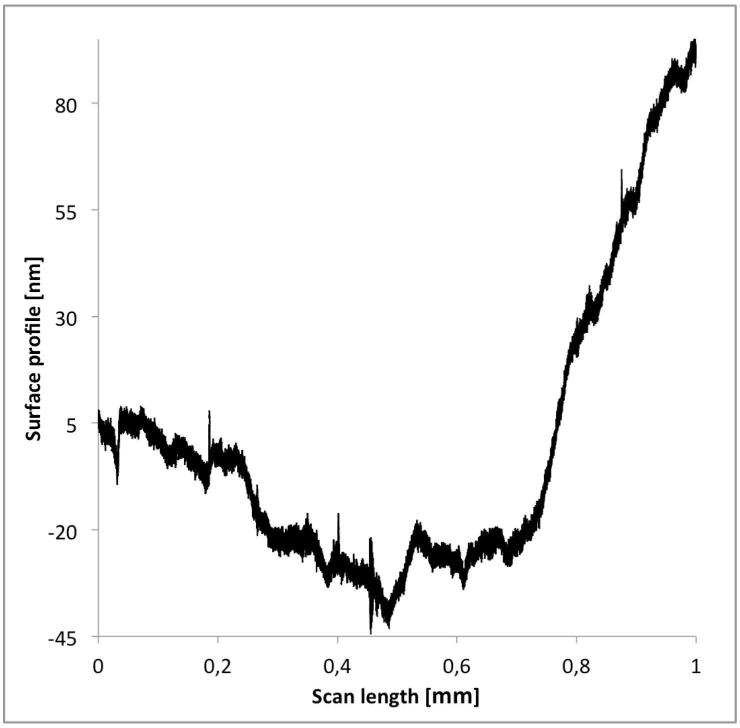

Figure E.3: Profilometer scan for the ITO15%-1-g-RTP thin film with scan time 360 seconds and scan length 1 mm.

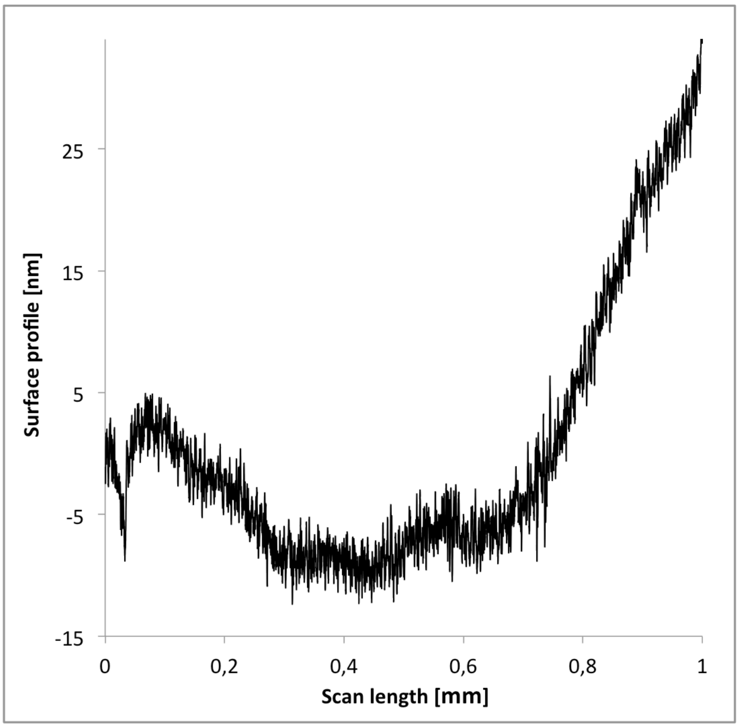

Figure E.3: Profilometer scan for the IZO40%-1-g-RTP thin film with scan time 30 seconds and scan length 1 mm.

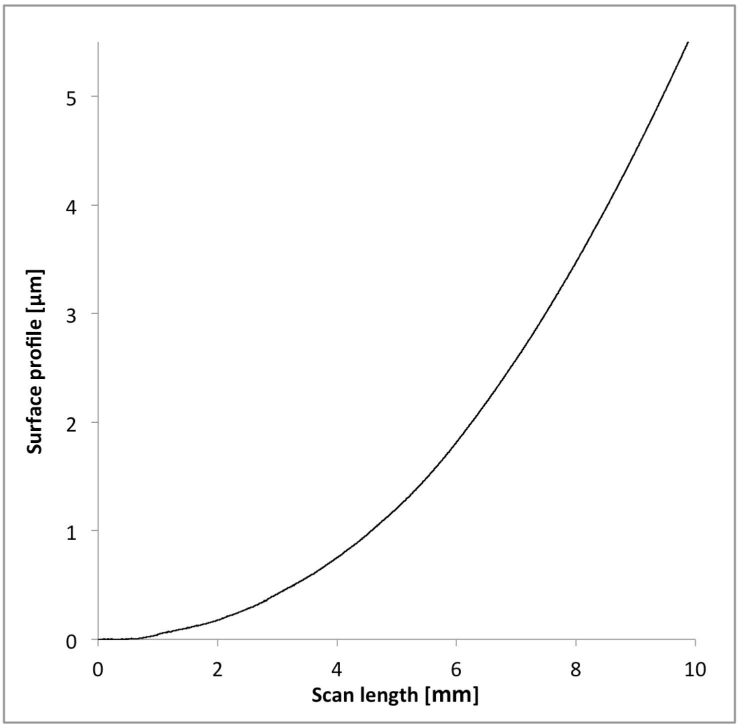

Figure E.3: Profilometer scan for the IZO40%-1-g-RTP thin film with scan time 30 seconds and scan length 10 mm. The scan was taken from the middle of the thin film to the edge of the sample.

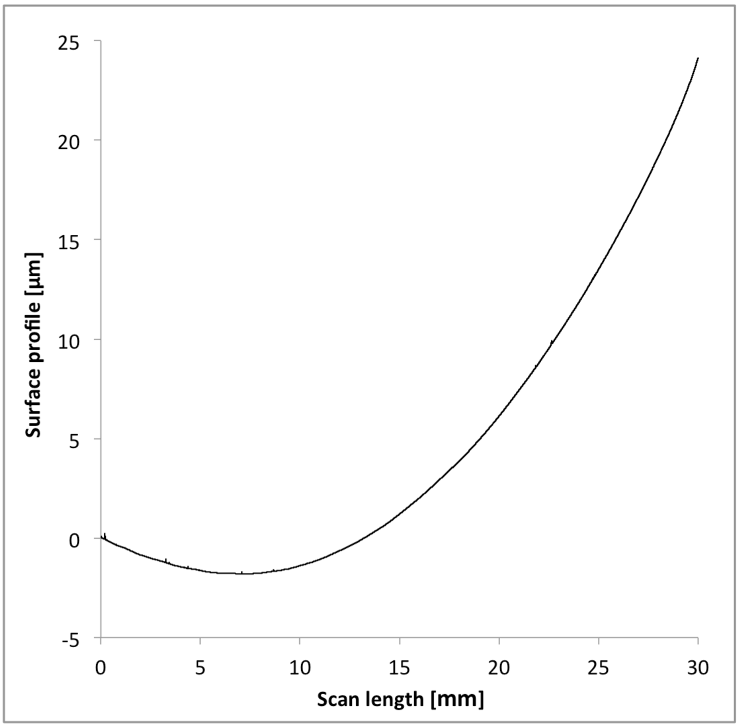

Figure E.4: Profilometer scan for the IZO40%-1-g-RTP thin film with scan time 180 seconds and scan length 30 mm. The scan was taken across the diagonal of the thin film.